UNIVERSITA' DI PADOVA   FACOLTA' DI INGEGNERIA

Dipartimento di Ingegneria Elettrica

Scuola di Dottorato di Ricerca in Ingegneria Industriale
Indirizzo: Ingegneria Elettrotecnica

CICLO XXIII°

AUTO-ADAPTIVE MULTI-COIL INDUCTORS
FOR TRANSVERSE FLUX INDUCTION HEATING
OF METAL STRIPS

Direttore della Scuola: Ch.mo Prof. Paolo Bariani

Coordinatore di Indirizzo: Ch.mo Prof. Giovanni Martinelli

Supervisore: Ch.mo Prof. Sergio Lupi

Dottorando: Ing. Aristide Spagnolo

Sommario

Il riscaldamento ad induzione è una delle tecniche maggiormente utilizzate per il riscaldamento di nastri metallici in movimento continuo. Una tecnologia che si sta sempre piu affermando per questo tipo di lavorazioni è il riscaldamento ad induzione a flusso trasverso (TFH) il quale consente di ottenere rendimenti elettrici molto buoni per il riscaldamento di nastri metallici anche molto sottili e non-magnetici, utilizzando frequenze di alimentazione relativamente basse. Il maggiore svantaggio di questa tecnica è che l'adattamento dell'induttore a diverse dimensioni del nastro è molto problematica. Una tecnologia che potrebbe efficacemente risolvere il problema è quella degli induttori autoadattativi multibobina (MCH). Questo tipo di induttori sfrutta l'interazione esistente tra diverse bobine in modo da regolare il profilo di temperatura tramite il controllo delle correnti di alimentazione. Per prima cosa nella tesi viene esposto un resoconto sulla bibliografia esistente relativa al TFH. Successivamente viene descritto ed analizzato un sistema di riscaldamento MCH con bobine di forma circolare utilizzanto differenti metodi di calcolo analitici e numerici. Il sistema analizzato corrisponde ad un prototipo esistente per il riscaldamento di dischi d'acciaio inox. Nel seguito viene progettato e analizzato un induttore di riscaldamento per nastri in movimento continuo. Sono stati in particolare considerati l'ottimizzazione della geometria e delle correnti delle bobine e l'analisi del concentratore di flusso in riferimento all'uniformità della temperatura della sezione del nastro all'uscita dell'induttore e all'efficienza elettrica del sistema.

Abstract

Induction heating is one of the most effective methods to heat metal strips in continuous movement. Nowadays transverse flux induction heating (TFH) is one of the most interesting induction techniques for this kind of industrial process. TFH allows to reach good electrical efficiency also in the case of non-magnetic and very thin strips heating , using very low supply frequency. The main drawback of this technique is the great difficulty to adapt the same inductor to heat different dimensions of the load. One induction heating method that could solve this problem is the use of auto-adaptive multi-coil inductors (MCH). This kind of inductor uses the interaction among different coils in order to regulate the temperature profile in the strip by controlling the supply currents. In the thesis is firstly described the existent bibliography about TFH. Afterwards a MCH inductor for heating circular stainless steel plates is analyzed using different analytical and numerical computation methods. The analyzed system corresponds to an existing prototype. In the following the design of a MCH inductor able to heat moving steel strips has been designed and analyzed. In particular, for the design, the optimization of the coil geometry and currents has been considered in order to obtain uniform temperature profiles at the exit section of the inductor and good electrical efficiency. The inductor is provided by magnetic concentrators.

Table of Symbols

H: Magnetic field intensity [A/m]

ρ :   Resistivity of material [Ω m]

δ: Penetration depth $\delta = \sqrt{\rho/(\pi f \mu)}$ [m]

f: Current frequency

$\mu = \mu_0\mu_r$: Magnetic permeability of the material [H/m]

μ_r :   Relative magnetic permeability

μ_0 :   Magnetic constant of vacuum [H/m]

$\sigma=1/\rho$:   Electrical conductivity of material [S]

t: Pole pitch [m]

D: Pole length [m]

h: Strip to coil air-gap [m]

P: Active power [W]

Q: Reactive power [var]

γ :   Material density [kg/m^3]

c_p :   Heat capacity [$J/kg/K$]

$\Delta\theta$:   Temperature difference [K]

S: Surface [m^2]

v_s: Strip Velocity [m/s]

$\eta = \eta_e\eta_t$: Total efficiency

η_e: Electrical efficiency

η_t: Thermal efficiency

F: Electromagnetic force [N]

J: Current density [A/m²]

B: Magnetic flux density [T]

∇ :   Gradient

$\nabla\cdot$:   Divergence

$\nabla\times$:   Curl

A: Magnetic vector potential

K:	Laminar current density,
a:	Half internal length of the coil (TFH3D) [m]
b:	Half internal width of the coil (TFH3D) [m]
d:	Width of the coil [m]
f:	Computation length in TFH3D [m]
2s:	Strip thickness
w:	Heat source density [W/m^3]
$c\gamma$:	Volumetric heat capacity [J/m^3/K]
λ:	Thermal conductivity [W/m/K]
T:	Temperature [°C]
t:	Time [s]
L:	Inductance [H]
C:	Capacity [F]
Z:	Impedance [Ω]
V:	Voltage [V]
I:	Current [A]
$[X]$:	Matrix
$\bar{X}$:	Complex number
$\check{X}$:	Conjugate of a complex number
$|X|$:	Module or absolute value
$\boldsymbol{X}$:	Vector
rms:	Root mean square
$\Re$:	Real part of a complex value
$\Im$:	Imaginary part of a complex value
ω :	Angular frequency [s^{-1}]
φ :	Current phase displacement [°]
Ψ:	Voltage phase displacement [°]
π :	Pi constant
$\Delta\theta$:	Temperature difference [K]
L_{strip} :	Length of the strip integration surface [m]
W_{strip}:	Strip width [m]
W:	Profile function of the accumulated energy [J/m^3]
N:	Turns number
NI:	Ampere-turns [Aturns]
Vol:	Volume [m^3]
Δ E%:	Minimum temperature profile deviation in respect to the mean temperature value
ZCIH:	Zone Control Induction Heating
TFH:	Transverse Flux induction Heating
MCH:	Multi-Coil transverse flux induction Heating
LFH:	Longitudinal Flux induction Heating
PSO:	Particle Swarm Optimization

Contents

Introduction

Nowadays we are about to witness an historic turning-point in the way to design industrial facilities and devices. As response to the problem of the global warming the European Union produced the "EU Climate and Energy Package". In this document a big challenge is planned for the European Union: within the year 2020, 20% consumption coming from renewable energy, 20% less greenhouse gas emission, 20% reduction in primary energy use, to be achieved by improving energy efficiency.

The big contribution is expected from the progress of the technology and, to reach the goal, the most energy consuming and polluting hot spots have to be determined. Concerning this, industry in Europe consumes almost 1/3 of the total European energy, and the potential energy savings by using "Best Available Technologies" (BAT) are estimated at 20% of the baseline energy consumptions [1], [2].

In this context the steel industry has been recognized to be one of the most energy consuming hot spots and one of the main possible savings are for furnaces and dryers as shown in the diagram of Fig. I.1. Now the focus of the industrial design is not only aimed to obtain a good and economical product, but also to obtain a product with the least loss of raw matter and fuel in form of electricity, gas and so on.

The great majority of the treatment of metallic materials is conventionally done in batch ovens and annealing furnaces based on gas-fired or electrical resistance heating methods. In these types of heating methods the loss of energy is very high; this is due mainly to the nature of the conventional processes which need long heating and pre-heating times, and which have low energy efficiency. Moreover, from an industrial point of view, the conventional heating methods have often low operation flexibility and productivity.

Concerning the steel industry, the strip heating is an important part of the manufacturing lines. Strip heating is applied mainly for coating, galvanizing, maintaining, annealing or drying strip of magnetic (ferrous) and non magnetic (stainless steel, aluminium, brass, copper, magnesium) and often precious materials (gold and silver). It can be considered that, depending on the country, the strips and slabs manufacturing can reach the 70 % of the manufacture of the steel industry. The great potential of en-

ergy saving in this field of industry, improving the efficiency of the installations, can be than understood.
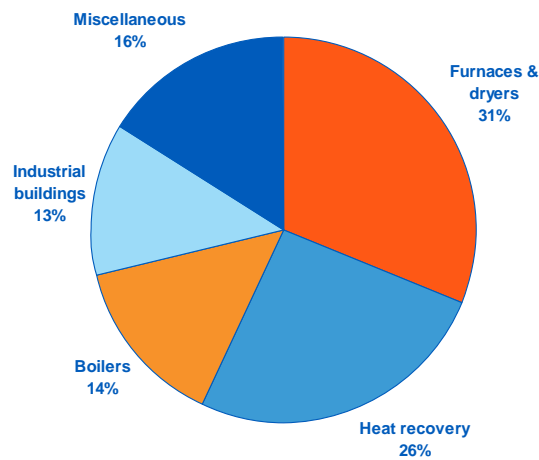
Fig. I.1: Energy saving potentialities

Since the early development of the induction heating techniques it was recognized its high potential on heating strips and slabs. The induction heating takes advantage of the production of eddy currents when a metallic work-piece is placed near to a conductor carrying a current. The induced currents heat the work-piece by means of the Joule effect. Two main induction technologies exist today to heat thin strips by induction (see chapter 1 for details):

- Longitudinal flux induction heating (LFH) in which the flux is tangential to the strip surface

- Transverse flux induction heating (TFH) in which the flux is perpendicular to the strip surface.

Between them the TFH method has some very attractive characteristics, confirmed by several installations running successfully worldwide:

- The possibility of applying very high power densities (which means heating lines much shorter in comparison e.g. with those with resistance furnaces); the heating rate reached can be of hundreds degrees per second;

- High energy efficiency values (up to 95% for the electrical efficiency)

- Use of much lower frequencies in comparison with the LFH, in particular with non-magnetic materials or for materials above the Curie point when the material becomes non-magnetic. This means fewer losses in the electronic switches of the power supply and simpler design of the apparatus that in fact reduces the total cost of the installations.

Naturally, TFH faces some drawbacks issues from the classic induction heating due to its own specificities. They can be summarized as follow:

- The difficulty of controlling the temperature uniformity, and the low flexibility of a given inductor in heating strips of different sizes

- The design problems cannot be solved with simplified 2D mathematical models since they are real 3D problems with a large number of influencing parameters

- The process could produce mechanical deformation, vibration and noise because of the non uniform shape of the heat pattern produced in the work-piece.

- The relatively high initial investment costs due to the sophisticated electric and electronic apparatus constituting the device.

Probably the most critical drawback is the problem of obtaining the temperature uniformity when the dimensions of the load change, which has been tentatively solved with inductors allowing mechanical movements of the inductor components, e.g. coil conductors or magnetic concentrators.

Recently a new method called zone controlled induction heating (ZCIH) has been proposed and optimized to solve these problems in the case of axis-symmetric configurations with stationary load. The technique consists in combining the effects of multiple concentric coils driven by currents with different amplitudes and phases, at the same frequency, in order to obtain a temperature profile as much as possible uniform along the radius. The feasibility of such a system has already been demonstrated in the literature for units with relatively limited power. [3]. Now the challenge is to verify if the ZCIH is applicable to industrial installations with moving loads and high power. This technique is called auto-adaptive multiple coils induction heating (MCH) in which the temperature profile is automatically set by a control system according to the metallurgic requirements Fig. I.2. The thesis is aimed to verify the current progress of this technique and to extend the method to the TFH for the continuous heat treatment of steel strip in which a metallic strip is in continuous movement inside the heating inductor.
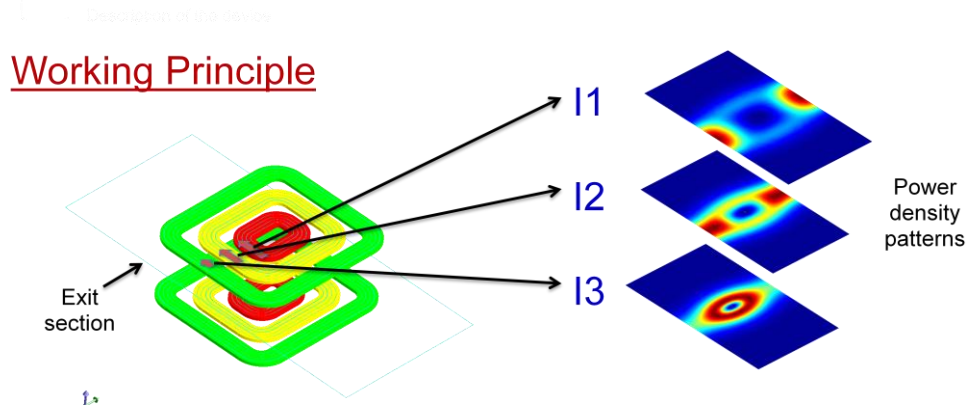

Fig. I.2: Working principle of a multi-coil inductor for heating moving strip

The final objective is to design a MCH device at a semi-industrial scale, capable to heat stainless steel strips between 800 and 1200 mm width with the same inductor, without making use of mechanical modifications on the inductor structure.

The main difficulties related to the project are the following:

- The large dimension of the whole system in comparison to the skin depth of the metal at the considered frequency, which means that computation models with high simulation time and memory consumption are needed.

- The coupling of magnetic-thermal-mechanical differential equations.

- The need to optimize the geometry of the inductor in presence of electrical constraints given by: power supply, mechanical constraints due to the different dimensions of the strip and characteristics of the industrial process. The difficulty is mainly due to the very large number of electrical and mechanical parameters to be optimized in the design.

Furthermore the design is strongly inter-dependent by the constraints of the power supply (analyzed in another thesis [4]), like the inverter structure, the resonant capacitors and the control algorithms.

The MCH technology could resolve the cold acceptance of the industries about the use of TFH for strips heating, thanks to the intrinsic simplicity of the installation, and the simplicity of operation in the manufacturing line. Once the device will be validated and tested, it is expected that more industries will become aware of the numerous advantages of induction heating, among which the energy saving due to the high efficiency of the installations.

▪ Actors of the project

The design of the multi-coil inductor was launched by Electricité de France (EDF R&D - EPI group) in collaboration with the University of Padua, and in parallel with another PhD works from the ENSSEIHT Toulouse dealing with the electronic power supply design [4]. EDF R&D, as energy distributor, makes research in the field of the energy efficiency in order to promote the use of electricity in the industry. In the final period of the thesis the manufacturer Five Celes, has been engaged in the manufacturing of the system.

▪ Structure of the thesis

Since the multi-coil induction heating has several characteristics similar to the classical TFH devices, in the first part of the thesis a review of the previous knowledge about the matter will be reported.

This work starts from a feasibility study previously done by EDF [5] which has allowed them to build a simplified prototype of a multi-coil induction heating system with three coils, for circular static loads. Since the prototype was never been tested before, the first part of the PhD work was devoted to analyze the circular system in order to define the characteristics of the bank of capacitors and the control sequence for the electronic switches. Several computation methods have been tested and the results have been compared with the data of tests performed on the prototype.

The main goal of the thesis work was to develop an inductor able to heat steel strips in continuous movement. The problem will be approached analyzing a first rectangular inductor for strips having widths in the range between 500 and 1000 mm, with a power supply of 200 kW max, defining the number and shape of coils, the characteristics of the magnetic concentrators and evaluating the performance of the system.

The results of the first analysis have shown that a margin of improvement exists as regard both the uniformity of temperature and the increasing of the maximum power of the inductor by means of a geometry optimization. In collaboration with Five Celes new specifications have been finally defined in order to build a prototype at a semi-industrial scale, able to heat stainless steel strips from 800 to 1200 mm width with a power supply of 600 kW comprising a rectangular six-coil inductor. A procedure to optimize the inductor geometry based both on analytical algorithms and an auto-parameterized stochastic optimizer (PSO) has been implemented. The optimization method is aimed to reach the best temperature profile at the exit of the strip from the inductor, with the maximum installed power. In particular the procedure has been initially tested for optimizing a system able to heat strips of width ranging from 600 to 800 mm. The results of the optimization have been afterwards completed in order to cover the whole range of strip widths, and the inductor has been adapted to match the specifications.

The last part of the work was devoted to the final analysis of the inductor verifying the performances and refining the optimization of the temperature profile.

Schematically the thesis is structured as follows:

- Chapter 1 - Transverse Flux Strip Heating: analysis of the bibliography on transverse flux heating. Description of the current knowledge on the matter and the main available solutions.

- Chapter 2 - Analysis of a circular MCH system: Analysis of the status of the art on MCH and of the computations made on the laboratory prototype of a circular MCH system. Modelling, impedance computation and comparison with test data.

- Chapter 3 - System for heating moving strips: analysis and design of a rectangular MC-TFIH system. Feasibility, geometrical optimization, modelling.

- Chapter 4 - Final inductor design: analysis and design of the final prototype, impedance computation, thermal analysis.

- Appendix A - Software FluxGrid

- Appendix B - Steel characteristic

- Appendix C - Computation of planar circular inductor

- References

Chapter 1

Transverse Flux Strip Heating

Transverse Flux induction Heating (TFH) has been used for many years to heat thin metal strips. This is due to the relative better efficiency of such kind of systems in comparison with longitudinal flux methods, which can be reached at low frequencies. High density transverse flux allows the induction heating of any metal strip, aluminum, stainless steel, and carbon steel even above the Curie point when the material becomes non-magnetic.

The main problem of this technology is the limited flexibility of the installations; when the geometrical characteristics of the strip to be heated change, the profile of the temperature obtained changes considerably in comparison with the previous one. In order to solve this problem, the common solution is to adjust the geometry of the inductor to the different load dimensions. Up to now several systems that use this principle have been developed, but all of these systems need the use of moving mechanical parts. These solutions are not practical in many cases and often expensive.

Another problem of TFH is that, due to the potential deformations and the transversal movements of the strip, the inductor should be capable to follow the movement of the strip and a real time control of the heating would be necessary. For the moving devices the control of the profile by means of automatic systems is difficult due to the complexity of the mechanical systems.

Despite these drawbacks the traditional TFH is nowadays used in a large number of applications, for replacing or boosting old furnaces with less space needed and more induced power density, or to realize new processes for metals like for examples the heating in protective atmosphere and the production of new steel products with better characteristics.

The development of TFH system started in the second half of the twentieth century, but at that time the available computation means didn't allow the complete knowledge

of all the involved parameters. Later, with the development of the computer technology, the TFH has been analyzed by many research groups worldwide, and now a solid know-how exists in the design methods of this kind of systems.

In the following sections an overview of the general theory and of the solutions developed to overcome the drawbacks of TFH will be reported. A good review of the main information and progress on the subjects can be found in [6] and [7]. Following these books and some other papers found in the literature, an overview of the main characteristics of the classical TFH will be reported. This basic theory is fundamental for understanding the design of the MCH system developed in the following chapters.

1.1 Industrial heating of metal strips

Since the early development of the induction heating techniques it was recognized its large potential on heating strips and slabs. As already remarked in the introduction, the two main induction technologies used nowadays in order to heat thin strips by induction are Longitudinal Flux induction Heating (LFH) (Fig. 1.1-a) and Transverse Flux induction Heating (TFH) (Fig. 1.1-b).

The use of LFH in thin strip heating, compared to the billet and bars heating, is not satisfactory due to its low efficiency, low power factor, relatively low power densities and the need of expensive high frequency power converters. Its limitations come mainly from the following points:

- Only a small part of the flux produced by the inductor passes through the cross section of the strip.

- Radiofrequencies (>100kHz) are required to obtain good coil efficiency.

(a)   (b)
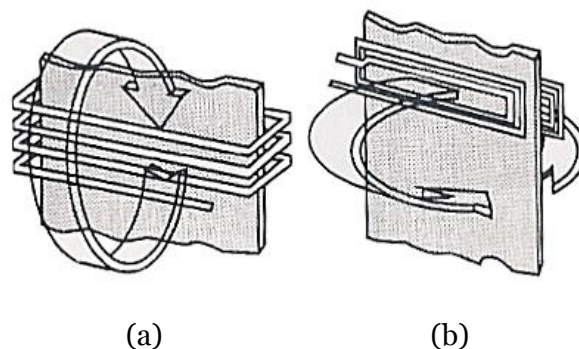
Fig. 1.1: Longitudinal and transverse flux induction heating

In order to understand the difference between TFH and LFH it in interesting to consider the simplified system shown in Fig. 1.2-a, in which there is a conducting slab with two conductors carrying currents, placed in both sides of the slab. The excitation currents circulate respectively in the opposite directions and the slab is considered having an infinite length along the direction of the current. This is the case of the conventional LFH. The magnetic field H is perpendicular to the currents and it has the same direction on the two sides of the metallic slab. As a consequence currents with opposite di-

rections on the two faces are induced in the conductor. The induced current in the middle of the thickness is null. The solution of Maxwell equations for this case gives eq. (1.1) for the value of the power P dissipated in a strip unit length.

$$P_{LFH} = H^2 \frac{\rho}{\delta} K_{LFH}$$ (1.1)

where:

- H: Magnetic field intensity

- ρ : Electrical resistivity of material

- δ: Penetration depth $\delta = \sqrt{\rho/(\pi f \mu)}$

- f: Frequency of the currents

- μ : Magnetic permeability of the material

- a: Thickness of the slab

(a)   (b)
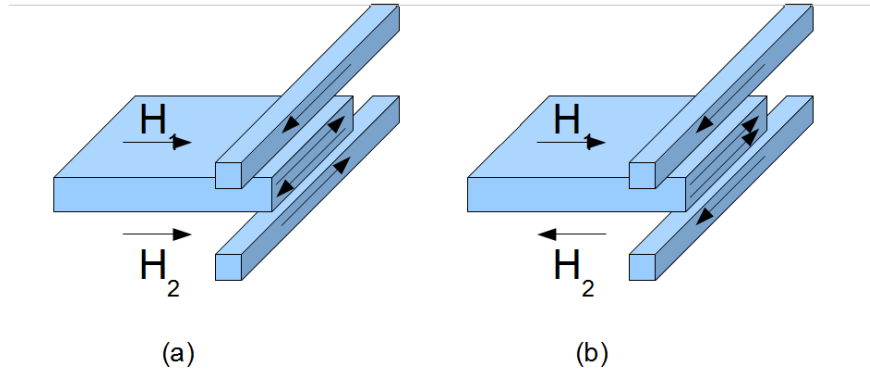
Fig. 1.2: Longitudinal and transverse flux induction heating principle

The coefficient K_{LFH} takes the following form, shown graphically in Fig. 1.3:

$$K_{LFH} = \frac{sinh\frac{a}{\delta} + sin\frac{a}{\delta}}{cosh\frac{a}{\delta} - cos\frac{a}{\delta}}$$ (1.2)

The maximum of power in this case can be obtained with a value of the ratio a/δ of about 2.5. Due to the thin thickness of the strip, very high frequencies are necessary to obtain high induced power values.

In the case of TFH (Fig. 1.2-b), on the contrary, the current flows in the same direction in the conductors. The magnetic field has opposite directions on the two sides and the solution of Maxwell equations gives the following expression for the power dissipated in the unit length:

$$P_{TFH} = H^2 \frac{\rho}{\delta} K_{TFH}$$ (1.3)

with the coefficient K_{TFH} given in eq. (1.4), shown in Fig. 1.3:

$$K_{TFH} = \frac{sinh\frac{a}{\delta} - sin\frac{a}{\delta}}{cosh\frac{a}{\delta} + cos\frac{a}{\delta}}$$

(1.4)
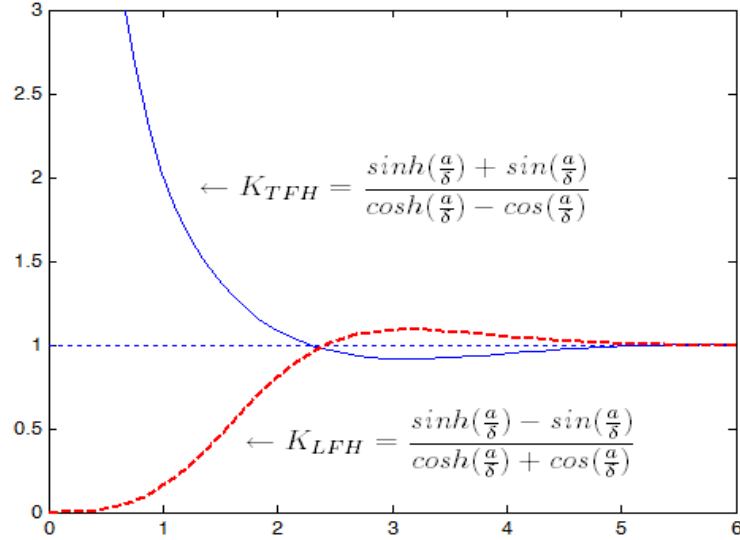
Fig. 1.3: Power coefficient for TFH and LFH as a function of a/δ

In this case the current in the middle of the slab thickness is not null and the induced power increases when the frequency decreases. Obviously in the real system the power is non infinite at zero frequency, but it can be understood that the advantage of transverse flux heating is to have the possibility to heat thin metal slabs with relatively low frequency.

From the considerations described in the introduction, it can be concluded that the design a transverse flux inductor is a complex matter and can be made only by means of sophisticated software or by extensive campaigns of tests on prototypes. In general the main points that have to be taken in account when designing an efficient TFH installation are:

- Achievement of the desired uniformity of the temperature distribution at the considered section of the load

- The permissible level of mechanical phenomena (strip deformation, vibration and noise)

- Good electrical characteristics (e.g. efficiency and power factor)

1.2 Physic of TFH

As above mentioned the result of TFH depends from several physical and geometrical parameters which modify in different ways the heating process. In the following paragraph these parameters will be analyzed, and their influence on the physic of the

TFH will be described. The main phenomena occurring in a TFH system are the edge effect, i.e. the modification of the current density distribution due to the edge of the strip, the modification of the power density patterns given by the non-linearity of the parameters, and the deformation of the strip due to the thermal effects and to the electromagnetic forces. The information of the next paragraphs was taken from [6], [7] in which the principles of TFH are well described.

1.2.1 Influence of parameters

In transverse flux induction heating the strip passes through the induction coil pairs that are located on both sides of the strip, as shown in Fig. 1.4. These coil pairs create a common magnetic flux that passes perpendicularly through the strip width. The alternating flux produces an induced current loop parallel to the surface of the strip, heating it by Joule effect.

Generally, electrical efficient heating can be provided when the coil-to-strip air gap h is relatively small and the strip thickness $2s$ is 1.5 to 2 times the penetration depth or less. Without satisfying the latter condition, the transverse flux effect will disappear and conventional proximity heating (similar to heating with two pancake coils) will take place. Proximity heating is known for having lower coil efficiency compared to transverse flux heating. In some cases however it is impossible to have small air-gaps, due to mechanical constraints, but the main advantages of TFH remain.

An important consideration that distinguishes TFH from longitudinal induction heating of bars and billets is that heating time of TFH is typically quite short; therefore the thermal conductivity does not help to equalize the temperature gradients across the strip width.
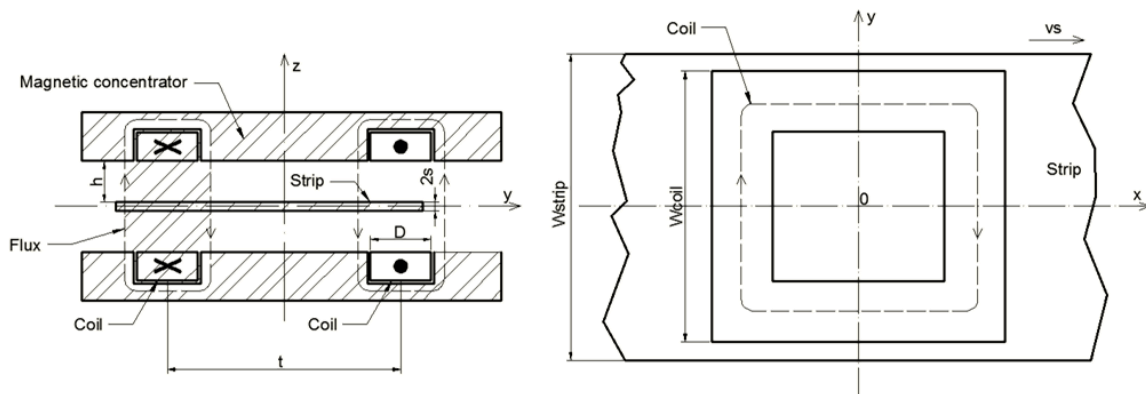
Fig. 1.4: Sketch of conventional TFIH (h: Air-gap, D: Pole length, 2s: strip thickness, t: Pole pitch, Wstrip: strip width, Wcoil: coil width)

As seen in par. 1.1, the physical parameters that influence the penetration depth into the metal to be heated have a strong influence on the transmitted power. In addition to the electromagnetic properties of the heated metal and strip dimensions, there are four other factors that have a major impact on the coil electrical parameters (i.e. coil efficiency and coil power factor) and greatly affect the temperature profile across the strip width (Fig. 1.4):

- Pole pitch - *t*,

- Pole length - *D*

- Air-gap - *h*

- Frequency - *f*

Fig. 1.5 shows as an example the results of evaluation of coil efficiency and coil power factor of a transverse flux induction heater for a 6 mm thick strip made of three different metals. Fig. 1.6 shows as example the coil efficiency and coil power factor of TFH of titanium strip (1 mm thick) as a function of frequency for four different pole pitches [8].

The above curves show that the coil power factor has a well defined maximum. This feature is critical for load matching the inductor to the power supply. At the same time, the maximum of the coil efficiency curves is not as pronounced as the maximum of the coil power factor.

A properly designed TFH should allow to obtain high coil electrical efficiency values in the range of 70% to 85 % in combination with a generous coil opening and the inductor's ability to produce repeatable temperature profiles that would be practically immune to variation of the work piece width, thickness and positioning inside the inductor.
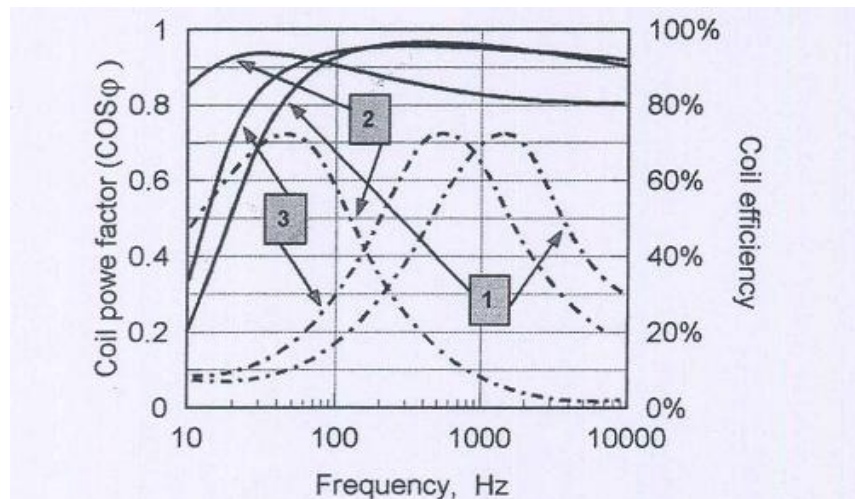

Fig. 1.5: Coil efficiency (solid lines) and coil power factor(dotted lines) of TFIH of a 6 mm thick strip made from different metals as a function of frequency: 1=titanium 2=aluminum 3=stainless steel, pole length = 90mm, pole pitch = 180 mm; and coil to strip air gap = 37 mm [8].
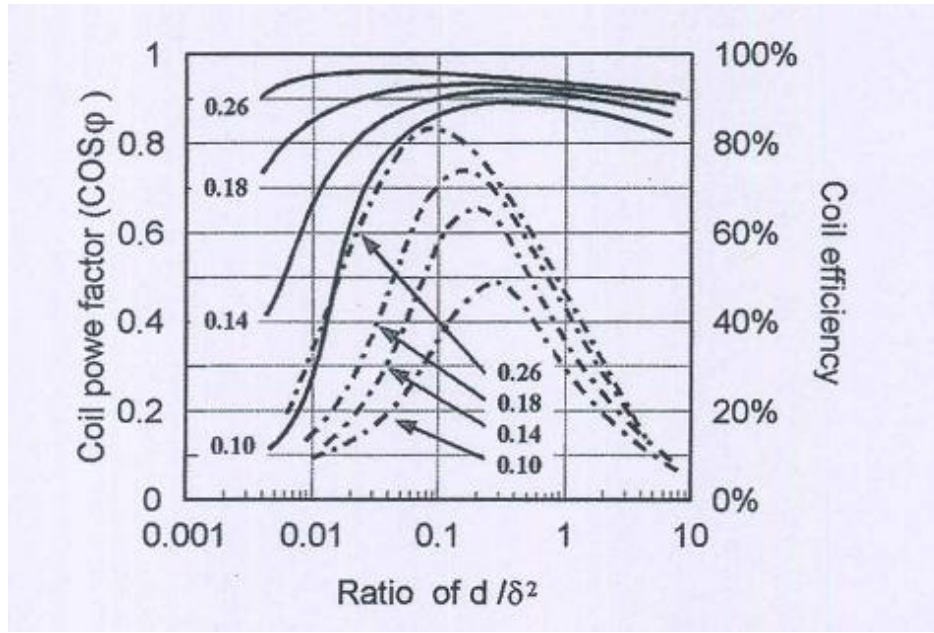
Fig. 1.6: Coil efficiency (solid lines) and coil power factor (dotted lines) of TFH of titanium strip (1mm thick) as a function of d/δ² for different poles pitches: 0.1-0.18-0.26 m (pole length/pole pitch = 0.5, half air gap/pole pitch = 0.23). (d:thickness, δ:penetration depth) [8].

Deep theoretical work and mathematical modeling, devoted to relate the TFH parameters with the heating process, have been conducted at Hannover University, Padua University, InductoTherm Corp., Inductoheat Inc., EDF R&D and some other University and research laboratories. In the bibliographic research made on the TFH subject more than 150 papers on TFH have been analyzed. In the following sections the influence of the main electrical and geometrical parameters on the heating of the strips will be more deeply presented making reference to a selection of these works.

Preliminary choice of design parameter

The first step of the design is the calculation of the power to be transformed into heat in the strip in order to obtain the required production rate.

$$P = \frac{\gamma c_p \Delta \theta S v_s}{\eta} \tag{1.5}$$

where

- P: Power of the supply system [W]
- γ: Material density [kg/m^3]
- c_p: Heat capacity [$J/kg/K$]
- $\Delta \theta$: Required temperature increase [K]
- S: Strip cross section [m^2]
- v_s: Velocity [m/s]

23

- η :   Total efficiency (thermal and electrical)

The subsequent step is the preliminary tentative choice of some design parameters according to the following rules suggested in the bibliography [9], [10]:

- The value of the air-gap *2h* should be assumed as small as possible from the electrical point of view, but cannot be reduced below certain values dictated by the space requirements of the thermal insulation and the necessity of assuring a free movement of the strip inside the inductor, considering the inevitable vertical vibration and horizontal oscillation. A suggested compromise is:

$$\frac{2h}{t} \leq 0.5 \tag{1.6}$$

- Several different formulas have been developed in the past for selecting the frequency that provides high electrical efficiency using transverse flux induction heating for non magnetic strips. The exciting frequency can be chosen for example according the relationship:

$$f = 2.1 \cdot 10^6 \cdot \frac{\rho}{t^2} \cdot \frac{h}{s} \cdot k\left(\frac{2h}{t}\right) \tag{1.7}$$

where ρ is the electrical resistivity [Ωm], h the distance from the coil and the strip [m], t the pole pitch [m] , s the strip thickness [cm], and k a coefficient depending on the ratio *2h/t*, ranging from 0.42 to 1.90.

- The optimum ratio between the slot width c (equal to the inductor coil width) and the pole pitch t should be chosen in the range:

$$0.4 \leq \frac{c}{t} \leq 0.75 \tag{1.8}$$

- The increase of this ratio towards the value 0.75 produces a more uniform power density distribution, but reduces notably the total power transferred to the strip. An acceptable compromise can be the value *c=t/2*.

In the following paragraphs some specificities that have to be taken into account in TFH installations will be discussed more in detail. These include the influence of the frequency on the design, the edge effect, the shape of the coil, the non-linear characteristics of the materials (thermal and magnetic), the deformation and the noise caused by the installation.

It is clear that due to the high number of factors that characterize transverse flux heating it is not possible to define a relative simple theory which describes completely the process.

Edge effects

In TFH, the induced current paths in the strip reflect the shape of the transverse flux induction coils. Therefore, where the coil width is greater than the width of the strip, when the currents reach the strip limit, it cannot follow the coil path, being obliged to flow along the edge (Fig. 1.7). Because of these natural phenomena the current

concentration will be higher in the strip edge area compared to the strip central area and, as a result, the strip edges will be overheated. On the contrary, if the coil transverse overhang is negative (i.e. the strip width is greater than the coil width) then the strip edge areas will be under-heated because the eddy current will not reach the strip edges. Somewhere between these extreme cases there is a condition for reasonably uniform heating. Fig. 1.8 shows three of the most typical temperature profiles across the strip width.
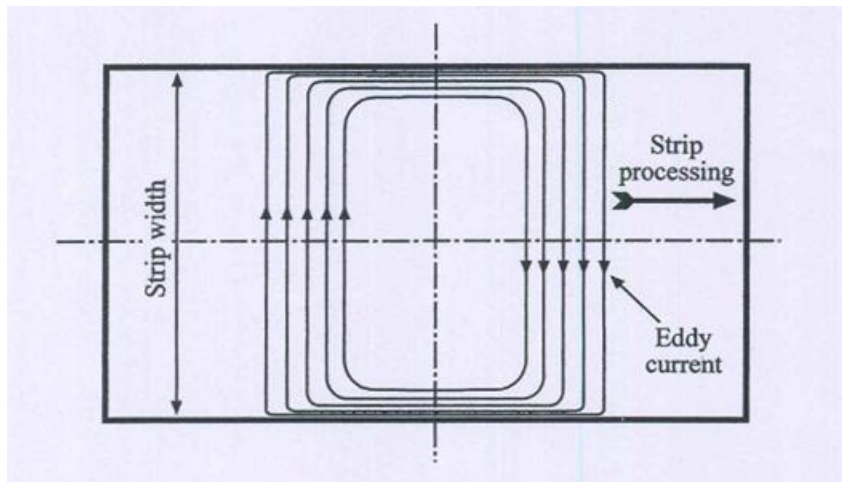
Fig. 1.7: Induced current flow in conventional TFIH [7].
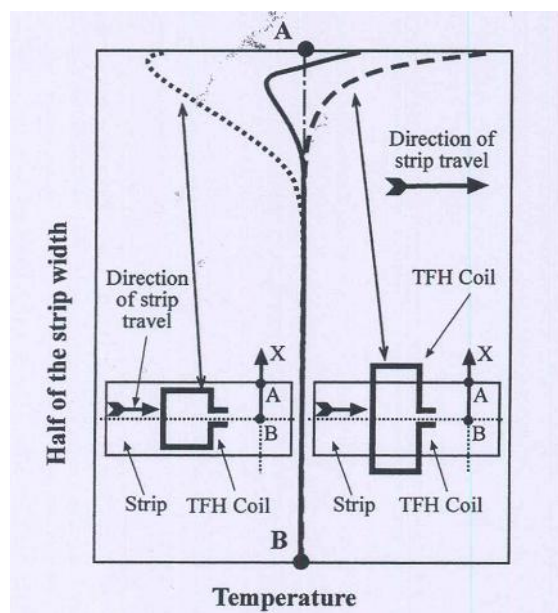
Fig. 1.8: Typical temperature profiles across the strip width using conventional transverse flux inductor [7].

The uneven distribution of the specific power of TFH leads to complicated heating profiles. In the longitudinal direction, a non-uniformity of the induced power exists, but it is not very important for progressive heating since the tape moves through the induction system. However problems for thermal deformation can appear if different parts of the work-piece start to be heated at different times.

The transversal edge effect, on the contrary, is the main problem of the heater design, which should be solved when a new inductor or technological process is developed. The heating uniformity can be estimated by integration of the volume induced power density in the work-piece along lines parallel to the movement direction. These integrals of volume power density evaluated at the output of the system along a line perpendicular to the movement direction define the energy transferred to the work-piece and therefore the uniformity of heating along the strip width. The total energy transferred to the edge can be considerably different in comparison with the one of the middle (or "regular") zone. Basically the edge effect depends on skin effect, inductor geometry and material properties. The edge effects always occur when TFH systems are used and the priority in most applications is to reduce this effect as much as possible. Two typical configurations of TFH inductors are shown in Fig. 1.9 [11]. Depending on the inductor configuration there are four or seven peaks of the induced power density.

The selection of suitable pole pitch and frequency values is the simplest method for controlling the edge effect. The relative power distribution (referred to the value in the central regular zone) along the width of the work-piece heated in the induction system of Fig. 1.9, is illustrated in Fig. 1.10. The edge effect, characterized by a "hole" of the energy and a subsequent increase near the edge, is clearly visible.
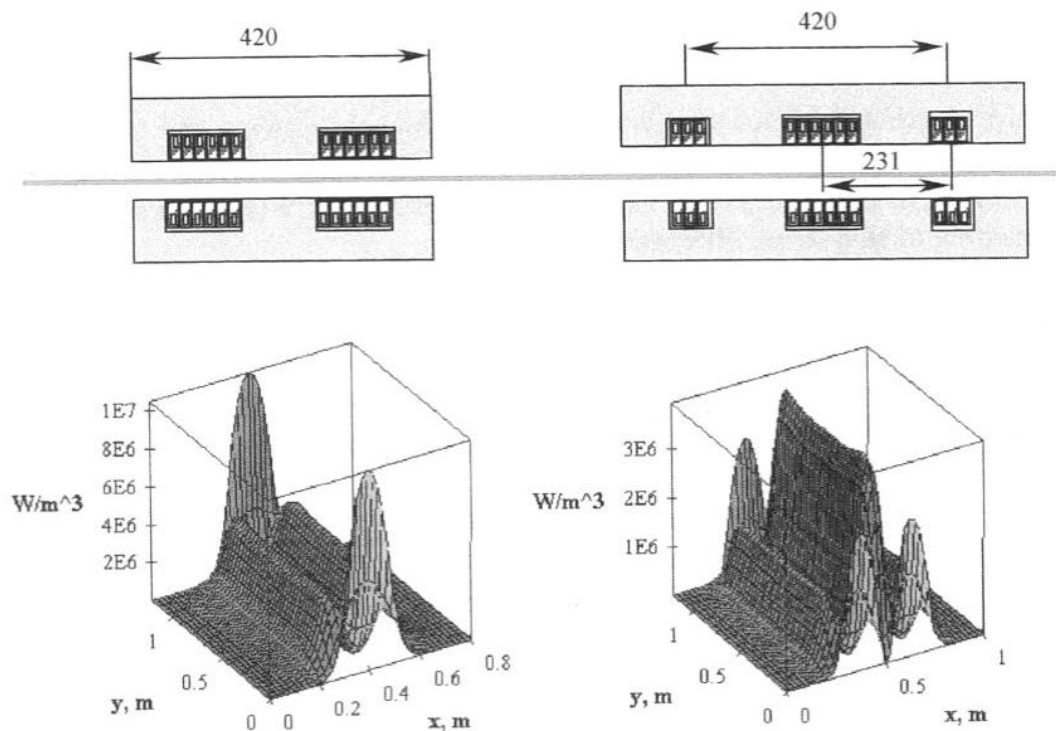
Fig. 1.9: Cross section of the inductor and 3D representation of the induced power density (x movement direction, y strip width) [11], f=50Hz, 2s=2mm.

Since the size of the work-piece can change according to the technological process (e.g. variation of thickness from 0.55 mm to 6 mm), the sheet width, the inductor pole pitch and the frequency have been taken into consideration as variable parameters to

analyze the necessary dependencies. Some results of the analysis referring the inductors of Fig. 1.9 are shown in Fig. 1.11 and Fig. 1.12 [11].

(a)   (b)
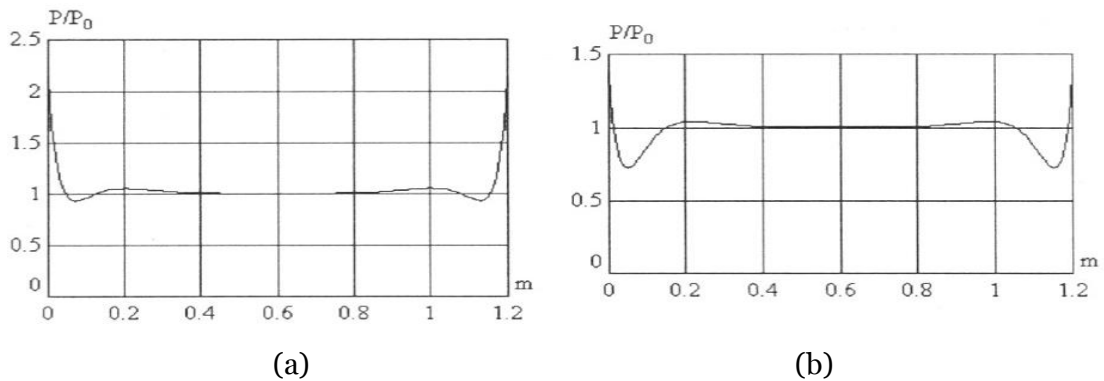
Fig. 1.10: Curves of relative power distribution [11].
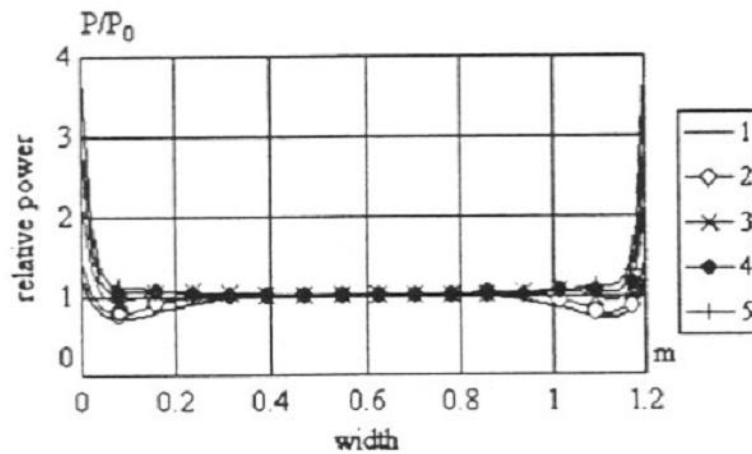
Fig. 1.11: Heat sources distribution for aluminum sheet at different thickness (1 - 0.55mm, 2 - 1mm, 3 - 2.5mm, 4 - 4mm,5 - 6mm), f=50 Hz [11].
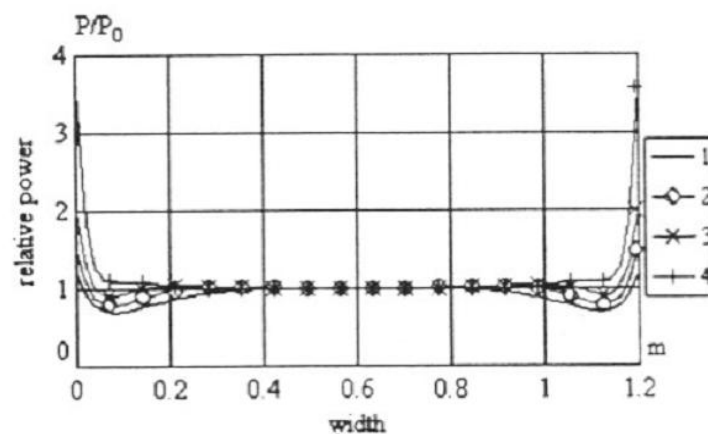
Fig. 1.12: Heat sources distribution for aluminum sheet as a function of the frequency (1 - 50 Hz, 2 - 100 Hz, 3 - 200 Hz, 4 - 500 Hz) [11].

Fig. 1.12 shows the distribution of the heating source as a function of the frequency. The lower is the frequency, the lower is the peak of the power density at the edge and

deeper the hole of energy near the edge. That means that at higher frequencies the overheating of the strip edge is higher. A very interesting conclusion is therefore valid for TFH: the hole of the curve practically disappears at the optimal frequency value and the residual overheating can be further reduced by additional control methods. Thus, in the classical TFH, the optimal frequency may be chosen either from high efficiency or temperature uniformity point of view.

In some applications however, such as the edge reheating of strips and slabs, the natural tendency of wide transverse flux induction heaters to overheat edges, that is usually considered an undesirable feature, works advantageously.

Non linearity

Different non-linear effects have significant influence on both electromagnetic and thermal processes [12]. Generally, two physical properties of heated metal make electromagnetic phenomena of the induction heating non-linear:

- electrical resistivity - ρ

- relative magnetic permeability - μ_r

Both of them strongly depend on temperature. Moreover the permeability depends also on the local magnetic field intensity. When the temperature increases, the specific resistance of most metals usually grows. The carbon steel has a specific resistance, which is very sensitive to the temperature. Magnetic relative permeability of the carbon steel drops from tens or hundreds down to one (Fig. 1.13) with increasing the temperature above the Curie point. Moreover, the magnetic permeability depends on the intensity of the local magnetic field.

The thermal properties of the heated metals also depend on the temperature. For example, for stainless or carbon steel the value of thermal conductivity λ can vary more than two times from room temperature up to 800°C (see Fig. 1.14). The thermal conductivity of carbon steel drops down while it grows with temperature in case of the stainless steel. The specific heat c and density γ of the metal are functions of the temperature as well. In particular the specific heat of the steel has a significant peak in the temperature range between 700 °C and 800 °C (see Fig. 1.15), which corresponds to the structural transformations in the alloy. Moreover, the temperature distribution in the heated thin strip is significantly influenced by the heat losses from the strip surface. Both convection and radiation heat fluxes strongly depend on temperature.
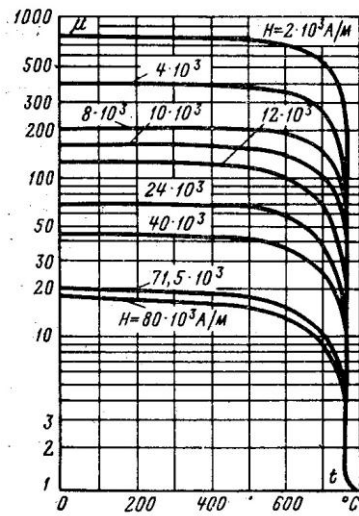
Fig. 1.13: Magnetic permeability vs. temperature as a function of the magnetic field for magnetic steel [13]
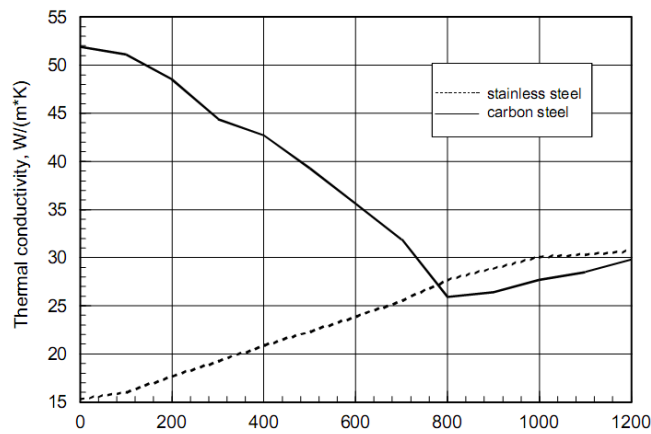
Fig. 1.14: Thermal conductivity of stainless steel and carbon steel as a function of the temperature [12].
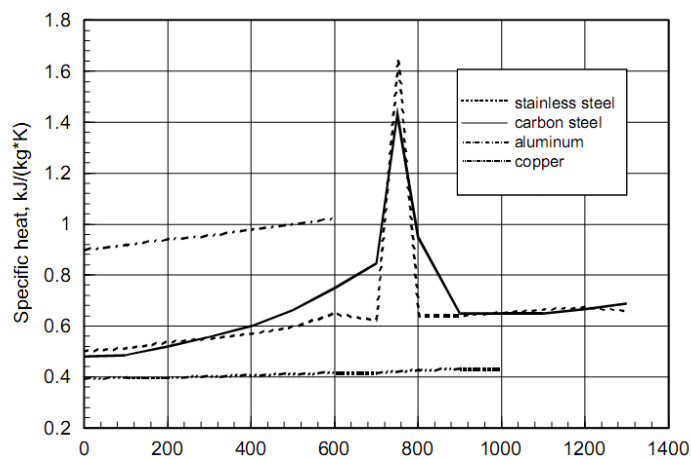
Fig. 1.15: Specific heat of some metals as a function of the temperature [12].
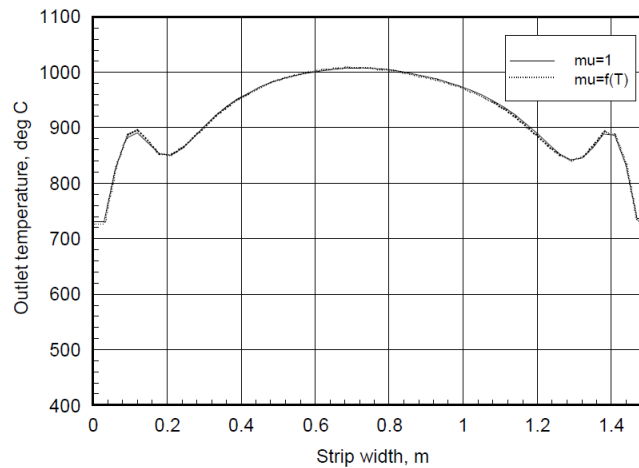
Fig. 1.16: Final temperature distribution in the strip with different magnetic permeability (The curves overlap) [12].
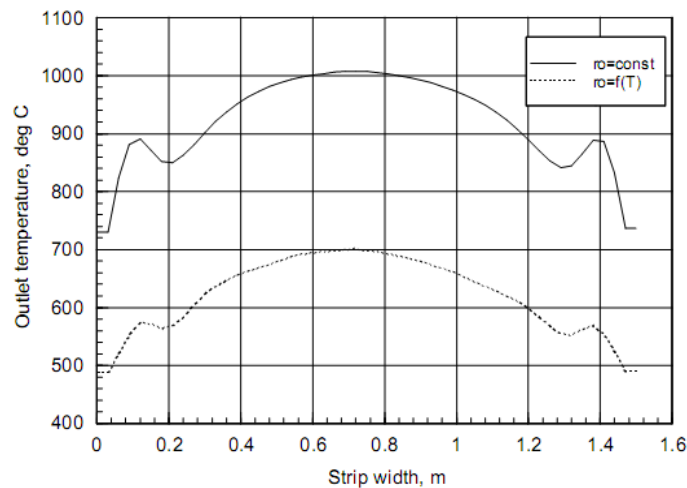
Fig. 1.17: Final temperature distribution in the strip with different specific resistance [12].

In [12] and [14] for high values of the strip speed, the influence of the non-linear electrical properties on the temperature at the end of the process was analyzed by 3D numerical simulation.

In these papers carbon steel has been chosen for the sensitivity analysis because of the strongest dependence of the properties on temperature including the magnetic permeability. The calculations have been carried out with a constant value of the electrical resistivity ρ=1.136·10^{-6} Ωm and a constant value of the relative magnetic permeability μ_r=1. The power of the system was adapted so that the temperature of the strip is about 1000 °C, i.e. above the Curie point. Then the same system has been calculated with the same constant value of the specific resistance, but with the magnetic permeability as a function of temperature. The results are compared in Fig. 1.16: the two curves are very close to each other, showing that the system is not sensitive to the magnetic properties of the strip material.

Steel strips can be heated in the TFH installation above as well as below the Curie point without any change or adjustment of the equipment. This conclusion is very important for the practical use of the TFH concept.

The influence of the resistivity of the strip material on the temperature profile has been investigated in the same way. The calculations with a constant value of the resistivity and a constant value of the magnetic permeability have been chosen as a reference for the comparison. In a second numerical calculation the specific resistance of the strip material has been changed as a function of temperature. The corresponding temperature profiles in the strip are shown in Fig. 1.17. On the contrary, the resistivity strongly influences the level of the strip temperature as well as the temperature distribution along the strip width. Because of the value of the reference resistivity corresponds to the temperature region of about 1000 °C, the temperature level reached in the non-linear example is lower than the basic one. Significant influence of the non-linearity is already visible in the power density distribution in the strip (see Fig. 1.18-a,b), where both linear and non-linear results are presented. The symmetry present in the linear case distribution (Fig. 1.18-a) is deformed in the non-linear calculation (Fig. 1.18-b). The corresponding steady-state temperature fields in the strip are shown in Fig. 1.18-c,d. In the non-linear system higher temperature gradients appear as a result of Joule heat redistribution. However in practice the most important result is the temperature profile at the exit section of the inductor. Both linear and non-linear outlet temperature profiles in the strip are compared in Fig. 1.18-c,d in which it can be noticed that the difference between the temperature distribution is practically negligible.

The thermal non-linearity has a main influence on the absolute level of the outlet temperature. Its influence on the temperature profile over the strip width decreases with increasing the speed of the strip motion. In most practical cases this influence can be neglected.

The previous results lead to the conclusion that the strip resistivity should be taken into account as a function of temperature in the modeling of TFH systems when high temperature gradients are expected.
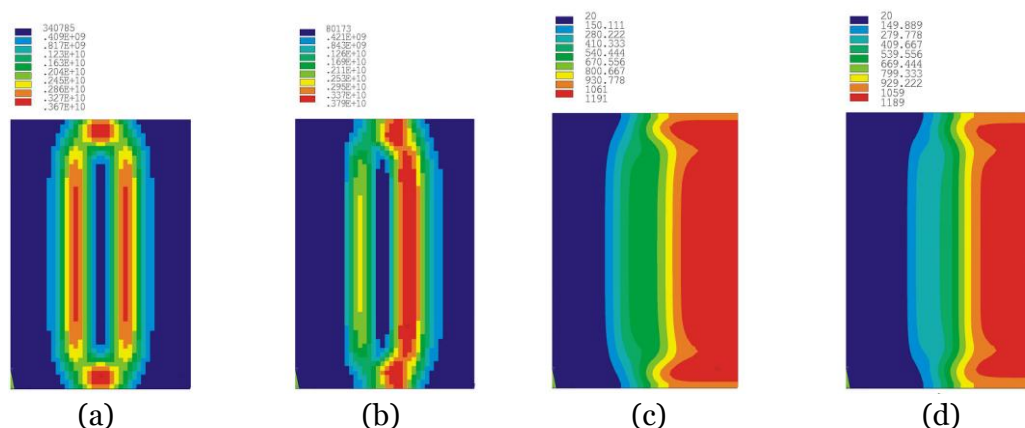

(a)   (b)   (c)   (d)

Fig. 1.18: Power density (a,b) [W/m³] and temperature (c,d) [°C] distribution in the strip with linear (a,c) and non-linear (b,d) electro physical properties [12].

1.2.2 **Deformations and noise**

During induction heating of thin metal strips, discs or slabs, different mechanical processes occur due to electromagnetic forces or thermal effects that can result not evident when considering the process only from a theoretical point of view. These effects can potentially influence the stability of the heating process and lead to dangerous mechanical contacts between strip and inductor. In this chapter the main effects and influencing parameters on mechanical deformation will be described.

As in all studies on TFH, it is not possible to generalize the results, due to the huge number of possible configurations and shapes of inductor, but although the following examples correspond to studies on specific simulation models on 2D and 3D FEM analyse, they can be taken as a description of how forces act on TFH.

The strip mechanical effects derive from different phenomena:

- Deformation due to the temperature gradient [15]

- Deformation and noise due to the electromagnetic forces [16] [17]

Deformation due to temperature gradient

The non homogeneous temperature distribution in the strip leads to thermal stresses [15]. Especially while heating thin strips thermal stresses may result in sizeable mechanical deformation. Mechanical stresses, appearing in the strip as a result of strong thermal expansion of the strip material, lead to the deformation of thin strip. Buckling of the strip inside the inductor can change the distribution of eddy currents in the strip and, as a result, the final temperature distribution in the strip at the output of the heater. In some extreme cases the deformation of the strip can lead to dangerous mechanical contacts between the strip and the inductor.

The TFH process including the mechanical behavior of the system is characterized by a great number of parameters. Intensity of the strip deformation has been investigated by extensive parametrical studies. The influence of the properties of the strip material and the main technological parameters will be described in the following.

The thermal deformation during the continuous heating processes is a result of thermal expansion of the strip. Internal stresses initiated in the heated material, result in deformation of the strip and can lead to its buckling.

The strip is transferred from the input zone to the output zone of the heating installation with constant speed. It is assumed that inside the heating zone the temperature of the strip is evenly increased from T_0 to T_A (Fig. 1.19). As a result of the thermal expansion effect, the geometry of the strip in the heating and output zones change. The areas of stresses and strains in the strip can be detected taking into consideration the uninterrupted nature of the strip (Fig. 1.20). For the strips, the areas with stresses are potentially predisposed to buckling. There are three well pronounced deformation areas in the strip. Two of them are located on the edges of the strip at the beginning of the heating zone. The third one appears in the middle of the strip at the end of the heating zone.
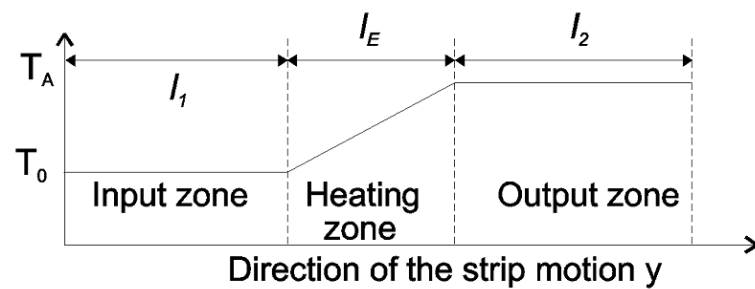
Fig. 1.19: Temperature of the strip [15].
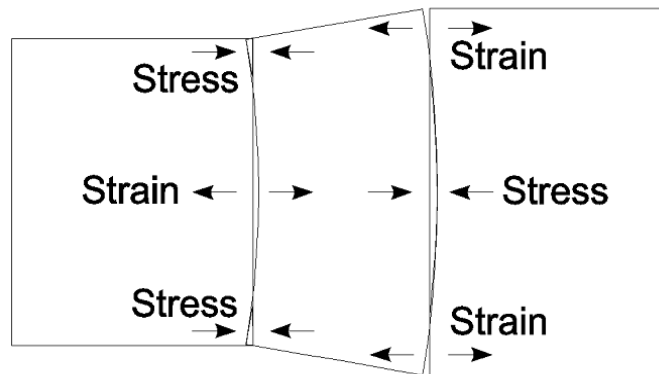
Fig. 1.20: Directions of the stresses and strains [15].

In industrial technological installations the strip is under tension in the direction of its motion. The tension cannot be effectively used to reduce the negative thermal deformation effect.

As regards the thermal deformations, the following considerations can be done:

- A thin strip is much more predisposed to buckling than a thick one, and what is more important, the buckling of the strip appears if the strip thickness is smaller than a certain critical value for each system.

- The mechanical properties of the strip material (elastic modulus) have no significant influence on the intensity of the deformation effect.

- The width of the strip is one of the most important parameters influencing the deformation intensity and the critical value of the strip thickness. Increasing of the strip width results in significant increasing of the maximum vertical displacement of the strip. The critical value of the strip thickness increases with increasing of the strip width.

- The thermal expansion effect and, as a consequence, the strip deformation intensity, strongly depend on the thermal expansion coefficient and the temperature difference $(T_A - T_o)$.

In Fig. 1.20 the shape of the deformation given by the temperature distribution of Fig. 1.19 is shown. As a conclusion it can be said that mechanically high temperature gradients cannot be reached mainly for mechanical reasons. The high power provided

by TFH systems can be used in order to improve the speed of the line, and several TFH inductors have to be installed in order to reach the specified temperature with a suitable value of deformation.
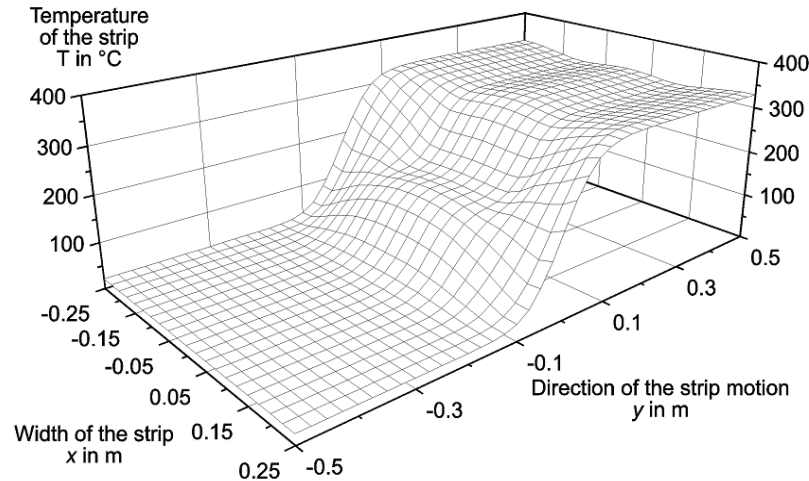
Fig. 1.21: Optimized temperature distribution in the strip
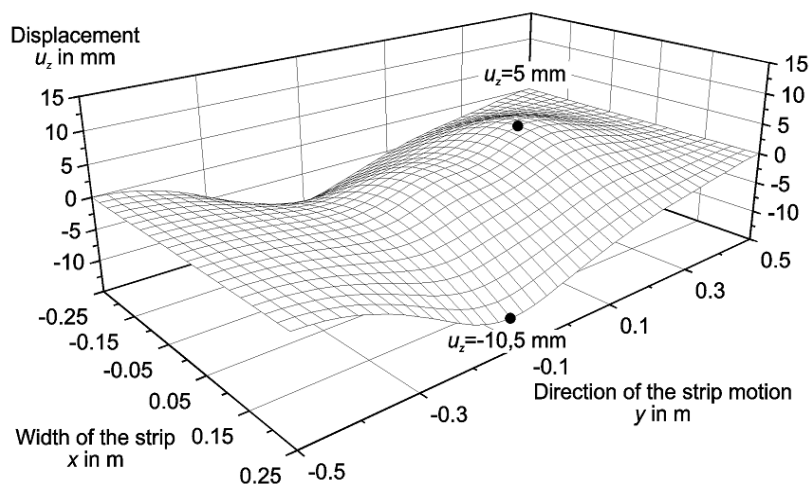
Fig. 1.22: Shape of the deformed strip under the optimized temperature distribution

Deformations due to electro-dynamic forces

The electromagnetic force acting on non magnetic sheets is the result of the interaction between the induced currents and the magnetic field. This force is a Laplace type electromagnetic force. In the case of ferromagnetic materials, the total electromagnetic force is a superposition of the Laplace and the magnetic type forces, the magnetic properties of the sheet influencing the intensity and the orientation of this force. Static components of electrodynamics forces may cause strip deformation in some cases but the problem is normally of low importance. The oscillating forces due to the oscillation of currents are rather more important. When the strip is heated these forces may excite

34

strong strip vibrations which can result in a high level of noise emission [17]. The calculation presented in the following sections are performed with reference to the FEM model shown in Fig. 1.23, which represents a quarter of a TFIH inductor with 2 types of strip material: magnetic and non-magnetic [16].
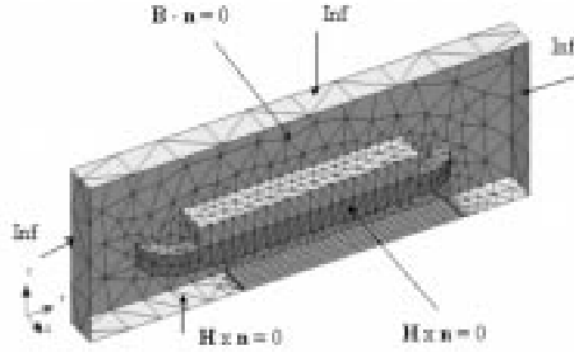
Fig. 1.23: FEM model for electromagnetic forces computation

▪ **Electromagnetic force computation methods**

The electromagnetic force acting on the volume of a sheet placed within the inductor air-gap can be evaluated as the volume integral of Laplace and Magnetic Forces densities:

$$F = \int_{Vol} (J \times B)dVol - \frac{1}{2} \int_{Vol} (H^2 \nabla \mu)dVol \qquad (1.9)$$

where

- F: electromagnetic force,
- J: current density,
- B: magnetic flux density,
- μ: magnetic permeability
- H: magnetic field intensity module.

For non-magnetic strips the relation (1.9) does not contain the second right-hand side term and the electromagnetic force is the volume integral of Laplace Force density:

$$F = \int_{Vol} (J \times B)dVol \qquad (1.10)$$

▪ **Influence of the sheet position in the inductor air gap on the electromagnetic force**

The resulting effect of the electromagnetic forces depends on the position of the strip in the air-gap. If the strip is perfectly centered the forces are globally compensated and the strip is in equilibrium and no global forces act on it.

If a non-magnetic strip is placed in a non-symmetrical horizontal position with respect to the longitudinal mid-line of the strip, the electromagnetic force, which is of Laplace type, pushes the strip out from the inductor air-gap. If the strip is magnetic the result of the forces depends on the value of the permeability. If the permeability is sufficiently high the strip is centered, on the contrary if the material is slightly magnetic the strip is pushed out as in the non-magnetic case.

If the strip is placed in a non-centered vertical position in the air-gap, in case of non- magnetic strip, the force always acts toward the horizontal symmetry plane of the air-gap. The larger is the distance between the sheet and this plane, the larger the value of the force. This is the result of the correspondent increase in the magnetic flux density and the induced current density.

In the case of a slightly magnetic sheet the orientation of the vertical force depends on the sheet position in the inductor air-gap. From the middle of the inductor air-gap up to a critical non symmetrical position of the sheet, the vertical force pushes the strip out from the centered position. After this critical position the force orientation changes. Gradually, the absolute value of the total force decreases and finally its orientation changes, giving a centering action of the sheet in the air-gap. Increasing further the distance from the center of the inductor, the magnetic component of the electromagnetic force becomes larger than the Laplace component, and consequently the sheet is pulled towards the closer magnetic core of the inductor.

▪ **Influence of the frequency on the force orientation**

The supply frequency has a specific influence on the electromagnetic force. For non-magnetic sheets the vertical force is always oriented towards the centre of the air-gap. The larger is the frequency the larger is the force value.

In the case of magnetic sheets, for low frequencies, the Laplace component has a little contribution to the total force, and as a result, the electromagnetic force pushes the sheet towards the closer section of the magnetic core. Increasing the frequency, this contribution becomes more important, and the orientation of the electromagnetic force changes. This value is strongly influenced by the sheet magnetic permeability. The larger the permeability, the larger the critical value of the frequency.

1.3 Overview of existing TFH solutions

As already said, the main problem of TFH is to reach a relatively uniform temperature of the strip suitable for the process requirements. In the past years several solutions have been proposed; all of them have advantages and drawbacks. In this chapter the most relevant solutions will be reported [6].

A TFH design parameter that has significant influence on the induced current, and therefore on the heat source distribution in the plane of the strip, is the shape of the inductor coil. Over the last four decades different complex shaped transverse flux coils have been proposed, e.g. diamond shaped coils, "J" and "O" type coils, pair of U-shaped, etc.

Theoretically some of these TFH coils were suitable for a broad production mix (including variation of strip width and thickness) and immune from unstable strip positioning inside the inductor. However, in practice most of the coils have noticeable limitations in providing the required temperature repeatability and uniformity across the strip width when the strip width and thickness vary widely or when the strip moves left to right or up and down inside the inductors.

One of the possible solutions for designing a TFH line that would be less sensitive to strip movement in the transverse direction would be to build moveable coils so they could follow the strip movement in real time. However this approach drastically increases the cost of the induction heater.

Reduction of sheet temperature non uniformity by shielding
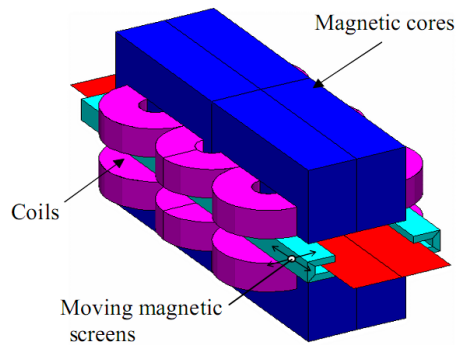
Fig. 1.24: Moving shields TFH device [18]

Studying the transversal temperature profiles of TFH with coils larger than the strip, an overheating at the sheet edges can be usually noticed which could be unacceptable in certain applications.

A solution for reducing the overheating at the sheet edges consists in equipping the classical TFH device with two conductive or magnetic shields used as regulating elements of transversal temperature profile of the sheet. The effect of these structures consists in changing the induced currents path by shielding the sheet edges. Such shields are placed around each sheet edge as in Fig. 1.24 and could have two separate movement directions, one longitudinal and one transversal. The simultaneous movement of the two magnetic structures along the two orthogonal directions (along x and y axes) allows the tuning of the transversal profile of the temperature in the metallic sheet depending on the sheet characteristics. The shielding is often a mandatory way to reduce the edge effect of the TFIH installation but it increases notably the total losses and then decreases the efficiency.

Movable cores

This kind of inductor is provided by a number of magnetic concentrators arranged in a parallel direction of the strip movement direction (Fig. 1.25) [19]. The particular feature of this inductor is that the magnetic concentrators can be moved in the direction of the width of the strip in order to control the distribution of the magnetic flux on the surface of the strip, hence the induced power on it. The inductor allows the user to adjust the strip temperature pattern by changing the position of the above described field correctors.

A regulating system controls all parameters of the inductor to reach the required temperature with a good homogeneity. The control system calculates the power to be injected in the strip and the position of the electromagnetic actuators in order to control the temperature profile.

Fig. 1.25: Movable cores TFIH system (US Patent 6498328)

Moving coil systems

Another method to assure the adaption of the inductor to different strip widths is to use movable coils. Different kinds of movable core systems exist. For example the double-inductor concept of the induction system consists of two or more induction coils, overlapping the strip from different sides (Fig. 1.26). By shifting the position of these induction coils from the strip edges, it is possible to control the temperature profile over the strip width [20].
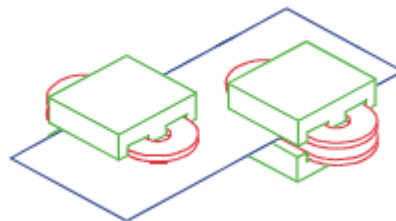
Fig. 1.26: Double inductor principle for flexible strip width and applications

Another inductor for variable band width (VABID) [20] has been developed at the ETP laboratory of Hannover. This system can be adapted to the requirements of different processes.

An inductor assembled with several inductor layers is used. Each layer consists of two sections which are independently adjustable (Fig. 1.27). Due to the layout of the inductor sections and their electrical connections, the electromagnetic field in the region of the supply connections is compensated.

In order to improve the final temperature uniformity of the strip, the inductor is provided by several layers. The optimal configuration for reaching uniform final temperature distribution is obtained by independent positioning of all inductor sections. At the same time, however, the complexity of the installation is substantially increased, because all inductor sections must be independently positioned.

Tab. 1.1 shows some results, obtained experimentally, on the temperature uniformity deviation in respect to the ideal uniform value.
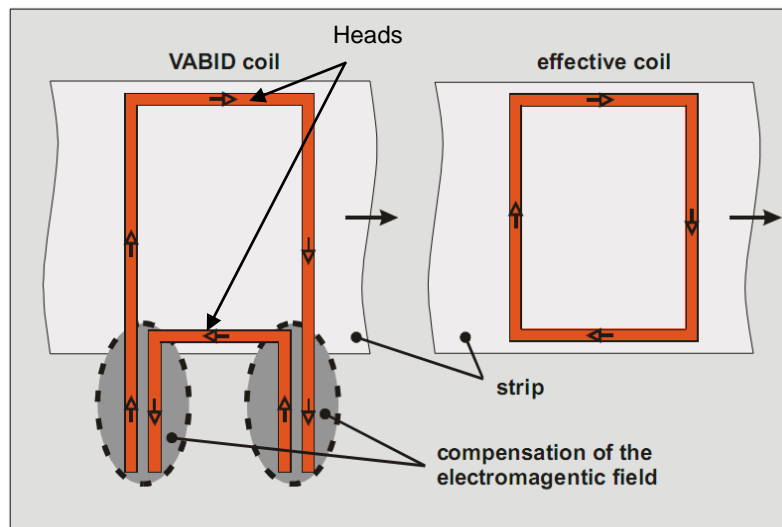
Fig. 1.27: Principle of VABID-concept – layout of one inductor layer

number of inductor layers	1	2	3	4
maximum deviation	21.2 %	6.2 %	5.8 %	5.5 %

Tab. 1.1: Maximum deviation of temperature from mean in function of number of layers

Inductotherm Corp solution.

The solution of Inductoterm Corp is shown in Fig. 1.28 [21]. The transverse flux induction heating inductor adjusts the level of edge heating in the work-piece by changing the pole pitch of the induction coils constituting the inductor in order to provide a more uniform final temperature in the work piece cross-section. The pole pitch, and therefore, the level of edge heating can be continuously changed, or conveniently adjusted prior to a production run, in a high speed continuous heat treatment process.
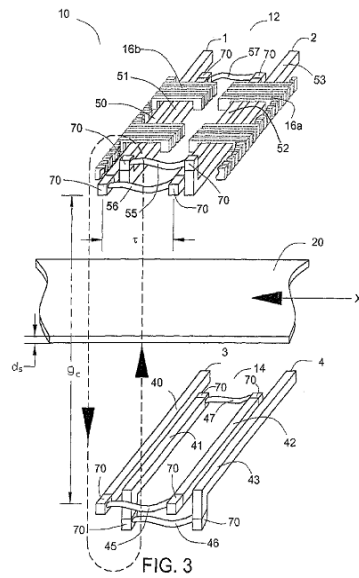
Fig. 1.28: Exploded perspective view of moving pitch apparatus

J-shaped moving coil

The Ajax Magnethermic TFIH inductor [22] is adjustable over a wide range of strip widths. Fig. 1.29 illustrates schematically its essential features.

The inductor conductors are arranged in a J configuration with a right hand J at one edge on one face of the strip and reversed left-hand J at the other edge on the other face of the strip. The curved J tends to guide the strip current through the transition zone. The two J_s are in series electrically connected to ensure that the same current flows in each conductor in order to form a loop of current in the strip.
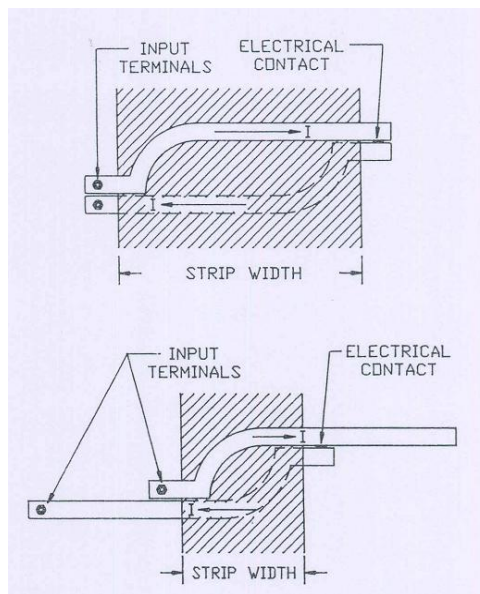
Fig. 1.29: Adjustable coils TFH inductor

1.4 Electromagnetic computations

One of the problems that make TFH technology not diffused in industry installations is the difficulty of designing the inductors, due to the lack of simple analytical methods for dimensioning coils, making the design of coils an ability only of elite groups of engineers and researchers having access to the available computation codes..

Several kinds of simulation tools can be used to model TFH systems. These tools make use of different simulation methods or algorithms such as analytic, Boundary Elements Method (BEM), Finite Difference Method (FDM), Finite Element Method (FEM), neural network or circuital model.

Among the analytical solutions mention must be made of the following:

Jackson [23] produced a mathematical field solution of the electromagnetic properties of TFH based on 5 dimensionless parameters.

Peysakhovich [9] has given an analytical solution taking into account the uneven distribution of the magnetic field along the air gap due to the actual geometry of the inductor, considering also multiple windings.

Haubitzer [24] finally has proposed an analytical solution based on the series expansion of the magneto motive force, taking into account the 3D nature of the problem.

Concerning the numerical methods, until the eighties it was possible to use only 2D methods for calculation of magnetic and temperature field resulting in a rough approximation of the real situation. This was due to limitation of the calculation resources available in those years.

Nowadays it is possible to use advanced 3D software that take into account the real geometry of the problem. In the following sections there is a walk-trough on the most useful methods used in the last years to design TFH inductors.

1.4.1 Analytical Methods

Analytical method for planar circular coils

An analytical model, capable of calculating the field distributions in a circular axisymmetric MCH system as well as the impedances seen at the terminals of the coils, has been developed in the frame of the thesis (Appendix C). The analytical method has been used to validate the measurements on the test inductor for circular plates, and to verify the behavior of the impedance matrix with the frequency (section 2.2).

Analytical model TFH3D

The TFH3D software has been developed in the past by the University of Padua taking advantage of the analytical solution for the electromagnetic problem proposed by Haubitzer [6].

A number of tests have been done to verify the usefulness of this software to design transverse flux induction heaters. In the frame of the multi-coil inductor design the software has been modified to take into account multiple concentric coils and to be

coupled with external optimization codes. The TFH3D code takes into account the presence of multiple basic sections, each with individual current and phase, and the velocity of the strip.
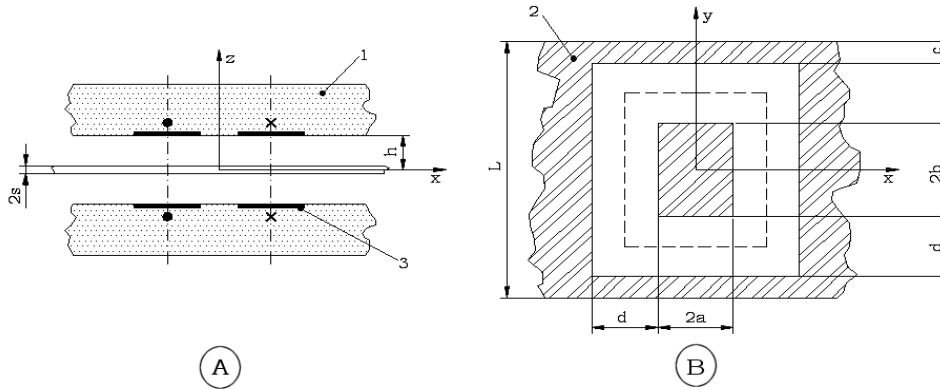
Fig. 1.30: Schematic of one inductor coil of the system in TFH3D (A-cross-section; B-view from above)

In TFH3D the analytical solution of the electromagnetic problem is implemented for the determination of current and power densities induced in the strip by the idealized exciting system shown in Fig. 1.30. Starting from the induced power density distribution obtained as solution of the electromagnetic problem, TFH3D can perform also the analysis of the thermal transient by the finite difference method (sec 1.5.1).

Despite the limitations of the electromagnetic solution, the code allows the designer to make a fast analysis of the problem and to have a useful preliminary evaluation of the main characteristics of the system.

The method of Haubitzer makes use of the double series expansion of the magneto motive force and gives the analytical solution by series of differential equations obtaining a 3D solution of the electromagnetic problem capable to calculate the amount of power density induced in the strip.

A typical section of the inductor is shown in Fig. 1.30 with the main geometrical parameters used for the implementation of the analytical-numerical code. The following assumptions have been made in order to solve the electromagnetic problem:

- The materials have linear and isotropic characteristics;

- The inductor thickness is neglected (sheet current distribution in the inductor coils are considered);

- The magnetic concentrator is assumed to have infinite magnetic permeability.

Thanks to these assumptions the problem formulation becomes:

$$\nabla H = K \; for \; z \leq |\delta|$$

$$H = \frac{1}{\mu} \nabla \times A$$

$$J = -\frac{1}{\rho}\frac{\partial A}{\partial t}$$

$$\nabla \times A = -\frac{\partial A_y}{\partial z}\vec{e}_x + \frac{\partial A_x}{\partial z}\vec{e}_y + \left(\frac{\partial A_y}{\partial x} - \frac{\partial A_x}{\partial y}\right)\vec{e}_z$$

$$\nabla \cdot A = \frac{\partial A_x}{\partial x} + \frac{\partial A_y}{\partial y} = 0$$

In terms of the corresponding phasors the above equations can be rewritten as follows:

$$\nabla^2 \dot{A}_x - \frac{j\omega\mu}{\rho}\dot{A}_x = 0$$

$$\nabla^2 \dot{A}_y - \frac{j\omega\mu}{\rho}\dot{A}_y = 0$$

$$\dot{H}_x(x,y,z) = -K_y(x,y)$$

$$\dot{H}_y(x,y,z) = -K_x(x,y)$$

where *A, H, K, J, μ* and *ρ* are respectively: magnetic vector potential, magnetic field strength, laminar current density, current density, magnetic permeability and electrical resistivity. In order to make the integration possible, the magneto-motive force (MMF) produced by the exciting currents, has been decomposed in two dimensional Fourier's series along x and y directions, supposing it periodical along both directions:

$$MMF = g(x,y) \cdot NI$$

where

$$g(x,y) = \sum_{i=1,3..}^{\infty} \sum_{k=1,3...}^{\infty} \alpha_{ik} \cos\left(\frac{2\pi}{\tau_t}ix\right)\cos\left(\frac{2\pi}{\sigma_t}ky\right)$$

$$\alpha_{ik} = \frac{64}{\sigma\tau}\cdot\iint_S g(x,y)\cdot\cos\left(\frac{2\pi}{\tau_t}ix\right)\cos\left(\frac{2\pi}{\sigma_t}ky\right)dxdy$$

$$\sigma_t = 2(2b + 2d + 2c) \quad and \quad \tau_t = 2(2a + 2d + 2f)$$

The analytical solution of the Helmholtz's equation in three dimensions gives the expressions of the electric field in the strip and in the air; by their knowledge, the power density distribution and all integral parameters of the system can be calculated.

One of the main limits of this model is that, because of the boundary conditions considered, the inductor transversal width must be narrower than the width of the strip. This leads to an underestimate of the power induced at the edge of the strip when the inductor width is equal or greater than the strip width.

In Fig. 1.32 a comparison between Finite Element Method (FEM) and TFH3D computations is shown. The calculations correspond to a stainless steel strip of 1000 mm width. The comparison refers to three simulation models:

- FEM model with massive turns corresponding to the final geometry of the coil. The FEM formulation used is the $T\Phi - \Phi - \Phi_{red}$.

- FEM model with stranded coils with thickness corresponding to the penetration depth in the copper at 1500Hz. The FEM formulation used is the $AV - \Phi - \Phi_{redT0W}$

- Analytical model TFH3D

The Fig. 1.32 shows the difference on the calculated patterns of the induced powers, and the difference among the computed power losses in the strip P and the reactive power Q supplying one coil with a current value of 1 A. The greatest difference was found on the reactive power Q.
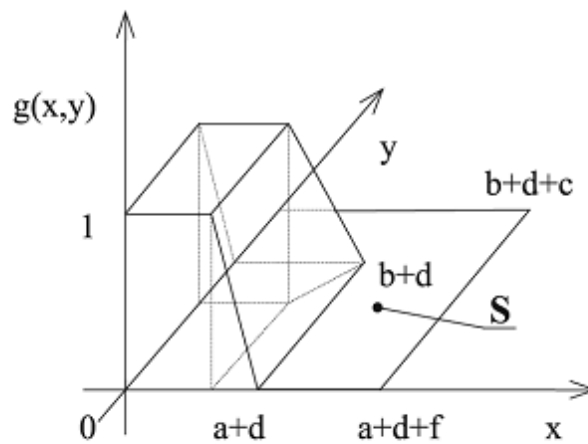
Fig. 1.31: Shape of magneto motive force on half section
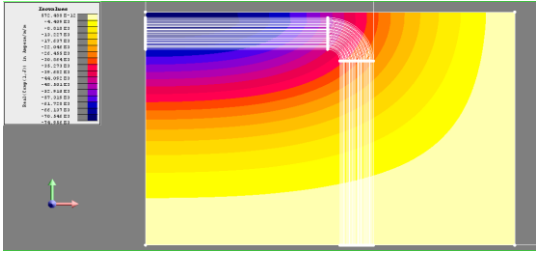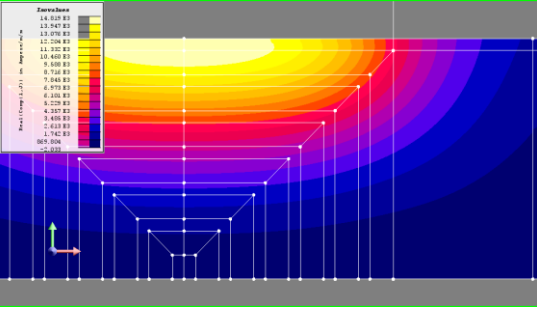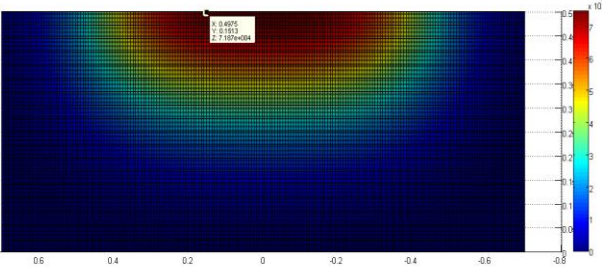
	Power density pattern	P[W]	Q[var]
a)		0,75	1,73
b)		0,73	1,94
c)		0,75	2,1

Fig. 1.32: Comparison among power density maps of : a) FEM TΦ-Φ-Φred scalar model with massive coils (1/4 of the strip); b) FEM AV-Φ-Φred model with stranded coils (1/2 of the strip); c) TFH3D analytical model (1/2 of the strip). (P=Strip power losses , Q=reactive power).

1.4.2 **Numerical codes**

The use of numerical simulation codes for TFH becomes mandatory if precise solutions are needed. There are several codes available to solve electromagnetic problems that make use of different numerical methods. One possibility is to use commercial FEM codes to model the system. This is the most accurate solution, but has the drawback of high computation time and as consequence the cost of the inductors design. In the past years several self developed numerical codes have been developed by different research labs and Universities to reduce the calculation time for TFH problems.

There are 2D or 3D methods available to solve electromagnetic problems [25]. The 2D methods neglect the transversal dimension of the strip and do not consider the closing path of the currents at the edge of the strip. 2D methods can then be used only to verify the influence of the longitudinal parameters like the pole pitch, the distance between inductors and the electrical parameters on the longitudinal dimensions of the system. 2D methods can be useful also to predict the induced power density distribu-

tions in systems in which the regular area is much wider than the edge one as shown in Fig. 1.33.

With the assumption that in TFH the electric penetration depth is greater than the strip thickness and hence the current distribution across the strip thickness is almost homogeneous, the electromagnetic problem inside the strip can be solved in 2D while the external electromagnetic field has to be calculated in 3D. Furthermore, under the above conditions a homogeneous temperature distribution across the strip thickness can be assumed, so that, a 2D simplification results also for the thermal problem.
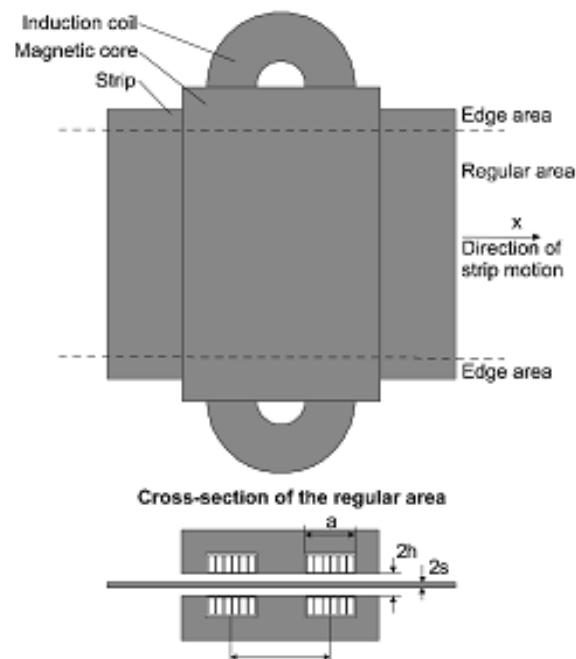
Fig. 1.33: TFH inductor

1.4.3 **PEEC Method**

The PEEC is a numerical method that allows modelling the connections of an electric structure by using an electric circuit with lumped components. The main advantage of this method in comparison with FEM is that it is possible to model only the electrical conductors avoiding the modelling of the surrounding air and then making possible to reduce considerably the computation time.

Inca 3D [26] is a software that implements the PEEC method. The software is composed by 2 main modules:

- Supplied conductors

    The electromagnetic device is supplied by current and voltage generators. The module in suitable for the calculation of the paths of the induced currents in the massive conductors

- Conductors impedances

With this module it is possible to analyze the PEEC network to find the impedance seen from any couple of point and the impedance matrix between different couples of points. The points are chosen using the impedance probes components.

More details on the use of Inca3D on induction heating systems will be given in sec. 2.2.2 with reference to a practical case.

1.4.4 Finite elements method

While the above mentioned codes are useful to have an overview of the problem or to optimize in a fast manner a system, they don't allow to study the TFH problem taking into account the following characteristics:

- The real geometry of the coil;

- The strong non-linearity of the TFIH system materials such dependencies of electrical and thermal characteristic of the strip material from the temperature, and eventually the magnetic non linearity of flux concentrators.

When the analysis of these characteristics is fundamental, the methods based on FDM and BEM cannot be used.

The Finite Element Method (FEM) is nowadays the most used method to solve electromagnetic problems with strong non linear dependencies. Modern commercial and non commercial packages are able to perform very accurate simulations of multiphysics problems coupling different physical problems such as electrical-thermal-mechanical ones.

The results presented in this thesis have been computed by means of the software Cedrat Flux [27] and JMAG [28].

The finite element method uses the discretization of the domain in elementary geometric entity called "elements" in which the variables are supposed to be constant or polynomial. The electromagnetic problem, analytically described by Maxwell equations, has to be represented by formulations defining electromagnetic field potentials in the different regions.

The research on TFH has nearly followed the evolution of FEM method, especially the development of robust and fast 3D codes. Various papers deal with comparison among the performances of various formulations [29], [30].

1.5 Thermal computations

In order to compute the temperature transient in the strip the electromagnetic solution issued from analytical or numerical models have to be coupled with a thermal simulator.

The solutions considered in this thesis are mainly two:

- Coupling between magneto-harmonic FEM code and thermal transient FEM code (Flux3D) with mechanical movement;

- Coupling between analytical or numerical code (FEM) for the electromagnetic solution, and the thermal solver of TFH3D based on the finite difference method.

The solved equation is in the 2 cases the heat diffusion equation combining the Fourier law and the equation of heat conduction:

$$c\gamma \frac{\partial T(P,t)}{\partial t} = \nabla \cdot \left(\lambda \nabla \mathrm{T(P,t)}\right) + w(P,t) \qquad (1.11)$$

where

- $w(P,t)$: heat source density (W/m³) at the point P at the time t

- $c\gamma$: volumetric heat capacity (J/m³/K)

- λ: thermal conductivity (W/m/K)

- $T(P,t)$: Temperature at the point P at the time t

In the induction heating the heat source is represented by the joule losses in the conductor:

$$w(P,t) = \rho J^2$$

where

- ρ: resistivity of the material in the considered point

- J: amplitude of the current density vector

Several kind of boundary condition can be applied to the differential problem:

- Constant temperature (Dirichelet): $T = T_0$

- Adiabatic condition (Neumann): $-\lambda \cdot \frac{\partial T}{\partial n} = 0$, used for the symmetries

- Thermal convection: $-\lambda \cdot \frac{\partial T}{\partial n} = \alpha \cdot (T - T_a)$

    with α:thermal transfer coefficient with a fluid and T_a the ambient temperature.

- Thermal radiation: $-\lambda \cdot \frac{\partial T}{\partial n} = \sigma_t \cdot \varepsilon \cdot (T^4 - T_a^4)$

    with ε: thermal emissivity and $\sigma_t = 5.67 \cdot 10^{-8}\, W/m^2/K^4$

Usually, in the actual materials, all electrical and thermal parameters depend on the temperature, resulting in a non-linear problem.

1.5.1 **Finite difference thermal solver**

The software TFH3D is provided of a thermal solver based on the finite difference method. In this solver the three dimensional thermal problem is treated by a series of two-dimensional computations. The strip is considered constituted by a number of transversal cross-sections. The thermal exchanges by the sections of the strip are considered adiabatic.

On the cross-section thermal process the considered thermal exchanges are:

- Conduction in the section of the strip. The material can have non-linear characteristics in temperature.

- Convection with the air. The relative movement of the strip can be considered by the coefficient α.

- Radiation with the refractory chamber. The software can calculate the emissivity from the geometry of the heating chamber and the material used. The thermal exchanges with the input and output section of the heater are neglected.

- Conduction losses between the refractory chamber and the ambient.

The thermal solver uses as input the pattern of the induced power density, issued from the analytical or the FEM module. It divides the specific power in section corresponding to the finite difference discretization considering the power density uniform in the thickness of the strip. For each iteration the code computes the temperature in the considered section and for each time steep it updates the thermal characteristics of the strip (from a material database).

1.6 Conclusions

In this chapter an overview of the previous knowledge on TFH has been reported. Extensive analysis and researches done both in computational and experimental way show that TFH is nowadays a well known and effective technique to heat metal strips. The main parameters that regulate the electromagnetic and thermal process have been described as well as the side effects of the technique.

However, the overview made on the existing solutions, shows that the design of an inductor combining at the same time flexibility, efficiency and reduced cost is very difficult. In order to improve the TFH technique, the MCH technique will be analyzed in the following sections. The results of this chapter will allow to understand the considerations done for this new heating process and to have a basis of comparison for the achieved results.

Chapter 2

Analysis of a circular MCH system

As remarked in the introduction, the TFH technique needs an improvement concerning the adaption of the inductor to different loads, and one of the most promising methods to do that is the ZCIH. As the analysis of a moving strip imply some modelling difficulties, like for example the use of 3D moving mesh and long computation times, it was decided to begin the analysis of the ZCIH in a simplified configuration with three coils and circular static loads. From this former work a simplified prototype of a multi-coil induction heating system was manufactured. This simplified configuration allowed to analyze, from a theoretical point of view, the basics of ZCIH, and allowed to verify the control strategy of the power supply with a pilot system. In the chapter a review of the literature on ZCIH has been done. Afterwards the general principles of the technique are described and finally some results of the computations done on the prototype are reported. The work done on the prototype was mainly devoted to verify and improve the concepts and the optimizations already developed in [5] using the actual geometrical dimensions of the pilot system and the measured electrical characteristics of the load material.

2.1 Generalities on multi-coil inductor

In Chapter 1, some existing solutions to obtain uniform heating in the strip have been described, but all of these make use of displacement of mechanical parts somewhere in the system. A solution that avoids the necessity of controlling mechanical facilities is to use an inductor composed by multiple concentric coils supplied with a set of independent currents having the same frequency. This type of inductors gives the

possibility to control the injection of the induced power in the different zones of the work-piece to be heated and, as a consequence, the desired temperature profiles can be obtained.

As shown in Fig. 2.1 for a circular configuration, a multi-coil system is principally composed by 2 sets of concentric coils, one for each side of the strip. Each coil is series-connected with the corresponding associated coil in the other side of the strip and the number of the concentric coils is chosen basically in function of the number of zones of the strip that must be controlled. The system is in conclusion a set of classical TFH inductors, interacting by mutual induction, and capable to exchange power among them.

The problems related to the strong mutual inductances existing between the coils and the consequent induced voltages, have made difficult in the past the production of inverters capable to drive multiple coil inductors. Nowadays, with the fast evolution of the power electronics, it is possible to design inverters able to control the magnetic interaction between coils. This justifies the application of the multi-coil induction technique to TFH.
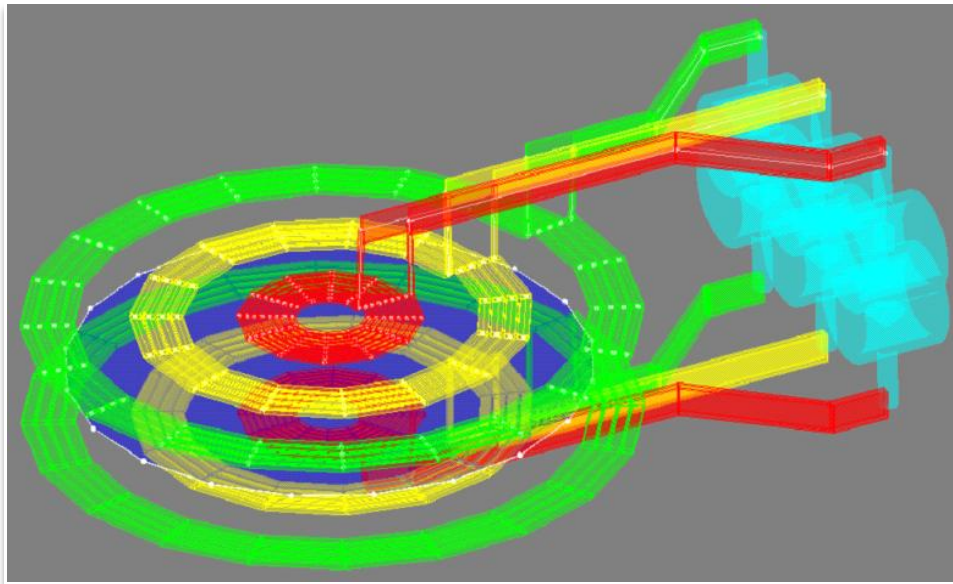
Fig. 2.1: Axi-symmetric multi-coil device composed by three coils

The idea of using multiple coils to control the induced power came initially from patents [31], [32] (Fig. 2.2). In the application described in these patents the system consists in a single inverter, connected to more working coil by switch gears. The switch gears are used to change connection of the working coil in series, parallel ore more complicated connections, in order to obtain the desired temperature distribution.

Another existing control method for multi zone induction system is made-up by a number of working coils and a number of resonant capacitors each supplying a work-piece to be heated (Fig. 2.3), which are tuned at different resonant frequencies. For example, with a 2-load system, the inverter can heat up one of the two work piece by setting the operating frequency at one of the two resonant frequencies. [33].

The so called "Zone Controlled Induction Heating" (ZCIH) was appeared in the literature in 2004 by Uchida et al., [3], [34], [35] in the field of semiconductor process-

ing. The system described in the papers was conceived to heat a graphite disc for the processing of semiconductor wafers. The system described consists of six inverter units rated at 25kW with a total rating of 150kW (see Fig. 2.4). In [3] a system composed by two or more sets of a high frequency inverter and a split work coil, which adjusts the amplitude of coil current in each zone independently, was proposed (Fig. 2.5).
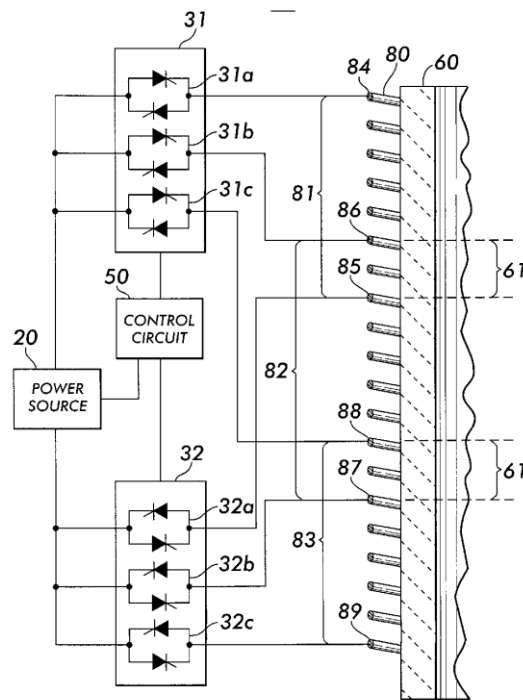
Fig. 2.2: Multiple zone induction heating with semiconductor switch gears [31]
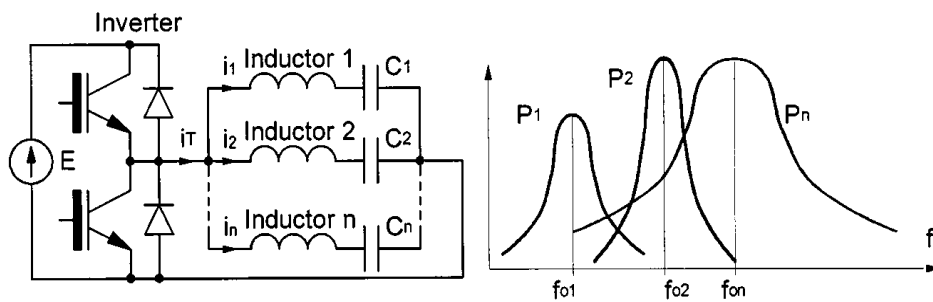
Fig. 2.3: Principle of multiple load/single converter system [36]
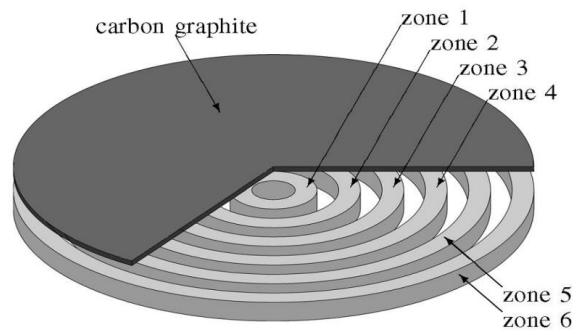
Fig. 2.4: 6-zone ZCIH for semiconductor processing [3]
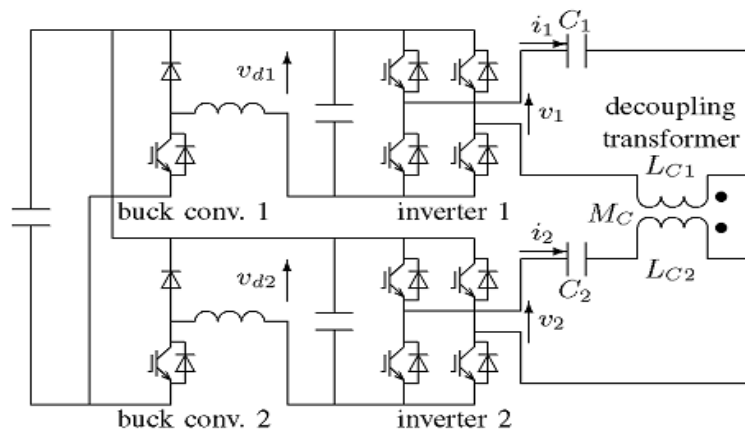
Fig. 2.5: Circuit of an inverter unit for ZCIH [3]

The control system described in the patent is composed by 6 DC buses with the voltage regulated in amplitude by 6 buck converters. In cascade to each DC bus there is a resonant inverter. Then each unit makes it possible to adjust both amplitude and phase angle of the resonant current, without changing the operating frequency of the inverter. A possibility to uncouple the interaction between the coils is to use decoupling transformers, but with this method it is possible to manage only the coupling between couples of near coils. The control solution adopted in the papers regulates the currents of each inverter in order to have the same phase shift among them. The amplitude of each current is regulated by a buck converter. In [35] the optimization of temperature profile in the graphite disc has been performed using an evolutionary strategy optimization method and finite element computations.

It can be seen that the publications and the patents regarding the ZCIH are limited and not clearly documented with measure and tests; therefore a lack of information exists in this domain.

2.1.1 Coil supply system

In the classical induction heating installations the coils are commonly supplied by resonant inverters made with thyristor, MOSFET or IGBT switches. A common connection scheme is a classical H bridge connected to a resonant load as shown in Fig. 2.6. Depending on the impedance of the circuit and on the application, the resonant RLC circuit can be set either in series or in parallel, each connection having its own advantages and drawbacks. The working principle of the inverter and its control system is the subject of another PhD thesis [4] and therefore it will not be deeply treated in this work. In the following how the general principle of the resonance has been used to control the power injected in the load will be explained.

The classical resonant inverter systems with single-coil load works compensating the reactive part of the power required by the coil Q_L, with a capacitor bank capable to exchange the reactive power Q_C at the chosen frequency. In this case, since only the electrical characteristics of the load are responsible of the power to be compensated, the resonance frequency can be calculated as:

$$f_r = \frac{1}{2\pi\sqrt{LC}} \tag{2.1}$$

where L and C are the inductance of the coil and the value of the resonant capacitor bank.

In the case of multi-coil systems the reactive power to be compensated depends not only by the self-parameter of the coil, but also by the exchanges of active and reactive power between coils. The reactive power is then a function of the electrical parameters (impedance matrix Z) of the system as well as of the currents value and ratio in the coils.

Making reference to the circular multi-coil induction system of Fig. 2.1, from the Fig. 2.7 it can be seen that each coil induces power in a different zone of a disc plate as in common transverse flux inductors. In order to simplify the calculation the system will be considered linear from an electromagnetic point of view. For the circular inductor here considered the aim would be to get a uniform temperature on the whole disc. Because of the axial symmetry of the system the distribution of the temperature along a radial coordinate can be considered as reference. It is obvious that in the centre of the disc the current cannot circulate, and then the uniformity of the temperature can be achieved only on a reduced part of the load radius. Each coil, when supplied by a current of suitable magnitude and phase, induces a current density in the load whose shape depends on the geometry of the coil and on the geometry and electrical characteristics of the disc. Because of the linearity of the electrical characteristics (linear materials and inductor in air), when the coils are supplied together, the resulting shape of the current corresponds to the superposition of the current density of the single coils. If the power supply is alternative, the current density profile along the radial coordinate can be represented by its real and imaginary part. In this way a combination of current values that impose the desired power density profile along the radius of the disc can be found. Successively, from the knowledge of the impedance matrix of the system and of the coil currents, the active and reactive powers absorbed by each single coil can be computed. When the power to be compensated is known, the value of the

capacitors of the three banks that make resonate the three loads at the same time can be calculated.
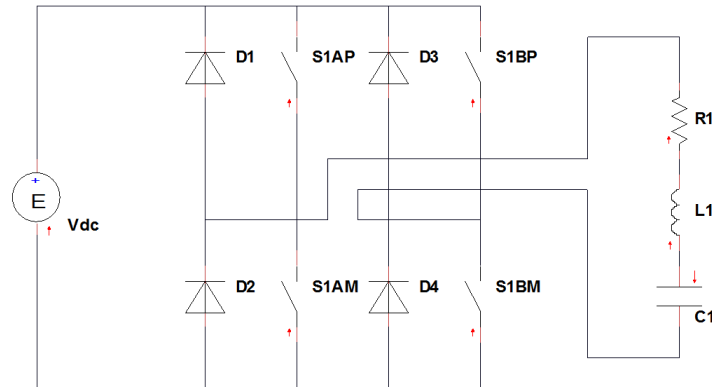
Fig. 2.6: Power supply inverter for each coil
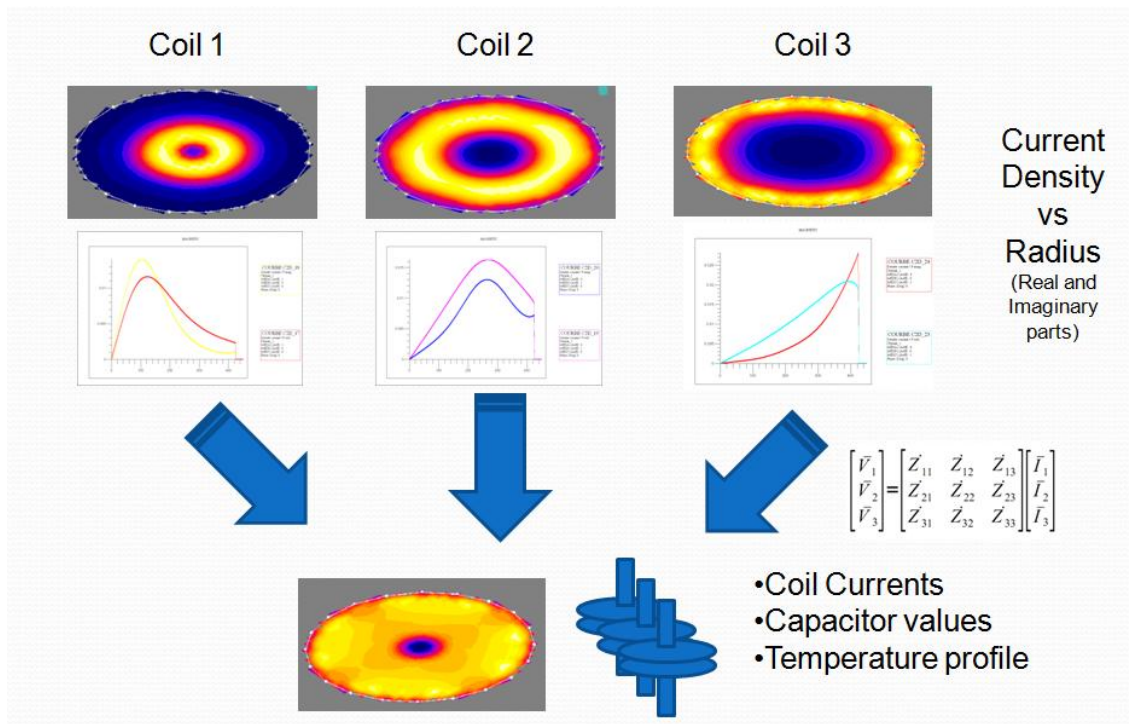
Fig. 2.7: Working principle of a multi-col inductor for the heating of thin circular plates

In the following paragraphs a theoretical explanation of how the complex imped-ance influences the active and reactive power of a system composed by more than one coil and by an external short circuited conductor is described. Afterwards how the presence of the massive conductor influences the impedance matrix of the system is shown. In presence of massive conductors a multi-coil device cannot be considered simply as a device composed by ideal transfer elements (i.e. mutual inductances) like in the equivalent circuit of transformers. The massive conductors (the load and the coil itself) are additional conductive elements in which induced currents can take place.

The system has to be modelled like a multi-port device described by an impedance matrix Z. For the analysis of induction devices like transformers or motors, the mutual resistances are often neglected. In multi-coil induction heating system it will be shown that this approach is not satisfactory and a complete impedance matrix must be considered.

Another difference with classical induction heating systems with a single coil is the harmonic propagation. The inverter system excites the resonant load by a square wave at a constant frequency that makes oscillate the RLC load depending on the quality factor of each coil. The square waves introduce in the circuit several harmonics that, because of the mutual coupling, propagate in the other coils and that have influence on the power density induced in the work-piece (sec. 4.4.2).

2.1.2 Characterization of the multi-coil inductor from supply side

In induction heating, the characterization of the inductor from the supply side has a great importance in the design of the system. For example, the equivalent circuit of an inductor for heating billets or other classical loads can be represented by an inductance with a series resistance. With this model it is possible to compute the performances of the system, or the value of the capacitor bank to be connected to the resonant inverter supplying the device.

In a multi-coil induction heating device the inductor system cannot be represented by separate dipoles, but it has to be represented by an impedance matrix that take into account the different exchanges of energy among coils. This means that both the reactive power to be compensated by the capacitors banks and the efficiency depend by the values of the current in the other coils and not only by the values of the self-impedance. This complicates considerably the control of the system since the series of capacitors values calculated in a given condition is suitable only for a particular series of currents. The effect of this principle is particularly annoying when the ratio between the current coil changes, and the values of capacitors should be changed to maintain the resonance in the three coils.

Powers

The considered multi-coil device can be modelled as a multi-pole or, more precisely, as a multi-port device. This possibility is due to the linearity of the system, as a consequence of the absence of magnetic materials. For this the inductances and the resistances don't depend from the currents values. In [3] the multi-coil inductor with two coils has been modelled as an impedance matrix, without taking into account the mutual resistances.

Making reference to a three-port device, useful to model the circular inductor of Fig. 2.1, in the frequency domain the equations governing the multi-port behaviour are:

$$[\bar{V}] = [\dot{Z}][\bar{I}]\tag{2.2}$$

where:

57

$$\left[\dot{Z}\right] = \left[R\right] + j\omega\left[L\right] \tag{2.3}$$

$$[R] = \begin{bmatrix} R_{11} & R_{12} & R_{13} \\ R_{21} & R_{22} & R_{23} \\ R_{31} & R_{32} & R_{33} \end{bmatrix} \tag{2.4}$$

$$[L] = \begin{bmatrix} L_{11} & L_{12} & L_{13} \\ L_{21} & L_{22} & L_{23} \\ L_{31} & L_{32} & L_{33} \end{bmatrix} \tag{2.5}$$

The voltages at the terminals of the inductor can be described by means of the following matrix system:

$$\begin{bmatrix} \overline{V}_1 \\ \overline{V}_2 \\ \overline{V}_3 \end{bmatrix} = \begin{bmatrix} Z_{11} & Z_{12} & Z_{13} \\ Z_{21} & Z_{22} & Z_{23} \\ Z_{31} & Z_{32} & Z_{33} \end{bmatrix} \begin{bmatrix} \overline{I}_1 \\ \overline{I}_2 \\ \overline{I}_3 \end{bmatrix} \tag{2.6}$$

To understand the energy meaning of the various elements of the impedance matrix ($Z_{i,j}$) it is convenient to make reference to a device with 2 ports instead of 3, as shown in Fig. 2.8, extending successively the conclusion to a multi-port device.

Fig. 2.8: 2-port device

In this case the resulting system is:

$$\begin{bmatrix} \overline{V}_1 \\ \overline{V}_2 \end{bmatrix} = \begin{bmatrix} Z_{11} & Z_{12} \\ Z_{21} & Z_{22} \end{bmatrix} \begin{bmatrix} \overline{I}_1 \\ \overline{I}_2 \end{bmatrix} \tag{2.7}$$

with

$$[Z] = \begin{bmatrix} Z_{11} & Z_{12} \\ Z_{21} & Z_{22} \end{bmatrix} = \begin{bmatrix} R_{11} & R_{12} \\ R_{21} & R_{22} \end{bmatrix} + j\omega \begin{bmatrix} L_{11} & L_{12} \\ L_{21} & L_{22} \end{bmatrix} \tag{2.8}$$

The voltages at the ports are:

$$\begin{cases} \overline{V}_1 = R_{11}\overline{I}_1 + j\omega L_{11}\overline{I}_1 + R_{12}\overline{I}_2 + j\omega L_{12}\overline{I}_2 \\ \overline{V}_2 = R_{22}\overline{I}_2 + j\omega L_{22}\overline{I}_2 + R_{12}\overline{I}_1 + j\omega L_{12}\overline{I}_1 \end{cases} \tag{2.9}$$

The complex power injected in the two ports of the multi-coil inductor can be written as:

$$\begin{cases} \overline{S}_1 = P_1 + jQ_1 = \overline{V}_1\breve{I}_1 = R_{11}I_1^2 + j\omega L_{11}I_1^2 + R_{12}\overline{I}_2\breve{I}_1 + j\omega L_{12}\overline{I}_2\breve{I}_1 \\ \overline{S}_2 = P_2 + jQ_2 = \overline{V}_2\breve{I}_2 = R_{22}I_2^2 + j\omega L_{22}I_2^2 + R_{12}\overline{I}_1\breve{I}_2 + j\omega L_{12}\overline{I}_1\breve{I}_2 \end{cases} \tag{2.10}$$

Where V_1 and V_2 are the voltages at the ports and I_1 and I_2 are the currents, both expressed as complex vectors:

$$\begin{cases} \overline{V}_1 = V_1(\cos\psi_1 + j\sin\psi_1) \\ \overline{V}_2 = V_2(\cos\psi_2 + j\sin\psi_2) \end{cases} \tag{2.11}$$

$$\begin{cases} \overline{I}_1 = I_1(\cos\varphi_1 + j\sin\varphi_1) \\ \overline{I}_2 = I_2(\cos\varphi_2 + j\sin\varphi_2) \end{cases} \tag{2.12}$$

Active power

The active power at the ports is:

$$\begin{cases} P_1 = R_{11}I_1^2 + \Re\{R_{12}\overline{I}_2\breve{I}_1\} + \Re\{j\omega L_{12}\overline{I}_2\breve{I}_1\} = R_{11}I_1^2 + R_{12}\Re\{\overline{I}_2\breve{I}_1\} - \omega L_{12}\Im\{\overline{I}_2\breve{I}_1\} \\ P_2 = R_{22}I_2^2 + \Re\{R_{12}\overline{I}_1\breve{I}_2\} + \Re\{j\omega L_{12}\overline{I}_1\breve{I}_2\} = R_{22}I_2^2 + R_{12}\Re\{\overline{I}_1\breve{I}_2\} - \omega L_{12}\Im\{\overline{I}_1\breve{I}_2\} \end{cases} \tag{2.13}$$

In order to understand the influence of the phase displacement on the powers, it is convenient to calculate the following complex values:

$$\begin{aligned} \overline{I}_1\breve{I}_2 &= I_1 I_2(\cos\varphi_1 + j\sin\varphi_1)(\cos\varphi_2 - j\sin\varphi_2) = \\ &= I_1 I_2(\cos\varphi_1\cos\varphi_2 + \sin\varphi_1\sin\varphi_2 - j\cos\varphi_1 sen\varphi_2 + j\sin\varphi_1\cos\varphi_2) \end{aligned} \tag{2.14}$$

$$\begin{aligned} \overline{I}_2\breve{I}_1 &= I_1 I_2(\cos\varphi_2 + j\sin\varphi_2)(\cos\varphi_1 - j\sin\varphi_1) = \\ &= I_1 I_2(\cos\varphi_1\cos\varphi_2 + \sin\varphi_1\sin\varphi_2 - j\cos\varphi_2 sen\varphi_1 + j\sin\varphi_2\cos\varphi_1) \end{aligned} \tag{2.15}$$

And to calculate the real and complex values:

$$\Im\{\overline{I}_2\breve{I}_1\} = -\cos\varphi_2\sin\varphi_1 + \sin\varphi_2\cos\varphi_1 = \sin(\varphi_2 - \varphi_1) \tag{2.16}$$

$$\Im\{\overline{I}_1\breve{I}_2\} = -\cos\varphi_1\sin\varphi_2 + \sin\varphi_1\cos\varphi_2 = \sin(\varphi_1 - \varphi_2) \tag{2.17}$$

The active power can now be written as

$$\begin{cases} P_1 = R_{11}I_1^2 + R_{12}I_1 I_2\cos(\varphi_1 - \varphi_2) + \omega L_{12}I_1 I_2\sin(\varphi_1 - \varphi_2) \\ P_2 = R_{22}I_2^2 + R_{12}I_1 I_2\cos(\varphi_1 - \varphi_2) + \omega L_{12}I_1 I_2\sin(\varphi_2 - \varphi_1) \end{cases} \tag{2.18}$$

The total active power injected in the structure is:

$$P_{tot} = P_1 + P_2 = R_{11}I_1^2 + R_{22}I_2^2 + 2R_{12}I_1 I_2\cos(\varphi_1 - \varphi_2) \tag{2.19}$$

because the mutual inductance terms have opposite signs.

From the above equation it can be seen which the parameters that influence the active power are. These depend on the values of the self-resistance of the windings and on the mutual resistances among them. The power due to the mutual resistances depends also on the phase displacement between the currents. Therefore, if the currents have the same phase, the power due to the mutual resistance is at the maximum. Considering the equations (2.18) and (2.19), the terms that make reference to the self-resistances include the losses in the coil and a part of the losses in the work-piece. The term containing the mutual inductance means that a circulating power between the two coils exist, and the term with mutual resistance means that one part of the power

consumed in the charge depends by the simultaneous existence of the two currents. An amount of active power is circulating from zone 1 to zone 2 when $\varphi_1 > \varphi_2$. This means that the current generator 1 should provide an additional active power to maintain the consumed power in zone 2. Moreover, the power provided by the inverter 2 could be negative.

Reactive power

The same calculations can be done for the reactive power:

$$\begin{cases} Q_1 = \omega L_{11} I_1^2 + \Im\{R_{12}\bar{I}_2\breve{I}_1\} + \Im\{j\omega L_{12}\bar{I}_2\breve{I}_1\} = \omega L_{11} I_1^2 + R_{12}\Im\{\bar{I}_2\breve{I}_1\} - \omega L_{12}\Re\{\bar{I}_2\breve{I}_1\} \\ Q_2 = \omega L_{22} I_2^2 + \Im\{R_{12}\bar{I}_1\breve{I}_2\} + \Im\{j\omega L_{12}\bar{I}_1\breve{I}_2\} = \omega L_{22} I_2^2 + R_{12}\Im\{\bar{I}_1\breve{I}_2\} - \omega L_{12}\Re\{\bar{I}_1\breve{I}_2\} \end{cases}$$

(2.20)

$$\begin{cases} Q_1 = \omega L_{11} I_1^2 + R_{12} I_1 I_2 \sin(\varphi_2 - \varphi_1) - \omega L_{12} I_1 I_2 \cos(\varphi_1 - \varphi_2) \\ Q_2 = \omega L_{22} I_2^2 + R_{12} I_1 I_2 \sin(\varphi_1 - \varphi_2) - \omega L_{12} I_1 I_2 \cos(\varphi_1 - \varphi_2) \end{cases}$$

(2.21)

And the total active power in input at the device can be calculated:

$$Q_{tot} = Q_1 + Q_2 = \omega L_{11} I_1^2 + \omega L_{22} I_2^2 - 2\omega L_{12} I_1 I_2 \cos(\varphi_1 - \varphi_2)$$

(2.22)

In this case, if the currents have the same phase, the contribution due to the mutual inductance is the highest, and the reactive power is the lowest. The terms that have been eliminated from the equations (2.19) and (2.22), represent the power that circulates between coils.

$$P_x + jQ_x = -\omega L_{12} I_1 I_2 \sin(\varphi_1 - \varphi_2) + jR_{12} I_1 I_2 \sin(\varphi_1 - \varphi_2)$$

(2.23)

This power exists only if the currents of the coils have not the same phase.

Frequency dependence of impedance matrix

The circuit modelling of multi-coil systems is usually studied with reference to electric transformers theory. In this kind of devices the losses in the iron core are generally negligible in comparison to the total power of the system. Then it is usually not necessary to have precise models, but a rough estimation of the losses in the ferromagnetic material is sufficient. In the classical transformer equivalent circuit, losses are included in the so-called "leakage resistance" connected in parallel to the primary circuit (Fig. 2.9). However it has been recognized that the leakage resistance does not provide a complete picture of the eddy current losses in the windings and in the metallic components of a multi coil system, especially when the losses are the main part of the power in the system such as in induction heating devices [37]. It is then necessary to relate the power losses calculations to the resistance parameters of an impedance matrix description of the device.
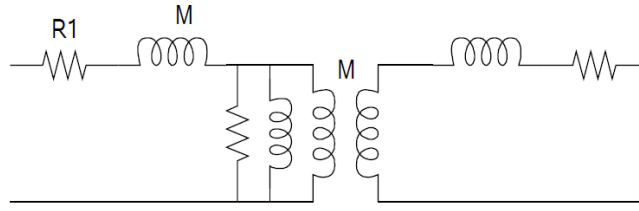
Fig. 2.9: Classic transformer equivalent circuit

The terms of the impedance matrix contain information on the power injected in the various parts of system. It is interesting to express the terms of the impedance matrix considering the load as an external short-circuited coil.

For example a 2-coil system with an external massive load can be represented, on first approximation, as a 3-coil system where two coils (*a* and *b*) are the inductors, and the third coil (*s*) represents the load, as shown in Fig. 2.10.
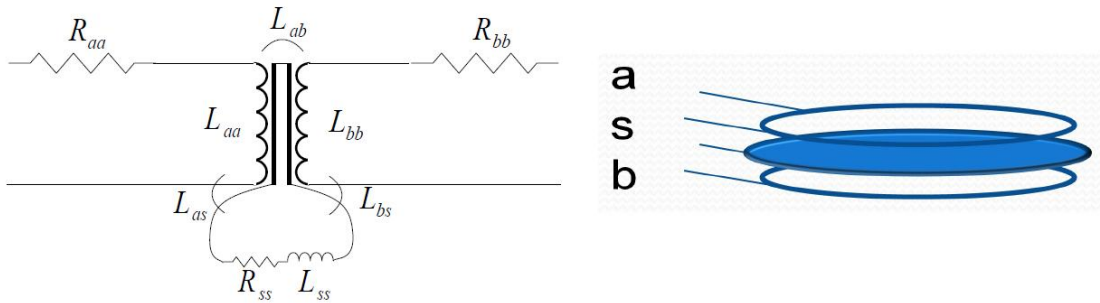
Fig. 2.10: Equivalent circuit of a multi-coil induction heating system

The current-voltage relation can be expressed as in (2.24):

$$\begin{bmatrix} \bar{V}_1 \\ \bar{V}_2 \\ \bar{V}_s \end{bmatrix} = \begin{bmatrix} \dot{Z}_{aa} & \dot{Z}_{ab} & \dot{Z}_{as} \\ \dot{Z}_{ba} & \dot{Z}_{bb} & \dot{Z}_{bs} \\ \dot{Z}_{sa} & \dot{Z}_{sb} & \dot{Z}_{ss} \end{bmatrix} \begin{bmatrix} \bar{I}_1 \\ \bar{I}_2 \\ \bar{I}_s \end{bmatrix} \tag{2.24}$$

where the impedance matrix contain the terms corresponding to the self-resistive terms and the self and mutual inductances terms:

$$[Z] = \begin{bmatrix} \dot{Z}_{aa} & \dot{Z}_{ab} & \dot{Z}_{as} \\ \dot{Z}_{ba} & \dot{Z}_{bb} & \dot{Z}_{bs} \\ \dot{Z}_{sa} & \dot{Z}_{sb} & \dot{Z}_{ss} \end{bmatrix} = \begin{bmatrix} \dot{R}_{aa} & 0 & 0 \\ 0 & \dot{R}_{bb} & 0 \\ 0 & 0 & \dot{R}_{ss} \end{bmatrix} + j\omega \begin{bmatrix} \dot{L}_{aa} & \dot{L}_{ab} & \dot{L}_{as} \\ \dot{L}_{ba} & \dot{L}_{bb} & \dot{L}_{bs} \\ \dot{L}_{sa} & \dot{L}_{sb} & \dot{L}_{ss} \end{bmatrix} \tag{2.25}$$

The voltages at the ports are:

$$\begin{cases} \bar{V}_1 = R_{aa}\bar{I}_1 + j\omega L_{aa}\bar{I}_1 + j\omega L_{ab}\bar{I}_2 + j\omega L_{as}\bar{I}_s \\ \bar{V}_2 = R_{bb}\bar{I}_b + j\omega L_{bb}\bar{I}_2 + j\omega L_{ab}\bar{I}_1 + j\omega L_{bs}\bar{I}_s \\ \bar{V}_s = R_{ss}\bar{I}_s + j\omega L_{ss}\bar{I}_s + j\omega L_{as}\bar{I}_1 + j\omega L_{bs}\bar{I}_2 \end{cases} \tag{2.26}$$

Since the slab has no open terminals, it can be assumed that the coil *s* is short-circuited ($V_s = 0$) and so the value of current I_s can be found as:

$$I_s = -\frac{j\omega L_{ab}I_1 + j\omega L_{sb}I_2}{R_{ss} + j\omega L_{ss}}$$

(2.27)

Substituting (2.27) in (2.26) the values of the impedance of the system considered as a 2-coil system of equation (2.7) can be calculated by the equations:

$$Z_{11} = R_{11} + j\omega L_{11} = R_{aa} + \frac{\omega^2 L_{as}L_{ab}R_{ss}}{R_{ss}^2 + \omega^2 L_{ss}^2} + j\omega\left[L_{aa} - \frac{\omega^2 L_{as}L_{ab}L_{ss}}{R_{ss}^2 + \omega^2 L_{ss}^2}\right]$$

(2.28)

$$Z_{12} = R_{12} + j\omega L_{12} = +\frac{\omega^2 L_{as}L_{sb}R_{ss}}{R_{ss}^2 + \omega^2 L_{ss}^2} + j\omega\left[L_{ab} - \frac{\omega^2 L_{bs}L_{ss}L_{as}}{R_{ss}^2 + \omega^2 L_{ss}^2}\right]$$

(2.29)

The self-impedance of the system Z_{11} is then composed by a term due to the self-resistance and inductance of the coil ($R_{aa} + j\omega L_{aa}$), plus a term that depends on the coupling with the load. The self-resistances R_{ii} (i=a,b) are the resistances that represent the part of the power lost in the supplied coil, whereas the second part of the resistance term (depending on the frequency) is the power dissipated in the slab when only the i coil is supplied. It can be noticed that when the frequency reaches a value of zero both the value of the mutual resistances and the part of self-resistances corresponding to the power dissipated on the slab are null. Obviously in the mutual impedance term Z_{12} the terms concerning the self resistance and impedance don't exist.

2.1.3 Optimization methods

In order to have a uniform temperature profiles in the work-piece, several optimizations have to be performed. These regard mainly the optimization of the currents to impose in the coils and the optimization of the geometry of the inductor, described in the next chapters.

The optimization of a device can be done in different ways. Optimization algorithms can be divided two main categories: *deterministic* and *stochastic*. *Deterministic* algorithms are devoted to find the optimum of a function when a single optimum point exists. When the presence of multiple local optimum points exists others methods should be used. These methods, called *stochastic*, scan the variables space in a "guided" random way in order to avoid false optimum localization.

In the present chapter due to the low complexity of the system to be optimized, only a deterministic algorithm will be used. The Tribes stochastic algorithm, here described, will be used in the Chapter 3 and Chapter 4 concerning the optimization of the inductor for heating moving strips.

Deterministic algorithm

A deterministic algorithm for the optimization of currents has been used in the case of the circular inductor with success (non-linear least-squares fitting) [5]. However the experience has demonstrated that deterministic methods are not always efficient in the case of electromagnetic problems because the search function often contains a number

of local minimums. For the case of the circular inductor for example the algorithm is run several times starting from different initial points [4], [5].

Particle Swarm Optimization

In case of more complex systems, that can have local minimums or a large number of parameters, the deterministic optimization algorithm can have problems for finding the actual minimum of the function to be optimized. In this case the stochastic optimizers could be done in order to reach a better precision. The stochastic optimization software used in the thesis is Tribes [38], an adaptive particle swarm optimization algorithm. Particle Swarm Optimization (PSO) is a biologically inspired optimization method. Recently, researchers have used it effectively in solving various optimization problems and it was found that it is particularly useful to solve electromagnetic design optimization [39]. However, like most optimization heuristics, PSO suffers from the drawback of being greatly influenced by the selection of its parameter values. Thus, the common belief is that the performance of a PSO algorithm is directly related to the tuning of such parameters. Usually, such tuning is a lengthy, time consuming and delicate process.

Tribes avoids manual tuning by defining adaptation rules which aim at automatically changing the particles' behaviours as well as the topology of the swarm. In Tribes, the topology is changed according to the swarm behaviour and the strategies of displacement are chosen in agree to the performances of the particles.

Fundamentals of TRIBES

Tribes, like all PSO-type algorithms, is inspired by the social behavior of flocks of birds. The basic elements of Tribes algorithm are:

Particles

The population, in Tribes, is called *swarm* and each individual is called *particle*. Each particle flies around in a multi-dimensional problem search space. In other words, a swarm consists of N particles moving around in a D-dimensional search space.

Informers

An informer for a given particle P is a particle Q that can pass some information to P. Typically this information includes the best position ever found by Q and the function value at this best position. The informer Q, therefore, influences the behavior of P.

Tribes

A tribe is a sub-swarm formed by particles which have the property that all particles inform all others belonging to the tribe. The concept is therefore related to the "cultural vicinity" (information neighbourhood) and not on "spatial vicinity" (parameter-space neighbourhood). It should be noted that, due to the above definition, the set of informers of a particle (its so-called i-group) contains the whole of its tribe but is not limited to it. This is shown in fig. 1 where the i-group of particle B1 contains all particles of its tribe (black) and particle W1 belonging to the white tribe.
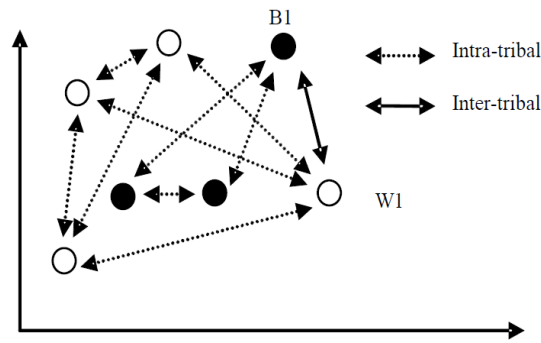
Fig. 2.11: Tribal relationships

Optimization procedure

Clerc's Tribes mechanism is auto-parameterising. The principles of Tribes are: i) the swarm is divided in tribes; ii) at the beginning, the swarm is composed of only one particle; iii) according to tribes' behaviours, particles are added or removed; and iv) according to the performances of the particles, their displacement strategies are adapted. The so-called structural adaptation rules describe when a particle is created or removed and when a particle becomes the informer of another, whereas so-called moving strategies indicate how particles modify their positions.

Structural adaption rules

The most important structural adaption rule is that "good" tribes may benefit from the removal of their weakest member, since they already possess good problem solutions and thus may afford to reduce their population by removing their worst particle; "bad" tribes, on the other hand, may benefit from the addition of a new member, increasing the possibility of improvement. In Tribes, for each "bad" tribe, the best particle generates a new particle and becomes an informer of it (all newly generated particles in an iteration are interconnected in a tribe and provide inter-tribe exchange of information).

The generation of the new particle can be done either with a uniform probability distribution or with a Gaussian one in order to emphasize the importance of the generating particle. Such choice, however, does not guarantee the improvement of the method in general and is therefore not considered here.

Crucial for the above steps is the definition of "good" and "bad" tribes: the more "good" particles a tribe has, the more "good" the tribe is. Algorithmically this is obtained by generating a random number between 1 and N_{tribe} (the number of particles in a tribe) and checking if it is less than or equal to G_{tribe} (the number of "good" particles in the tribe).

In contrast to most standard PSO approaches, in Tribes particles keep memory of their last two previous objective function values. If the last movement produced an improvement the objective function the particle is said to be "good", if the last two movements were both improvements the particle is said to be "excellent" (if the last movement is not an improvement the particle is labeled "neutral").

Structural adaption should not take place after each iteration since some time (iterations) are necessary for information to propagate throughout the swarm.

Moving strategies

In contrast with standard PSO algorithms particles do not have explicit associated velocities: their position is updated according to history only. "Excellent" particles are updated according to the "simple pivot" strategy, whereas "good" and "neutral" particles evolve according to the "noisy pivot" method.

In the "simple pivot" method two positions are used: the best position p of a given particle P and the best position q of its informer Q. Then two hyperspheres of radius $|p\text{-}q|$ are created around p and q and the new position is generated inside the intersection of the two hyper-spheres in such a way that the newly generated point is most likely to be nearer to the best between p and q. In order to obtain such behavior two weights w_1 and w_2 proportional to the relative fitnesses of P and Q are generated and the new position is obtained by $w_1h_p+w_2h_q$., where h_p and h_q are two randomly generated points in the hyper-spheres surrounding p and q respectively.

In the "noisy pivot" method the same procedure is applied but random noise is added to the obtained position in such a way that exploration beyond the hyper-spheres becomes possible.

The combined use of these strategies has a twofold effect: very good particles search in their close neighborhood (exploitation) whereas all other sample wider regions of parameter space (exploration).

Flowchart

Summarizing, the Tribes algorithm consists of following steps:

Initialization of swarm

Set iteration t=1. Initialize a population of 1 particle (real-valued D-dimensional vector) and 1 tribe with random values generated according to a uniform probability distribution within given upper and lower bounds.

Evaluation of each particle in the swarm

Evaluate the fitness (objective function) value of each particle.

Swarm moves

Apply the moving strategies ("simple pivot" or "noisy pivot") according to the quality of particles ("excellent", "good" or "bad").

Adaptation scheme

After every $L/2$ iterations, where L is the number of links in the population, adapt the structure of the swarm by applying the above described structural adaption rules.

Stopping criterion

Set the generation number for t = t + 1. Proceed to step Evaluation of each particle in the swarm until a stopping criterion is met, usually a maximum number of iterations or a maximum number of objective function evaluations.

2.2 Analysis of the prototype

A prototype of a multi-coil induction system was installed at EDF R&D Les Renardières laboratories. This prototype is the result of a former work made by EDF in 2005 and reported in its fundamental aspects in [5]. The pilot was built but never tested, and then the first part of the work has been devoted to verify the basic concept of the heating method and to characterize the multi-coil system viewed from the supply side. In the following paragraphs the results of the analysis of the prototype will be exposed.

The multi-coil induction system is composed by 3 concentric coils. A drawing of the system with its dimensions is shown Fig. 2.12 and Fig. 2.13. The medium and big coils are composed by 4 turns; the internal one has 8 turns. The coils are connected to the power supply by 3 bus bars of different length. The same bars connect in series-connection the upper and lower parts of each coil disposed on the 2 sides of the slab. The power supply is composed by an IGBT 3–phase parallel resonant inverter working at approximately 1500 Hz. The inverters can control the amplitude and the phase separately for each phase. The operating frequency is the same for the 3 arms and it is set by tuning the resonant capacitors. The load is a disc of stainless steel 316L (see Appendix B) with different diameters and a thickness of 1 mm. The inverter driver controls the power determining the resonant frequency of the big coil, and setting the whole system to this frequency. As a consequence the other two coils are at different power levels respect to the main coil. In Fig. 2.15 and Fig. 2.16 there are some photos of the existing prototype at the EDF Laboratories.

The characteristic of the system are the following:

- 3-phase system

- Frequency f≈1500 Hz

- Max power P=100kW

- Capacitor banks:

    o Little coil: 10 x 12 uF + 5 x 22 uF+5 x 33 uF = 395 uF

    o Middle coil: 5 x 12 uF + 5 x 22 uF + 3 x 33 uF = 269 uF

    o Big coil: 4 x 12 uF + 5 x 22 uF = 158 uF
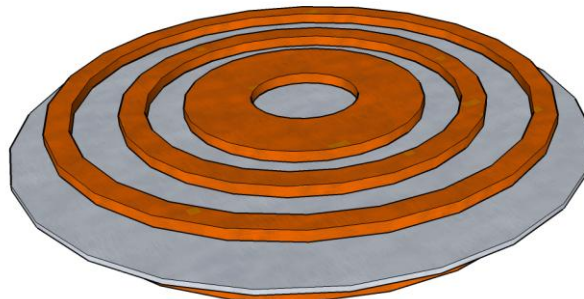
Fig. 2.12: Sketch of one side of the multi-coil transverse flux heating system
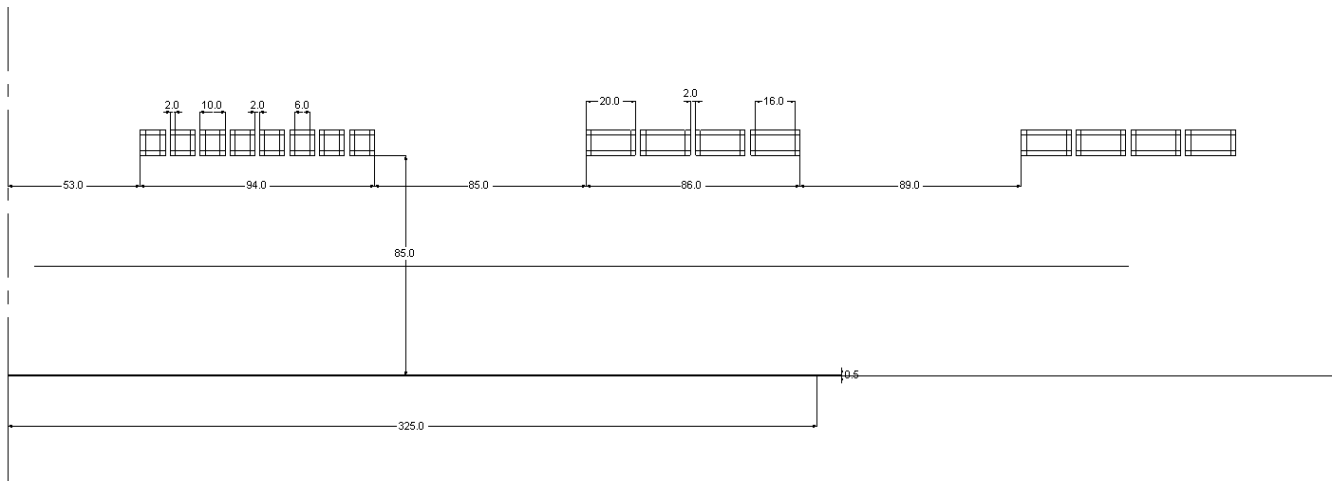
Fig. 2.13: Section of the inductor with the metal disc
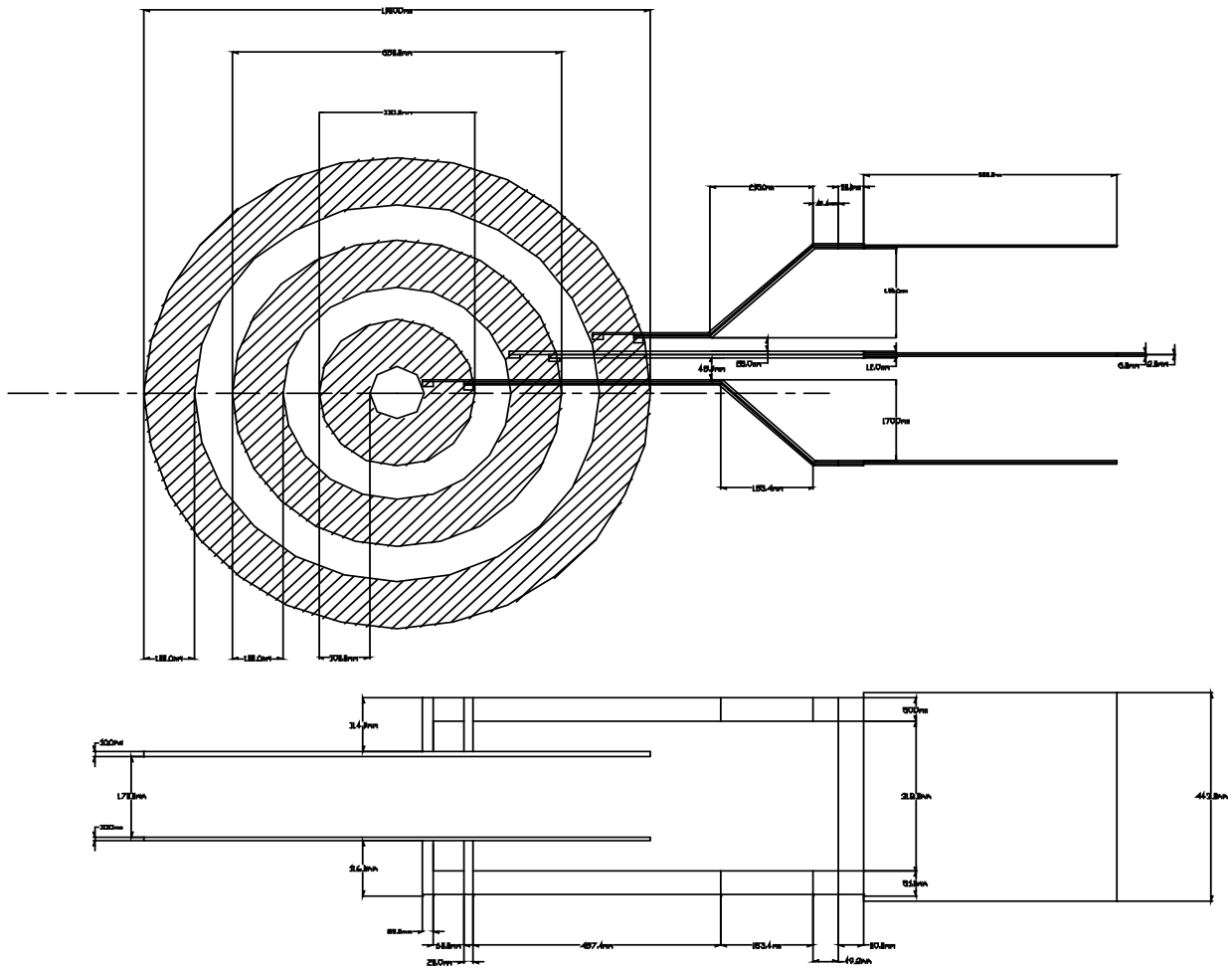
Fig. 2.14: Dimensions of the circular multi-coil inductor
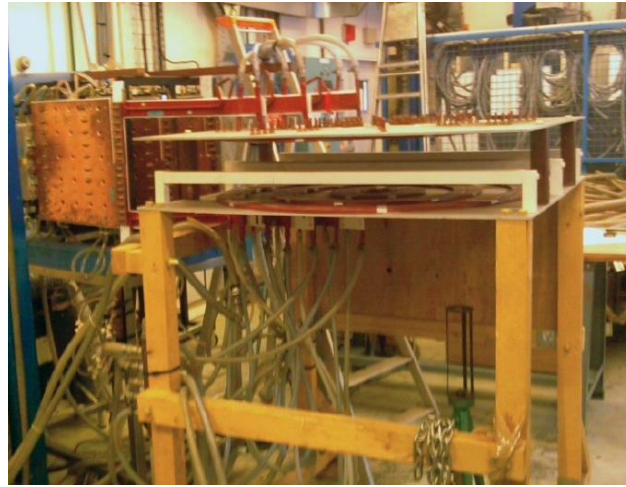
Fig. 2.15: Prototype installed at EDF laboratories
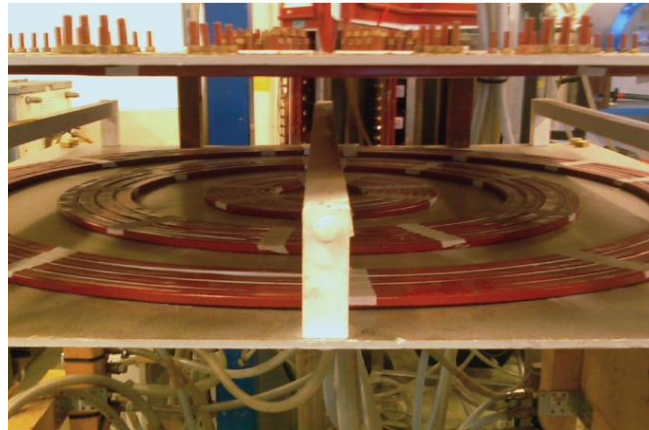
Fig. 2.16: View of the coils

2.2.1 **Impedance matrix computations with 2D FEM method**

This section describes the simulations performed with the numerical FEM software Flux 2D [27] for the analysis of the pilot multi-coil system. The main aim of the simulations is to compute the impedance matrix of the system, necessary to define the control algorithm. The characteristics of the model used for the computations of the impedance matrix are described in the following.

▪ **Materials**

The domain has been subdivided in various regions: the metallic disc to be heated, the three inductor coils and the surrounding air. The materials of the various regions have been considered having linear magnetic characteristics. The impedance computations have been done considering the system at ambient temperature. In the following table the physical characteristics of the materials are given.

• Strip	• Stainless steel 316L
	• Solid conductor
	• Relative Magnetic Permeability $\mu_r=1$
	• Resistivity $\rho=730E\text{-}9$ Ωm
	• Penetration depth at 1500 Hz - $\delta_{Steel1500Hz}=11{,}62$ mm
	• thickness: 1 mm
• Coils	• Copper
	• Solid conductor
	• Relative Magnetic Permeability $\mu_r=1$
	• Resistivity $\rho=18E\text{-}9$ Ωm
	• Penetration depth at 1500 Hz $\delta_{Cu1500}=1{,}74$ mm

▪ **Circuit**

The circuit associated with the model is shown in Fig. 2.17. Each coil is associated to a coil region of type "solid conductor" in the FEM model. Solid conductors are conductors in which the eddy current computation is performed. The use of the solid conductors is necessary because the field is strongly influenced by the induced current distribution in the coils (see par. 2.2.4).

Three independent current generators are connected to the three coils. Each turn of the coils is associated to a region and each region is associated to a solid conductor in the circuit. In order to simulate the open circuit condition the generators have been forced to a current of zero amperes.
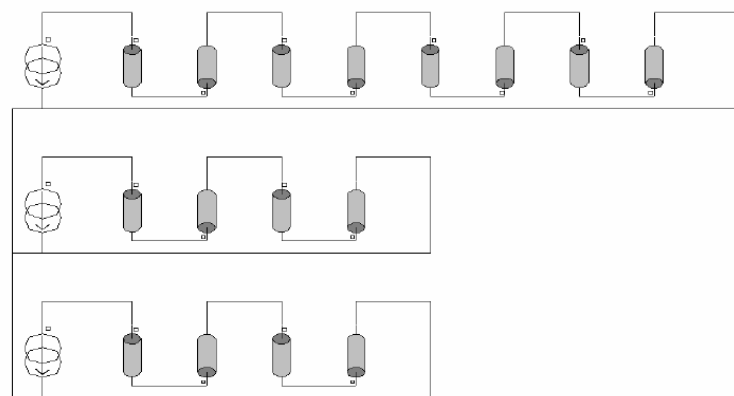
Fig. 2.17: Supply circuit for impedance matrix computations

- **Geometry and mesh**
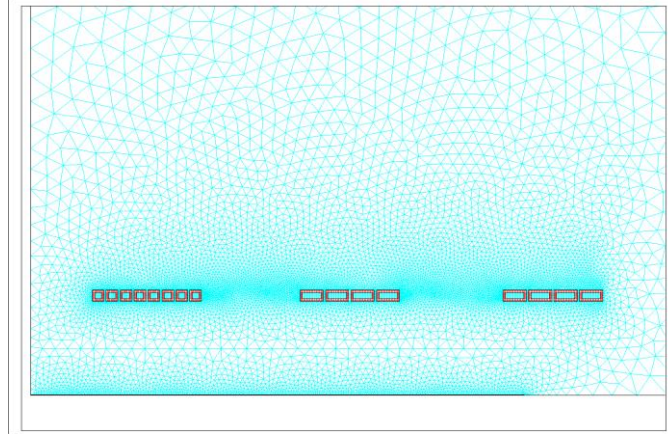
Fig. 2.18: Detail of the mesh

An axi-symmetric 2D model has been made. The computation therefore does not take into account the influence of the connection bars. The symmetry in the middle plane of the slab has been considered. The mesh elements are of the 2nd order. In Fig. 2.18 a detail of the mesh is shown.

- **Simulation**

A time-harmonic magneto-dynamic simulation of the electromagnetic system has been performed with Flux 2D. The frequency has been set to 1500 Hz. A parametric analysis has been done in order to calculate the values of the inductances for different diameter of the load. The simulations are performed considering three diameters of the disc (650 mm, 750 mm, 850 mm) and calculating the inductances for each diameter. The equations are solved for the magnetic vector potential with approximating function of the 2nd order in the finite elements.

- **Impedance matrix computation**

The calculations of the terms of the impedance matrix can be done with Flux 2D with various methods. In this case the calculated inductances have been obtained directly from the computation of voltages and currents in the circuit used for the simulation. If we consider the current I at null phase we have:

$$R_{ij} = \frac{\Re \overline{V}_i}{\left| \overline{I}_j \right|} \tag{2.30}$$

$$L_{ij} = \frac{\Im \overline{V}_i}{\left| \overline{I}_j \right| \cdot 2 \cdot \pi \cdot f} \tag{2.31}$$

where $\overline{V}_i$ is the complex voltage at the inductor terminals, $\overline{I}_j$ the current injected in the coil and f the supply frequency

▪ **Results**

In Tab. 2.1-Tab. 2.3 the values of auto and mutual resistances and impedances as a function of the disc radius are shown. The Fig. 2.19 shows graphically the behaviour of the impedances as a function of the dimension of the slab. It can be noted that the values of the impedance change more for the most external coils. This means that the diameter does not affect the impedance of the inner coils and that the power distribution along the radius does not change considerably for these coils.

Radius	R11	R21	R13	L11	L12	L13
0	16,0	3,55	2,00	25,1	7,72	5,35
325	31,6	25,6	19,0	23,5	5,29	3,47
375	31,5	26,1	20,7	23,5	4,89	2,89
425	31,3	25,8	21,4	23,4	4,66	2,36

Radius	R21	R22	R23	L21	L22	L23
0	3,55	10,1	3,90	7,72	33,8	20,7
325	25,6	61,6	47,3	5,29	28,9	16,8
375	26,1	68,2	60,9	4,89	27,3	14,6
425	25,8	69,4	69,9	4,66	26,3	12,4

Radius	R31	R32	R33	L31	L32	L33
0	2,00	3,902	16,8	5,35	20,7	70,9
325	19,0	47,3	55,0	3,47	16,8	67,7
375	20,7	60,9	80,8	2,89	14,6	64,8
425	21,4	69,9	114	2,36	12,4	60,4

Tab. 2.1: Auto and mutual resistances and inductances values as a function of the diameter of the disc (RS: radius of the disc) and without disc (RS=0)

Radius	Z11=R+jωL		Z12		Z13	
0	16,0	237	3,55	72,7	2,00	50,4
325	31,6	222	25,6	49,8	19,0	32,7
375	31,5	221	26,1	46,1	20,7	27,3
425	31,3	221	25,8	43,9	21,4	22,2

Radius	Z21		**Z22**		Z23	
0	3,55	72,7	10,1	318	3,90	195
325	25,6	49,8	61,6	273	47,3	158
375	26,1	46,1	68,2	258	60,9	138
425	25,8	43,9	69,4	248	69,9	117

Radius	**Z31**		**Z32**		**Z33**	
0	2,00	50,4	3,90	195	16,8	669
325	19,0	32,7	47,3	158	55,0	638
375	20,7	27,3	60,9	138	80,8	611
425	21,4	22,2	69,9	117	114	569

Tab. 2.2: Impedances (real and imaginary parts at 1500 Hz) values as a function of the diameter of the disc (RS: radius of the disc) and without disc (RS=0)

Radius	Z11=mod,cosφ		Z12		Z13	
0	237	0,067	72,8	0,049	50,5	0,040
325	224	0,141	56,1	0,458	37,8	0,503
375	223	0,141	53,0	0,494	34,2	0,604
425	223	0,140	51,0	0,508	30,8	0,693

Radius	Z21		**Z22**		Z23	
0	72,8	0,049	318	0,032	195	0,020
325	56,1	0,458	280	0,220	165	0,286
375	53,0	0,494	266	0,255	150	0,404
425	51,0	0,508	257	0,269	136	0,513

Radius	**Z31**		**Z32**		**Z33**	
0	50,5	0,040	195	0,020	669	0,025
325	37,8	0,503	165	0,286	640	0,086
375	34,2	0,604	150	0,404	616	0,131
425	30,8	0,693	136	0,513	581	0,197

Tab. 2.3: Impedances (module and power factor at 1500 Hz) values as a function of the diameter of the disc (RS: radius of the disc) and without disc (RS=0)
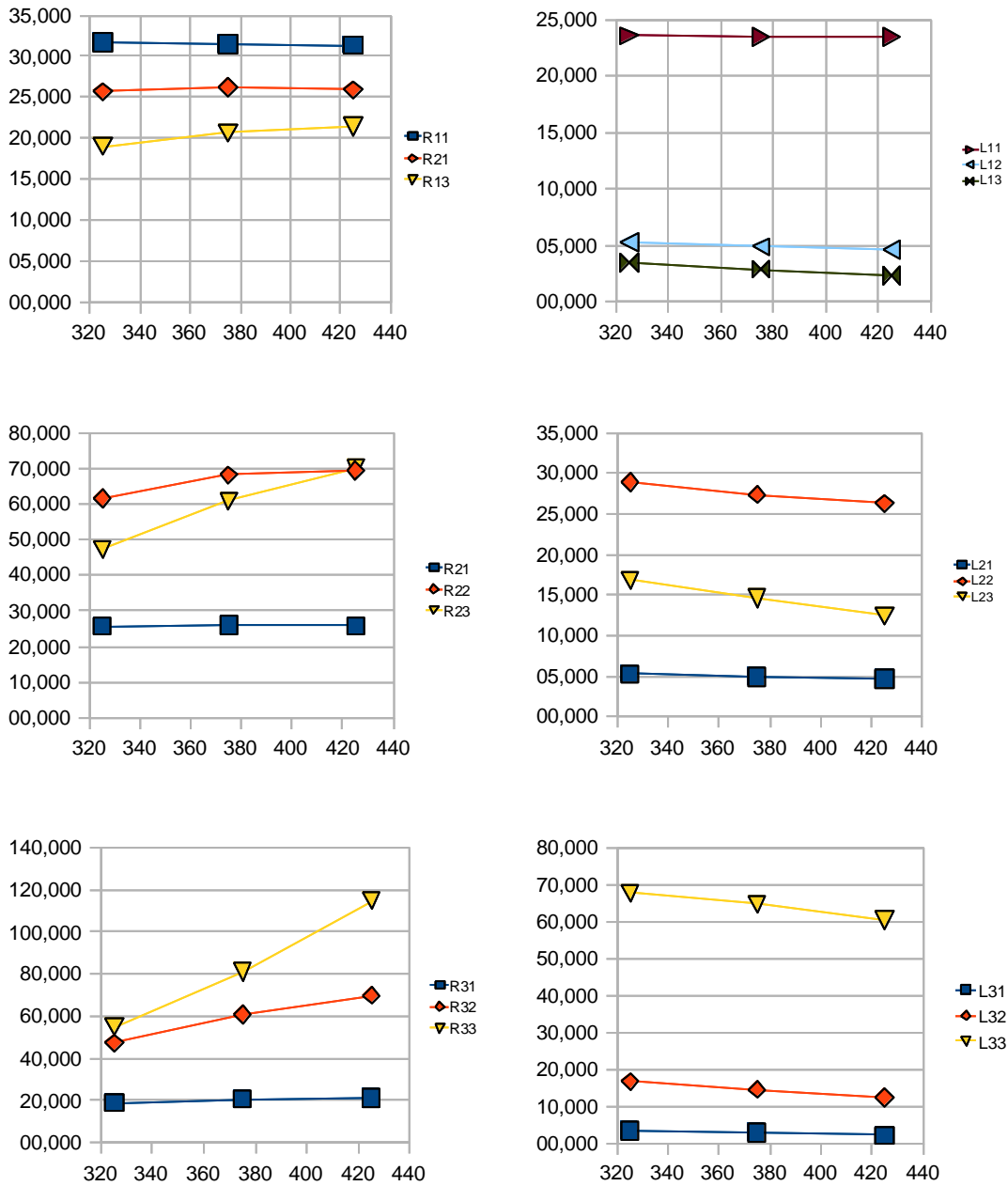
Fig. 2.19: Impedances values as a function of the disc radius

2.2.2 **Impedance computation with PEEC Method**

This paragraph describes the simulation performed on the pilot system with the software Inca3D which is based on the numerical method called Partial Equivalent Element Computation (PEEC) [26]. The previous computations, done with Flux 2D, does not take into account the connection bars and this could give some error on the

impedance matrix values. The software Flux 3D has been also tried, but the simulation time and the memory requirements were too high to introduce in the model these parts. The PEEC method allows reducing the memory and the computation time (see par. 1.4.3), and for this it has been tested.

The current density profiles along the radius have been computed with each coil individually supplied. The "individual" current profiles are useful to optimize the values of currents in order to obtain a uniform total profile in the disc it will be described in the paragraph 2.2.5.
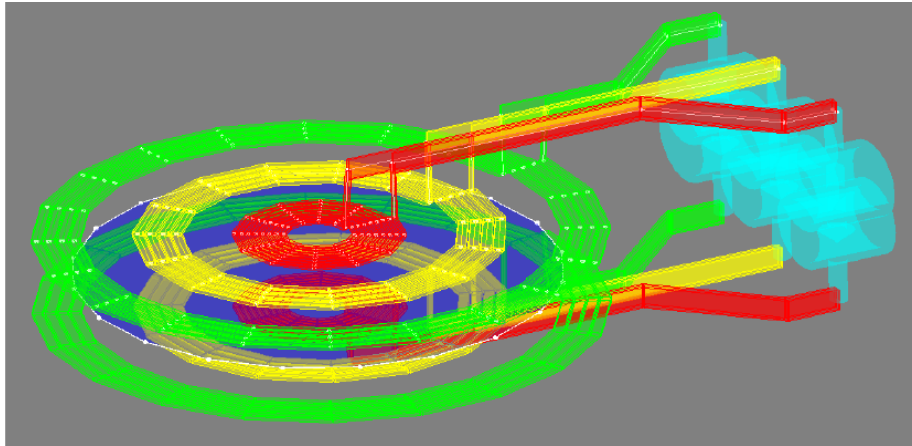
Fig. 2.20: Inca3D model with connection bars

Geometry and mesh

The geometry is shown in Fig. 2.20. Because of the memory restriction to 8GB RAM, it was necessary to make some simplification to reduce the size of the matrix to be solved. In particular it has been neglected the skin effect in all conductors. The availability of more powerful machine allows a further refinement of the mesh.

In order to compare the PEEC results with the results from Flux 2D two models have been used. The first with connection bars (Fig. 2.20) and the second without connection bars (Fig. 2.21).
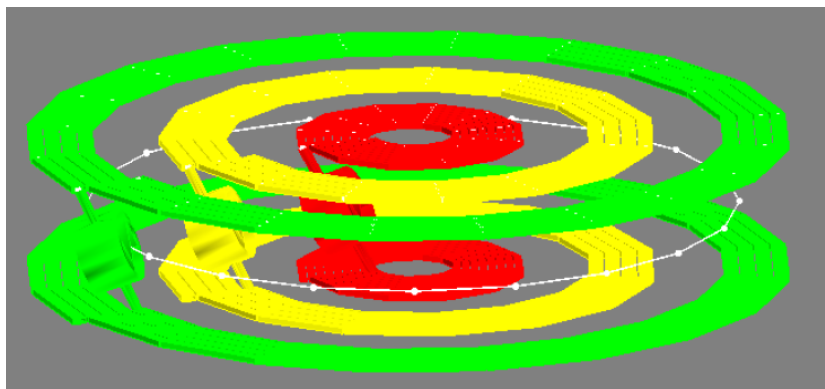
Fig. 2.21: Inca3D model without connection bars

Simulation Results

As described in chapter 1, Inca 3D includes 2 applications. The first is called "supplied conductors" and it is suitable for computing the distribution of the induced currents in the conductors. The second application is called "impedance computation" and allows computing the impedance matrix of the system. In the following the results given by the two applications will be described.

- **Supplied conductors**

Three different computations, each with a current supply of 1A rms injected in only one generator for each simulation, have been performed to see the influence of the different coils on the current density profile in the disc. As it can be seen in the Fig. 2.22 the precision of the computation is of very poor quality. There are several factors that, at the time of the computations affected the results:

- The path of the currents calculated by Inca3D is not perfectly circular due to the limitations of the meshing techniques. Inca allows only rectangular elements, and for that, the power density distribution is then dependent on the chosen radius.

- The curvature of the coils has been approximated by straight elements. This approximation doesn't allow taking into account the "ring effect" and then the real distribution of the currents in the coils.

- The region type that simulates the load can have only one mesh element in the thickness.

- The memory limitations did not allow refining the mesh in order to take into account the actual skin effect in the coils.

Fig. 2.22: Real and imaginary part of the current density in the disc load, along a radial coordinate, computed by Inca3D

▪ **Impedance matrix computation**

The impedance matrix computation has been done in two cases:

• with connection bars

• without connection bars

The results of the computations in the different cases are given in Tab. 2.4. Comparing these results with those obtained by Flux 2D (Tab. 2.1), a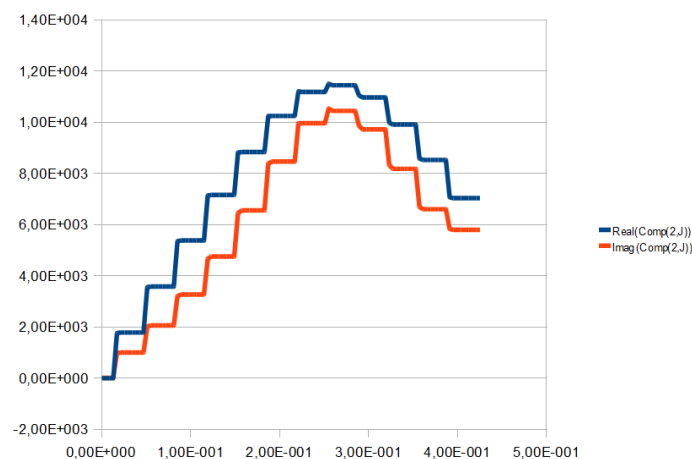 difference can be seen mainly on the self-resistance of the smallest coil. The difference is probably due to the fact that in the thickness of the coil only one element was used due to available memory resources. In this case the skin effect on the conductors is not taken into account, and this certainly gives an underestimation of the self-resistance of the conductor.

Model	Z11=R+jωL		Z12		Z13	
Inca3D with connections	26.6	238	25.2	44.8	21.1	23.8
Inca3D without connections	26.1	232	25.3	45.2	21.1	24.4

Model	Z21		**Z22**		Z23	
Inca3D with connections	25.2	44.8	69.4	253	68.8	119
Inca3D without connections	25.3	45.2	69.1	250	68.0	123

Model	**Z31**		**Z32**		**Z33**	
Inca3D with connections	21.1	23.8	68.8	119	107	586
Inca3D without connections	21.0	24.3	68.0	123	102	589

Tab. 2.4: Comparison between Inca3D with and without connection

2.2.3 **Comparison of computations and measurements**

In the previous paragraphs some methods to calculate the impedance matrix of the system have been described. It is convenient to compare these computations with the measures performed on the prototype. In addition to the Flux 2D and the Inca 3D methods, an analytical method capable to compute the induced currents and the impedance matrix of a multi-coil inductor has been developed and used. This method, that is described in Appendix C, does not take into account the edge effect (see par. 1.2.1) because it considers the disc having an infinite radius. Therefore the comparison with the analytical method can be done only for the two internal coils where the currents flow enough far from the disc edge.

The measurements have been performed with two methods: by impedance-meter and by the method of the "pseudo-energy" [4], [40]. The measurements have been done on the prototype, at the terminal level (point A of Fig. 2.23).

The first method makes use of an Agilent E4980A Precision LCR Meter. The second method makes use of the average of the voltages and currents, measured by an oscilloscope, of the different coils in order to calculate the so-called "pseudo-powers". From these pseudo-powers the impedance values can be computed. In this way the errors coming from the ripple of the power supply can be minimized, and the error on the measured phase displacement is reduced at the minimum.
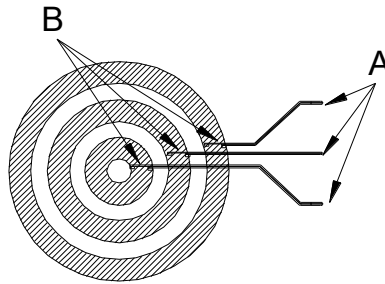
Fig. 2.23: Measuring points

	Z11=R+jωL		Z12		Z13	
Imp-meter	34.9	248	-	-	-	-
Ps-energy	32,4	237	25,7	42,7	21,3	25,0
Flux 2D	31,3	221	25,8	43,9	21,4	22,2
Inca 3D	26.6	238	25.2	44.8	21.1	23.8
Analytic	22.6	262	25.3	45.3	-	-

	Z21		Z22		Z23	
Imp-meter	-	-	68.4	251	-	-
Ps-energy	25,4	42,4	66,6	242	65,9	113
Flux 2D	25,8	43,9	69,4	248	69,9	117
Inca 3D	25.2	44.8	69.4	253	68.8	119
Analytic	25.3	45.3	69.1	251	-	-

	Z31		Z32		Z33	
Imp-meter	-	-	-	-	110	574
Ps-energy	20,8	21,4	66,0	112	105	560
Flux 2D	21,4	22,2	69,9	117	114	569
Inca 3D	21.1	23.8	68.8	119	107	586
Analytic	-	-	-	-	-	-

Tab. 2.5: Comparison among computations and measured values (Note: The analytical computations have been done with an air-gap value of 80 mm for considering the equivalent position of the ideal inductor)

The differences existing among the different values are due to several reasons:

- The non-accurate values of material properties used for numerical computation. Even if the material properties have been measured (see Appendix B), a

difference due to the room temperature exists. Moreover it has been found that the strip is slightly magnetic at a low temperature.

- The accuracy of the used numerical model. The numerical model suffers of some simplifications, and the geometry doesn't correspond exactly to the proto-type. This is due to the geometrical tolerances of the actual inductor and to the centring of the disc load.

- The accuracy of impedance-meter. The impedance meter has a maximum supply current of 200mA that cannot be enough to reach a good precision on the measurements.

2.2.4 Current distribution on the coil conductor

The coil conductors are made by copper tubes of rectangular cross-section, in order to allow the cooling of the inductor by water circulation. Since the skin depth of the copper at 1500 Hz is about 1.8mm, the turn wall has been chosen to 2 mm. Neverthe-less in the massive conductors an uneven distribution of the current density is usually found. From the Flux 2D model, described in par. 2.2.1, the current distribution on the coils can be observed. The uneven distribution of currents is mainly due to the follow-ing well known phenomena:

- Ring effect

- Proximity effect

- Skin effect

The ring effect appear in curved conductor; the internal path of the current results shorter than the external one, so the resistance in the internal loop is less important and the current density tends to concentrate in this path. As shown in Fig. 2.24 this ef-fect is more evident in the smallest coil, due to its little radius.

The proximity effect exists when a massive conductor is placed closed to another one. The eddy currents induced by the alternating field modify the overall distribution of current flowing through them. In the specific case, shown in Fig. 2.24, the currents in the turns tend to be concentrated in the adjacent walls. The proximity effect between the current of the disc and those of the coils is negligible.

The skin effect occurs when an alternating current flows in a solid conductor. Thanks to the induced electromagnetic forces the current tends to be concentrated to the external part of the conductors (the "skin"). The skin effect adds to the ring and the proximity effects in order to obtain an uneven distribution of the current density in the conductors.

It is important to take into account these effects in the coils constituting the induc-tors, because the uneven distribution of the current density reduces the overall mag-neto-motive force affecting the disc, compared to an even distribution of the currents, and therefore reduce its induced power. The difference on the induced power, com-puted by a flux 2D model, between the coils supplied with even and uneven current

distribution is estimated to be about 10% less for the conductors carrying an uneven current.
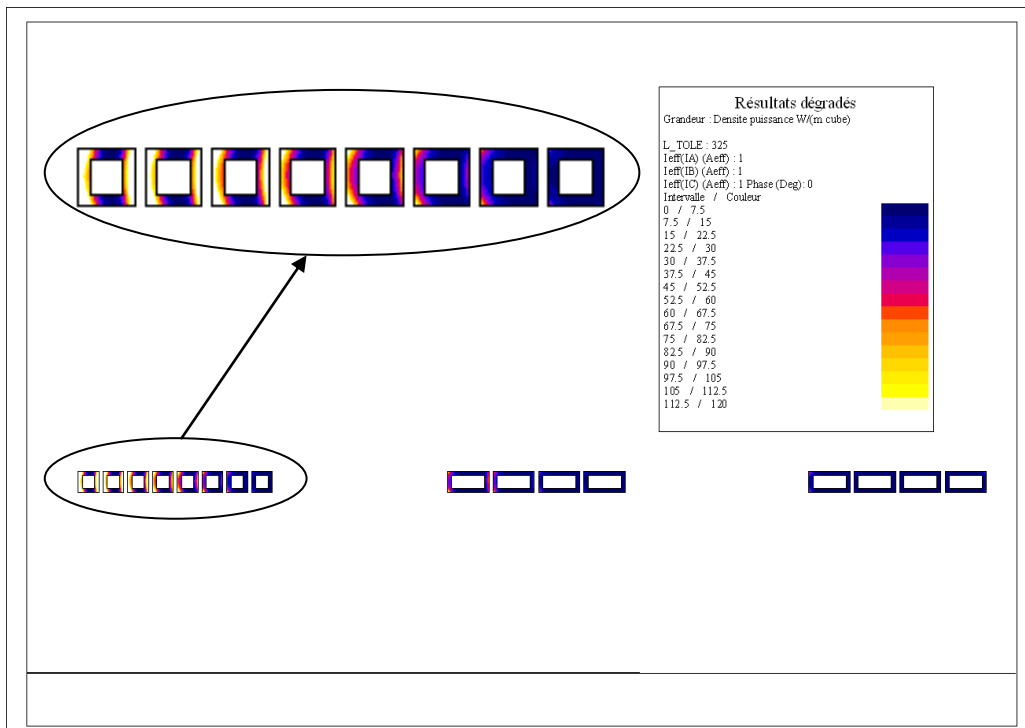

Fig. 2.24: Power density distribution in the coils with imposed current of 1 A in each coil.

2.2.5 **Profile optimization in the circular system**

The circular prototype was built with the idea to test the principle of the multi-coil inductor. The measurements and the computations done in the previous paragraphs were aimed to compute the impedance of the system and the distribution of the temperature along a radial coordinate. Let's recall that the geometry of the system has been chosen with the purpose of reducing the number of variables that could influence the problem. Also the use of non-linear materials has been avoided to give the possibility to apply the superposition effect on the currents. In this section the optimization method used to obtain the desired temperature profile, and the corresponding values of the coil currents will be described [5].

Considering the three coil system of sec. 2.2, each coil individually supplied with an alternating current, gives a distribution of the current field $\bar{J}$ in the disc volume that depends on the frequency, on the physical parameter of the materials, and on the geometrical dimensions and positions of the disc and the coils. The considered system is axi-symmetric so the vector $\bar{J}$ is directed along the azimuthal coordinate and its distribution on the volume can be represented by a field of scalar phasors in any azimuthal cross-section of the strip. Another assumed simplification is that in the thickness of the disc the current density is uniform, so it can be represented by its values along any line in the disc cross section parallel to the surface.

The profiles of the current density $\bar{J}$ created by each coil can be computed by analytical or numerical methods. Supplying each coil k with the normalized current of 1A_{rms} , the computations gives the normalized real ($f_{kR}(r)$) and imaginary ($f_{kI}(r)$) components of the current density phasors along the radial coordinate of the disc. As example the Fig. 2.25 shows the shape functions for the pilot calculated by flux 2D.

By the knowledge of the functions $f_{kR}(r)$ and $f_{kI}(r)$, the real and imaginary parts of current density profile $J_{kR}(r), J_{kI}(r)$, corresponding to an arbitrary imposed coil current $\overline{I_k} = I_k e^{j\varphi_k} = I_{kR} + jI_{kI}$ can be calculated. Finally the functions $J_{kR}(r)$ and $J_{kI}(r)$ of the three coils can be added to find the total curves of current density $\overline{J_t}(r)$ along the radius:

$$\overline{J_t}(r) \quad = J_{tR}(r) + jJ_{tI}(r) =$$

$$= \sum_{k=1}^{3}\left\{\left(f_{kR}(r) + jf_{kI}(r)\right)\left(I_{kR} + jI_{kI}\right)\right\} = \tag{2.32}$$

$$= \sum_{k=1}^{3}\left\{\left(f_{kR}(r)I_{kR} - f_{kI}(r)I_{kI}\right) + j\left(f_{kR}(r)I_{kI} + f_{kI}(r)I_{kR}\right)\right\}$$

From the knowledge of the total current density, the power density distribution along the radius can be computed:

$$w(r) = \rho\left(J_{tR}^2(r) + J_{tI}^2(r)\right) \tag{2.33}$$

Optimization process

By the use of this computation method it is possible to implement an optimization procedure suitable for finding the series of currents (in module and phase displacement) that satisfies a required power profile $w_{ref}(r)$. The optimization process is performed minimizing a difference function between the required power profile and the power profile given by the triplet of currents making use of a standard deterministic optimization algorithm "lsqnonlin" [5], [41]. The vector of current values to be optimized (considering I_1 as reference for the phase displacement) is:

$$X = \left(I_1, I_2, \varphi_2, I_3, \varphi_3\right) \tag{2.34}$$

The value of the current density is then a variable depending by r and **X**. The function to be minimized is:

$$g(r,x) = \left|w(r,X) - w_{ref}(r)\right| \quad / \forall r \in \left[r_{min}, r_{max}\right] \tag{2.35}$$

Since the functions $f_{kR}(r)$ and $f_{kI}(r)$ are calculated by finite element software the function $w(r,x)$ is defined for a set of N points of the radius of the disc, the norm of the vector to be minimized become:

$$\Gamma(X) = \sum_{i=1}^{N}\left(\frac{w(r_i,x) - w_{ref}(r_i)}{w_{ref}(r_i)}\right) \tag{2.36}$$

A deterministic optimization algorithm can be used to find the value of the vector **X** that satisfies the precision requirements in respect to the desired power profile.

A problem that arises in the application of the optimization algorithm is that, for the physic of the problem, in the centre of the disc there is no induced current and as a consequence there is no induced power. The optimization algorithm can then be applied only to a restricted part of the radius of disc, neglecting the central part.

An example of the power profile obtained with the application of the algorithm is shown in Fig. 2.26, obtained by the Flux 2D model supplied with the currents indicated. In the optimization the profile has been optimized with the radial coordinate ranging from 0.1 to 0.425 m
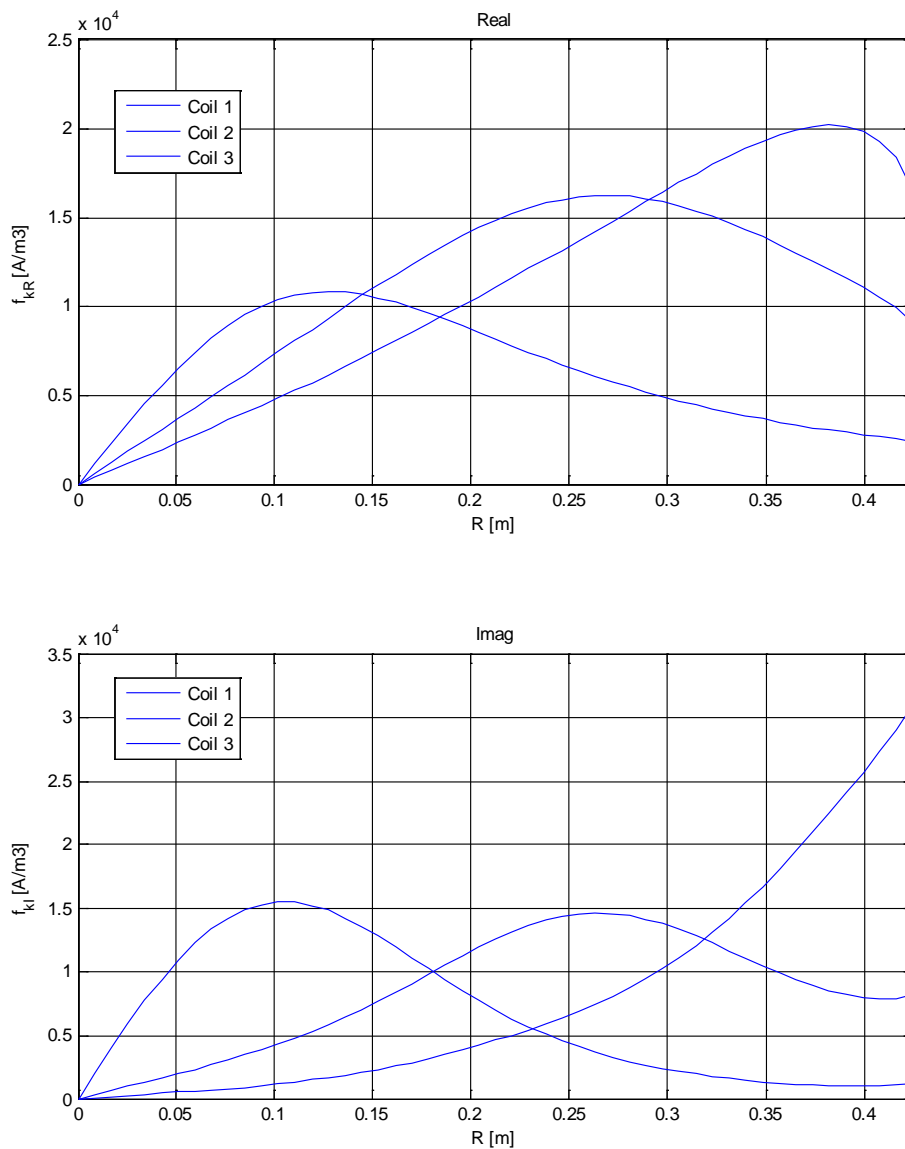

Fig. 2.25: Real and imaginary part of induced current density (azimuthal component) along the radius for coils supplied separately with 1 Arms (R=425mm, f=1500Hz, ρ=73.34E-8 Ωm)
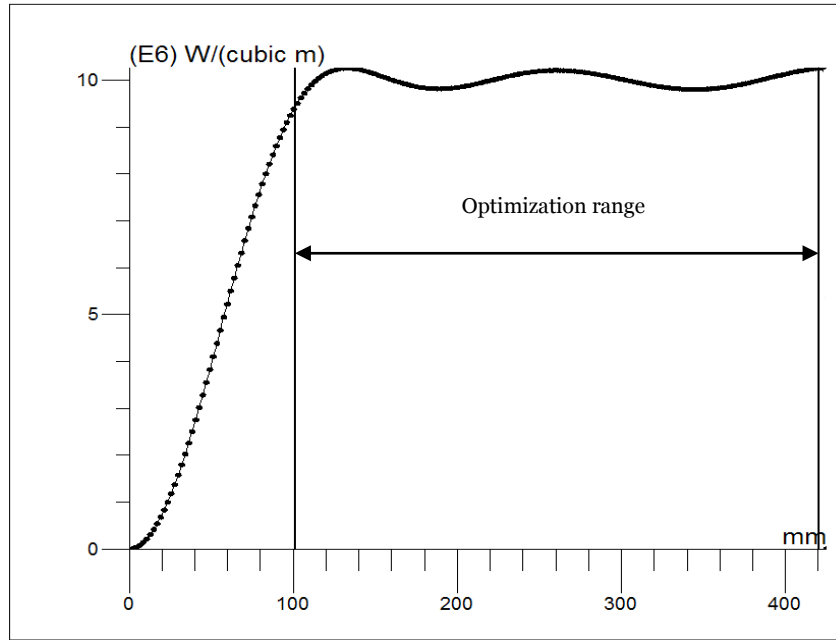
Fig. 2.26: Optimized power profile for the disc (R=425mm) with the following optimization currents: $I_1 = 212.87$, $\varphi\_1 = 0°$, $I_2 = 100.28$, $\varphi_2 = -39.86°$, $I_3 = 94.60$, $\varphi_3 = -45.13°$

Computation of capacitors

When the temperature profile has been chosen, the values of the resonant capacitors can be computed. Starting from the values of the coil currents and from the impedance matrix of the system, the vector of the reactive powers absorbed by each coil can be found:

$$[Q] = \Im[\bar{S}] = \Im[\dot{Z}][\bar{I}][\check{I}]$$

Depending on the connection scheme the resulting capacitance can be calculated as follow:

- Parallel connection:

$$C_p = \frac{Q}{\omega V^2}$$

- Series connection

$$C_s = \frac{I^2}{\omega Q}$$

2.2.6 **Multiple resonances**

The inverter that supplies the resonant circuit excites the system with a square wave. It is well known that the spectrum of a non-sinusoidal wave contains a number of harmonic components that depend on the shape of the wave. It can be interesting to show what happen when the 3-coil system is excited at different frequencies.

Inca3D has been used to verify the frequency behaviour of the resonant 3-coil system. The values of the capacitors have been chosen using the results of the optimization. The results given by the software are shown in the Fig. 2.27. In the figure the presence of a secondary peak of power at 2500 Hz can be seen. For the supply with a square wave this don't gives any problem because square waves contains only odd harmonics components, but must be highlighted that the problem exists and has to be verified when the inductor geometry and dimensions are chosen.
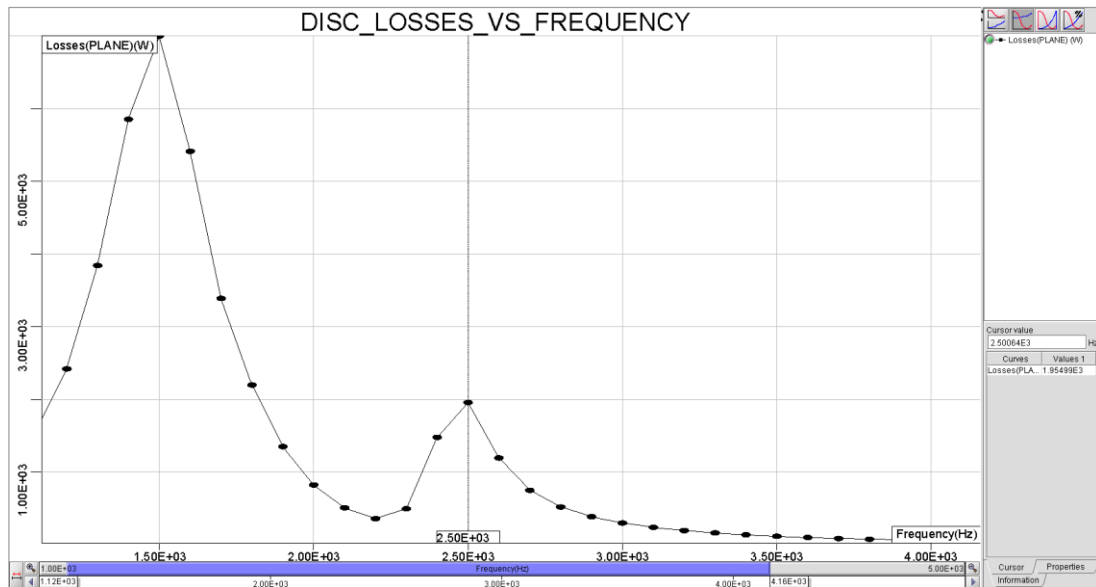
Fig. 2.27: Total induced power in the disc vs. frequency

2.3 Inductance computation with magnetic material

In the previous paragraphs all the materials have been considered having linear magnetic properties. This has simplified the analysis and the optimization process. However it can be interesting to verify the limits of this assumption when magnetic materials are heated. Moreover the stainless steel considered for the test was supposed to be non-magnetic, but the results of a campaign of measures (Appendix B) show that at low temperature this material is slightly magnetic. This paragraph describes the simulations performed with Flux 2D on the multi-coil transverse flux induction heating in development at EDF laboratories considering a magnetic load. The described simulations concern the behaviour of the impedance matrix of the system when the load is constituted by a 316L stainless steel disc 1 mm thick.

The nominal currents of the machine will be in the range from 50 to 300 A and the current in the final industrial equipment will be of the order of magnitude of a thousand of amperes. The currents for the simulations have been chosen in this range.

In order to analyse the influence of the magnetization on the impedance matrix a simulation with a linear permeability with relative value of 80, corresponding to the linear part of the real magnetization characteristic, have been done.

2.3.1 **Simulations**

A time-harmonic magneto-dynamic simulation of the electromagnetic system has been performed. The frequency has been set to 1500 Hz. A parametric study has been done in order to calculate the values of the complex impedances as a function of the permeability of the load. The simulations have been performed considering only one diameter of the circular slab (850 mm) and calculating the inductances as the ratio between voltages and currents taken directly from the electrical circuit of the simulation software.

In the following paragraph the results of the simulations done with linear and non-linear permeability, considered in the range of currents that will be used for the test on the device at ambient temperature, are shown.

Linear magnetization

In Tab. 2.6 are compared the values of self and mutual resistances and impedances calculated with relative permeability of 1 and 80. The first corresponds to the steel considered non-magnetic, and the second corresponds to the magnetic steel considered in the first linear part of the BH curve (Appendix B). It can be seen that the difference between the values calculated with different permeability are generally not negligible.

μ_r	R12	R12	R13	L11	L12	L13
1	31.4	25.4	20.7	23.3	4.44	2.17
80	29.9	23.1	18.7	23.3	4.52	2.28

μ_r	R21	R22	R23	L21	L22	L23
1	25.4	68.6	68.8	4.44	25.8	11.8
80	23.2	62.8	62.3	4.53	25.9	12.0

μ_r	R31	R32	R33	L31	L32	L33
1	20.7	68.9	115	2.17	11.8	59.6
80	18.7	62.3	105	2.28	12.0	59.7

Tab. 2.6: Auto and mutual resistances and inductances values as a function of the linear magnetic permeability.

Non-linear magnetization

In Tab. 2.7 the values of auto and mutual resistances and impedances calculated at various current intensities are shown. As it can be seen from the table, the results don't change substantially if the current don't reach the saturation knee. From the results it can be seen that in practice, with the current values that have been used, only relatively small variations of the impedances values are produced.

However it must be pointed out that in the analysis a constant temperature as been considered; as a consequence the magnetization curve is always the same. Approaching the Curie point, at the contrary, the saturation can be reached at lower magnetic field.

The simulations performed with Flux consider all the values being alternative and sinusoidal. The harmonic generation due to the non-linearity of the materials is then taken into account by means of an energy equivalence principle. Actually these harmonics are produced and they should be taken into account in the design o inverter. In this case the effect of harmonics is negligible, but with more strongly magnetic materials it must be analyzed.

μ_r	R12	R12	R13	L11	L12	L13
50	29.9	23.2	18.7	23.3	4.52	2.28
1000	30.9	24.8	19.5	23.3	4.49	2.23

μ_r	R21	R22	R23	L21	L22	L23
50	23.2	62.9	62.4	4.52	25.9	12.0
1000	24.8	67.1	67.0	4.46	25.8	11.9

μ_r	R31	R32	R33	L31	L32	L33
50	18.8	62.6	106	2.27	12.0	59.7
1000	20.1	67.4	111	2.20	11.9	59.7

Tab. 2.7: Auto and mutual equivalent resistances and inductances values in function of coil current with non linear magnetization

Supplying the inductor with the optimized currents indicated in Fig. 2.26, the influence of the non-linearity on the power density profile can be analyzed. As shown in Fig. 2.28, the power induced in the strip is less important. This is due mainly for the reason that the increasing of the permeability yield a skin depth (about 1.3 mm with a relative permeability of 80) comparable to the strip thickness and then the current is no more uniformly distributed in the strip thickness.

The magnetic characteristic of the steel used for the tests is a classical consequence of the lamination process necessary to produce the thin plate. In fact, beyond a temperature of about 100°C, the material becomes linear, with unitary relative permeability. For that reason in a strip manufacturing facility, usually an annealing process is scheduled in order to remove residual magnetism (in addition to the mechanical stress relieving).
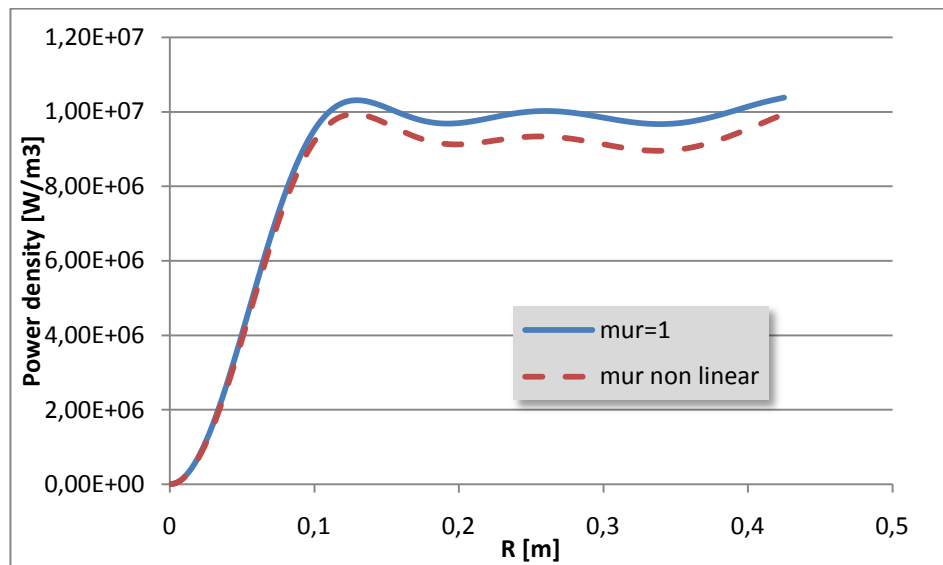
Fig. 2.28 : Comparison between power densities induced in the strip with linear and non-linear magnetic permeability.

2.4 Conclusions

This chapter deals with the analysis of an existent prototype of multi-coil inductor for the induction heating of stainless steel discs. The inductor had been previously conceptualized and built in the frame of a previous work done at EDF R&D [5]. This work has modified the ZCIH technique to fit the requirements of the steel industry.

The theoretical results obtained in the former work has been verified and updated with the measured dimensions of the actual inductor and the electrical characteristics of the material chosen for the disc load.

First, an analysis of the models suitable to represent the multi-coil inductor from the supply side has been done, verifying the effects of the different components of the impedance matrix on the power transmitted to the disc.

Afterwards the characterization of the pilot system has been done comparing the results of different computation methods (FEM, PEEC, and Analytic) with the measures performed on the prototype, in order to have a good estimation of the impedance matrix of the system. Each method has shown its advantages and limits given by the simplifications done in the model.

The software Flux 2D has been finally used in order to compute the functions representing the current density in the disc along its radius. These functions are necessary to optimize the profile of the induced power along the radius of the disc.

From the measures of the electrical properties of the stainless steel used for the disc load it has been seen that the steel is slightly magnetic, and the effect this characteristic on the resulting power profile has been analyzed.

The previous work was useful to provide the necessary information in order to perform the first experimental tests on the prototype which was aimed to verify the feasibility of the ZCIH concept and the chosen control algorithm.

Chapter 3

System for heating moving strips

The circular prototype analyzed in Chapter 2 has allowed to approach the multi-coil induction heating in a simplified way, i.e. without magnetic yoke and using 2D computation methods where axi-symmetric geometries are conveniently analyzed. However the aim of the PhD work was to design an auto-adaptive multi-coil inductor for heating metal strips in continuous movement. The development of such system could have a remarkable impact in the metal strip industry from a point of view of the acceptance of the technique.

In this chapter the definition of a suitable geometry for the multi-coil inductor is described. The main parameters involved in the design have been analyzed with analytical and numerical software in order to verify the feasibility of such kind of inductors in a semi-industrial scale. In particular the definition of the inductor geometry has been done with reference to the optimization of the power induced into the strip, in order to obtain a suitable temperature profile in the strip at the exit section of the inductor. The final inductor design has been preceded by an extensive analysis, described in this chapter, useful to understand the peculiarity of such kind of systems.

The design of an electromagnetic device should involve the following steps:

- Feasibility study following the performance specifications;

- Individuation of the input and output design variables;

- Analysis of suitable simulation models;

- Decision of the optimization criteria;

- Verification of the model by simulation;

- Construction of a prototype;

- Verification by tests on the prototype;

This sequence has been followed in the thesis starting from a feasibility analysis of the inductor; the feasibility study has been validated making use of the simplified analytical software TFH3D which allows the analysis of a TFH inductor despite some simplification indicated in more details in the paragraph 1.4.1.

The second step was devoted to analyse a non-optimized geometry composed by 6 coils, designed using classical TFH design methods in order to understand the limits of this kind of systems. The inductor has been provided of magnetic concentrators in order to reduce stray flux and to improve the global efficiency of the heating system. The characteristic of the magnetic concentrator will be analyzed in section 3.5.

The third step, described in the Chapter 4, concerns the optimization of the coils geometry in order to improve the performance of the inductor in a wide range of strip width. In order to validate the optimization method a 3 coil inductor capable to heat strips of width between 600 and 800 mm has been designed. Afterwards the results obtained for the 3 coil inductor have been extended in order to design a new inductor with 6 coils capable to heat strips ranging from 800 to 1200 mm width. The target performance of the system is a temperature increase in the load up to 300 °C and a maximum temperature gradient in the strip moving direction of 300 °C/m. These performances correspond to the maximum temperature gradient to avoid thermal deformation as discussed in section 1.2.2. The simulation results, obtained for this inductor, seem to overcome all the drawbacks of the previously known TFH systems.

These results have to be confirmed by experimental data on a pilot system, using as supply system the inverter under development at the Laplace Laboratories of the University of Toulouse (France) [4].

3.1 Description of the inductor-load system

In Fig. 3.1 the principle of the space control heating system is illustrated with reference to a 3 coil MCH inductor. The inductor in the figure consists of two sets of three coils, with rectangular shape, symmetrically placed on both sides of the strip. Each coil is series connected with the corresponding coil on the other side of the strip in order to produce a transverse flux and it is supplied with a current of suitable amplitude and phase by an independent IGBT inverter. The inverters supplying the coils run at the same frequency. In summary, the system is a set of coaxial TFH inductors, strongly magnetically coupled, capable of adapting the distribution of the induced power in the strip depending on the strip dimensions, by the use of suitable sets of exciting currents. Each coil induces a current density in a particular zone of the strip whose value depends on the imposed currents. Therefore the shape of the resulting pattern of the total power density in the strip depends on the ratio of the currents flowing in the coils. The induced current produces heat inside the strip and, as a consequence, the temperature of the strip increases continuously while the strip moves. A cross-section of the strip, passing at constant speed inside the inductor, receives a quantity of heating energy equal to the time integral of the induced power density. It is possible to find a geometrical and electrical configuration of the inductor, in which each elementary volume, lying on a cross-section of the strip, receive almost the same quantity of energy, making thus possible to obtain an almost uniform temperature of the strip at the exit section of the inductor.

The load is constituted by a non-magnetic steel strip, moving at constant velocity. The gap between the strip and the coils is 100 mm in order to allow the natural vibration of the strip in an industrial line, and to leave the necessary space for the refractory chamber. In the first prototype, due to the limited temperature increase of the strip, the refractory chamber was not necessary, but since in the industrial installations the strips are heated to temperatures up to 1200° C, the use of the refractory chamber will become mandatory. For classical TFH system the reduction of the air-gap is desirable from the point of view of the electrical efficiency, on the contrary, for MCH, the strip must be far enough to overlap the zones of influence of the currents induced by the different coils.

The inductor will be placed in vertical position and will be supported by an overhead travelling crane. It will be provided of flanges allowing the connections to the tracks.
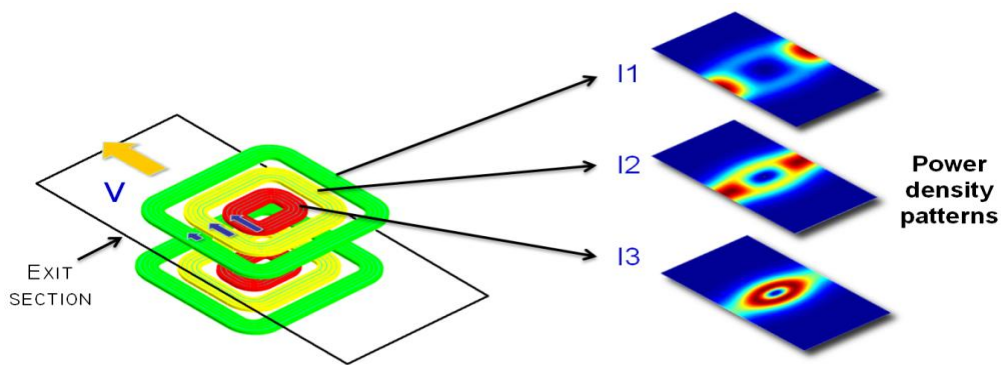

Fig. 3.1: Principle of space control heating

3.2 First Rectangular system

The first inductor designed in this work has been conceived to be tested in the EDF laboratories at Les Rénardieres – France; therefore the limitations on the available floor space and the maximum power of the laboratory generators led to the limitation of the inductor performance. The inductor, shown in Fig. 3.2, is characterized by six independent coils designed for the uniform heating of non magnetic steel strips with different width ranging from 500 to 1000 mm. This section presents the analysis of a multi-coil inductor capable to transfer a maximum induced power of 200 kW to a non-magnetic steel strip. For the first design the analytical tool TFH3D has been used. The design starts from the classical method used for TFH coils design, adding successively a suitable number of coils in order to provide the space control of the power density in the strip. The performance of the pilot system will be then analyzed for different strip widths.

To reach a uniform temperature on the strip the inductors must be driven with currents of well defined intensities and phases. The computation of the currents has been done with the optimization procedure described in the paragraph 3.4.

The analysis begins with a feasibility study, in which the main parameters and dimensions are defined. The optimization performed to reach uniform heating in the strip will be described making reference to analytical and numerical models. Subsequently the design of the flux concentrator will be illustrated.
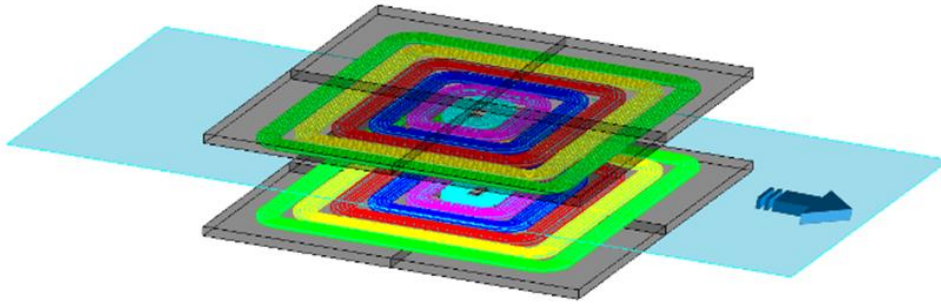
Fig. 3.2: MC-TFIH system with 6 coils and magnetic flux concentrator.

3.2.1 Technical Specifications

According to the specifications given by EDF, the induction heater had to be capable to heat strips in continuous movement with the following characteristics:

- Alloy of steel : Stainless steel;

- Electrical resistivity: $\rho = 730 \cdot 10^{-9}\,\Omega m$ (at 20°C);

- Volumetric heat capacity: $\gamma c_p = 4 \cdot 10^6\,\dfrac{J}{m^3 K}$;

- Thermal conductivity: $\lambda = 18\,\dfrac{W}{Km}$;

- Width : from 500 to 1000 mm;

- Thickness: from 1 mm.

The mechanical constraints on the device are:

- Distance between the two coil plates : 200 mm minimum;

- Coils covered by magnetic cores to avoid magnetic stray field outside the system and to increase efficiency.

The required performances are:

- Final temperature of the strip : 300 °C±2%;

- Maximal temperature gradient acceptable : 300 °C/m;

Each inverter supplies the coils with a square wave current, exciting a parallel resonant circuit like the one described in section 2.1.1.

3.2.2 Power and frequency

According to the considerations of the Chapter 1, the frequency must be chosen in order to obtain a uniform power density in the thickness of the strip. This means that the penetration depth must be larger than the strip thickness (1 mm). A frequency between 500Hz and 5000Hz has been considered. As shown in Tab. 3.1, in the range of

frequencies considered the required condition on the penetration depth is satisfied up to a temperature of 1200°C.

f [Hz]	$\delta_{20°C}$ [mm]	$\delta_{1200°C}$ [mm]
500	19.2	25.6
1000	13.5	18.1
1500	11.1	14.8
2000	9.62	12.8
3000	7.85	10.4
4000	6.79	9.07
5000	6.08	8.11

Tab. 3.1: Penetration depth for stainless steel at several frequencies

A first rough calculation of the power needed to satisfy the requirements on the temperature rise can be deduced by the following formula (sec. 1.2.1):

$$P = \frac{\gamma c_p \Delta\theta S v_s}{\eta} \tag{3.1}$$

By the (3.1) the computation of the velocity of the strip can be found. According to the specifications the following data are used:

- $P = 200\text{kW}$

- $\Delta\theta = 280°C$ (considering the ambient temperature at 20°C)

- Estimated total efficiency: $\eta = \eta_E \cdot \eta_T = 80\%$

- $S = 1 \cdot 0.001 \ m^2$

The strip velocity results:

$$v_s = \frac{200 \cdot 10^3 \cdot 0.8}{4 \cdot 10^6 \cdot 280 \cdot 0.001} = 0,143 m/s \tag{3.2}$$

3.2.3 Feasibility study

The TFH3D software (par. 1.4.1) has been used to analyse the feasibility of the inductor. Despite the approximations assumed in the algorithm, it can give some useful information conserning the order of magnitude of electrical values.

Some previous tentative optimizations (not reported in the thesis) performed on 2 and 3-coil inductors, have shown that, with multiple coil inductors, the best performance on the temperature uniformity are obtained with the maximal extension of the surface covered by each coil. In the literature several papers that analyze the influence of the coil shape on the heating transient exist (Chapter 1), but the simpler choice, considering the relation between the manufacturing simplicity and the performances, is to use rectangular coils. Rectangular coils are suitable to reach good uniformity of temperature in the strip and, in comparison with coils of circular shape, they avoid the ring effect (par. 2.2.4) that contributes to the non-uniformity of the current density distribution inside the copper and that has a negative effect on the inductor efficiency.

Starting from the previous considerations, the geometry has been chosen in order to divide the width of the strip in 6 zones equally spaced filled with rectangular coils. A sketch of the geometry with its dimensions is shown in Fig. 3.3. Each coil is composed by 5 turns of hollow copper tube with rectangular section of 10x10 mm. Each coil is devoted to control a specific zone of the induced power by the selection of a convenient exiting current value in magnitude and phase.
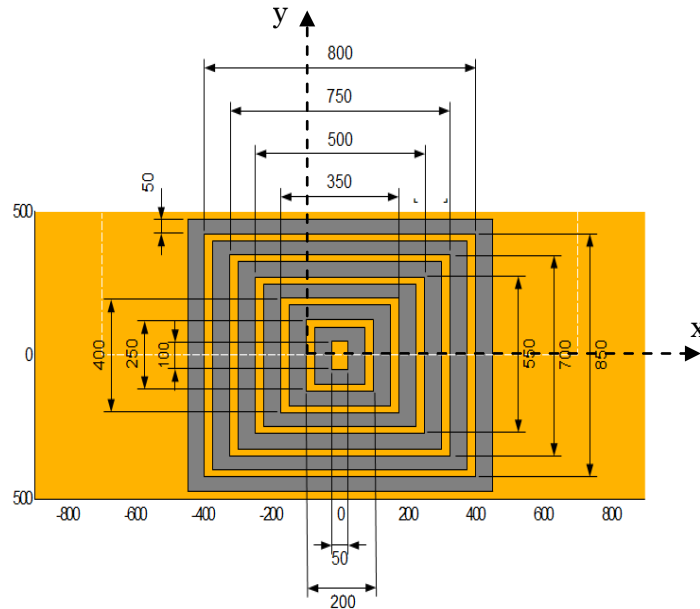

Fig. 3.3: Schematic drawing of the inductor coils analyzed

3.3 Optimization of the temperature profile

Once the geometry has been defined, the possibility to obtain uniform temperature profiles optimizing the supply currents of the coils has to be verified. Since the optimization of the temperature profile is a long process, the verification of the power profile in all the possible range of widths is not convenient and a simplified procedure has been used instead. The currents have than been optimized making reference to a reduced number of strip widths, covering the range between the maximum and minimum strip dimension. The goal of the optimization procedure is to define a set of exciting currents (in magnitude and eventually in phase displacement) which can assure specified temperature uniformity in the strip cross-section at the exit of the inductor indicated in Fig. 3.4.
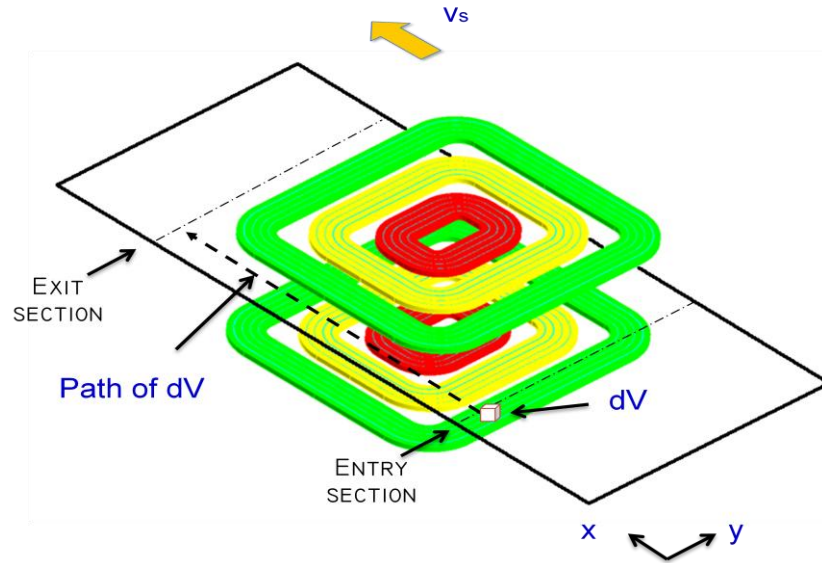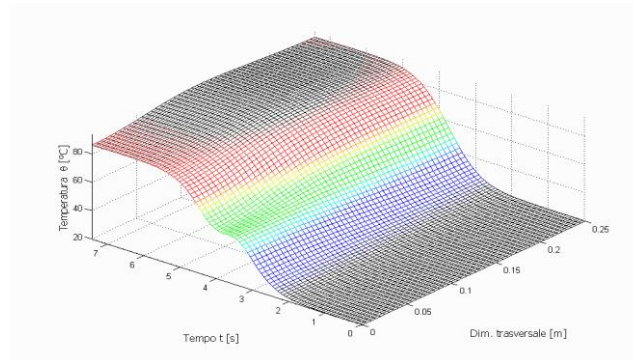
Fig. 3.4: Principle of TFIH

Fig. 3.5: Evolution of the temperature in a cross-section of the strip

However, taking into account that the stainless steel has a very low thermal conductivity, the optimization can be done with reference, instead of the temperature, to the uniformity, to the exit section of the inductor, of the energy transferred to the strip during its movement inside the inductor. During the optimization, the variation of the electrical resistivity as a function of the temperature has been neglected. This has been done because of the limited variation of the resistivity of the steel in the specified range of temperature (i.e. 73-90 $\mu\Omega m$ in the range 20-300°C).

3.3.1 Optimization procedure

In order to obtain the best temperature profile in the strip at the exit section of the inductor an optimization procedure must be implemented to compute the suitable currents to be imposed in each coil. The method of optimization has already been used in [5] for the circular inductor. As already mentioned, due to the chosen excitation frequency and the characteristics of the strip, the skin depth is larger than the strip thickness, and it can be assumed that the current density is uniformly distributed in the strip thickness. As a consequence, all field quantities are functions only of the two surface coordinates x and y.

93

Each *n-th* inductor coil, individually supplied with a sinusoidal excitation current, produces an induced current density distribution, represented in each point by a vectorial phasor in the $x - y$ plane, characterized by four scalar values, of which an example is shown in Fig. 3.6:

$$\bar{J}_n(x, y) = (J_{x\Re} + jJ_{x\Im})\boldsymbol{u}_x + (J_{y\Re} + jJ_{y\Im})\boldsymbol{u}_y \tag{3.3}$$
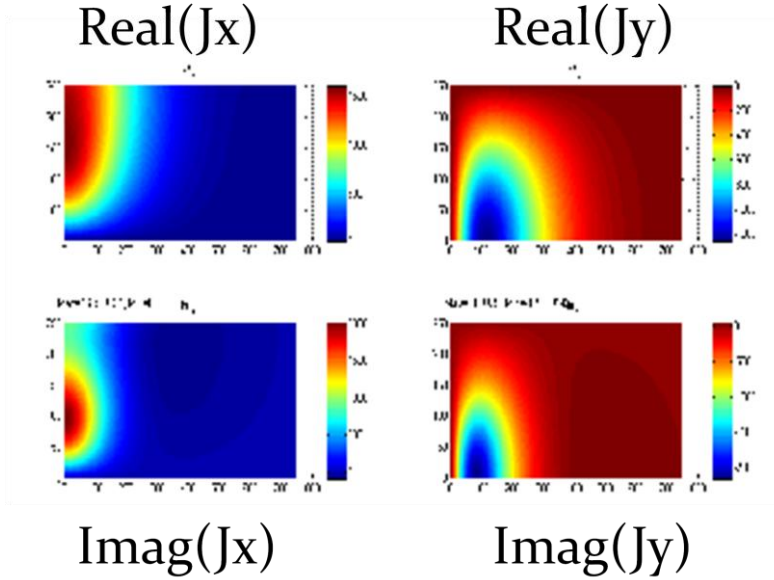

Fig. 3.6: Example of distribution patterns of the current density in the strip, represented by its 4 components.

The pattern of the current density, and as a consequence of its scalar components, depends on the frequency, the physical parameters of the strip material, the geometrical dimensions, and the relative position of the strip and the coils.

With reference to the Fig. 3.4 it can be considered that each elementary volume dV, lying in a section of the strip perpendicular to the movement direction at the position y, receives a quantity of energy $W(y)$ proportional to the integral of the power density computed along a path parallel to the strip movement:

$$W(y) = \int_0^{L_{strip}} \frac{w(x, y)}{v_s} dx \tag{3.4}$$

where $w(x, y)$ is the power density distribution in the strip plane, v_s is the velocity of the strip and L_{strip} is the length of the integration lines. This quantity can be than assumed as reference for the optimization instead of the temperature.

Thanks to the linearity of the model, the power density $w(x, y)$ can be obtained by superposing one by one the current density distributions induced by the single coils, computed with a normalized exiting current of 1 A$_{rms}$ (and imposing null current in the others), and scaled by the current flowing in the same coil.

Naming:

- $[\bar{I}] = [\bar{I}_1, \dots, \bar{I}_6]$: the vector of the currents phasors imposed in the coils,

- $[\bar{J}(x, y)] = [\bar{J}_1(x, y), \dots \bar{J}_N(x, y)]$: the vector of the normalized current density maps of the six coils, computed by analytical or numerical methods,

the spatial distribution of the power density in the strip results:

$$w(x, y) = \rho \left| [\overline{J}_1(x, y)][\overline{I}]^T \right| \tag{3.5}$$

The optimization process minimizes the maximum difference between the profile of $W(y)$ and its mean values. This allows to remove the absolute values of the currents using the ratio between the $n-1$ current and the $n-th$ current, therefore reducing by one the number of variables to be optimized. Successively, thanks to the linearity of the problem, the current are re-scaled, maintaining their ratio, in order to reach the required total power. Even the phase displacements can be reduced in number imposing $\varphi_1 = 0°$ in the reference coil.

Assuming $I = [I_1, \ldots, I_N, \varphi_1, \ldots, \varphi_N]$ the vector of the currents (magnitudes and phases) of the N coils, the vector to optimize become:

$$\boldsymbol{X} = [X_1, \ldots, X_{2(N-1)}] = [I_1/I_N, \ldots, I_{N-1}/I_N, \varphi_2, \ldots, \varphi_N] \tag{3.6}$$

The value of the integrated current density in a path line with coordinate x is then a variable depending on the y coordinate and the $\boldsymbol{X}$ vector. The function to be minimized in order to reach the least deviation ΔE% in respect to the ideal uniform profile is (indicating with W_{strip} the width of the strip):

$$g(X) = max \left| \frac{W(y, X) - W_{mean}(y, X)}{W_{mean}(y, X)} \right| \quad / \forall y \in \left[0, W_{strip}/2 \right] \tag{3.7}$$

where:

$$W(y, X) = \int_0^{L_{strip}} \frac{w(x, y)}{v_s} dx \tag{3.8}$$

and:

$$W_{mean}(y, X) = \frac{1}{W_{strip}} \int_0^{W_{strip}} W(y, X) dy \tag{3.9}$$

For the numerical computations, the function $W(y, X)$ is defined for a discrete set of H points along the strip width, so the objective function becomes:

$$\Gamma(X) = max \left| \frac{W(y_h, X) - W_{mean}(X)}{W_{mean}(X)} \right| \quad / h = 1 .. H \tag{3.10}$$

An optimization algorithm can be used to find the value of the vector $\boldsymbol{X}$ that satisfies the uniformity requirements in respect to the desired power profile. The optimization algorithm used to find the optimum is Tribes (section 2.1.3), a variant of a particle swarm optimization algorithm with auto-adaptive internal parameterization. The value of the current to be applied to each coil (six coils in this case) must be known in module and phase: this means that the optimization problem can have up to 10 degrees of freedom, 5 intensity and 5 phase values of the currents, having assumed the first current as reference. The high parameter number and the nature of the system justify the use of a stochastic algorithm in the optimization.

After the optimizations, a complete finite element analysis, which takes into account also the variation of resistivity with temperature, has been performed to check the results.

3.3.2 **Analytical and numerical results**

An example of the results obtained with TFH3D is given in Fig. 3.7-Fig. 3.9, which refer to the heating of strips 1000-750-500 mm widths, 1 mm thickness, with the optimized sets of the supply currents specified in Tab. 3.2. The diagrams of the figures shows the optimized energetic characteristics for the above three strip widths. In particular the curves show the following:

- Fig. 3.7: induced power density distributions in the strip. These distributions show, for all strip widths, the typical pattern of the induced power in the transverse flux heating, characterized by two central peaks located under the exciting conductors normal to the strip movement, and two lateral peaks near the strip edges. Their shape explains the great difficulty of obtaining a uniform temperature distribution in the strip cross-section at the exit of the inductor.

- Fig. 3.8: the distributions of total energy transmitted to the strip, evaluated in the strip cross-section at the inductor exit. These curves show, in particular, that each elementary volume of the strip cross-section will receive, at the exit of the inductor, nearly the same quantity of energy and, consequently, nearly the same temperature increase can be expected.

- This prediction is confirmed by the results of the calculations of the corresponding thermal transients (in half of the strips) given in Fig. 3.9. In particular, the final temperature distribution, shown by the top region in the figures, shows a fairly good agreement with the curves of Fig. 3.8.

The above results show that good temperature patterns can be achieved without phase displacement among the supply currents for large strip widths, i.e. when more than 4 coils are excited. Some difficulties arise when the number of excited coils is lower, concerning both the temperature uniformity and the value of the ampere-turns in the internal coil. However, in this case the phase displacement allows to improve the uniformity, but at the price of higher current values in the coil conductors. Moreover the use of phase displacement among the coil currents, could give rise to some problem when considering the exchanges of power among the coils, considered in section 2.1.2.

With the considered geometry and the set of optimized currents, an almost uniform heating of strips of width between 500 and 1000 mm and thickness 1 mm has been obtained, with a deviation on the energy profile lower than ±5%. The above preliminary results obtained by the program TFH3D demonstrate the possibility to reach sufficiently uniform heating of strips of different widths in an inductor without movable parts, by supplying the inductor coils with suitable sets of currents of different amplitudes and phases.

Taking into account the limits of TFH3D, the design of the inductor has to be finalized by the use of a numerical FEM program. This final design stage is particularly important not only for the determination of the effective sets of intensities and phases of the exciting optimized currents, but also for the evaluation of the impedance matrix of the coils, necessary for driving the supply inverters.

L [mm]	$N_1 I_1$ [A] φ_1 [°]	$N_2 I_2$ [A] φ_2 [°]	$N_3 I_3$ [A] φ_3 [°]	$N_4 I_4$ [A] φ_4 [°]	$N_5 I_5$ [A] φ_5 [°]	$N_6 I_6$ [A] φ_6 [°]	P [kW]	Δ E%
1000	739 0°	777 0°	888 0°	440 0°	1656 0°	479 0°	174	**±0.98%**
750	-	-	1633 0°	554 0°	955 0°	5106 0°	138	**±1.8%**
500	-	-	-	866 0°	1114 -19°	14370 73.5°	125	**±5.7%**

Tab. 3.2: Optimized exciting currents for the six inductor coils and the corresponding total induced power [1...6 – from external to internal coil], Δ E%: Deviation in respect to the uniform energy profile.
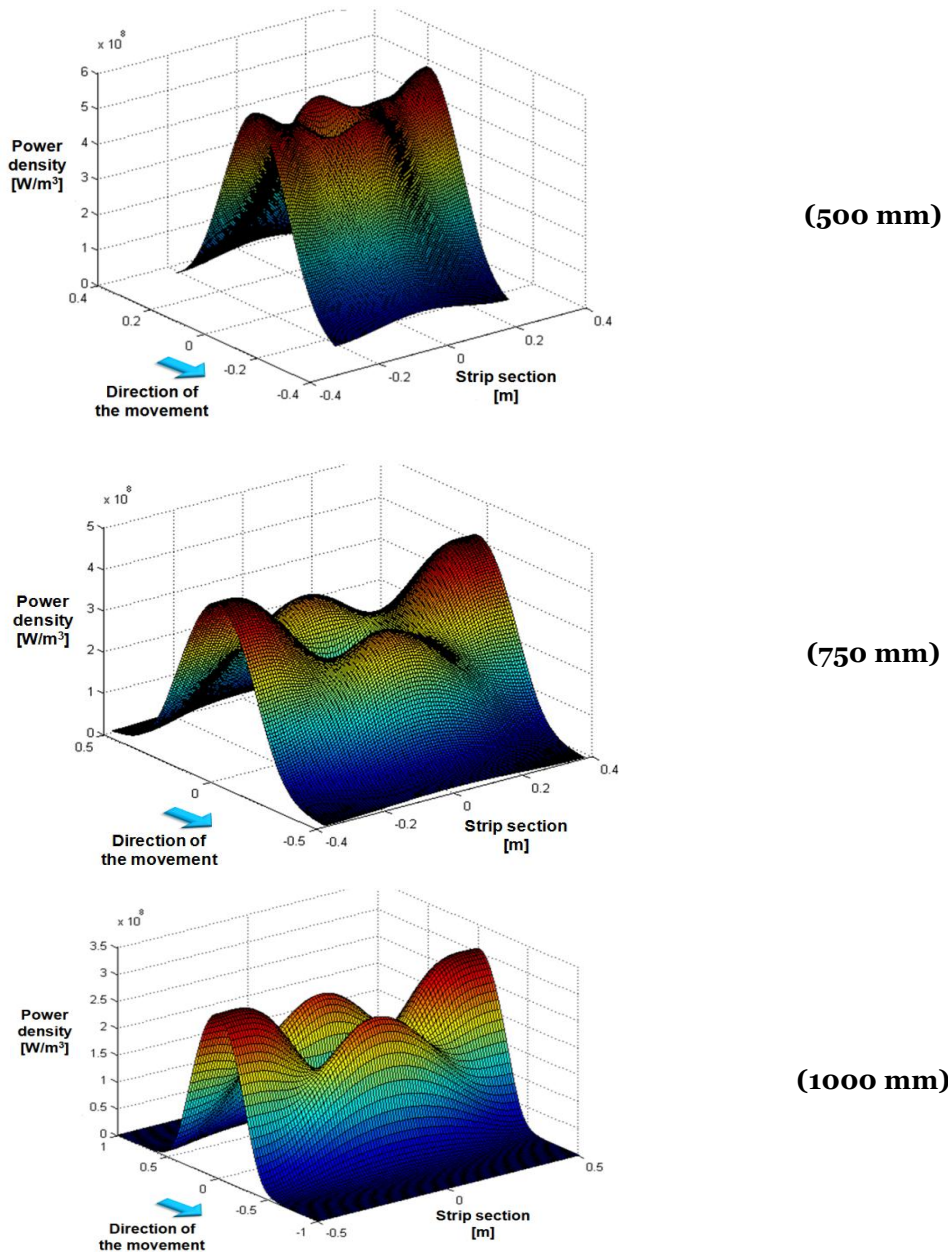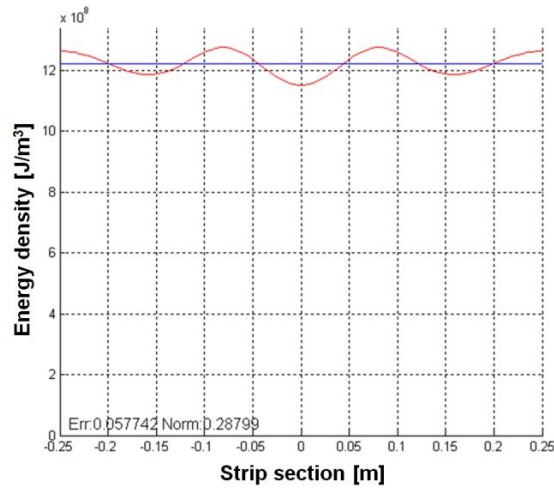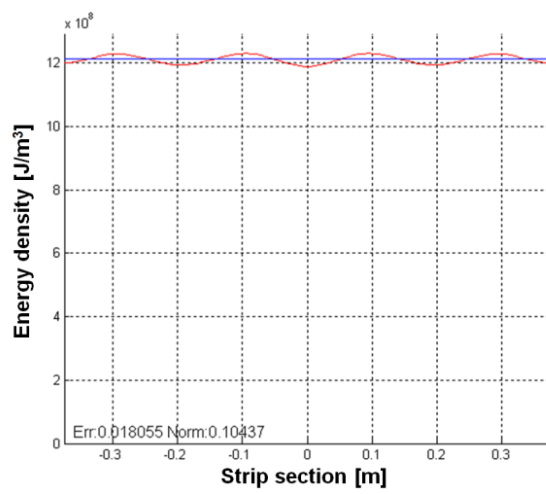

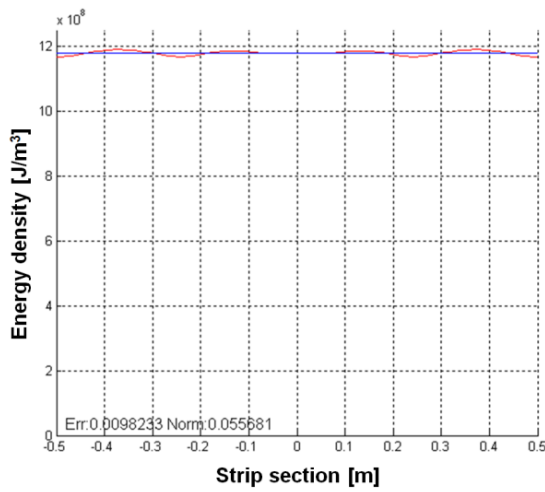(500 mm)

(750 mm)

(1000 mm)

Fig. 3.7: Optimized energetic characteristics for three strip widths : Induced power density distribution in the strip

(500 mm)

(750 mm)

(1000 mm)

Fig. 3.8: Optimized energetic characteristics for three strip widths: Energy distributions in the strip cross-section at the inductor exit
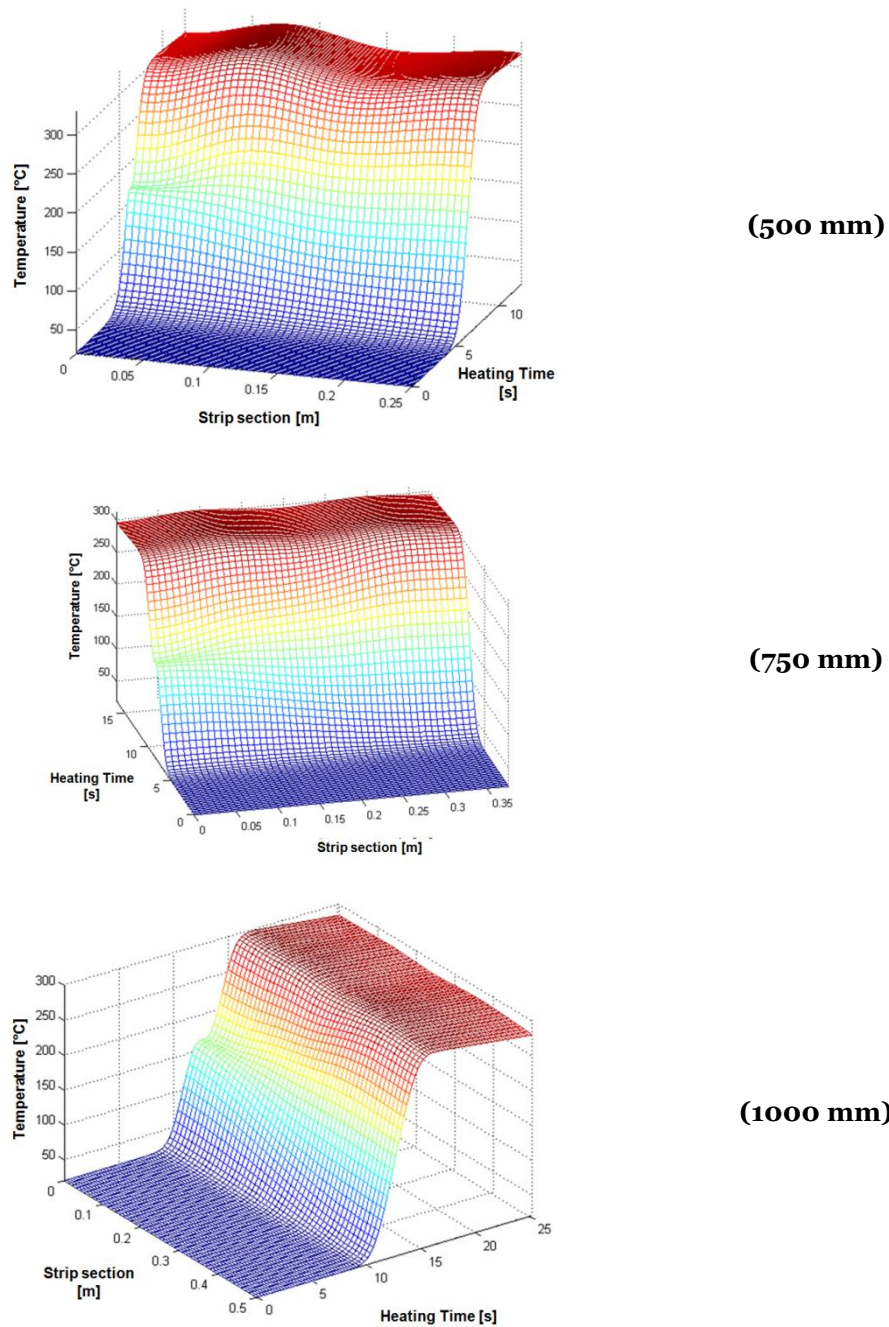
(500 mm)

(750 mm)

(1000 mm)

**Fig. 3.9: Optimized energetic characteristics for three strip widths: Tempera-
ture distribution during heating transient (only half strip is shown)**

3.3.3 FEM Computations

A number of numerical FEM calculations have been done with the package FLUX 3D in order to investigate the limits of the analytical results and evaluate the influence on the previous conclusions of the real inductor geometry, e.g. real shape and cross-section of the inductor turns, shape and permeability of the yokes.

An example of the results obtained is given in the following with reference to the strip 1000 mm width and two different types of inductors:

- inductor constituted by 6 coils, each with 5 solid copper turns 10x2 mm cross-section spaced by a 2 mm air-gap, and external "semi-closed" yokes (as in Fig. 3.10-a) with no losses and relative permeability μ=1000;

- inductor constituted by 6 coils, each with 5 copper turns 10x10x2 mm cross-section, spaced by a 2 mm air-gap, and external "open" yokes (as in Fig. 3.10-b) with no losses and relative permeability μ=90

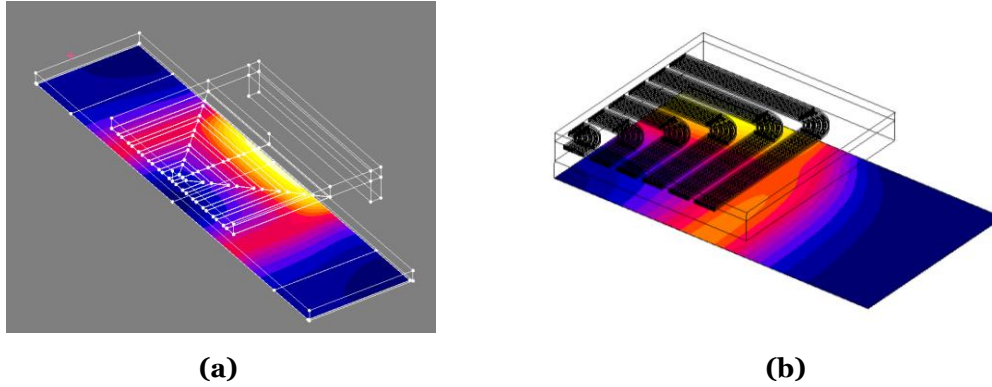**(a)**   **(b)**

Fig. 3.10: Geometries of the inductor-load system used for the FEM calculations

The first one approximates the ideal geometry used in TFH3D, the second one represents the actual inductor. The diagrams of Fig. 3.11-Fig. 3.12, which give the energy distributions at the inductor exit analogous to those of Fig. 3.8, have been obtained by FEM applying to the inductors of Fig. 3.10 the set of optimized currents of Tab. 3.2, i.e. the currents calculated with TFH3D. The corresponding values of the total induced power are 165.9 kW and 129,9 kW respectively.
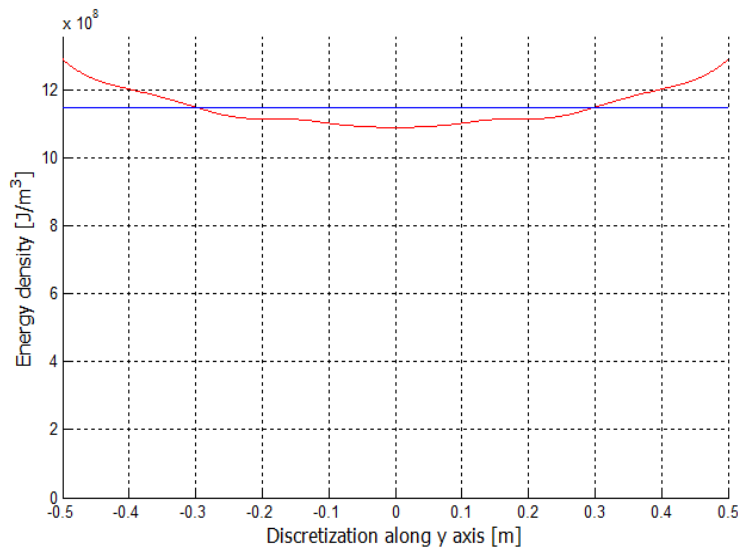

Fig. 3.11: Energy distributions at the inductor exit calculated with FLUX3D with the excitation currents of table I and the geometry of Fig. 3.10-(a)
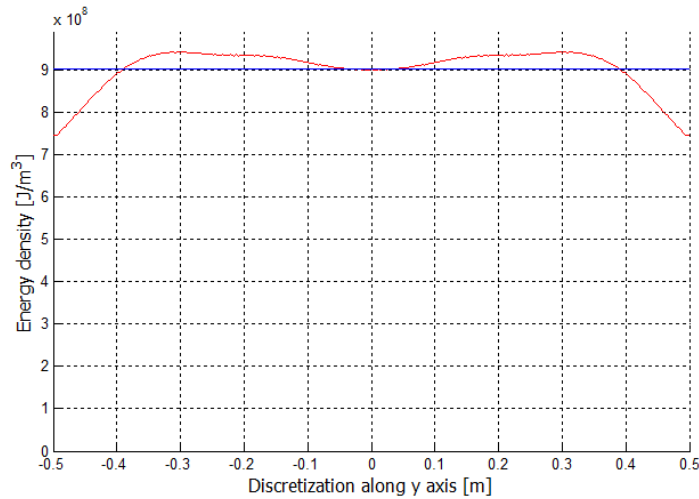
Fig. 3.12: Energy distributions at the inductor exit calculated with FLUX3D with the excitation currents of table I and the geometry of Fig. 3.10-(b)

Model	Δ E%	η %	Pstrip [kW]
TFH3D	**±0.99%**	**95.3**	**170**
Massive coil	**±17%**	**92.6**	**118**

Tab. 3.3: Comparison of the results obtained with analytical and FEM model with solid conductors

The results allow the following conclusions:

- The Fig. 3.11 shows a good agreement of the total induced power, corresponding to an average value of about $12 \cdot 10^8$ J/m³, while the energy distribution predicts an overheating of the strip edges;

- The Fig. 3.12 on the contrary shows that for obtaining the same total induced power the values of the currents optimized with TFH3D must be increased of about 17%; the energy distribution is more uniform, but in this case a certain lack of energy is present near the strip edges.

Concerning the complexity of the FEM models

In order to perform the verification with FEM models, the Cedrat Flux tool has neen mainly used but, due to the very long time of the computations, the Powersys JMAG package was tested in the context of a master thesis stage done at EDF. At the time in which the computations were performed, the performances shown in Tab. 3.4 were obtained. The FEM models were built for a eighth of the model coupled with the supply circuit.

As it can be seen the use of the simplified models allows to reduce considerably the computation time and for a first feasibility analysis the non negligible difference existing among the quality of the results can be accepted.

Package	Version	Model	Time	RAM
TFH3D	2	Analytical	3 min	300MB
Flux3D	10.3	Stranded conductors	3 Hours	6GB
Flux3D	10.3.3	Solid conductors	11 Days	40GB
JMAG	10.3.1	Solid conductors	4-10 Hours	15GB

Tab. 3.4: Comparison of resolution times of different computation methods

Comparison of electrical quantities

In addition to the considerations and the results obtained on the energy profile, the values of the electrical parameters characterizing the inductor from the point of view of the power supply must be considered. Concerning the power supply, the knowledge of parameters such as voltages, phase displacements, power factors, and efficiency is fundamental. All the computation models considered allow the computation of these parameters. In Tab. 3.5 a comparison among the electrical parameters obtained with TFH3D and Flux3D with massive coils is shown. As seen before for the energy profile, a consistent difference can be noted among the two methods. The largest difference is due to the modeling of the magnetic concentrator made using different permeability ($\mu_r = \infty$ for TFH3D and $\mu_r = 90$ for Flux 3D), which modify substantially the amount of magneto motive force that induce current in the strip. Another difference is due to the eddy currents induced among the turns and among the coils, and to the uneven distribution of the currents due to ring, proximity and skin effect in the coil conductors.

Model	Coil n.:	1	2	3	4	5	6
	V	**481**	**486**	**408**	**277**	**221**	**48**
	P	**45.9**	**45.2**	**42.5**	**14.1**	**28.8**	**1.8**
TFH3D	**Q**	**54.3**	**60.5**	**58.6**	**19.8**	**67.5**	**4.2**
	Cp	**24.8**	**27.1**	**37.3**	**27.4**	**145**	**190**
	V	**395**	**401**	**337**	**226**	**164**	**38**
	P	**30.5**	**32.3**	**31.2**	**10.5**	**21.7**	**1.5**
Massive coil	**Q**	**49.9**	**53.1**	**51.3**	**16.8**	**49.9**	**3.3**
	Cp	**33.8**	**35.0**	**47.7**	**34.9**	**195**	**241**

Tab. 3.5: Comparison of the results obtained with analytical and FEM model with solid conductors (V: coil voltage [V], P: Absorbed active power of the coil [kW], Q: Reactive power of the coil [kvar], Cp: Resonant capacity with parallel connection scheme [μF])

In order to verify the possibility of achieving the same uniformity of the energy profile obtained with TFH3D (as in Fig. 3.8), for the geometry of Fig. 3.10 a new set of optimised exciting currents has been determined, in the case of 1000 mm strip width, using the current patterns obtained by FLUX3D and applying the optimization algorithm

previously described. In Tab. 3.6 the optimized set of the optimized ampere-turns, the corresponding values of the total induced power and the system electrical efficiency are given.

The Fig. 3.13 shows the profile of the energy transferred in the strip at the inductor exit when the exciting currents are those of Tab. 3.6. The results show that, despite the different geometry now considered, in comparison with the ideal one used in TFH3D, a quite good induced energy profile can be obtained.

The computation of the impedance matrix, the evaluation of the electrical efficiency and the power factor of the multi-coil inductor can also be easily done. Finally, the use of the FEM models, allows taking into account inductor coils larger than the strip. However, in many cases this is not necessary since it becomes convenient to switch off the coils having dimensions exceeding the strip edge. The previous calculations show that more the strip width is narrow, more the efficiency decreases, since in the internal coils is necessary to increase the values of the magneto-motive force, in comparison with the previous ones.

L [mm]	$N_1 I_1$ [A] Ψ_1 [°]	$N_2 I_2$ [A] Ψ_2 [°]	$N_3 I_3$ [A] Ψ_3 [°]	$N_4 I_4$ [A] Ψ_4 [°]	$N_5 I_5$ [A] Ψ_5 [°]	$N_6 I_6$ [A] Ψ_6 [°]	P [kW]	η %
1000	1430 0°	460 0°	590 0°	1375 0°	1235 0°	1710 0°	174	92

Tab. 3.6: Optimized exciting currents for the six inductor coils, the corresponding total induced power and efficiency computed with the FEM model for the strip width 1000 mm
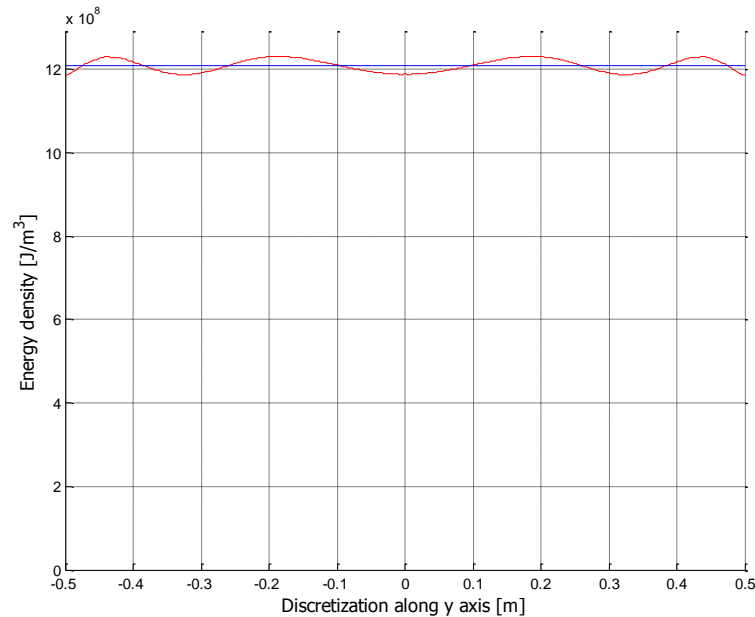

Fig. 3.13: Optimized energy distribution at the inductor exit, induced power and efficiency with the excitation of Tab. 3.6

3.4 Optimization with FEM model

It has been verified that, with the method described in the previous paragraph, the computation of a set of currents suitable to reach a good power profile at the exit of the inductor is possible. The optimizations done with TFH3D allows taking into account only coils not exceeding the strip width. In order to verify the previous results with a more detailed model, and to verify the benefit of using coils larger than the strip width, a number of optimizations using current density patterns issued from FEM computations have been done. The results obtained by the stochastic optimizations, performed by Tribes, have been further analyzed and some considerations on the currents obtained will be done. With this method, in addition to the previously analyzed strip widths (500 mm, 750 mm and 1000 mm), some intermediate values can be considered and then the influence of coils exceeding the strip width can be taken into account (for example a 600 mm width).

3.4.1 FEM Model

A number of FEM computations have been done in order to obtain the current density maps at the considered width of the strip. For the first computation a magnetic concentrator with very high isotropic relative permeability ($\mu_r = 1000$) has been used. The magnetic concentrator is closed around the strip in the lateral parts. Because of the huge amount of time needed to simulate the real geometry of the coils, a simplified inductor system has been used. The inductors are represented by stranded coils with imposed magneto-motive force, i.e supplied with imposed currents. The geometry of the model is shown in Fig. 3.14.
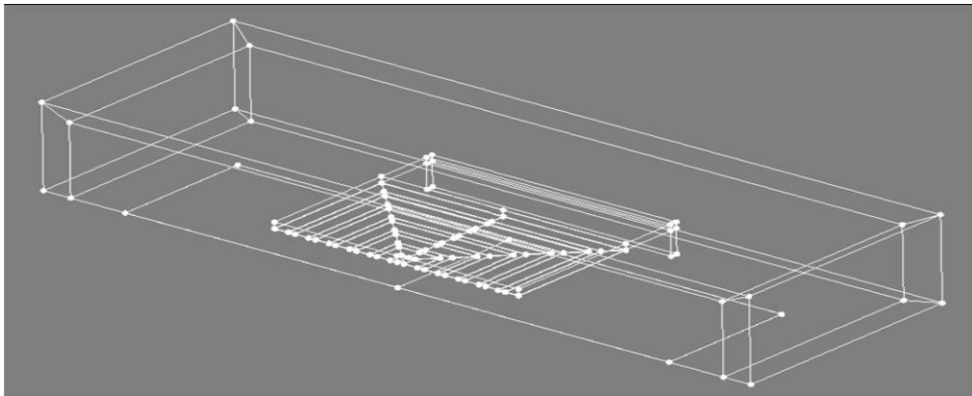

Fig. 3.14: Geometry of the FEM model

3.4.2 Optimization results

In the following paragraph the results of the optimizations performed are shown. The used optimization procedure, described in par. 3.3, gives as result the ratio between N-1 currents and the N-th one. This means that to compute the actual currents needed to reach a given amount of power in the strip the currents must be rescaled with the following formula:

$$I_w = \sqrt{\frac{P_w}{P_{ref}}} \cdot I_{opt} \qquad\qquad (3.11)$$

where:

- I_w: Current to obtain the required power
- P_w: required power in the strip.
- P_{ref}: Power computed with the optimized currents
- I_{opt}: Currents resulting from the optimization.

It is clear that, there are several current vectors that can satisfy a given limit for the maximum profile deviation. The choice between the different possibilities must be finally done with reference to the power supply, the required maximal energy profile deviation, the power factor, etc.

Profile optimization

In Tab. 3.8 the results of the optimizations performed with only the current amplitudes are shown. The optimizations constraints for the 4 cases relatives to strips of width 1000, 750, 600 and 500 mm are reported in Tab. 3.7. A single optimization run needs 5000 fitness evaluations i.e. 5000 solutions of the electromagnetic problem. In Fig. 3.15-Fig. 3.17 the corresponding power profiles are shown.

For the 1000 mm strip the optimization of the current amplitudes is sufficient to obtain good power profiles. The deviation on the energy profile is also very good and in accordance with the order of magnitude calculated in the feasibility study. Also the efficiency remains at very high values as predicted by the previous computations.

As in the case of the 1000 mm strip, satisfying results can be obtained using only the current amplitudes also for the 750 mm strip. Here it can be seen that the lowest deviation that can be obtained with the different sizes of the strip increases when the size of strip decreases. This is due to the lower number of coils having influence on the strip. As shown in Tab. 3.8 in the case of the 500 mm width, the optimization of the amplitude of the coils gives a deviation over 9%. In the case of the 500 mm strip the smallest coil has to be supplied with a magneto-motive force of more than 10 kA-turns. For this reason the number of turns and the dimension of that coil could not be adequate to evacuate the heat losses. In some cases the currents on the two external coils tend to reach a low values near to zero. This means that these coils can be switched off.

Phase displacement

For the strip of 500 mm width, in the optimization involving only the amplitudes of the currents, the deviation on the power profile results higher than in all other cases, as shown in Tab. 3.10.

By the use of the phase displacement among the currents, it is possible to improve the power profile. Tab. 3.9 shows the results. In this case the deviation results much lower than in the previous case, but the efficiency results worse due to the higher currents that must be supplied. The use of the phase displacement could be an efficient method to reduce deviation in the temperature profile, but the cost of the improvement

is high also concerning the complexity for the phase shift control of the power supply [4].

Efficiency

The efficiency of the process decreases as the number of coils having influence on the strip become lower i.e. with narrow strips. The reason is that the majority of the current is carried by the inner coils with currents that can reach more than 10 kA-turns. In Chapter 1 it was seen that the efficiency depends considerably from the ratio between the coil surface and the distance coil-strip. From that it can be understood why the internal coils are less efficient in comparison with the others.

Multiple local minimums

The search space of the optimization algorithm can be represented by a number of scatter plots that relate the current of each coil with the minimum deviation of the energy profile $\Delta E\%$. As example the plots of the search space related to the 1000 mm strip is shown in Fig. 3.18 -Fig. 3.20. In these plots the complete scan performed by the optimization in all the range of the variables can be seen. Moreover the presence of multiple local minima can be seen. Local minima are points in which a false optimum can be found.

In the case of the multiple coil inductors the goal of the process engineer is to satisfy the specification requirements on the deviation of the temperature in respect to the uniform one. As example in Fig. 3.18 it can be seen that several solution with a deviation under ±2% exist. All of these solutions can be used indifferently when the specifications allow this maximum value.

Variables	Min	Max
X(1)=I1/I6	0	0,5
X(2)=I2/I6	0	0,5
X(3)=I3/I6	0	0,5
X(4)=I4/I6	0	0,5
X(5)=I5/I6	0	0,5

Tab. 3.7: Constraints for the optimization of the 1000, 750, 600, 500 mm strip

W [m]	Err %	I1 [A]	I2 [A]	I3 [A]	I4 [A]	I5 [A]	I6 [A]	η%
1000	1,25	390,6	890,2	474	414,1	1445	311,3	98%
750	3,38	-	12,35	1375	158,9	2171	1888	96%
600	6,92	-	6,62	688	-	2528	6023	86%
500	9,32	-	8,51	165,8	402,9	956,3	12325	64%

Tab. 3.8: Best optimization result for the 1000, 750, 600, 500 mm strip

Variables	min	max
X(1)=I4/I6	0	0,5
X(2)=I5/I6	0	0,5
X(3)=ϕ_{45}	-90	90
X(4)=ϕ_{46}	-90	90

Tab. 3.9: Constraints for the optimization of the 500 mm strip (amplitudes and phases)

W [m]	Err %	I4 [A]	I5 [A]	I6 [A]	Φ_{45} [°]	ϕ_{46}[°]	η %
500	3,34	0,3	4884	20005	-38,96	83,11	56%

Tab. 3.10: Best optimization result for the 500 mm strip (amplitudes and phases)
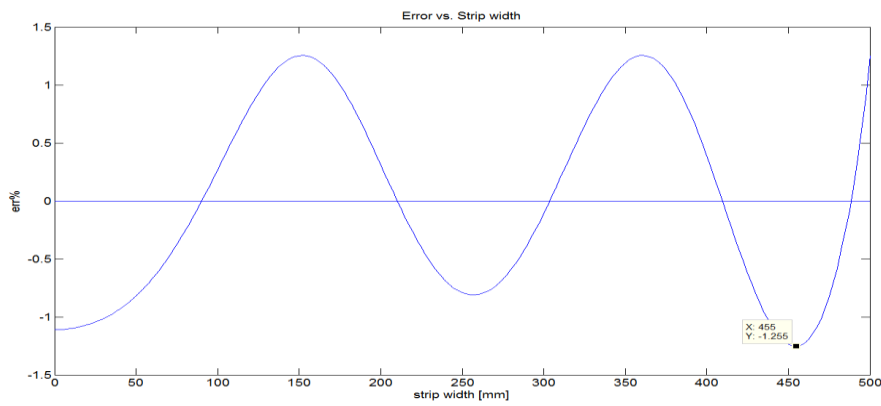
Fig. 3.15: Percentage error on the integrated power profile at the exit of the inductor 1000
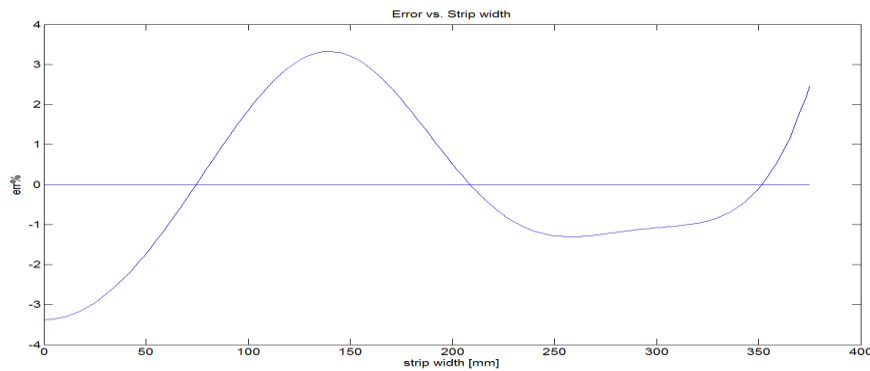

Fig. 3.16: Percentage error on the integrated power profile at the exit of the inductor 750
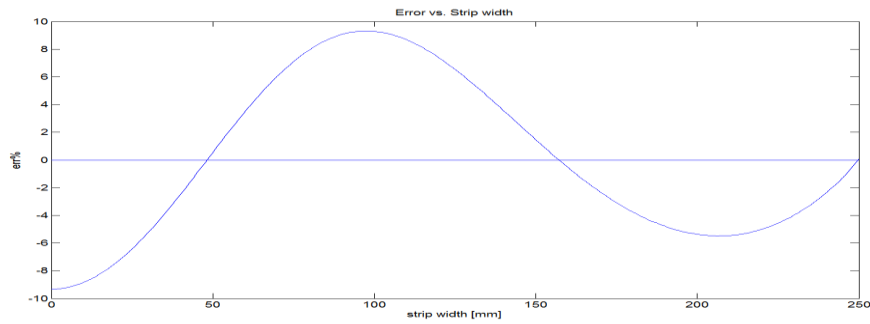
107

Fig. 3.17: Percentage error on the integrated power profile at the exit of the inductor 500
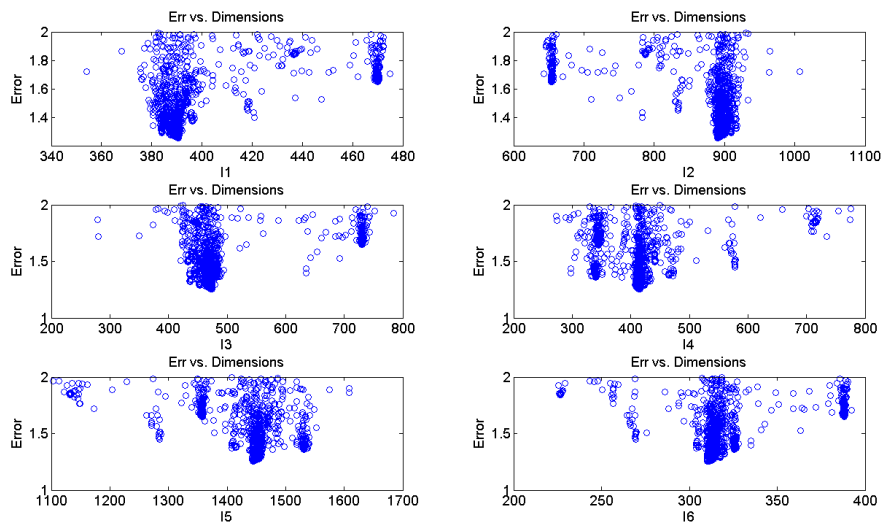

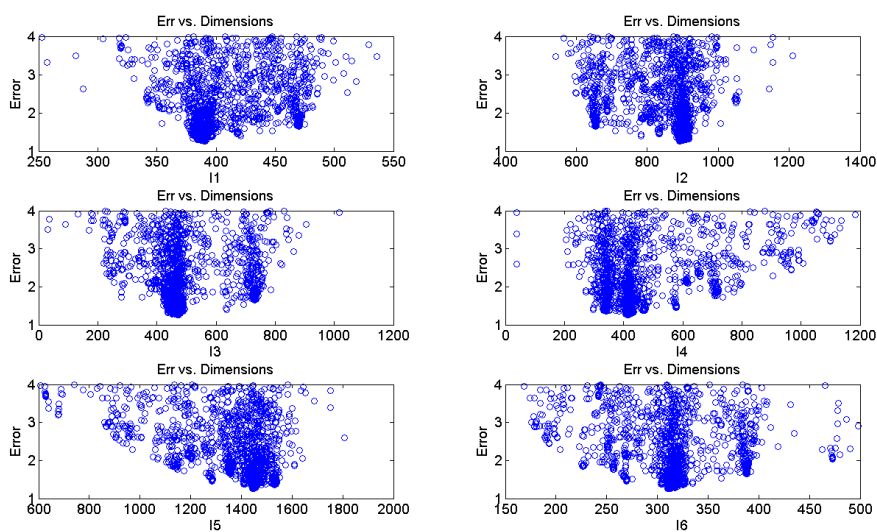**Fig. 3.18: Scatter plot of exploration currents of TRIBES for the 1000mm strip (error<2%)**

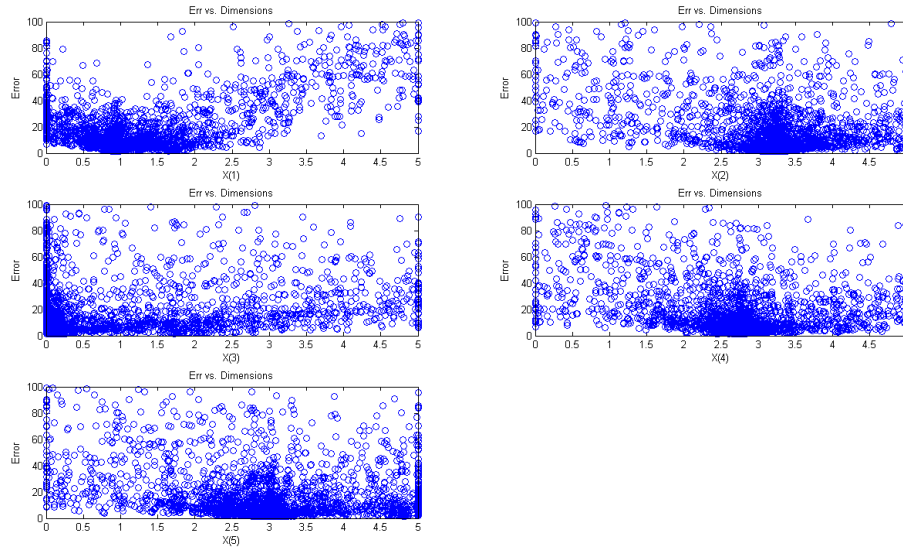**Fig. 3.19: Scatter plot of exploration currents of TRIBES for the 1000mm strip (error<4%)**

Fig. 3.20: Scatter plot of optimization variables of TRIBES for the 1000mm strip (all points)

3.4.3 **Frequency analysis**

In order to verify if the chosen frequency is optimal, a frequency parameterization has been performed by means of TFH3D software. The current injected in the coils is the same used in the optimization of Tab. 3.2 . As can be seen from Fig. 3.21 the active power transmitted to the strip doesn't increase uniformly with the frequency, but above a certain frequency it tends to be constant. On the contrary, the reactive power increases continuously with the frequency. The curve in Fig. 3.23 shows on the other hand that the efficiency increases up to 400 Hz and subsequently it tends to a constant value at higher frequencies. However it would be appropriate the use a higher frequency in order to take advantage of the increased power induced in the strip, but the limitations given from the ratio between the strip thickness and the skin depth must be taken into account. The used frequency will be then between 1000 and 2000Hz. In Fig. 3.24 and Fig. 3.25, the variation of the energy profiles at different frequencies is shown for the coil 1 and 3. It can be noticed that, although the absolute value of the induced energy varies a considerably, the shape does not. This signifies that the frequency can have a big influence on the absolute values of the optimized currents, but the zone of influence of the coil doesn't change significantly with this parameter.
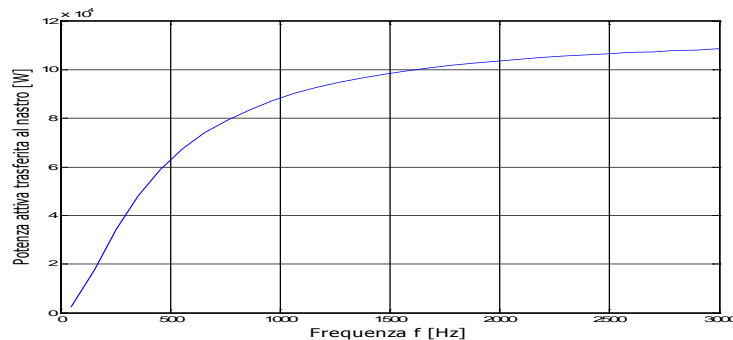

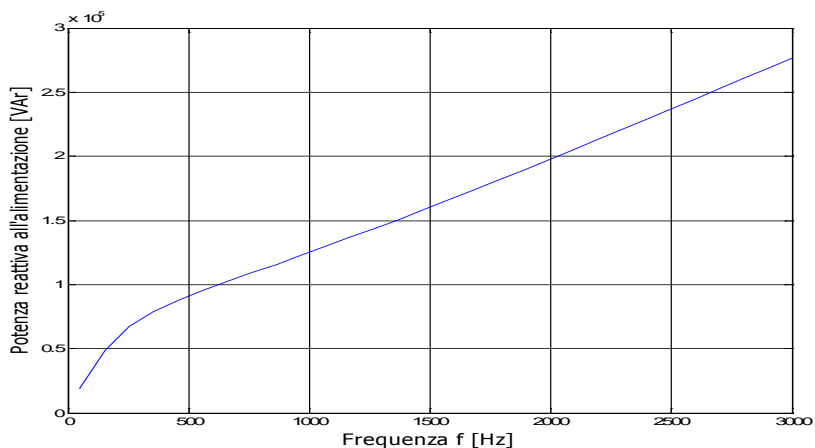**Fig. 3.21: Active power as a function of the frequency**

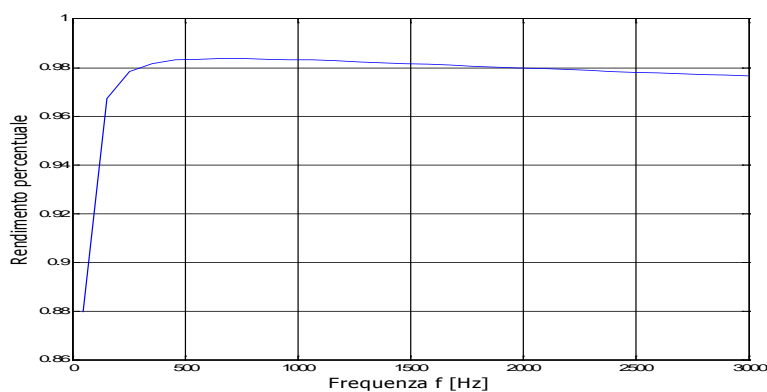**Fig. 3.22: Reactive power as a function of the frequency**

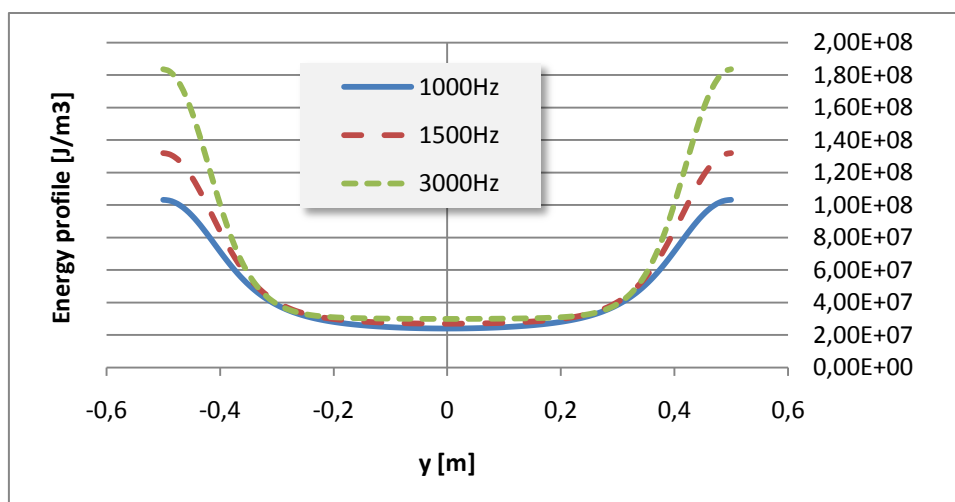**Fig. 3.23: Efficiency as a function of the frequency**

Fig. 3.24: Energy profile as a function of the frequency for the coil n.1
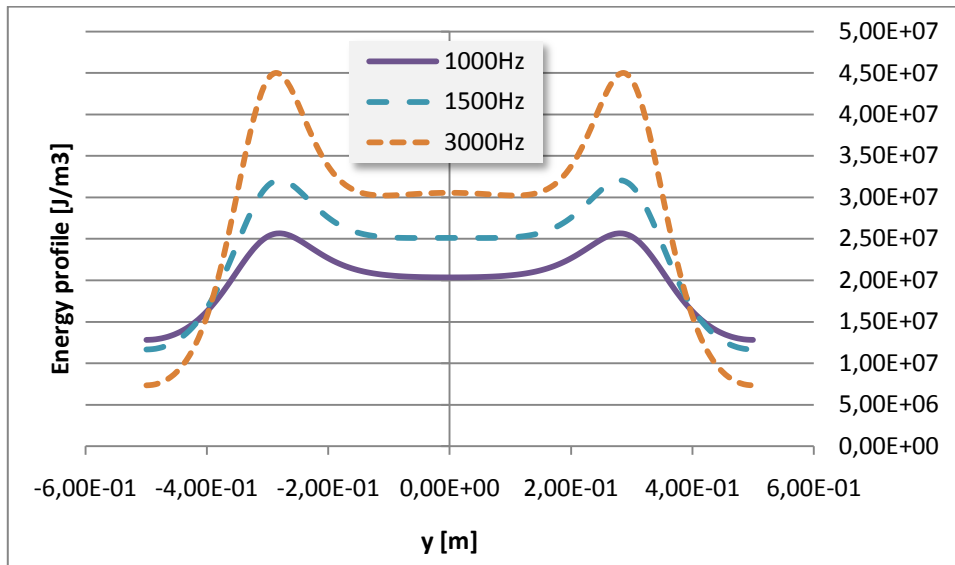
Fig. 3.25: Energy profile as a function of the frequency for the coil n.3

3.5 Magnetic concentrator

The inductor is provided with external magnetic concentrators, in order to avoid stray flux and guarantee EMC safety. Two types of magnetic concentrators have been considered i.e. a closed or open magnetic yoke, as shown in Fig. 3.10. Considering that the shape of the induced current density inside the strip depends by the mutual interactions among the coils, it can be understood that interferences with other inductors, (for example TFH inductor of successive reheating stages) can alter the magnetic configuration. It has then been chosen to maintain the different MCH inductors of an eventual heating line composed by several stages, independent among them i.e. each stage will have its independent magnetic concentrator. The analysis of the influence of the magnetic yoke on the current density will be done making reference to a 2D plane FEM model for simplicity. This model takes into account the phenomena appearing in the cross-section plane perpendicular to the direction of the strip movement.

As already remarked, in the circular prototype analysed in Chapter 2 the concentrator has not been used in order to simplify the analysis. In the case of the prototype here described, the use of the yoke is in practice mandatory. The main motivations are the following:

- Protection of the user against electromagnetic fields

- Reduction of the power factor of the inductor and, as a consequence, reduction of the resonant capacitors value.

- Increase of the magneto-motive force in the air-gap, with consequent reduction of the supply current required to induce a given power in the strip.

A 2D finite element planar analysis (which considers an infinite planar domain) has been performed to verify the influence on the inductor of the magnetic yoke geometry and of its permeability. The model is shown in Fig. 3.26.
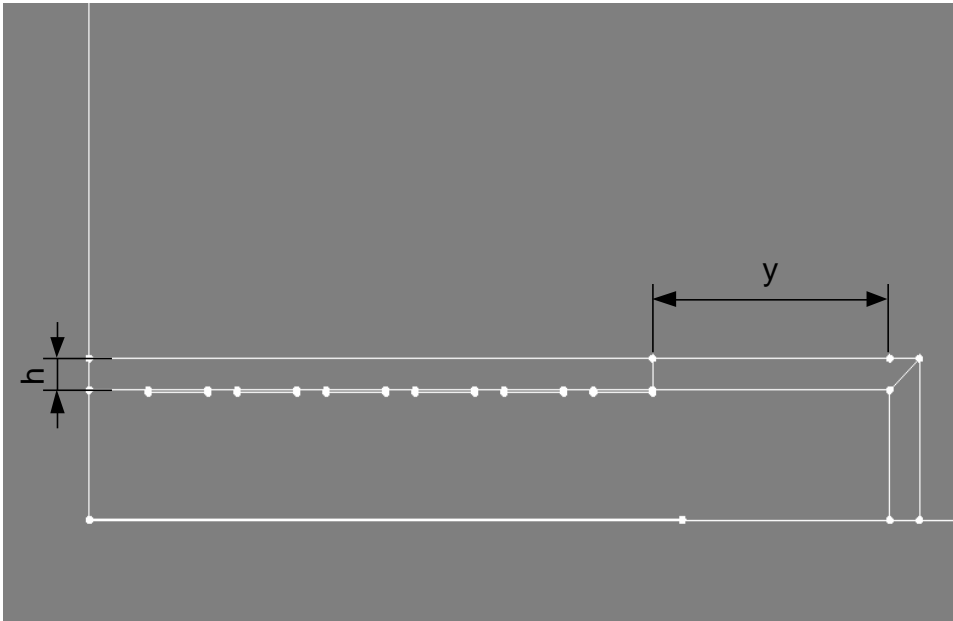
Fig. 3.26: 2D planar FEM model for magnetic concentrator calculation

3.5.1 **Influence of the magnetic concentrator material**

The material permeability has influence on the path of flux lines in the magnetic circuit. The more high is the permeability the more the flux lines are confined in the magnetic yoke. The superposition principle is used to compute the induced power in the strip, so the materials suitable to constitute the magnetic circuit should be linear and isotropic in at least the two directions parallel to the strip. The previous requirement makes the choice of the classical laminated ferromagnetic materials not useful.

Ferrite cores could be used, having high relative permeability $\mu_r > 2000$), but the temperature characteristics (max working temperature 100°C) and the saturation flux density ($B_s \cong 0.3T$) makes them not attractive for the pilot system. In the future the use of ferrite cores and laminated materials has to be further investigated in order to analyze the possibility of reducing the cost of the installation.

The most attractive material for the case in analysis seems to be the Fluxtrol LRM whose characteristic are shown in Fig. 3.27. This material presents several advantages with respect to the classic Ferrite or FeSi materials:

- High saturation flux density

- Good linearity of the permeability as a function of the magnetic field

- High working temperature
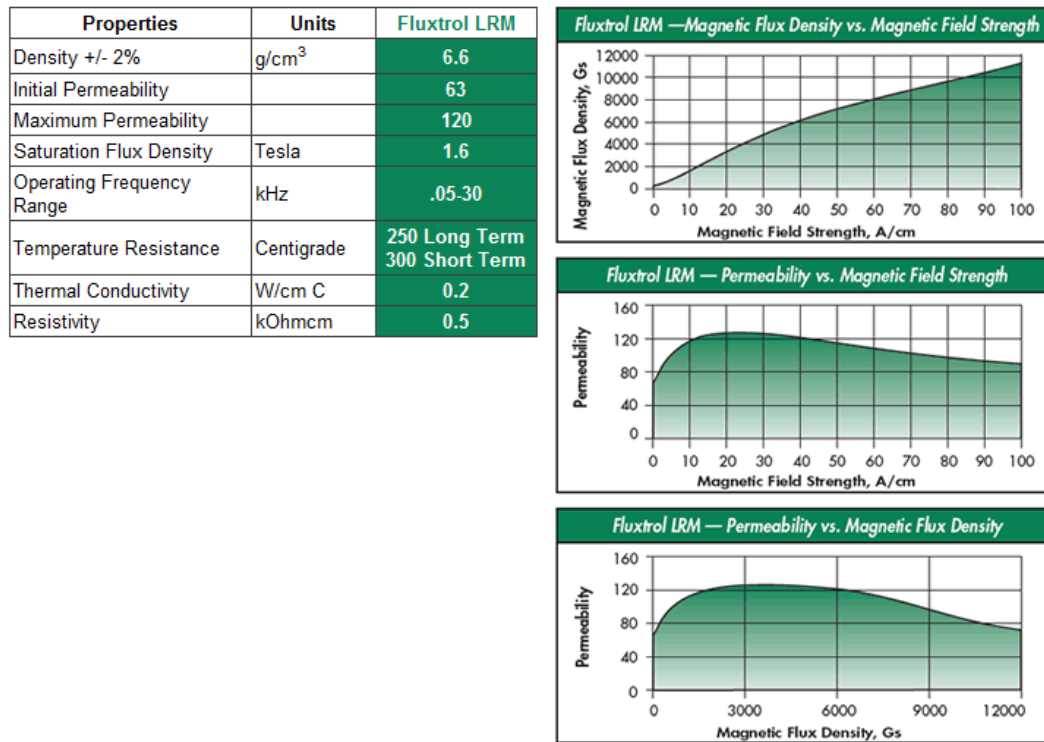
- Isotropy in two directions

Properties	Units	Fluxtrol LRM
Density +/- 2%	g/cm^3	6.6
Initial Permeability		63
Maximum Permeability		120
Saturation Flux Density	Tesla	1.6
Operating Frequency Range	kHz	.05-30
Temperature Resistance	Centigrade	250 Long Term 300 Short Term
Thermal Conductivity	W/cm C	0.2
Resistivity	kOhmcm	0.5

Fig. 3.27: Characteristics of Fluxtrol LRM magnetic material

For the simulations three cases has been taken into account with different relative permeability values μ_r of 0, 90 and 1000 corresponding to the cases of no yoke, Fluxtrol and ideal ferrite yoke. The thickness of the concentrator corresponds to the maximum standard industrial thickness of Fluxtrol (25 mm). A current value of 1000 A has been imposed in each turn, since this is a reasonable upper limit for the current in the coils, and corresponds to the maximum current of the generators. The resulting active and reactive power and power factor are shown Tab. 3.11. It can be seen that the power factor increases dramatically when the magnetic concentrator is used, while the value of the magnetic permeability has less impact on the performance of the inductor. In Fig. 3.28 the distribution and the magnitude of the flux density are shown in case of μ_r=90 and μ_r=1000.

μ_r	0	90	1000
P [W]	3324W	87263	96073
Q [var]	23917	105440	104205
cos φ	0.13	0.63	0.68

Tab. 3.11: Active and reactive powers in the strip with different yoke materials with supplying currents of 1000 A in each coil.
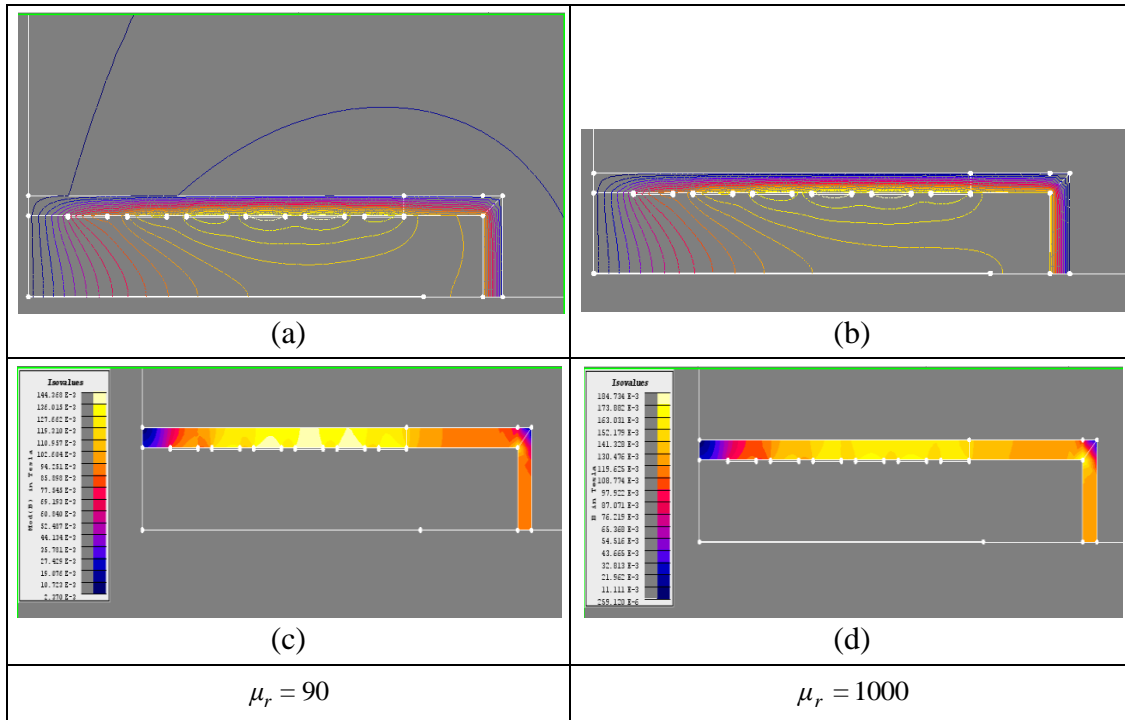
(a)	(b)
(c)	(d)
$\mu_r = 90$	$\mu_r = 1000$

Fig. 3.28: Flux lines and flux density at different permeability of the magnetic core

3.5.2 **Magnetic flux density**

A FEM simulation with the optimized currents has been done in order to verify the results. The model is the same (μ_r=1000) used to extract the current density pattern for the optimization. An image of the total current density pattern given by the currents in Tab. 3.2 for a strip width of 1000 mm is shown in Fig. 3.29. The total power induced into the strip is practically the same computed with the superposition of the currents. A little difference is due to the grid used in the optimization procedure used to superpose the different current density pattern. To have results with a better precision a more re-fined grid should be used.

In general it must be said that the computation models does not have high degree of precision in the calculation of the local parameters. The precision of FEM computations depends on the precision of the material characteristics on the used formulations, and on the mesh. However the results on the energy deviation computed in the previous computations can be considered as an order of magnitude of the profiles that will be obtained in the actual installation. In order to obtain the same degree of uniformity in the prototype, a real time control of the temperature profile has to be provided.
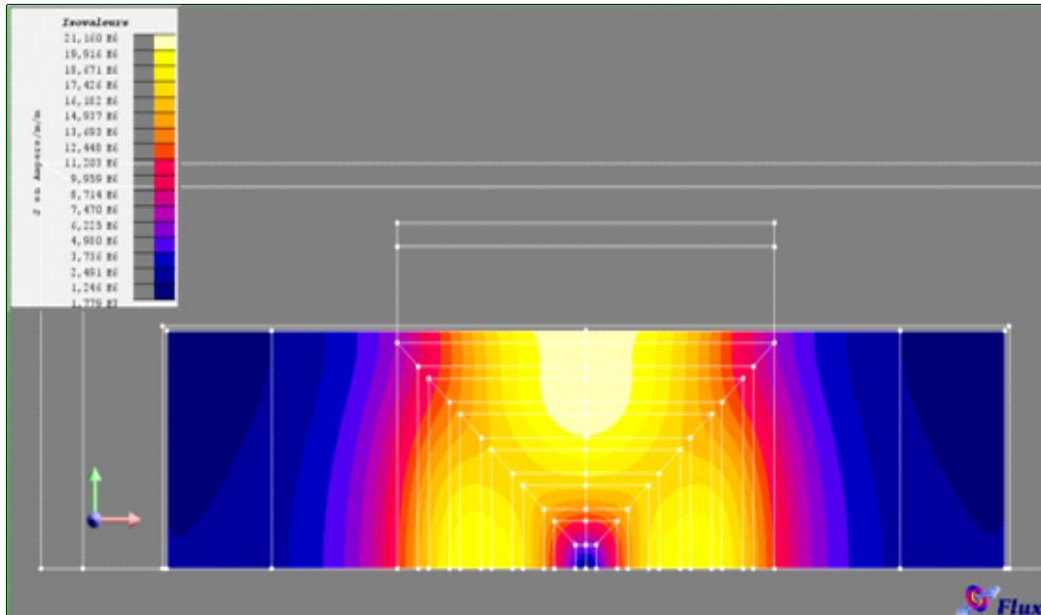
Fig. 3.29: Current density pattern with optimized currents for the 1000 mm strip.

With the same currents the values of the magnetic fields on the concentrator has been computed. The Fig 3.31 shows that in this case the maximum magnetic flux density is 0.4 T, the higher values being in correspondence to the corners of the coils. For this reason in the following it has been chosen to manufacture the coils with rounded corners.

The lateral part of the inductor ((1) in Fig 3.31) gives an improvement on the induced power and a reduction on the reactive power of the order of 10% while it increases the hysteresis and eddy current losses, so it could be eventually eliminated. The analysis of the magnetic concentrator without the lateral part will be described in the next sections.
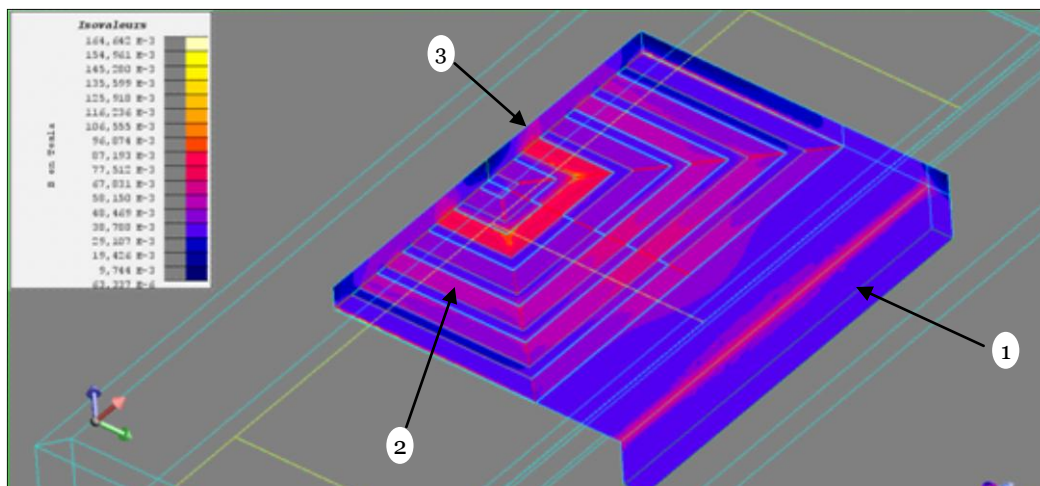

Fig 3.31: Values of the magnetic flux density in the middle section of the inductor width (1-lateral part of the concentrator, 2-upper part of the concentrator, 3-coils)

115
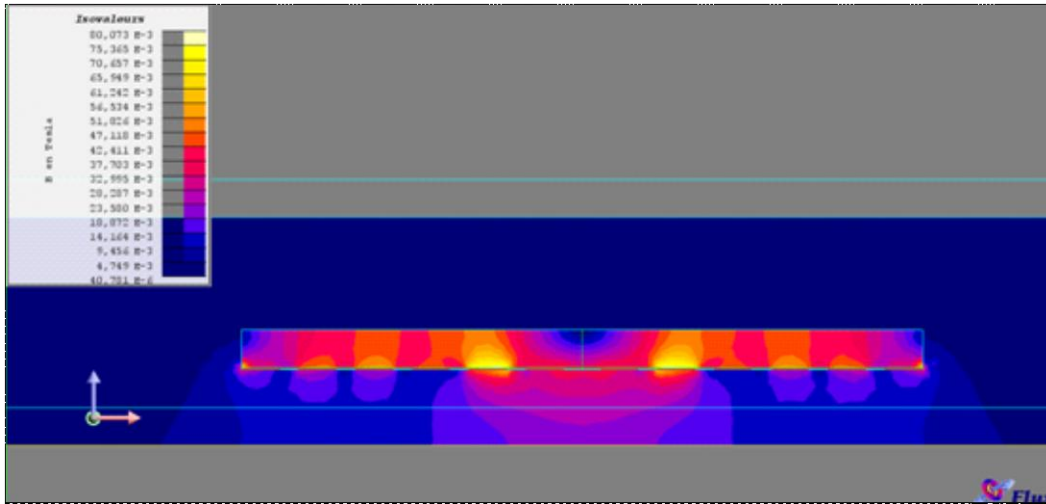
Fig 3.32: Values of the magnetic flux density in the middle section of the inductor width

3.5.3 **Frequency parameterization**

A frequency parameterization on the 3D FEM model has been performed to verify the results obtained in the analytical computations (3.4.3). The Fig. 3.33 shows the behaviour of the active and reactive power in the strip as a function of the frequency. The maximum of the power factor is found at a frequency of about 1500 Hz.
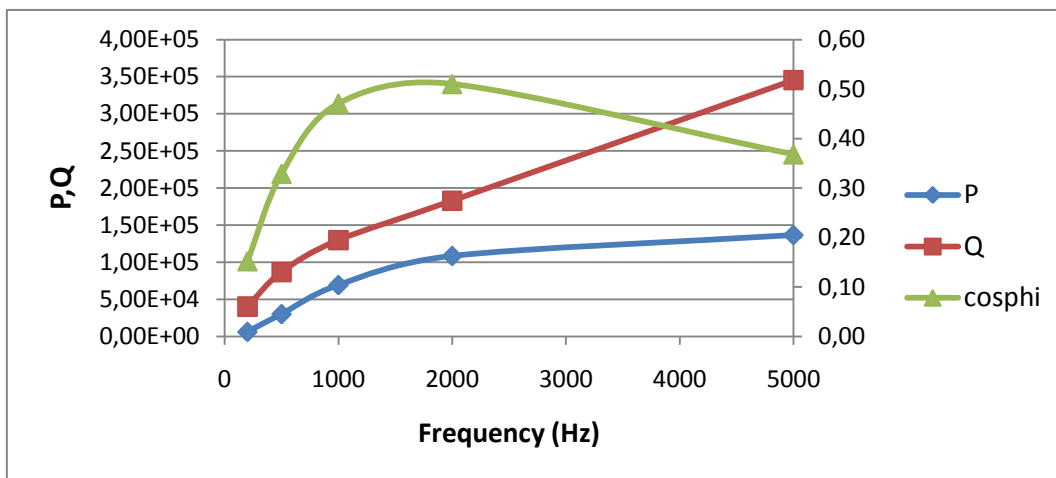
Fig. 3.33: Power factor, active and reactive power on the 3D FEM model in function of the frequency

3.5.4 **Losses in the magnetic yoke**

The losses in the magnetic yoke have been computed, with the currents of Tab. 3.2, via the following formula [42] that relates the magnitude of the flux density and the frequency to the dissipated power:

$$P_{diss} = \int_{Vol} 2.1 \cdot 10^{-11} \cdot B^2 \cdot f \cdot 10^8 \cdot 10^6 \, dV$$

(3.12)

116

Strip size [mm]	Yoke Power [W]
1000	708
750	851
500	1764

Tab. 3.12: Losses in the magnetic concentrator at different strip width. Coil supplied with the currents in Tab. 3.8

The results are shown in Tab. 3.12. These are approximated values due to the simplifications of the model, but they give the order of magnitude of the losses due to the magnetic yoke when the optimized currents are used.

The previous considerations suggest that the magnetic concentrator is oversized in respect to the actual needs and a reduction on the quantity of the magnetic material is certainly possible at the price of greater losses in the magnetic material.

3.5.5 **"Open" magnetic concentrator**

The closed magnetic concentrator analyzed in the previous section allows improving some of the performance of the multi-coil inductor. However the following drawbacks of such configuration exist:

- Supplementary cost due to the material lateral of the lateral part

- Difficulty of survey and re-insertion of the strip in case of failure.

- Excessive reduction of the quality factor of the coils making difficult, in some case, to reach the resonance of the circuit.

For that a configuration with open magnetic concentrator has been considered and analyzed in the following sections. In particular the effect of the dimensions of the magnetic yoke on the induced power density and on the integral electrical parameter will be shown.

3.5.6   **Model**

The 2D FEM model is shown in the Fig. 3.34 with the dimensions. The analysis has been done on different shapes and dimension of the magnetic yoke.

- w_turn=10 mm

- d_turn=2 mm

- t_yoke=25 mm

- d_yoke=100 mm

The currents indicated are the current flowing in each turn, so the total ampere-turns for the coil must be computed multiplying the current by the turn number. The comparison has been done with reference to the different geometries indicated in the next figures. The first geometry considered is a simple slab of magnetic material leant on the coil plan. The second geometry considers a piece of additional material under the overhang of the concentrator as shown in Fig. 3.35 . The third geometry considered comprises the closure of the magnetic core in the lateral part. The relative permeability

for the computation was considered on first approximation to be linear and isotropic with μ_r=90.
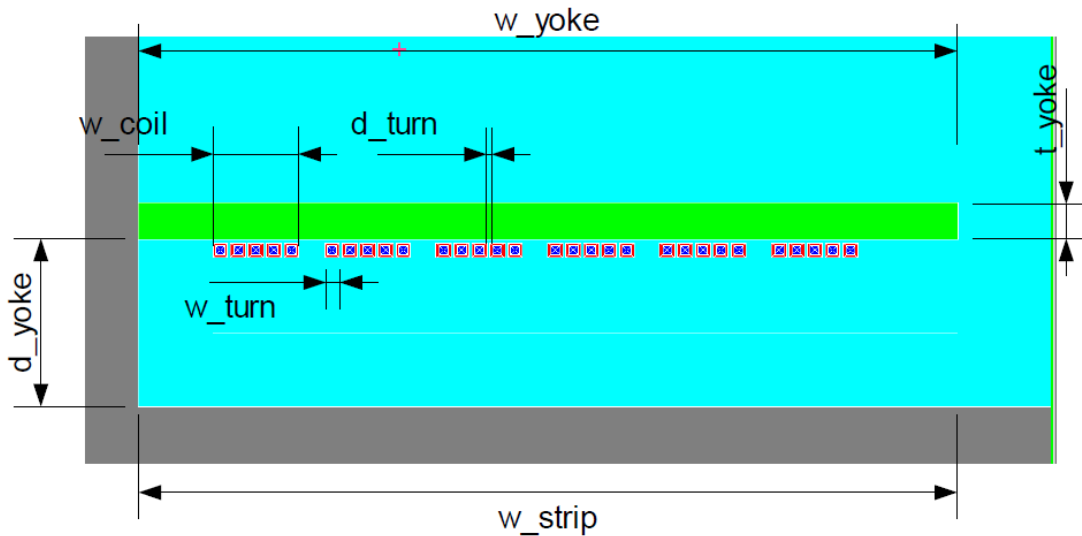

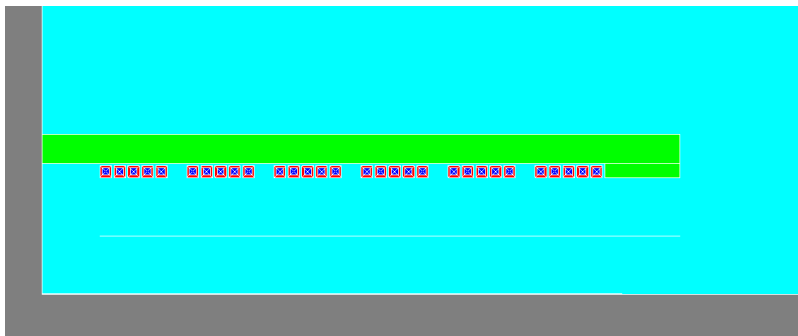**Fig. 3.34: 2D model used to analyze the geometry of the magnetic concentrator**

Fig. 3.35: 2D model with slot

3.5.7   **Magnetic concentrator configurations**

Fig. 3.36-Fig. 3.39 show a comparison between the power densities on the strip at different overhang lengths of the yoke. It can be noted that the larger differences are found in the induced power density produced by the coil n.1 (the most external). In particular, for this coil, the effect of the lateral closing part of the magnetic yoke is to increase considerably the power density on the strip. This has certainly influence on the optimization results because of the different edge effect in the strip. The effect of modifying the overhang of the magnetic concentrator with additional magnetic material does not imply large differences on the power density curves. Considering supplied the coil n. 2 instead, the differences among different overhangs are less important, and for the more internal coil the difference is practically imperceptible. On the contrary the difference is more evident when considering the closed yoke. In this case the peak value of the power density is very high for the closed concentrator case respect to the open concentrator case as shown in Fig. 3.36. In any case for the power density of the coil n.6 there is not remarkable difference.

As already remarked the use of the concentrator allows to transfer more power to the strip in comparison to the same inductor in air in which flow the same currents. In

Fig. 3.40 a comparison between the two cases is reported. It can be seen that, for the same supply currents the use of the concentrator improve notably the mean value of the power profile.
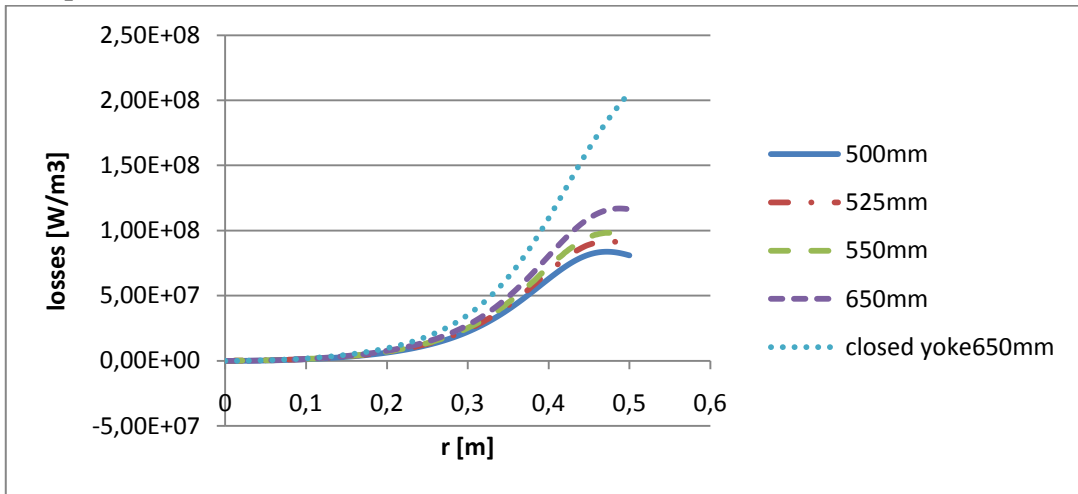

Fig. 3.36: *Power density in the strip with i1=300A*
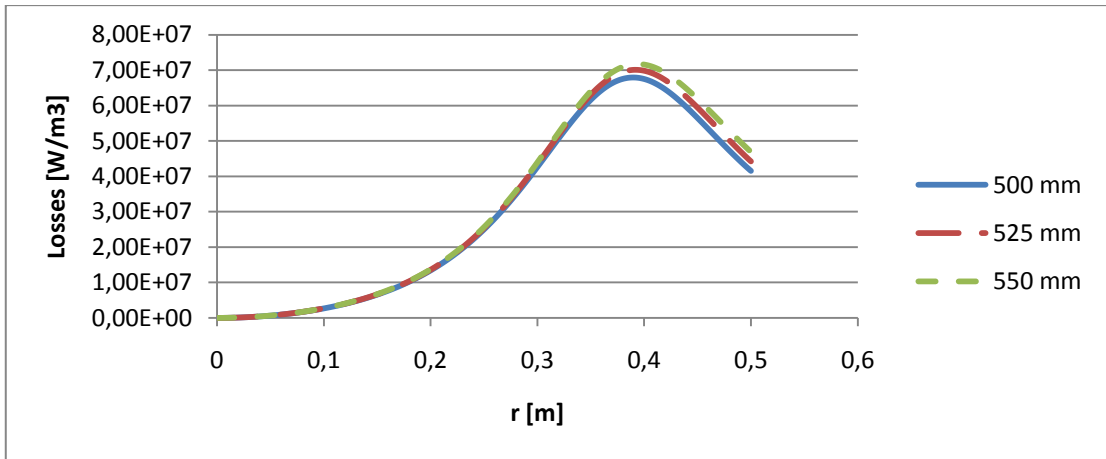
Fig. 3.37: *Power density in the strip with i2=300A*
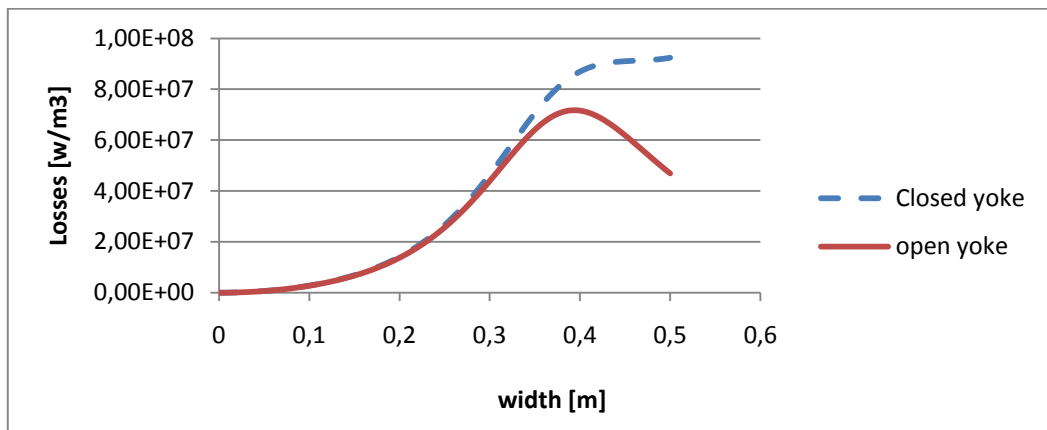
Fig. 3.38: Comparison between open yoke and closed yoke configuration I2=300A
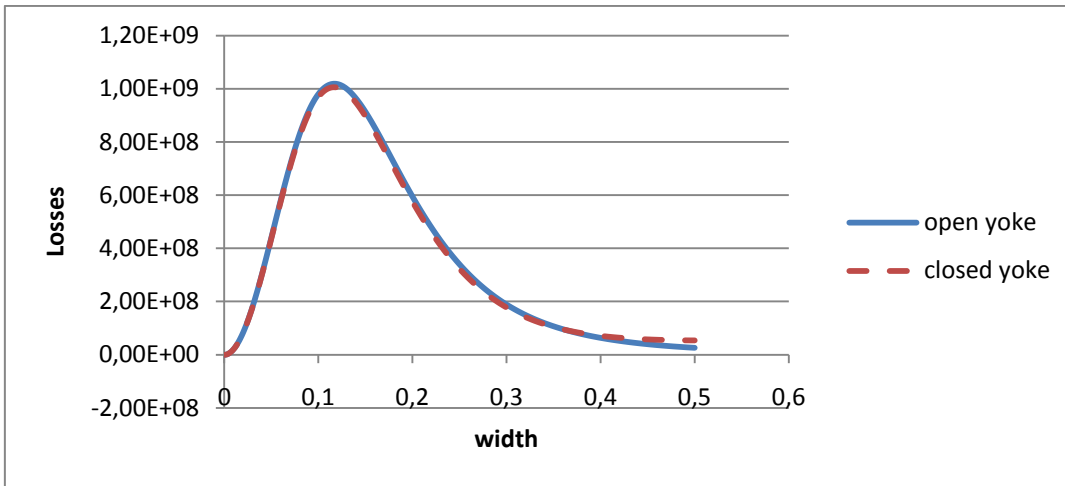
Fig. 3.39: Comparison between open yoke and closed yoke configuration I6=2000A
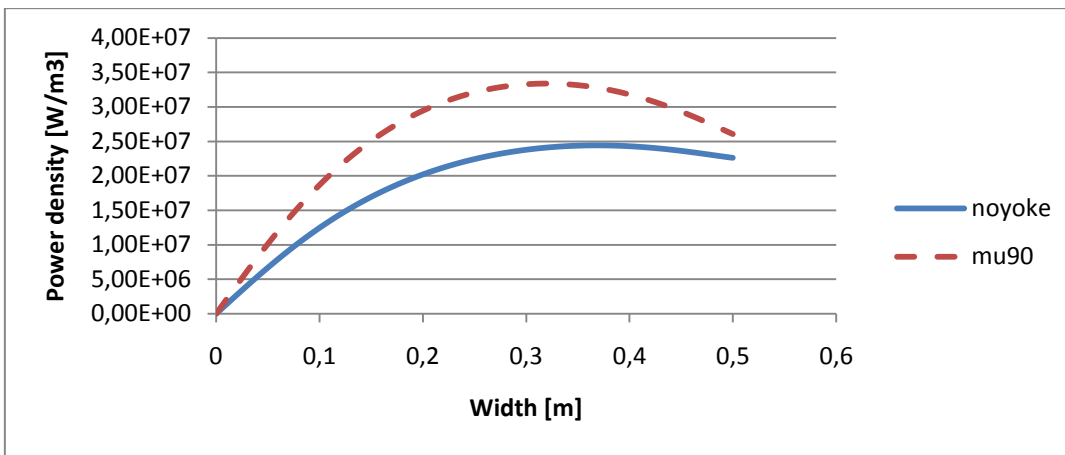
Fig. 3.40: Comparison between Fluxtrol open yoke and no yoke power profiles

3.5.8   **Flux density and losses in the concentrator**

In the Fig. 3.41-Fig. 3.42 the flux density in the core is shown for overhang lengths of 500 mm and 550mm. The Fig. 3.43 shows the value of the flux density when all coils are supplied with the same current. In the figures it can be seen that the magnetic flux does not exceed the magnetic saturation of the Fluxtrol LRM even with all turns are supplied at 300A which means the very high value of 15 kAturns for each coil. It has to be noted that the maximum values for the currents computed by optimization doesn't exceed this values except on the case of the 500 mm strip. Tab. 3.13 shows the losses in the magnetic yoke computed with the Eq. (3.12). The table shows that a cooling system must be designed to evacuate the losses produced from the yoke in order to stay below the temperature limits of Fluxtrol LRM.

Supplied coils	I [A]	P_{yoke} [W/m]
all	300	3768
coil 1	300	176
coil 2	300	192
coil 6	2000	5536

Tab. 3.13: Losses in the yoke at several current configurations, w_strip=1000 mm, w_yoke=1100 mm

Fig. 3.41: Flux density with I1=300A, w_yoke=500 mm
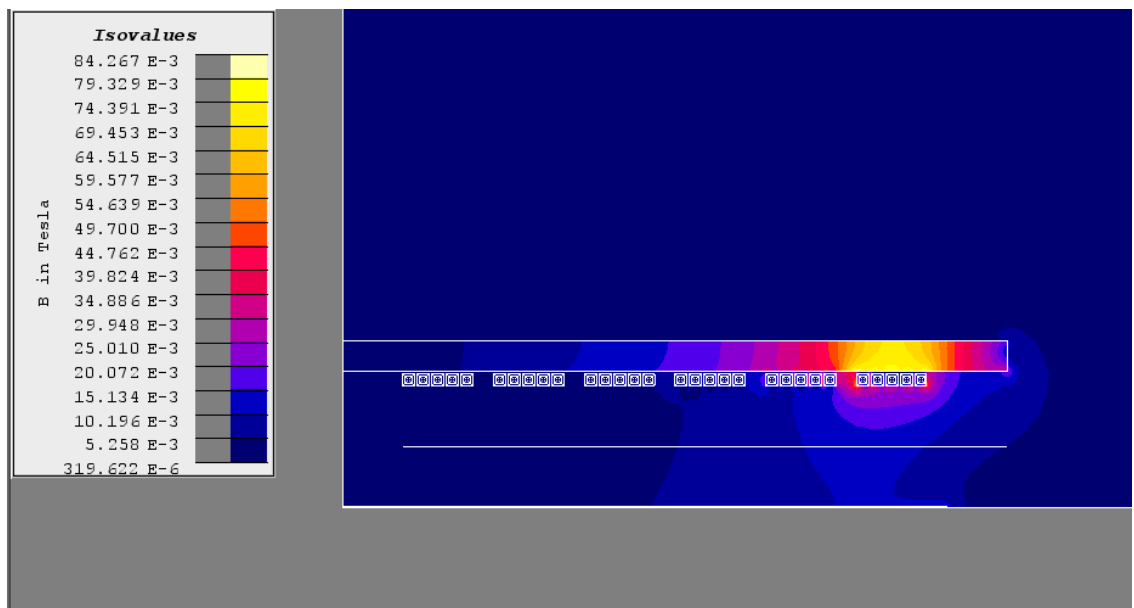
Fig. 3.42: Flux density with I1=300A, w_yoke=550 mm
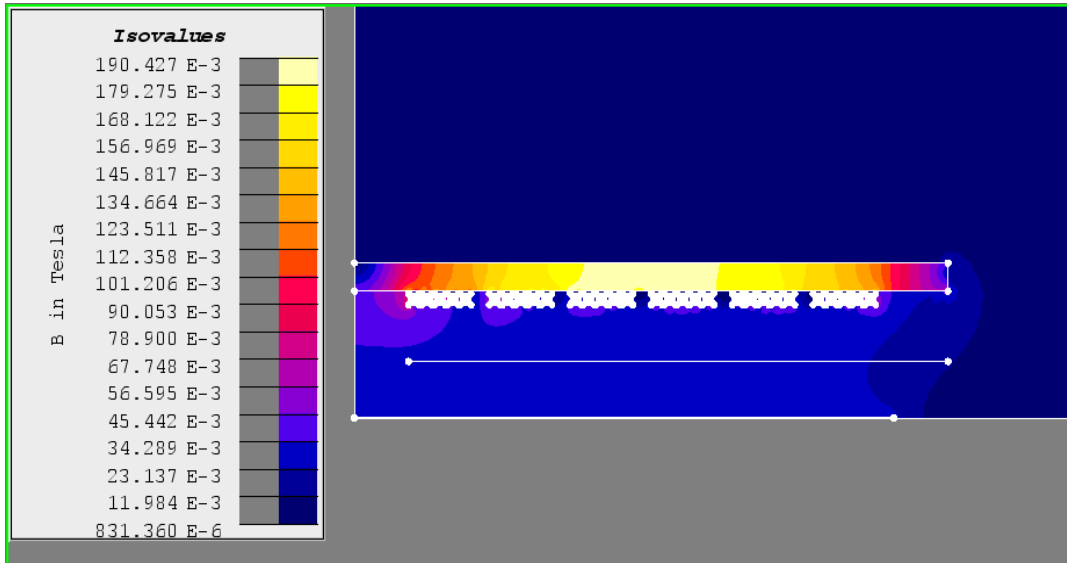
Fig. 3.43: Flux density with I1..I6=300A

3.5.9 **Electrical parameters**

In Tab. 3.14 the electrical parameters, (powers, quality factor, and efficiency), in function of the geometry of the yoke are shown, considering all the coils supplied with the same current. From the table it can be seen that the increase of the concentrator overhang allows to obtain a relatively small increase of powers (active and reactive) in the system. On the contrary, the closure of the mag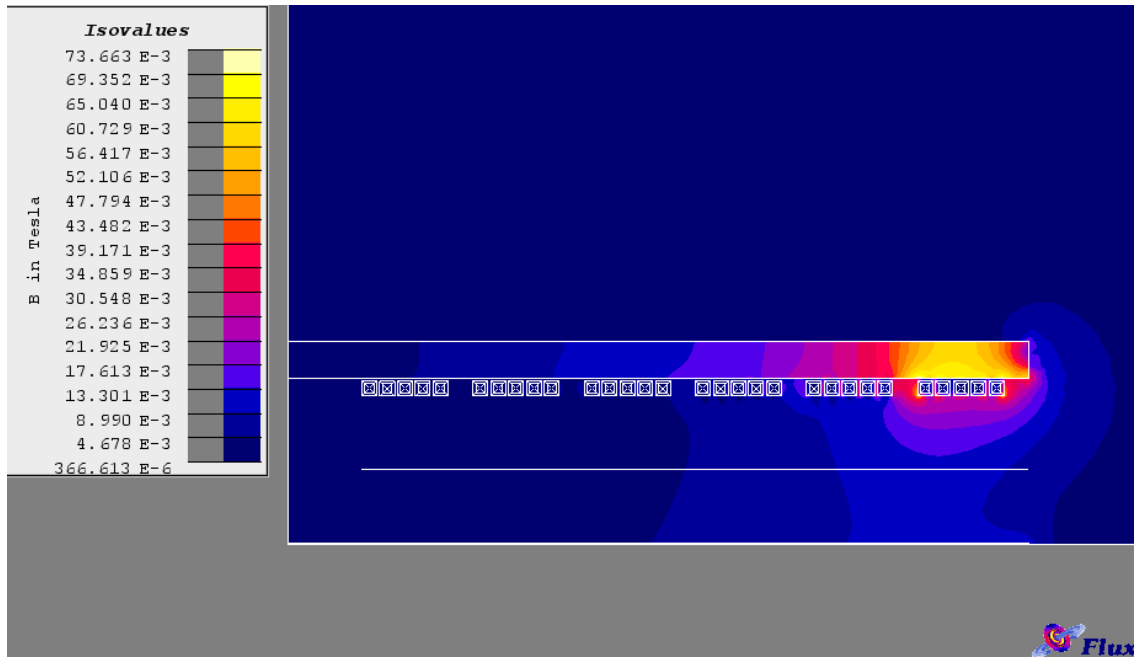netic yoke increase notably the active power involved in the system. Moreover the lateral part of the yoke has not a big influence on the reactive power. As the coils must be supplied with resonant converters it is convenient to provide a high quality factor in order to have a better efficiency of the power supply. From this point of view the use of the lateral part of the yoke may have a negative influence.

w_yoke	Pstrip [W]	Ptot [W]	Qtot [var]	η	QF	cosφ
500	3383	3864	9778	0.876	2.531	0.368
525	3673	4167	10130	0.881	2.431	0.380
550	3887	4392	10305	0.885	2.346	0.392
650	4415	4942	10560	0.893	2.137	0.424
650 **Closed magnetic circuit**	6353	6965	10916	0.912	1.567	0.538

Tab. 3.14: Electrical parameters for different configuration of the magnetic yoke, strip width= 1000 mm, I=300A in each turn

3.5.10 **Power density along the longitudinal direction**

After the analysis of the influence of the magnetic concentrator on the width of the system, the 2D model can be used to analyze the behaviour of the system along the longitudinal coordinate of the strip i.e. in the mid-line parallel to the direction of the strip movement. The analysis (Fig. 3.44 and Tab. 3.15) shows that there is no substantial dif-

ference on the shape of the power density, when the overhang in the direction of the strip length changes. However, since the induced power increases, it can be justified the use of the overhang in the magnetic yoke also in the longitudinal direction.
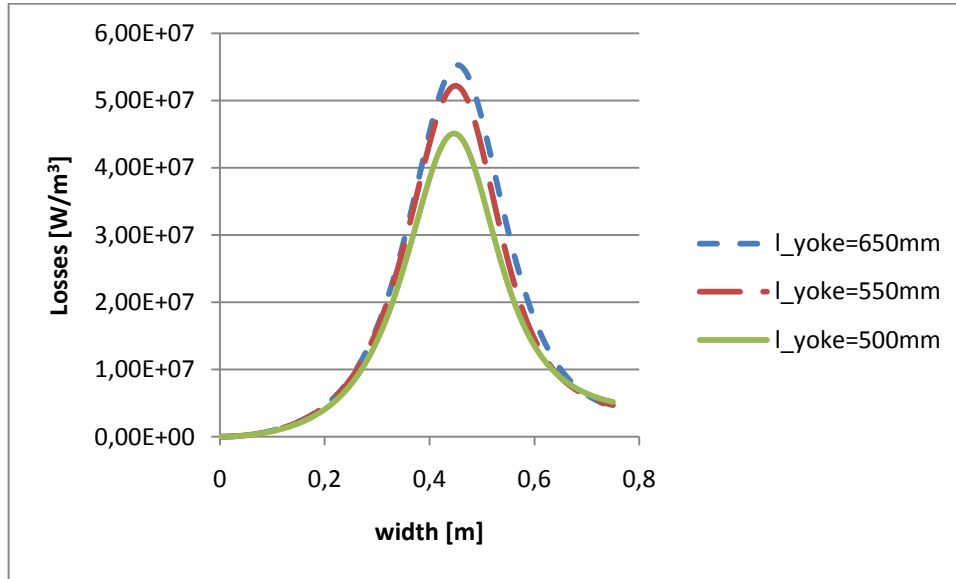
Fig. 3.44: Power profile in the longitudinal mid-line of the strip for several values of the longitudinal dimension of the magnetic yoke

l_yoke	Pstrip [W]	Ptot [W]	Qtot [var]	η_e%	QF	cosϕ
500	2848	3266	8288	87.2%	2.53	0.367
650	3454	3884	8748	88.9%	2.25	0.406

Tab. 3.15: Electrical parameters for a strip 1000 mm supplied with I=300A per turn and with different values of the overhang length (l_yoke).

3.5.11 Limits of the simplified model of the magnetic material

If on one hand the simplified model of Fluxtrol LRM considered with an average relative permeability of 90 simplifies notably the computations, on the other hand it gives necessarily different results in comparison to the actual non linear material. In the Fig. 3.44 the results of the comparison of the power losses in the strip are shown. Each coil is supplied with a current of 300 A. The non linear model of Fluxtrol (given by the manufacturer) considers an isotropic permeability with saturation and knee adjusting given by the following formula:

$$B(H) = \mu_0 H + \frac{H_a + 1 - \sqrt{(H_a + 1)^2 - 4H_a(1 - a)}}{2(1 - a)} \tag{3.13}$$

with

$$H_a = \mu_0 H \frac{\mu_r - 1}{J_s} \tag{3.14}$$

The parameters used in the simulations are the following:

123

- Js=1.7 T

- a=130

- C_0=0.48

It can be seen that the error on the power density profile is less than 2%.

Fig. 3.45: Difference on power losses density between complete model of Fluxtrol and simplified model with constant permeability

Fig. 3.46: B-H courve of Fluxtrol LRM

Choice of the magnetic concentrator

From the above results it can be concluded that the use of the lateral part of the magnetic yoke is not convenient. The choice of using an open magnetic concentrator has been done with reference to:

- The cost of the magnetic material;

- The difficulty of building the prototype;

- The requirements from the supply side (Quality Factor);

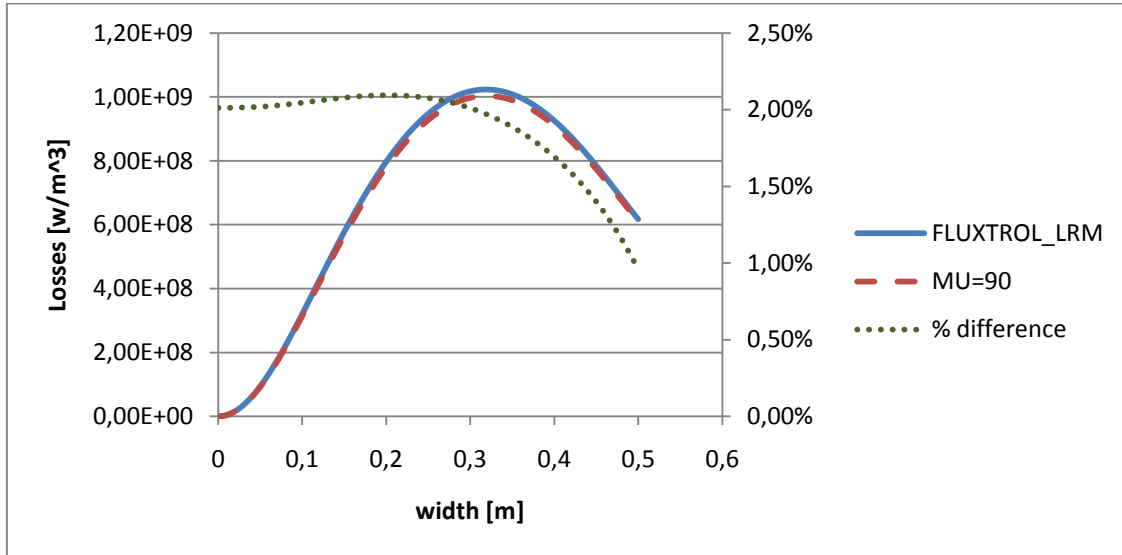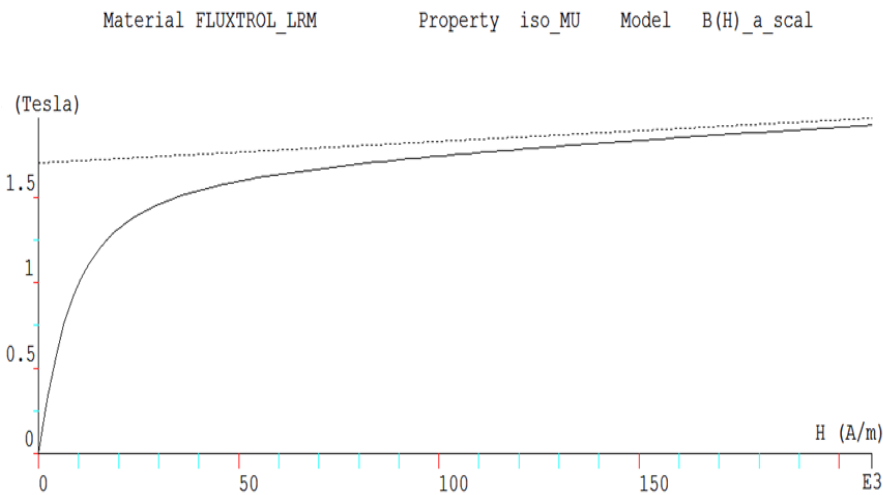- The optimization results obtained by a 3D analysis without closure.

3.6 Conclusions

The possibility of obtaining uniform TFIH of strips of different widths in an inductor without movable parts, by supplying the inductor coils with suitable sets of optimized currents of different amplitudes and phases, has been analyzed and demonstrated by the use of the program TFH3D. Thanks to the reduced computation requirements, this software can be conveniently used for a rough preliminary design of the system. With the geometry considered the heating of strips of width between 500 and 1000mm is possible, with an error on the energy lower than 5%.

The required power profile must be reached optimizing the supply current values in the 6 coils composing the inductor. The analysis of the optimization results has shown that multiple values of currents can reach a required precision when that one is fixed by the industrial process specifications. Moreover the use of the phase displacement between currents as optimization parameter has been demonstrated to improve the precision of the energy profile with the drawback of a larger current magnitude.

The choice of the materials and the geometry of the magnetic flux concentrator has been done with reference to the material Fluxtrol LRM, which has been chosen for the excellent quasi-linearity and isotropy of the magnetic properties as well as the mechanical and thermal properties.

Despite the reasonably good results obtained with the non-optimized geometry, the possibility to improve the performances of the inductor by the optimization of the coils geometry is therefore necessary, with reference to the actual requirements of the steel industry. In the next chapter the previous considerations will be taken into account in order to design the final prototype of MCH inductor.

Chapter 4

Final inductor design

In the last period of the development of the project, the introduction of a new industrial partner for the design of the inverter led up to redefine the technical specifications of the inductor. The idea was to design an inductor for a new prototype devoted to demonstrate to the industry the applicability of this technology; for this reason it was decided as objective the heating of strips with dimensions consistent with the requirement of the industry. The chosen dimensions were between 800 and 1200 mm width with thickness of 1 mm. The installed power has been decided to be 600 kW, supplied by 6 standard inverters with maximum current of 1000 A in soft-commutation switching mode and voltage 500V with the resonant capacitors in series connection.

The first part of the chapter will describe the optimization method with reference to a test 3 coil inductor capable to heat strips having width between 600 and 800 mm. The results of the Chapter 3 and the considerations on the geometry optimization, allowed us to understand that the most critical part of the inductor is the smaller coils. This means that the geometrical optimization can be conveniently performed only with reference to the narrower strip width, and dividing the remaining part of the strip surface, for the wider strip widths, in several zones affected by uniform distributed coils. This method has been used to design the first tentative prototype which will be described hereafter for the sake of clarity.

The software Fluxgrid (see Appendix A), that combines the results of FEM computation with the Tribes optimization algorithm, has been used in order to verify the results of the geometry optimization and the performance of the designed inductor. After the design of the first optimized inductor it has been recognized that because of the command strategy the inverter current should be limited to 500 A. Moreover the dimensions of the turns has been slightly changed in order to use standard commercial dimensions of copper tubes and to satisfy the mechanical constraints due to the

manufacturing. The final inductor has then been designed, and the overall results of the computations performed on it will be described. The data on the final geometry are not complete for reason of confidentiality.

4.1 Geometry optimization with analytical approach

The use of a regular geometry for the inductor, like the one analysed in Chapter 3, allows to obtain good results in a number of industrial applications. However in several industrial manufacturing lines the maximal accepted deviation on the temperature profile at the inductor exit is less than ±2% for a wide range of strip widths and thicknesses. Moreover multi-coil heating inductors must be supplied with new advanced inverter systems in order to control the mutual interaction among coils, and the coils design must take into account the impedance matching of the load to the supply. These requirements practically force to adopt modern optimization methods to improve the inductor performance. In fact it will be seen that one characteristic of this kind of inductors is that the maximum power that can be achieved is in inverse proportion to the temperature uniformity that can be obtained in the strip.

Since the optimization of the geometry requires several computations of different geometric and electromagnetic configurations, the Tribes optimization algorithm has been coupled with the analytical software TFH3D in order to reduce the computation time in comparison with FEM computations. The feasibility of such procedure has been demonstrated in the previous sections of this chapter. Despite the optimization of TFH geometries has been demonstrated before [43] [44], up to now such attempts have been limited to the design of single or multiple coils connected in series (i.e. only one supply current) and placed sequentially along the length of the strip in spatially separated zones.

In this section the optimization of all system parameters of a multi-coil inductor, i.e. supply currents and geometrical dimensions, is considered. The main technical challenge of such problem consists in designing a single configuration capable of heating strips of different widths while satisfying geometrical, electrical and heating process constraints [45].

The goal of the design process was to conceive a large inductor capable to heat strips up to 1200 mm wide but an optimization with narrower strips has been done first in order to test the method. Moreover, from these optimizations, some general considerations for MCH inductors will be done.

The goal of the first optimization was to design a system consisting of a small number of coils which can heat strips of widths between 500 mm and 800 mm with a required deviation on the temperature profile of less than ±3%. The optimization problem has been solved by means of the Tribes variant of the particle swarm optimization (PSO) algorithm described in par. 2.1.3.

4.1.1 Analysis Methods

Several numerical methods are available today for the analysis of electromagnetic and thermal problems, but the optimization of a 3D coupled electromagnetic-thermal

system with eddy currents is still high time-consuming if FEM codes are used for the solution of the forward problem. For this reason the preliminary design of the inductor has been carried out with the semi-analytical code TFH3D. In this approach a semi-analytical solution of the electromagnetic problem, based on the Fourier series expansion of the field quantities, is used for the determination of the current and the power density induced in the strip by the exciting system. Runtimes range from tens of seconds to a few minutes to perform a single magneto-thermal simulation depending on the chosen number of harmonics and on the discretization of the domain. These parameters impact significantly on the optimization time.

In order to verify the reliability of the results obtained with TFH3D a further comparison with FEM has been performed on a number of different configurations, and the results are shown here as an example for the 500 mm width strip (see Fig. 4.1). TFH3D is compared with two FEM models: the first one with magnetic concentrators closed in the lateral part and with very high magnetic permeability and the second with a more realistic magnetic yoke constituted by 2 slabs of magnetic material with relative permeability of 90. In the first case the integral results given by the analytical and the FEM models are quite close, but they show a difference on the power profiles. In the second case with the open concentrator with low permeability, the results show a considerable difference in the transferred power. In spite of the above partial lack of accuracy it should be noted that the shape of the energy density profiles given by TFH3D is very similar to the one obtained by the FEM model (see Fig. 4.1).
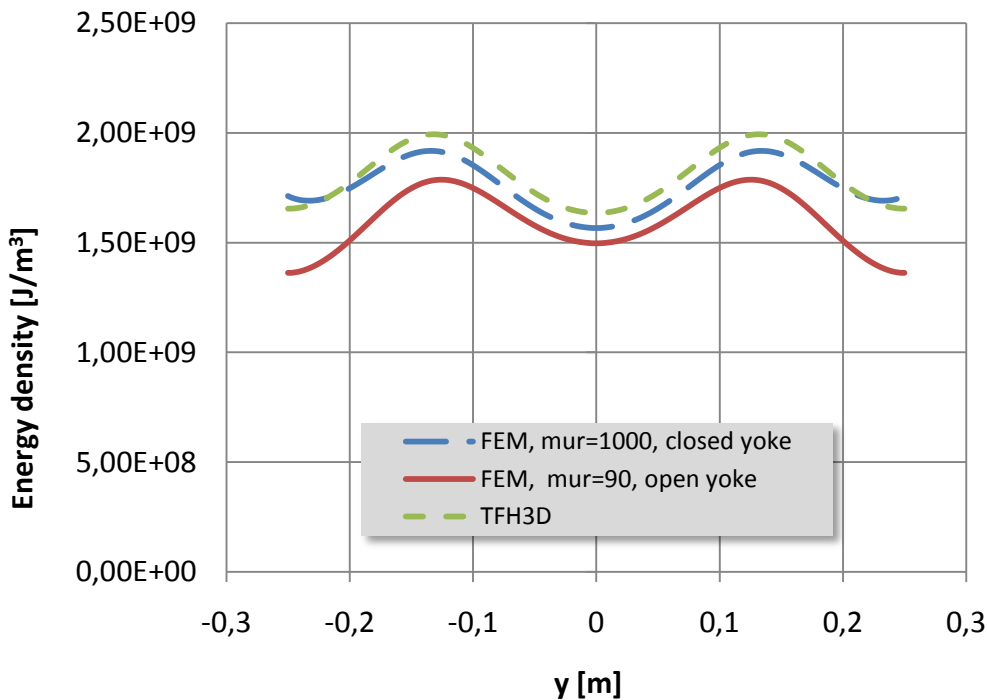

Fig. 4.1: Comparison between FEM and TFH3D energy density profiles at the inductor exit

4.1.2 Optimization Problem

The difficulty of optimization of the multi-coil inductor optimization derives from the intimate relationship between electrical and geometrical parameters i.e. the same effect can be obtained either from a current regulation or from a geometrical shape

change. Since the system should be capable of heating strips of different widths, a step-by-step procedure has been adopted [45].

The design process has considered three typical strip widths (500, 600 and 800 mm), optimizing the inductor with two or three coils, starting from the narrower one, and proceeding by adding coils to cover the larger widths. The problem of the temperature uniformity at the exit section of the inductor is the first main goal of the optimization, and depends on the energy $W(y)$ accumulated by each elementary volume of the strip while moving inside the inductor as described in section 3.2.

Some preliminary simulations have shown that the optimization of the uniformity as single objective tends to produce geometries with small coils and, as a consequence, the rather limited power transferred to the strip. Since the considered industrial process requires a temperature increase of 300°C/m, the injected power must be of the order of 200 kW for a strip of 1 m width and 1 mm thickness. The second goal is thus to maximize the power transferred to the strip. The amount of the transferred energy depends on the geometry of the coils, which determines the shape of the induced current density, and on the magnitude and phase of the current flowing in each coil. The coils can be described by their length and width, and each coil consists of several turns with their own dimensions. The turns of the actual inductor are composed by rectangular shaped copper tubes, in order to allow for the water cooling.

The following consideration must be taken into account for defining suitable constraints:

- The cooled copper has a maximum allowed current density to avoid overheating. As a consequence the value of the maximum allowed current in the coils depends on the dimensions of the turns

- The total width of the inductor cannot exceed the strip width (constraint given by the TFH3D model)

- Coils cannot overlap

- The internal coil must be large enough to allow for the turns bending

- The maximum voltage of each coil cannot exceed the maximum available supply voltage (500V). The voltage can be computed on the basis of the impedance matrix that depends on the geometry and on the number of turns

The constraints are taken into account by the optimization procedure by penalizing the objective in case of constraint violation.

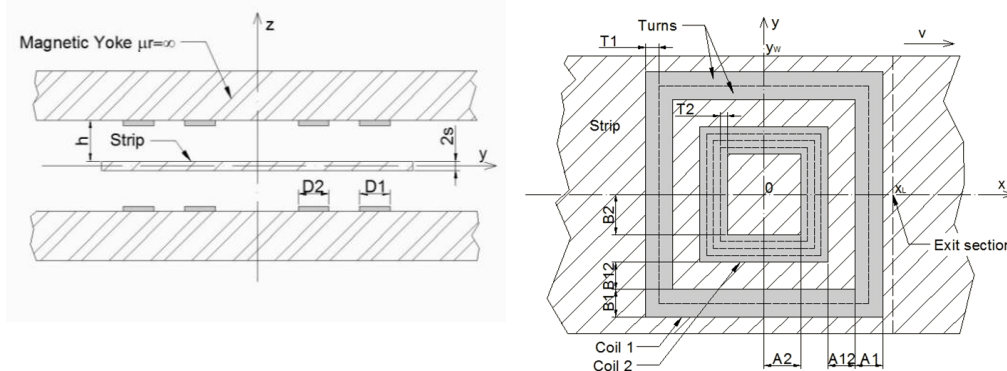In Tab. 4.1 and Fig. 4.2 the main parameters of the optimizations are indicated.

Fig. 4.2: Side and top view of the MC-TFIH, with optimization parameters

Parameter	Description
A12	Distance between coil 1 and 2 in the x direction
B12	Distance between coil 1 and 2 in the y direction
A2	Internal half-width of coil 2 in the x direction
B2	Internal half- width of coil 2 in the y direction
T1, T2	Thickness of the turn conductor of coils 1 and 2.
N1, N2	Number of turns of coils 1 and 2
J1, J2	Current density of coils 1 and 2

Tab. 4.1: Optimization parameters

4.1.3 **Results**

In the following subsections the results concerning the optimization of 2-coil and 3-coil heating inductors applied to strips of different widths are presented.

System with 2 coils, 500 mm strip

At first the feasibility of heating a 500 mm wide strip with two coils has been analyzed. The ten parameters to be determined are summarized in Tab. 4.1.

The constraint on the minimum required power was 60kW and on the maximum allowed deviation on the uniformity was ±20%. This means that the optimizer reject the solutions not satisfying these requirements. These constraints reduce the search space of the optimization algorithm in order to focus the solutions in a suitable range close to the power and uniformity requirements. As it can be seen from the Pareto front shown in Fig. 4.3, for a considered power of 100 kW the minimum found deviation is of the order of ±10%; for higher power the deviation increase. It can be observed with the chosen maximum current density, the target uniformity (<±3%) cannot be reached with this configuration at the minimum required power. Accepting a lower power i.e. reduction of the performance of the inductor, a better uniformity can be reached. This is mainly due to the limitations given on the parameters A2 and B2 which, because of the building constraints, cannot be smaller than certain values (A2>25mm, B2>50mm). The optimizer tries to reduce these dimensions, but because of the large air-gap between the coils and the strip, the ratio between transferred power and current ratio is very low, and the current needed to improve the profile would be too high for the cooling system.

System with 3 coils, 500 mm strip

In order to achieve the desired goals, a three-coil configuration has also been examined. Fig. 4.4 shows a comparison between the Pareto fronts obtained with two and three coils, and it can be seen that the even this solution does not improve substantially the performance of the inductor.
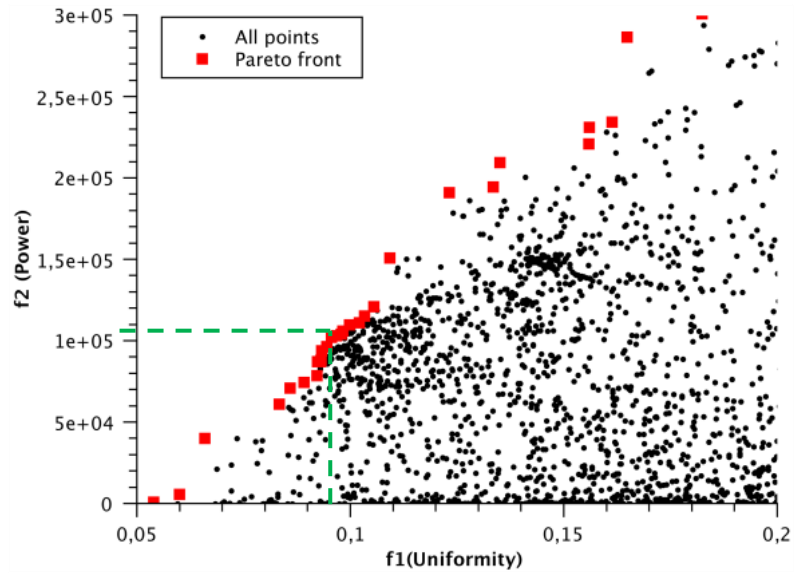
Fig. 4.3: Pareto front for the 2-coil inductor, 500mm strip
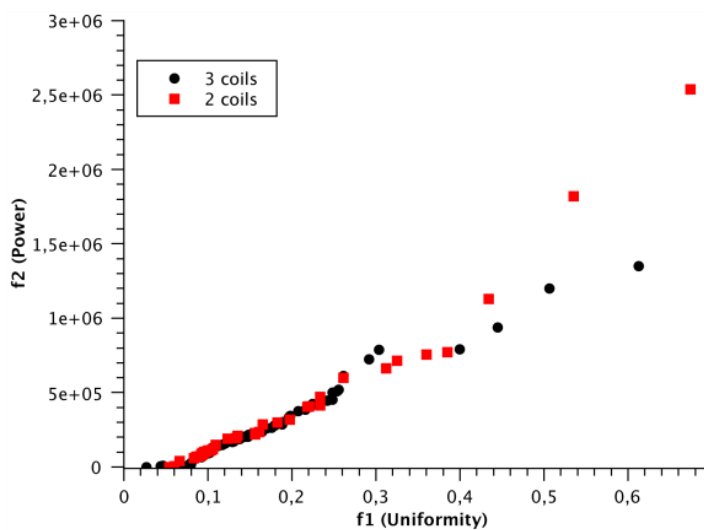
Fig. 4.4: Comparison of Pareto fronts for 2-coil and 3-coil cases, 500mm strip

System with 2 coils, 600 mm strip

Having noted that, due to the constraints, the 500 mm strip cannot be heated with the required uniformity at the desired power level, a 600 mm wide strip has been considered. In this case the two-coil system can reach very good performance, i.e. a ±2% uniformity at a power exceeding the requirements. The Pareto front for this case is shown in Fig. 4.5.
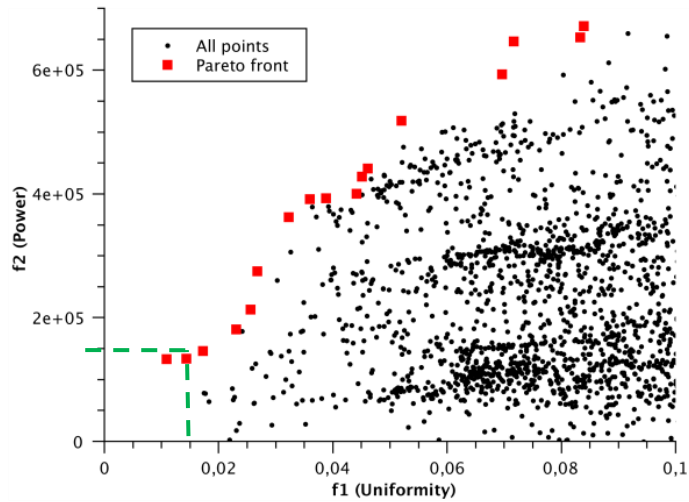
Fig. 4.5: Pareto front for the 2-coil case, 600mm strip

System with 3 coils, 800 mm strip

To show the possibility of heating strips of different width with the same inductor, the geometry of the previous two-coil solution has been fixed and a third coil has been added and optimized for a 800 mm wide strip. The optimization parameters in this case are the geometrical dimensions of the third coil, and the currents in the three coils. Also in this case good performance can be reached with very high power levels, as shown in Fig. 4.6 .
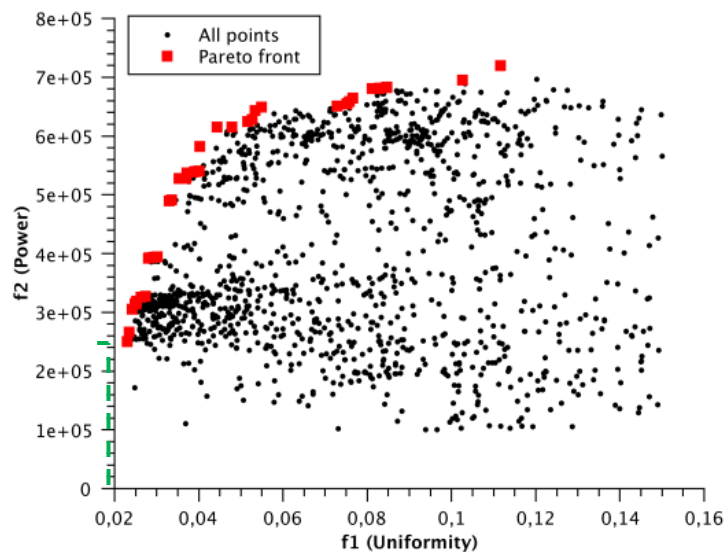
Fig. 4.6: Pareto front for the 3-coil case, 800mm strip

4.1.4 Possible technological solutions

Tab. 4.2 summarizes the results of a selected possible technological solution derived from the previous optimizations. It can be noted the high number of degrees of freedom (DOF) i.e. the number of parameters of the optimization problem.

Quantity	2 coils 500mm		2 coils 600mm		3 coils 800mm		
	Coil1	Coil 2	Coil 1	Coil 2	Coil 1	Coil 2	Coil 3
I [A]	96	3000	2002	1140	1079	1549	535
A [m]	0.148	0.025	0.097	0.025	0.240	0.097	0.025
B [m]	0.221	0.087	0.207	0.066	0.314	0.207	0.066
D [m]	0.012	0.090	0.044	0.060	0.028	0.044	0.060
N	1	3	2	4	2	2	4
V [V]	63	291	259	208	278	215	116
Δ E%	9.78%		1.71%		2.3%		
Induced Power [kW]	104		146		250		
DOF	10		10		7		

Tab. 4.2: Results of geometry optimizations for a strip 600 and 800 mm wide. (I: currents, A,B: half width of coil in x and y direction, D: total coil width, N: Turn number, V: supply voltages, ΔE% :Deviation of the energy profile, D.O.F.: Number of degree of freedom of the optimization problem)

4.1.5   Thermal analysis and verification of the results

In order to validate the results of the optimizations several thermal simulations have been performed. The thermal simulations can be done using either by a complete FEM coupling, or by using a finite difference method applied to the FEM magnetic computations by the Fluxgrid software expressly developed for this purpose (see Appendix A).

The FEM simulation has been performed with the package Flux 3D. Since a complete model, considering the eddy currents in the coils, would take a long time to be solved, a simplified magneto-thermal model that make use of non meshed coils, has been used. This model allows computing the initial magnetic field produced by the coils, by a semi-analytical method based on the Biot-Savart law. It has to be underlined that in this way the eddy currents in the coils are not computed and as a consequence a lack of accuracy in the computation exists. The FEM model considers a coupled magneto-thermal analysis. The movement of the strip is simulated by a moving mesh. An image of the final temperature distribution of the thermal transient for the 800 mm strip is shown in Fig. 4.7 in which the new values of the optimized currents are also indicated.

The method used in Fluxgrid has as an advantage the reduced simulation time. This software has the capability of optimize the currents by means of the current density patterns of the different coils issued by other software such as Flux 3D or JMAG. The advantage of this method is that the electromagnetic solution has to be computed only one time for each coil and for each strip width before performing the optimization. Fluxgrid allows also the computation of the profile of energy density at the exit of the inductor and the calculation of the electrical parameters. Moreover the finite difference solver of TFH3D has been coupled with the electromagnetic solution in order to allow the evaluation of the heating times and the temperature profiles in a very short simulation time.

In figure Fig. 4.8 a comparison between the calculated temperature profiles in the 2 cases is shown. The temperature profile has also been compared with the energy profile obtained by Fluxgrid. It can be seen that globally the temperature levels are in

good agreement, and the differences between the two methods are less than 3%. The currents are the same computed in with TFH3D. As previously noted, TFH3D under-estimates the temperature profiles near the edge of the strip.

As emerged from the experience, it is always possible to obtain a final uniform temperature distribution using the geometry of TFH3D and a new set of currents obtained by a new optimization that make use of a more realistic model of the inductor, in this case a FEM model with stranded coil conductors. This will be further investigated in the next chapter with reference to the final inductor.
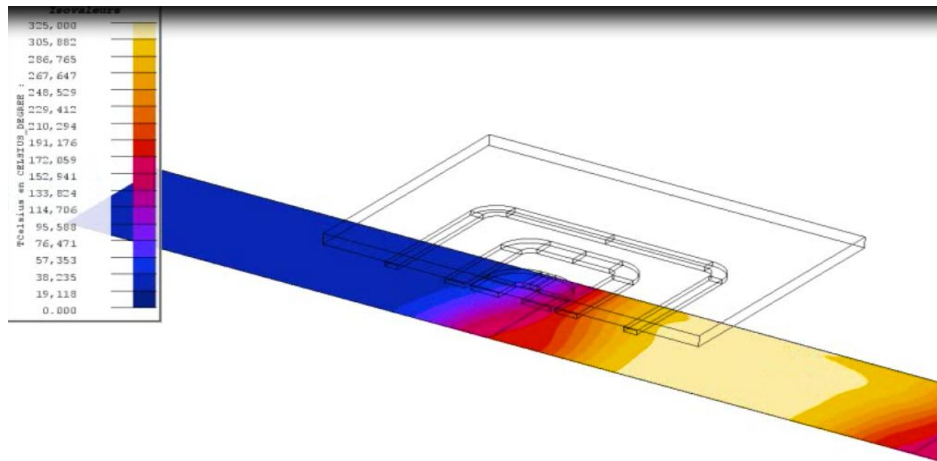

Fig. 4.7: Final temperature distribution for a strip 800 mm width with the following supply currents: I1=1079, I2=1549, I3=535
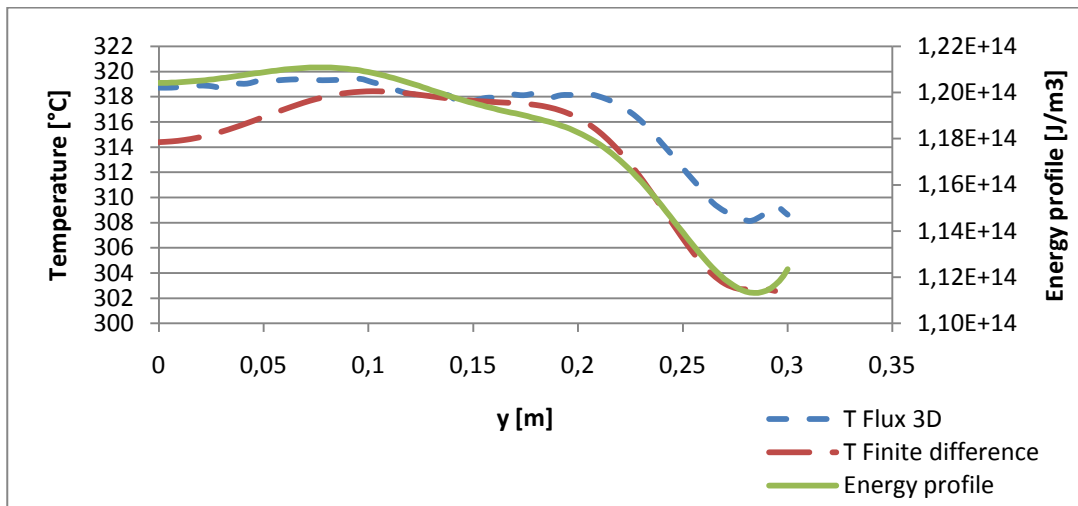

Fig. 4.8: Temperature profile obtained with FEM and finite difference methods, and energy profile for a strip 600 mm wide with the following supply currents : I1=0, I2=2002, I3=1140

4.2 Extension of the results of the optimizations to a wider inductor

The results of the Chapter 3 have allowed us to understand that the importance of the geometric shape of the coil is less important, when the number of the coils that has influence on the strip is large. This means that in multi-coil inductors, the critical part of the optimization is of finding the best coils configuration for the narrower dimensions of the strip and therefore the dimension of the most internal coils. As a consequence a new optimization has been performed, with the method described at the paragraph 4.1, in order to optimize the geometry of the three smaller coils, capable to heat strips of 800 mm.

Concerning the resonant circuit, differently from the case of the circular inductor and because of the characteristics of the inverters given by the manufacturer, it was decided to use the series resonant scheme. The voltage specifications of the supply was a maximum voltage of 500 V. Due to the existence of resonant capacitor bank connected to each coil, the voltage of the inductor can increase, with respect to the inverter voltage, in a ratio in first approximation equal to about the quality factor ($QF = Q/P$) of each coils. Considering a quality factor value of about 3 for the coils and a coefficient for the voltages, which takes into account the approximation introduced by TFH3D, the maximum voltage admitted at the terminals was set to 1000V. Since a maximum current per turn of 1000 A was fixed also a constraint on the currents was introduced. Moreover since each coil has a different quality factor, it was difficult to give a precise constraint on the voltage ratio between inverter and inductor.

The optimization performed with the new constraints and with the same objectives as in paragraph 4.1, i.e. maximum uniformity of temperature and maximum induced power, has given the results shown in tab. 4.3.

The following step has been to fill the remaining space between the 800 mm strip and the 1200 mm strip with three more coils in order to cover the most external zones to heat, in the case of large strips. The number of turns of the coils 1, 2 and 3, were chosen in order to not exceed the maximum voltage allowed. The characteristics of the coil turns are indicated in Tab. 4.4 and the resulting geometry is schematically shown in Fig. 4.9 and Fig. 4.10.

A number of computations have been done in order to verify the performance of this inductor for the strip widths indicated in the table. The computations have been done by means of Flux 3D in order to obtain the impedance matrix and the current density patterns (sec. 3.3.1). An optimization for each strip width has been done with the software Fluxgrid, in order to obtain the best possible energy density profile.

Some result of these optimizations, concerning the geometry of Fig. 4.9, is shown in Tab. 4.5-Tab. 4.7. These results show the power that can be expected by the six-coil inductor and the uniformity of the final temperature profile. The possibility to reach about 600 kW, with the given constraints on the currents, has been verified for all the considered dimensions of the strips. The energy unevenness results lower than ±2% as required by the specifications.

The computation of the electrical efficiency η_e has been done "a posteriori" by Fluxgrid, computing the ratio between the induced power in the strip, given by integration of the power density, and the absorbed power, calculated by the impedance

matrix. As expected, the efficiency is lower for the strips of small size when the heating coils having influence on the strip are the smallest ones, which have a lower efficiency in comparison with the larger ones. However in any case the electrical efficiency values can be considered satisfactory for a TFH installation.

The currents computed by the optimization procedure have been obtained without criteria on the distribution of the power in the individual coils; as a consequence the currents and voltages value are unevenly distributed among the inverters. This can give some problems for the control of the power supply. Moreover in Tab. 4.7 it can be seen that the set of capacitors necessary to make resonate the coil circuits should be modified quite a lot, when heating different strip width. This could increase notably the cost of the system and could make it less flexible loosing the initial advantages of this technology.

Quantity	3 coils 800mm		
	Coil 1	Coil 2	Coil 3
I [A]	777	806	724
A [m]	0.320	0.138	0.043
B [m]	0.329	0.223	0.071
D [m]	0.030	0.058	0.090
N	3	5	9
V coil [V]	642	960	855
P [kW]	262877	306927	174971
Q [kvar]	424474	710814	593979
Q factor	1.615	2.316	3.395
Cap series [uF]	151	97	93
V inverter [V]	338	380	241
Profile Uniformity	±0.78%		
Strip Power P [kW]	718		
Efficiency η%	95 %		

Tab. 4.3: Results of geometry optimizations with TFH3D and Tribes, for a strip between 800 mm width. (I: currents, A,B: vector of half width of coil in x and y direction, D:vector of total coil width N: vector of coil numbers, V: vector of supply voltages)

Coil n.	1	2	3	4	5	6
Turn Nb.	2	2	2	3	5	9
Width [mm]	15	15	15	10	10	8
Height [mm]	10	10	10	10	10	10

Tab. 4.4: Turns number, width and height of turns for the coils of the optimized inductor.
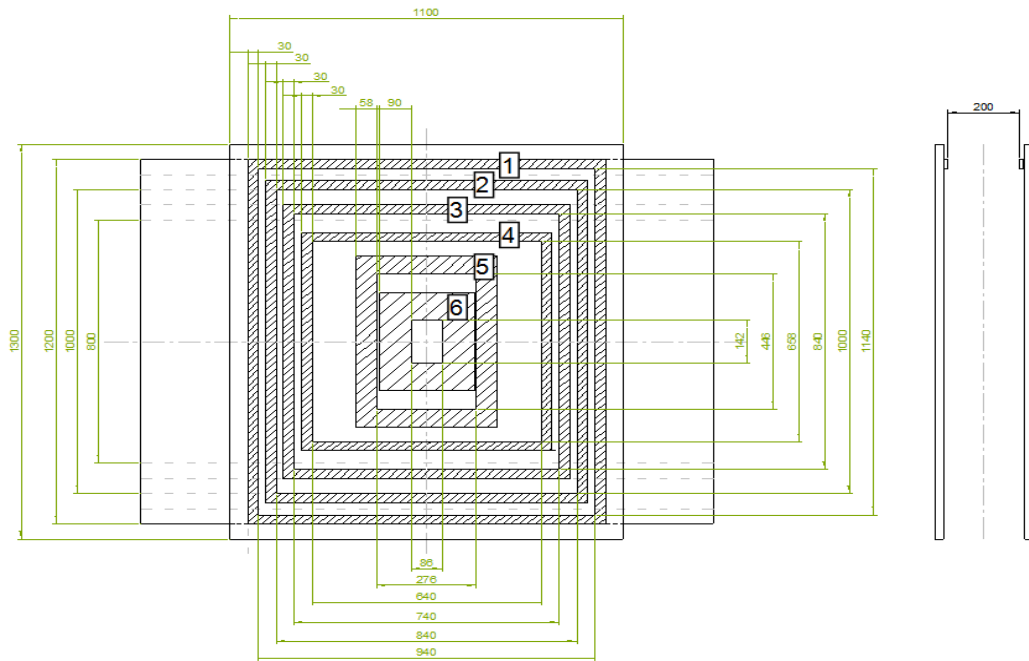
Fig. 4.9: General dimensions of the installation
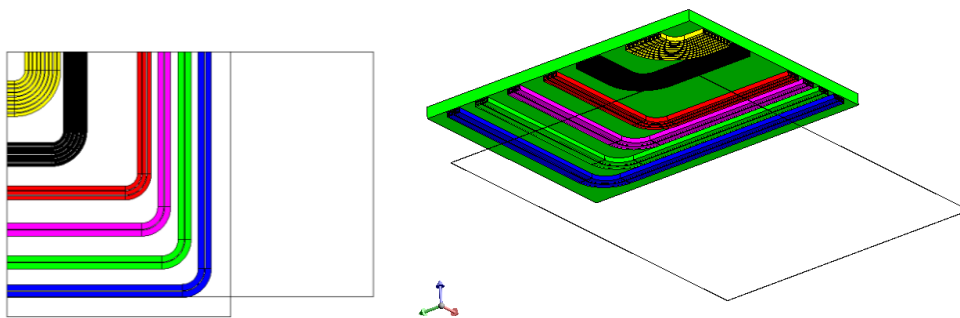
Fig. 4.10: Details of the coils

W [mm]	Energy Deviation	P [kW]	η %	I1..I6 [A]					
800	±1,1%	636	84	102	28	22	497	938	764
900	±1,5%	630	87	114	2	273	478	829	562
1000	±1,08%	623	90	40	196	368	429	713	406
1100	±1,6%	624	92	208	231	318	479	510	385
1200	±1,36%	618	93	432	113	445	222	719	37

Tab. 4.5: Uniformity of the temperature and max power obtained with geometrical optimization of the inductor on a steel strip 1 mm thick, and the corresponding values of optimized currents.

W [mm]	V1..V6 [V]					
800	228	238	265	542	916	656
900	252	267	350	554	801	514
1000	255	348	398	538	686	399
1100	352	389	392	538	557	348
1200	447	376	402	428	564	181

Tab. 4.6: Coil voltages corresponding to the optimized current values of Tab. 4.5

W [mm]	C1..C6 [µF]					
800	110	30.8	22.4	147	116	127
900	114	1.5	192	138	118	120
1000	41.4	139	223	129	120	114
1100	143	145	198	143	109	124
1200	225	75.1	267	89.2	148	25.8

Tab. 4.7: Resonant capacitor values corresponding to the optimized current values of Tab. 4.5

4.3 Final inductor

In the previous paragraph a prototype of multi coil inductor having very good performances has been designed and analyzed. However this inductor can be improved mainly concerning the load matching with the sources. It has been seen that the voltages of the coils for a given size of the strip are very different from one another. On the contrary, for a good behavior of the supply inverter it is convenient that the voltages are as much similar as possible. This can be done by adding some turns to the external coils and by optimizing the currents using only the coil having influence on the induced current density pattern, i.e. switching off the most external ones. Moreover, the dimensions of the copper tube forming the coils have been normalized to 10x10 mm. In this inductor it has been taken into consideration that the currents should be limited to 500 A according to the specifications of the power supply. The final inductor is shown in Fig. 4.11-Fig. 4.13. The complete characteristics of the final coils cannot be given because of confidentiality reasons.

The availability of the software JMAG has allowed to obtain FEM solutions of the electromagnetic problem in a reduced time compared with the Flux 3D software, at

the price of a more complex procedure to follow in order to construct and mesh the model [46]. The optimizations have been then performed with Fluxgrid, using the current density patterns obtained by JMAG.

The results of the new optimizations are shown in Tab. 4.6-Tab. 4.12. From the tables it can be noted that the voltages are more uniformly distributed among the coils, and that in some case the most external coils have been switched off for the narrowest strips. As a consequence also the capacitor values are closer among the different strips widths, allowing for a better flexibility of the system.

The values of the inverters voltages, reported in Tab. 4.10, results lower than the ones allowed by the inverter characteristics (500 V), allowing an increase of power once the inverters have been recognized as capable to deliver a higher current.

In any case the supply circuit is provided by voltage transformers in order to decouple the earth systems of the resonant load from the earth system of the inverter. For some inverter the voltage ratio will be 1, for other circuits, as the one supplying to the smaller coil, the voltage ratio will be different. In any case no further considerations on the transformers will be done because their characteristics will depend on the final power supply performance that is not available due to the confidentiality of the work.
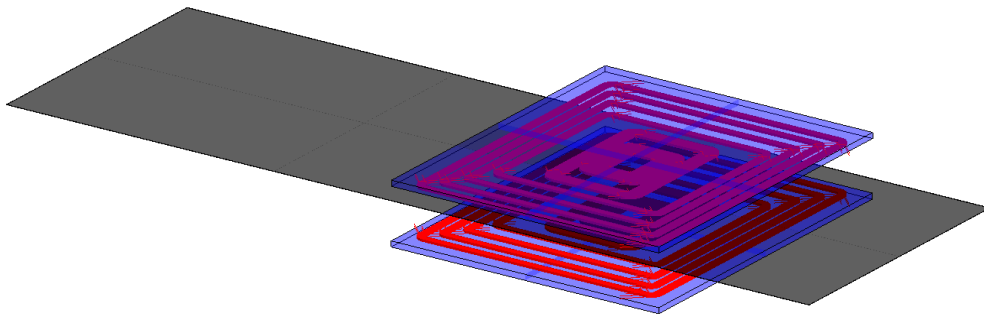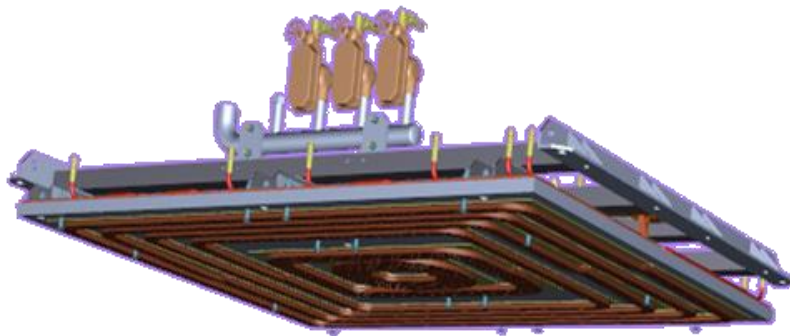

Fig. 4.11: Geometry of the final inductor

Fig. 4.12: Drawing of the final inductor

Fig. 4.13: Photo of the final inductor

W [mm]	Energy Deviation	P [kW]	η %	I1..I6 [A]					
800	±1.7%	230	85.2	-	-	121	318	500	500
900	±1.36%	346	87.4	-	-	398	394	494	495
1000	±1.2%	523	89.9	-	355	362	487	500	500
1100	±1.3%	678	91.9	180	498	422	492	497	408
1200	±1.64%	693	93.3	500	497	298	450	489	229

Tab. 4.8: Uniformity of the temperature and max power obtained with geometrical optimization of the final inductor on a steel strip 1 mm thick, and the corresponding values of optimized currents.

W [mm]	V1..V6 [V]						φ1..φ6					
800	(155)	(199)	271	433	609	388	(46)	(48)	55	59	66	71
900	(220)	(291)	430	555	629	389	(47)	(51)	60	60	65	70
1000	(351)	511	527	663	656	396	(53)	59	58	59	63	69
1100	512	653	609	709	642	348	58	61	58	58	61	67
1200	679	689	565	656	583	249	62	61	56	57	61	62

Tab. 4.9: Coil voltages corresponding to the optimized current values of   Tab. 4.5 for the final inductor.

W [mm]	C1..C6 [V]						Vco1..Vco6					
800	-	-	57.7	90.6	94.7	144	-	-	155	222	241	126
900	-	-	113	87.3	92.3	144	-	-	215	280	269	134
1000	-	85.6	85.5	90.8	90.9	143	-	260	275	339	300	144
1100	44.1	92.9	86.4	86.6	93.5	135	275	321	320	373	307	138
1200	88.0	87.8	67.6	86.9	101	110	313	338	316	357	280	115

Tab. 4.10: Resonant capacitor values and inverter voltage (Vco) corresponding to the optimized current values of Tab. 4.5 for the final inductor.

W [mm]	P1..P6 [kW]						Q1..Q6 [kvar]					
800	-	-	18.7	70.6	120	63.2	-	-	26.8	118	280	183
900	-	-	85.7	110	133	66.6	-	-	148	188	280	180
1000	-	92.4	99.7	165	150	72.1	-	156	162	277	291	184
1100	49.5	160	135	183	152	56.6	77.8	283	218	296	280	130
1200	156	168	94.1	160	137	26.4	301	298	139	247	249	50.5

Tab. 4.11: Values of active and reactive powers corresponding to the optimized current values of Tab. 4.5

W [mm]	QF1..QF6 [V]					
800	-	-	1.43	1.67	2.32	2.90
900	-	-	2.10	2.71	1.73	1.71
1000	-	1.69	1.63	1.68	1.94	2.56
1100	1.57	1.77	1.62	1.61	1.84	2.30
1200	1.92	1.78	1.48	1.54	1.82	1.91

Tab. 4.12: Power factor values corresponding to the optimized current values of Tab. 4.5

4.4 Use of the 2D analysis for the computations

The analysis performed with 3D software allows to reach a high degree of precision in the computations of the induced power and the electrical parameters of the inductor. However they are large time consuming; for example, to make an optimization of the currents in a 6 coils inductor only for one width and thickness of the strip, six computations of a complete 3D model have to be performed. From the Tab. 3.4, in which typical calculation times for each kind of model are shown, it can be understood that the optimizations take a huge calculation time. Moreover the large quantity of data processed is liable of producing errors, and each 3D model needs long user time for constructing the mesh due to the complexity of the geometry, in particular when the materials and shape of the coils are considered.

A simplification of the model in order to reduce the development time is therefore needed. Furthermore, the simulations concerning the electronic power supply are performed using circuit simulators in the time domain [4], which need models that allows a good characterization of the multi-coil load. For a first approach the model represented by the impedance matrix can be used, but, considering the filter effect on voltages and currents given by the mutual coupling at the different frequencies, some more complex models have to be considered. In the last years nearly all FEM commercial packages allow the coupling with circuit simulators. This is the case for example of Flux-Portunus, or JMAG-PSim.

In the following the use of 2D FEM software to compute the values of the magnetic field in the air regions and in the magnetic concentrator will be described. The possibility to couple Flux 2D with Portunus has been verified and it has been found to be effective. However the results will not be presented due to the confidentiality of the work. In any case some consideration on the induced power in the strip, produced by the harmonic content of the current, will be done.

A 2D axi-symmetric model with massive coil conductor similar to the one used of par. 2.2.1 has been built in order to have nearly the same impedance matrix of the original one. The 2D equivalent model considers the same turns and coil number of the final geometry of the inductor. This has been reached by considering a circular inductor with coils which have the same surface of the rectangular ones. The dimensions of the coils are indicated in Tab. 4.13. A comparison among the 2D model and the other 3D models previously used is shown in Tab. 4.14 in which a quite good correspondence among the electrical supply values can be seen.

Coil N.	D [mm]	2A [mm]	2B [mm]	Equivalent radius [mm]
1	30	1140	940	601
2	30	1000	840	534
3	30	840	740	461
4	30	658	640	383
5	58	448	276	231
6	90	142	86	114
	Strip diameter:	1250		

Tab. 4.13: Dimension of the equivalent circular model corresponding to the final optimized inductor.

W [mm]	Energy Deviation	P [kW]	η %	V1..V6 [V]					
Stranded JMAG 3D	±2.06%	734	96.9	717	727	589	689	637	275
Massive JMAG 3D	±1.64%	693	93.3	679	689	565	656	583	249
TFH3D	±24%	1022	96.8	849	795	663	757	741	367
Massive Flux 2D	-	734	94.8	684	684	555	647	559	258

Tab. 4.14: Comparison of different models of the inductor with the following supply currents: I1..I6: 500,497,298,450,489,229

4.4.1 Stray fields

According to the law, an electromagnetic device must be designed in order to protect the user from stray electromagnetic fields at high frequency. In the European Directive 2004/40/EC of the European Parliament on the minimum health and safety requirements regarding exposure of workers to the risks arising from physical agents (electromagnetic fields), the limits for the human expositions to the magnetic fields are given. The limits as a function of the frequency are shown in Tab. 4.15.

The 2D equivalent model can be used in order to compute the electromagnetic fields in the regions around the inductor as well as in the magnetic flux concentrator, in order to verify the magnetic saturation of the material.

From the Fig. 4.14 the respect of the limits on the flux density for the Fluxtrol material (section. 3.5) can be seen.

Considering the surrounding air as in Fig. 4.15 it can be seen that the limits of the Tab. 4.15 are satisfied at a distance of more than 2 m from the magnetic concentrator.

Frequency [Hz]	Flux density field [mT]	Electric field [kV/m]
0 - 1Hz	$2x10^5$	-
1 - 8 Hz	$2x10^5/f^2$	20 000
8 - 25 Hz	$2,5x10^4/f$	20 000
0,025 - 0,82kHz	25/f	500/f
0,82 — 2,5 kHz	30,7	610
2,5 - 65 kHz	30,7	610
65 - 100 kHz	2000/f	610
0,1 - 1 MHz	2/f	610
1 - 10 MHz	2/f	610/f

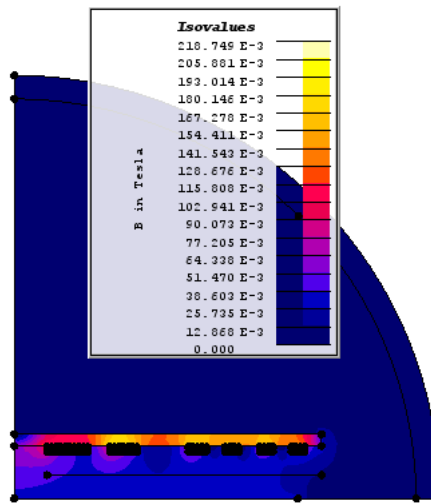**Tab. 4.15: Exposure limit values for the electromagnetic fields in the industry**
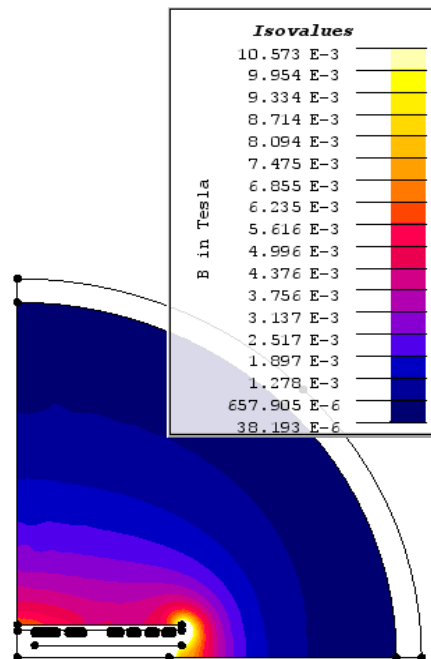

Fig. 4.14: Magnetic flux density in the domain

Fig. 4.15: Magnetic flux density in the surrounding air

145

4.4.2 **Harmonic analysis**

As already seen, the resonant coil-capacitors is supplied by square wave currents as shown in Fig. 4.16. The harmonic content of the phase shifted voltage wave is given by the following formula [4]

$$E_n = \frac{4}{n\pi}\cos(n\alpha) \cdot E \tag{4.1}$$

where E_n is the magnitude of the harmonic , n is the harmonic number, α is the switching delay of the square wave and E is the reference continuous voltage of all coils.

The harmonic content could induce a supplementary power in the strip that could modify the resulting temperature profile. Several successive simulations on the 2D model have been performed in order to evaluate this additional induced power. These simulations have been done applying the voltage resulting from a Fourier decomposition of the supplying square waves and evaluating the induced power in the strip. The results in Tab. 4.16 show that the additional induced power is negligible in comparison to the power induced by the first harmonic. This is due to the double filtering effect of the resonant circuit RLC and the diffusion of the electromagnetic fields in the massive conductors.
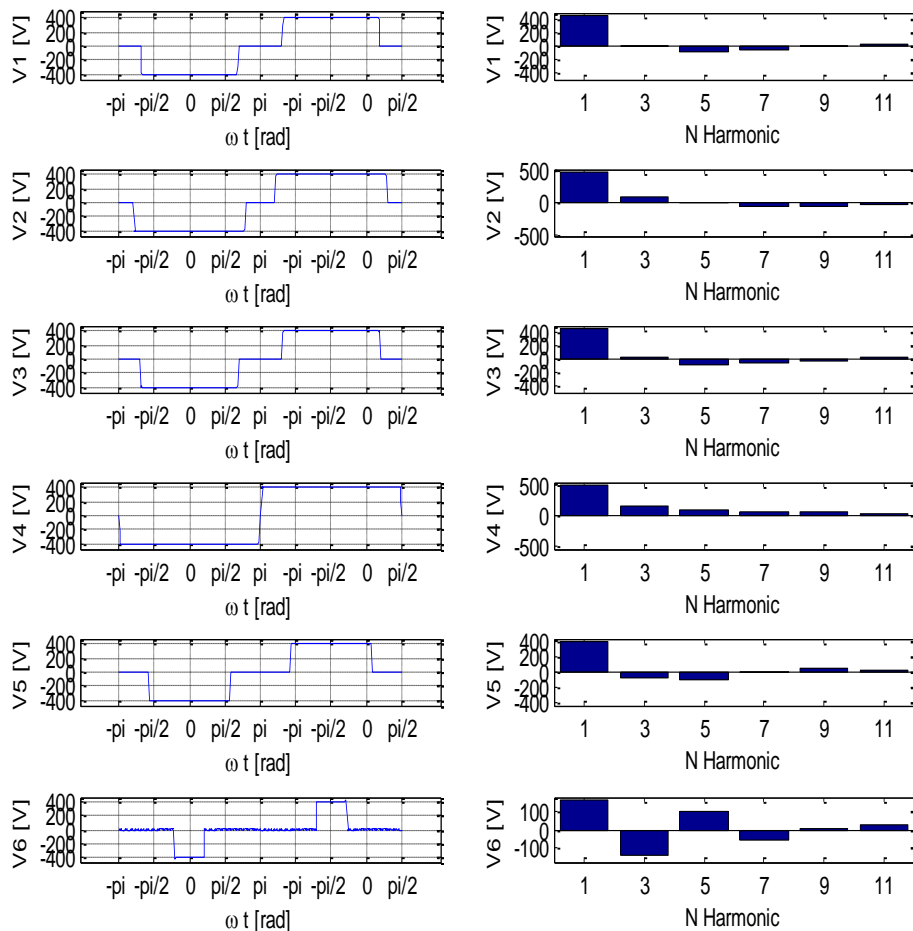

Fig. 4.16: Example of inverter voltages form with harmonic decomposition.

f [Hz]	V1	V2	V3	V4	V5	V6	Pstrip kW
1500	316	351	334	385	285	126	770
4500	8.4	65	13	118	-50	-99	1.8
7500	-56	-5	-53	70	-70	70	0.2
10500	-47	-33	-48	50	-1.4	-37	-

Tab. 4.16: Induced power corresponding to the voltages and frequency of the square wave inverter supply

Yoke Losses computations.

In addition to the total losses due to the eddy currents in the coils, the losses in the electromagnetic concentrator must be considered. For the evaluation of these the 2D model results useful another time. For the case of Tab. 4.14 the resulting losses in the two magnetic concentrators are of 4086 W. This value is practically negligible in comparison with the total induced power in the strip, equal to 770 kW.

4.5 Thermal analysis

Also for this final inductor some magneto-thermal computations have been performed. In Fig. 4.17 the result of the thermal transient at the time 5.1 s, for a 1100 mm strip width is shown. The resulting deviation of the temperature profile at the exit section in respect to the main uniform value results of ±1.56% and the corresponding profile is shown in Fig. 4.18. The deviation result below the value of ±2 % required by the specifications.
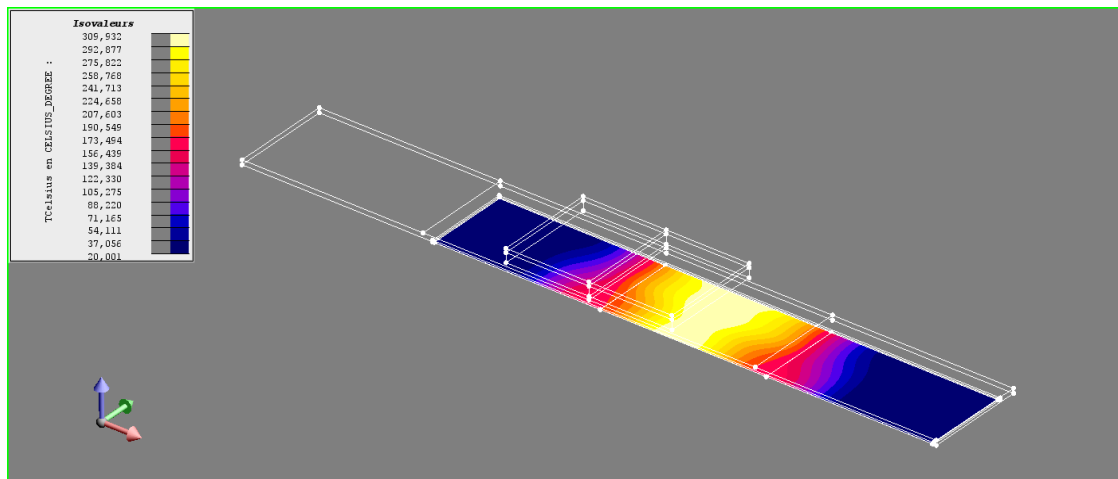

Fig. 4.17: Distribution of the temperature in the strip after a transient of 5.1 s for a 1100 mm strip.
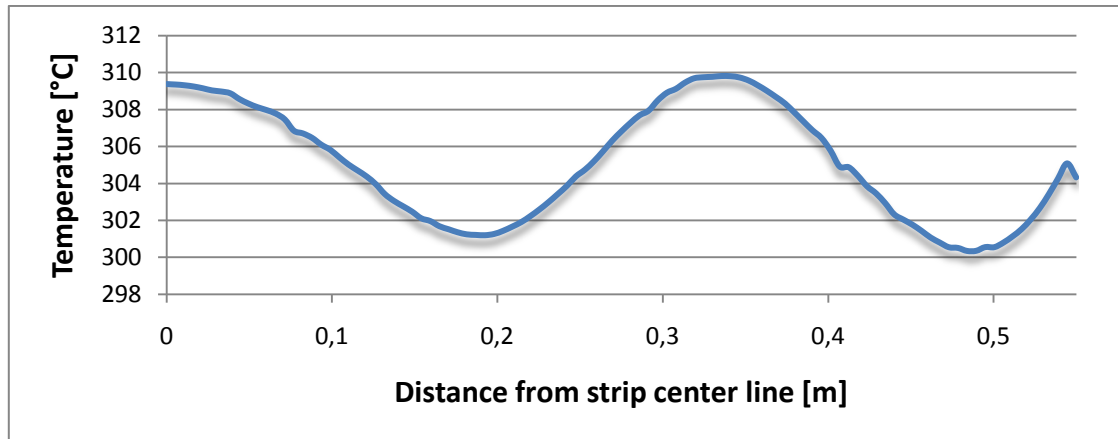
Fig. 4.18: Temperature profile at the exit section of the inductor for the thermal analysis of Fig. 4.17

4.6 Conclusions

In this chapter the optimization of a MCH device has been considered. It has been experienced that the initial goal of heating strips of widths between 500 mm and 800 mm cannot be achieved with the considered air-gap and under the given constraints and that a minimum width of 600 mm must be accepted. In any case in the industry it is difficult to find the heating of such narrow strips with so large air-gaps. The final industrial prototype has been therefore designed to heat strips of width ranging between 800 and 1200 mm. It has been recognized that the inductor geometrical optimization is critical for the narrowest strip width, while for larger strips the non-uniformity given by the non optimal geometrical configuration can be easily compensated by an optimization of the excitation currents. In the last part of the chapter the performance of the final inductor has been described. The data show that the inductor satisfies the expected technical specifications. The inductor in its final configuration has been built, but not tested, because the power supply was not finalized and the mechanical support structure was not ready.

Conclusions

The work described in the thesis was aimed to realize a multi-coil transverse flux inductor for the heating of stainless steel strips.

Since the multi-coil inductors are a variant of the classical TFH inductors, the first part of the thesis was devoted to analyze the current knowledge about this technique. The analysis of TFH allowed to understand which are the variables having influence on the heating and on the electrical characterization of the system. An extended analysis of the existing solutions of TFH capable to reach a uniform temperature of the strip at the end of the heating process has been done in order to be compared with the new MCH process. Furthermore an overview on the computation methods that have been used to compute the solution of the Maxwell equations in TFH and MCH problems has been done.

The MCH technique was formerly known as ZCIH from previous works, but a real industrial application had never been realized. For that EDF realized a prototype of inductor with three circular coils for the heating of steel discs supplied by independent inverters. Some theoretical works has been done but the inductor has never been tested. The second part of the work was then devoted to analyze the circular system and to characterize the inductor in order to be supplied by the inverters. Different computation methods have been tested and used in order to compute the impedance matrix of the inductor and the shape of the induced power patterns in the strip.

Some experimental tests have been performed by the researchers engaged on the analysis of the control system, using the computations and measurements results in order to calculate the characteristics of the control algorithm in open loop i.e. without automatic control of the inductor currents. The results of the tests resulted satisfactory and it was decided to apply the principle to a more complex induction heating system for heating strips in continuous movement. The intrinsic 3D nature of this system requires more complex models to be analyzed. If for a circular system a 2D axi-

symmetrical analysis was sufficient to optimize the temperature profile, for the more complex 3D system a so strong simplification is not possible. The complete heating transient must consider the effect of the movement of the strip on the final temperature profile. In the past some effective computation methods have been developed in order to simplify the computations for the classical TFH. For MCH these methods are still useful, but the contemporary existence of several independent currents in the coils, that have to be optimized, increases the complexity of the problem.

In chapter 3, after a description of the basic theory of MCH, the methods to compute and optimize the final temperature profile have been described. The analytical software TFH3D has been recognized as a good solution to reduce the computation time in the optimizations. Afterwards the FEM software Flux 3D has been used and coupled with the Tribes optimization algorithm in order to have a more precise solution of the electromagnetic problem. These methods have been applied for a feasibility study of an inductor capable to heat strips with width in the range 500-1000 mm.

Furthermore the use of a magnetic concentrator has been considered. Some geometrical characteristics and materials for the concentrator have been taken into account and several computations have been done in order to recognize the best solution. Among the different possibilities the magnetic material Fluxtrol LRM has been chosen because of the isotropy and linearity of its magnetic properties.

The analysis of this first inductor allowed understanding that the deviation from the uniformity of the energy profile becomes larger for narrow strips. Moreover the analysis of the optimization problem, performed by analytical and FEM models of different complexity has shown that the series of coil currents that optimize the temperature profile is not unique, giving different possibilities to the designer regarding the choice of the more convenient solution.

To overcome the problem of the increasing deviation on the energy and temperature profiles for narrow strips, in chapter 4 the optimization of the geometry has been considered. The MCH geometrical optimization is a complex matter, because of the interaction among electrical and geometrical parameters on the uniformity of the temperature.

At that time the specifications of the system have been modified in order to design an inductor that comply the requirement of the industry in terms of dimensions of the strip. Finally the optimization of an inductor capable to heat strips of widths between 800 and 1200 mm and a thickness of 1 mm has been done.

The performance of this final inductor has been successively analyzed with reference to the temperature uniformity and the load matching. In particular the currents have been optimized in order to use as much as possible the same capacitors when considering different strip widths.

The inductor has been finally built, but for reason of time and for the absence of a suitable supply system, still under development, it has not been tested.

However the results of the simulations show the very good performance of MCH system mainly as regards the temperature uniformity, the flexibility of the installation and the electrical efficiency. It has been recognized that performing an accurate coil design allows to obtain powerful systems with improved technological results.

Despite the quantity of work done on the inductor and the control system, a number of problems are still unsolved. The multi-coil inductor has to be tested in a pilot system in which the real performances will be verified. This is not yet possible because

the control system provided with real time temperature and current control will be finalized in the next years.

Regarding the future developments, the possibility to use MCH to heat magnetic materials has to be further investigated.

In conclusion it has been verified that MCH inductors can solve many of the existing problems of the TFH process and, although there is still a lot of work to do, a first concrete step has been done.

Appendix A

Software FluxGrid

The computation and optimization of the currents of a MCH inductor requires the treatment of a large amount of data. As described in the paragraph 3.3, the computation of the energy profile at the exit of the inductor is performed by superposing the pattern of the normalized current density induced in the strip by the different coil, scaled by the excitation currents of the coils. This means that for each inductor coil and for each dimension of the strip to be considered, a set of four patterns has to be memorized and treated. Moreover the information about the electrical characteristics of the system, i.e. impedance matrix, resistivity and velocity has to be stored in order to compute the supply parameters of the inductor in the different cases. The software Fluxgrid, developed under Matlab environment, has been implemented on order to perform these tasks with an integrated interface.

The main interface of Fluxgrid is in shown in Fig. A.1. The dialog is divided in different zones:

1. Work directory list
2. Parameter of the analysis
3. Import files of current densities and impedance matrix from FEM models
4. Single superposition module
5. Optimization module
6. Thermal module

In the following paragraphs the main functionalities of the software will be described.

Note: The Fluxgrid software is in alpha version. This means that the software is unstable and a lot of bugs exist. Moreover the software has not been tested for users with no programming abilities.
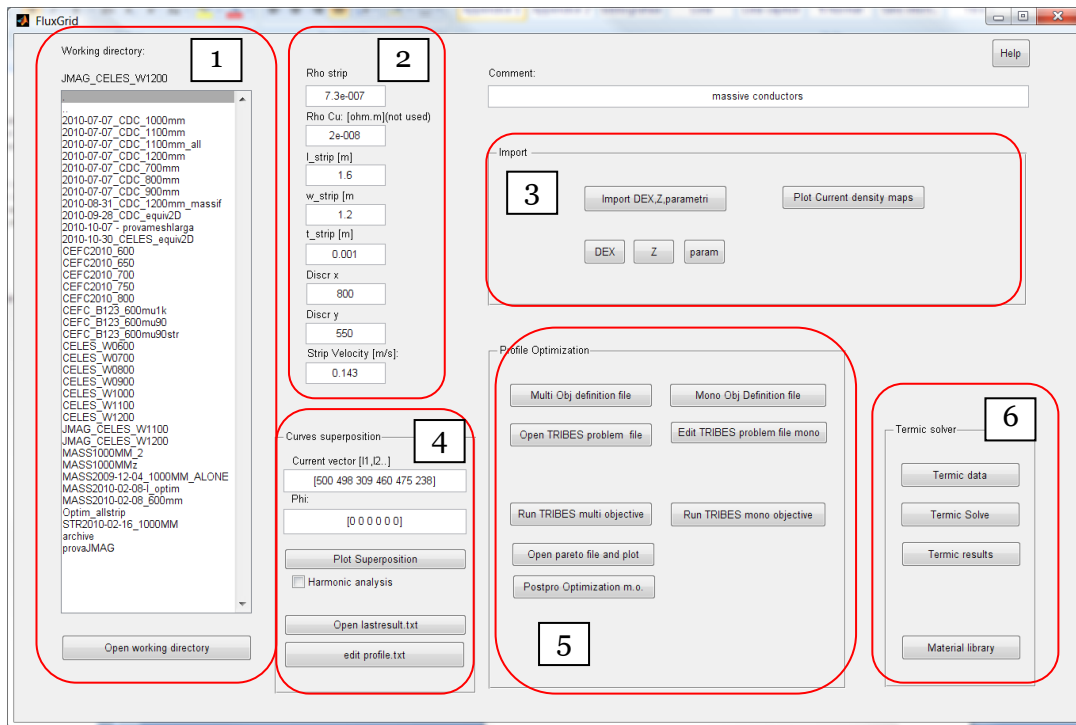
Fig. A.1: Main graphic user interface of Fluxgrid

A.1 Importing working files

The computation of the total current density uses the current density patterns computed by FEM software. The FEM software must export the values of the current density induced in the strip by each different coil and the impedance matrix in the text files "J_STRIP.DEX" and "tensioni_massive.dat". In the Flux 3D and JMAG codes, some macros have been implemented in order to make automatically the export action. The files relative to each coil must be copied in the projects directory under a project folder which will be shown in the projects list of the interface. The exported files of each coil must be copied in a subdirectory called "bobx" where x is the coil number. An example of the directory tree is shown in Fig. A.3. Afterward the directory created must be selected in the main interface with a double click.

The parameters of the strip must then be typed in the parameters zone of the interface. The strip zone considered in the FEM model makes reference to ¼ of the model. The dimensions of the strip indicated in the parameter zone make reference to the whole dimension of the strip. If the dimensions of the imported FEM model are larger than the inserted dimension, the software cut the computation surface of the strip and store only the part of the strip matching the indicated dimensions.

The importation is launched by the "Import DEX, Z, parameters" button. It consists in the interpolation of the data of the FEM mesh in a regular grid with the chosen discretization.

When the import is complete the imported files can be verified with the button "Plot current density maps" (Fig. A.2).
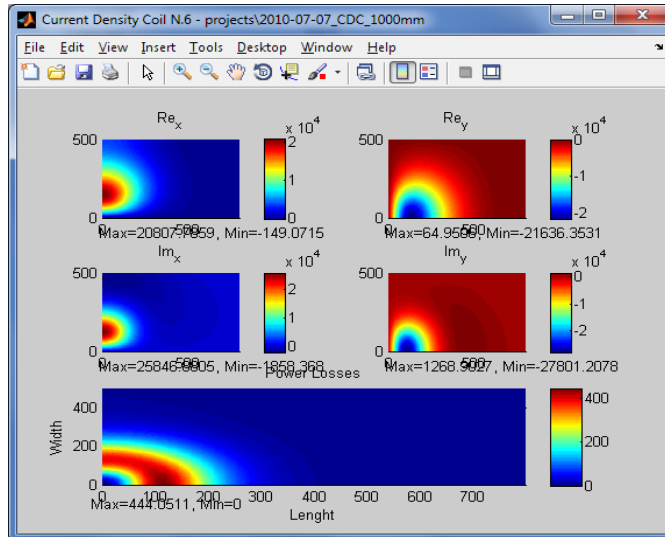
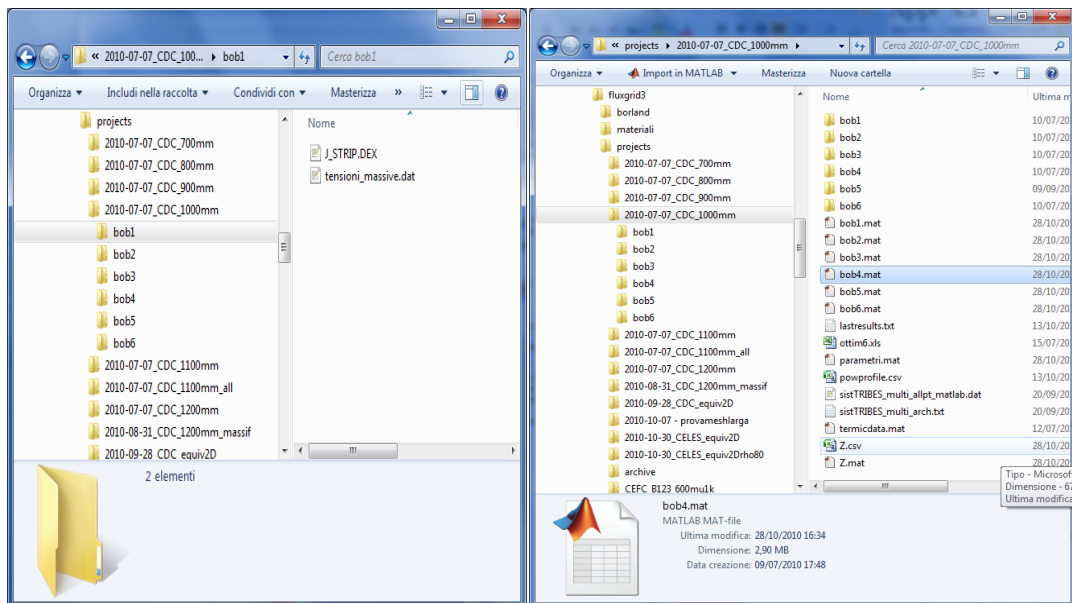**Fig. A.2: Example of imported current density pattern**

Fig. A.3: Project directory tree

A.2 Computation of energy profile

With the "Plot superposition module", the following results can be obtained:

- Energy profile

- Powers

- Efficiency

- Electrical values of the individual coils (Voltages, powers, resonant capacitors)

To obtain these results the value of the desired supply current in magnitude (rms) and phase must be inserted in the appropriate text box.

A.3 Current Optimization

The optimization module couples the Matlab superposition module with the Dos program Tribes.exe.

The settings of the constraints and of the search space of the algorithm can be done by means of two text files that can be opened by the two first button of the module:

- The file sistTRIBES_multi.m can be modified in order to choose the output values of the multi-object optimization as well as the constraints on the results.

- The file sistTRIBES_multi_problem.txt contains number and the limits of the optimization variables, and the number of the objective to optimize. The number of evaluation of the objective function must also be indicated.

The optimization starts with the button "Run Tribes multi objective".

The button "Open pareto file" opens the file that contains the pareto optimal solution.

The button "Postpro m.o." analyzes the file containing all the computation in order to recalculate the pareto front. The pareto front is ordered and shown as a diagram. The scatter plot of the deviation as a function of the current is also shown.

A.4 Thermal transient

The TFH3D finite differences thermal solver (see par. 1.5.1) has been coupled to Fluxgrid in order to compute the thermal transient related to the last energy profile computation. The button "thermal data" open the dialog of Fig. A.4 in which it is possible to insert the materials of the strip and of the refractory, and the simulation parameters.

The characteristics of the materials can be modified by the material library in the main Fluxgrid interface.

The computation of the thermal transient can be launched by the button "Compute" in the Thermal GUI or by the button Thermal solve in the main dialog, after saving the thermal data.

The button "Thermal results" opens the interface shown in Fig. A.5 from which the thermal transients and the thermal profiles can be shown.
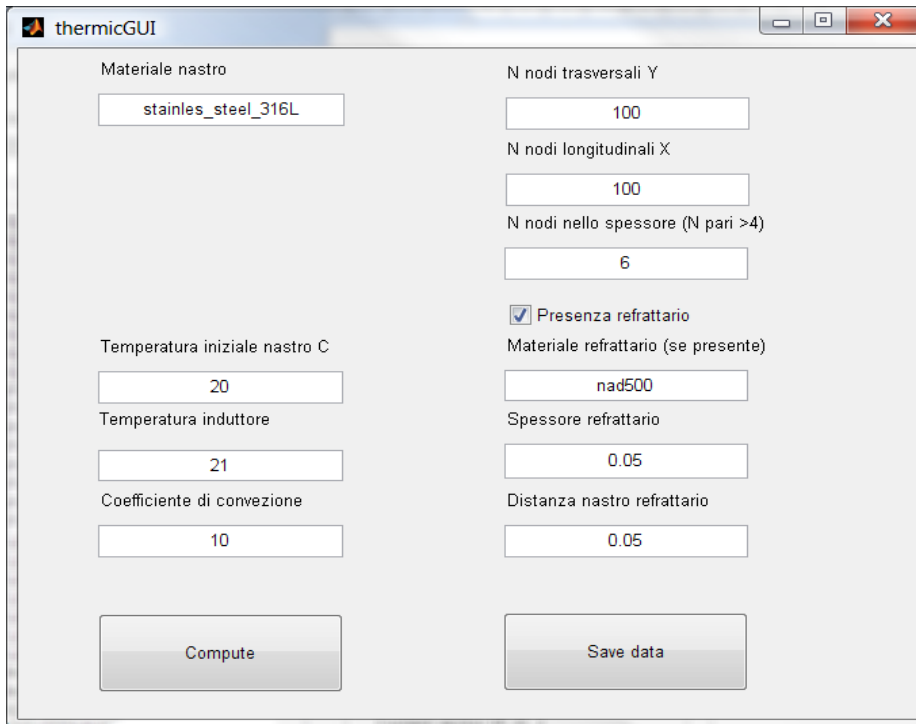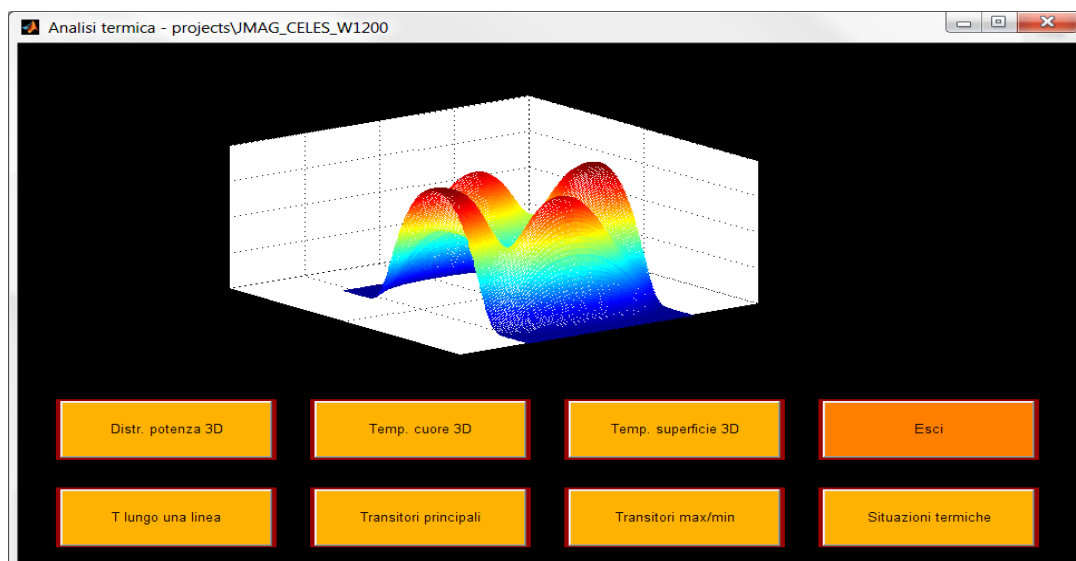
Fig. A.4: Interface of Thermal module

Fig. A.5: Interface of the thermal results module

Appendix B

Steel characteristics

In order to compute the impedance matrix of the MCH inductor, the electrical characteristics of the materials i.e. electrical resistivity and magnetic permeability, of the stainless steel have to be precisely known.

The measurements have been done using an EDF procedure based on the use of an electrical oven provided by a measurement apparatus, which allows to measure the resistivity and the magnetic moment of a test-piece as a function of the temperature.

B.1 Material

The metal used for the impedance measure is an inox steel AISI 316L (UNI X2 CrNiMo 17 12). The declared metallurgic composition of this steel is shown in Tab. B.1.

%C	%Si	%Mn	%P	%S	%Cr	%Mo	%Ni	%Nb+Ta	%Ti	Others
≤0,03	≤1,00	≤2,00	0,05	0,03	17,0 - 19,0	-	9,00- 12,00	-	-	-

Tab. B.1: Metallurgic characteristic of 316L steel

B.2 Resistivity

The resistivity is measured by means of the "4 points method". The measurement scheme is indicated in Fig. B.1. The method consists to connect on the test piece one contact at the extremities to assure the current supply, and two interme-

diate measure points to measure the voltage potential difference. In this way the resistance is measured between the two points of voltage measurement in order to avoid considering the resistance of connection cables and overall of the contact resistance of current supply.

For the connections between the measuring instruments and the test-piece a thermocouple cable of type K (Chromel (Ni-Cr) - Alumel INi-Al)) has been used. The advantage of this type of cable is that it can be used in the range of temperature 200°C-1260°C and that can be simply welded by a resistance welder to the test-piece. In order to limit the direct voltages caused by the thermocouple the alumel cable has been used for the current supply and the chromel cable for the voltage measure.

The circuit configuration for the measure is shown in Fig. B.2. It is composed of a voltage source capable to supply a current of 16A max, a resistance, a shunt resistance of 40 mΩ and Imax=5 A and the test-piece. The current is measured by means of the voltage in the shunt. The voltage on the test piece is measured by a Schlumberger micro-voltmeter.

The test piece is a small bar of stainless steel with rectangular section of 1 x 5.49 mm and a length of 100 mm.

The measure is composed of two steps:

- When the temperature of the test piece is at the desired temperature the resistance supply is switched off. To reduce the temperature fluctuation during the measure the oven cooling is stopped. The voltage due to thermocouple effect is relieved with the μ-voltmetre (typ. 0-3mV).

- The DC current circuit is supplied since the current reach about 5A. The voltage of the test piece is detected by the μ-voltmetre (typ. 4-15mV). The ohmic voltage drop corresponds to the difference between the two measures.
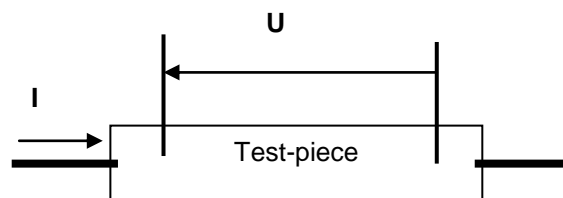

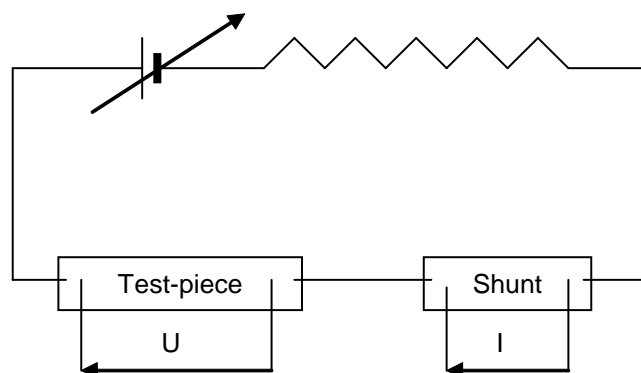**Fig. B.1: Principle of the "4 points" measure**

Fig. B.2: Circuit for the measurement of the resistivity

The measured resistivity is shown in Fig. B.3 as a function of the temperature. This curve has been obtained interpolating the measured data with the following analytical equation:

$$\rho(T) = \rho_\infty \left(\alpha_\infty e^{-\frac{T}{\tau_\infty}} + 1 \right)$$

(B.1)

The numerical values of parameters used in the equations are:

- $\rho_\infty = 160$

- $\alpha_\infty = -0,5525$

- $\tau_\infty = 1128$
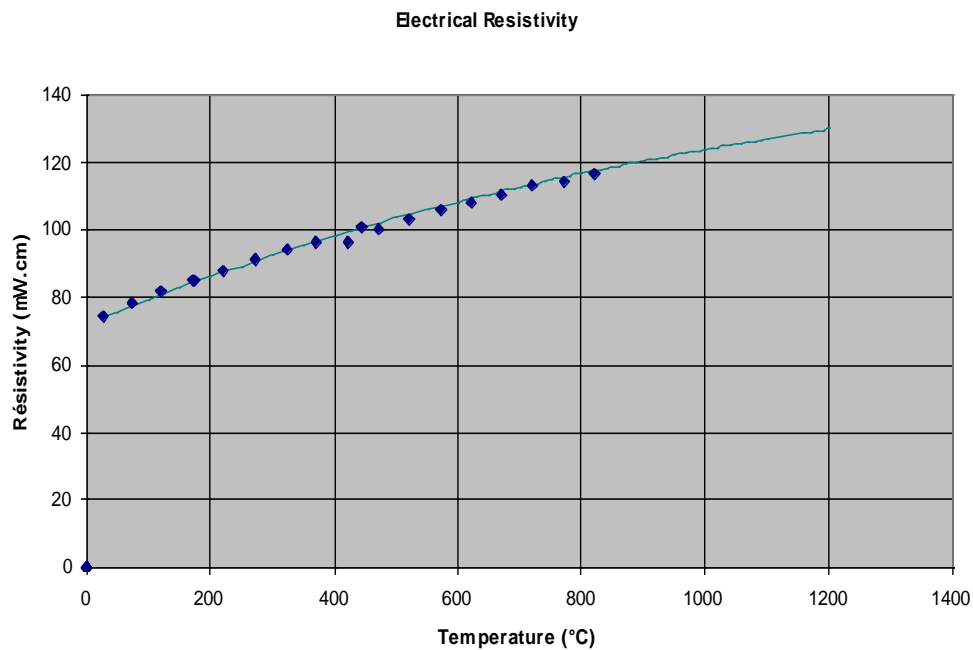
Electrical Resistivity

Fig. B.3: Analytical electrical resistivity in function of the temperature for the 316L Steel with measured data

B.3 Measure of the magnetization characteristic

The magnetization characteristic is obtained thanks to a permeameter commercialized by MPS. The permeameter is composed by:

- An Helmoltz coil able to create a nearly uniform magnetic field with a maximum value of 120 kA/m.

- A cylindrical oven heated by AC resistance with water cooled walls.

- An electrical inductor placed inside the four.

- A thermocouple to be fixed on the test piece.

To trace the magnetization curve the magnetic field H and the magnetic polarization field M, must be measured simultaneously. The magnetic field value is obtained by measurement of the current of Helmoltz coil, measured by means of a shunt resistance in series with the coil.

The magnetic polarization is obtained by the measure of the flux density that flow in two coils, one inside to the other, having the same surface, but with different diameter and number of turns. This allows to compensate the induction of the field coil and to measure only the field (magnetic moment) due to the presence of the piece. The scheme of the apparatus is shown in Fig. B.1.

The apparatus is capable to give signals proportional to magnetic field and to the magnetic polarization that are delivered and reconditioned by means of a YO-KOGAWA oscilloscope. The same instrument can record the file data on a hard disk. The data are after treated with an Excel spreadsheet.

The measurement procedure consists of the following steps:

- When the test piece reach the wanted temperature, the power supply of the heating resistance is switched off on order to eliminate the interference of the excitation field. Also the cooling is stopped in order to reduce the temperature fluctuation during the measurement.

- The test piece is demagnetized by an automatic series of field cycles of decreasing amplitude in the two directions. No measurement is performed in this step. This point is important to determine the correct initial slope of the permeability.

- Finally the instrument measures the curve of first magnetization in the positive direction, and after it makes a complete hysteresis cycle in negative and positive directions. The variation of the temperature of the heating chamber is negligible at low temperature values. At high temperatures instead the temperature varies up to 30°C during the measurement. The temperature is measured by a thermocouple connected to an oscilloscope channel.

The measured magnetization characteristic at room temperature is shown in Fig. B.2 The curve has been obtained interpolating the measured data points at a temperature of 21°C, with the analytical equation:

$$B(H) = \mu_0 H + \frac{2B_s}{\pi} arctg\left(\frac{(\mu_{r0} - 1)\pi}{2B_s} \mu_0 H\right) \tag{B.2}$$

The coefficients used in the equation are:

- Saturation flux density - $B_s = 0.18\ T$

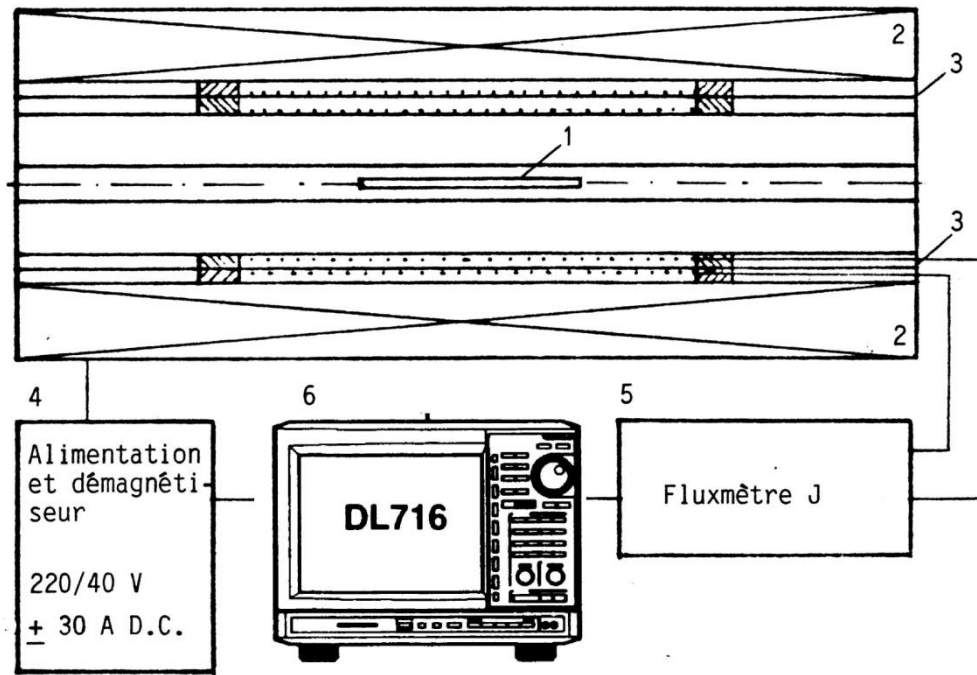- Initial permeability - $\mu_{r0} = 81.41$

Fig. B.1: Test circuit for the measurement of the magnetic permeability.
1 – test-piece, 2 – magnetic field coil, 3 – measurement coil, 4 – power supply,
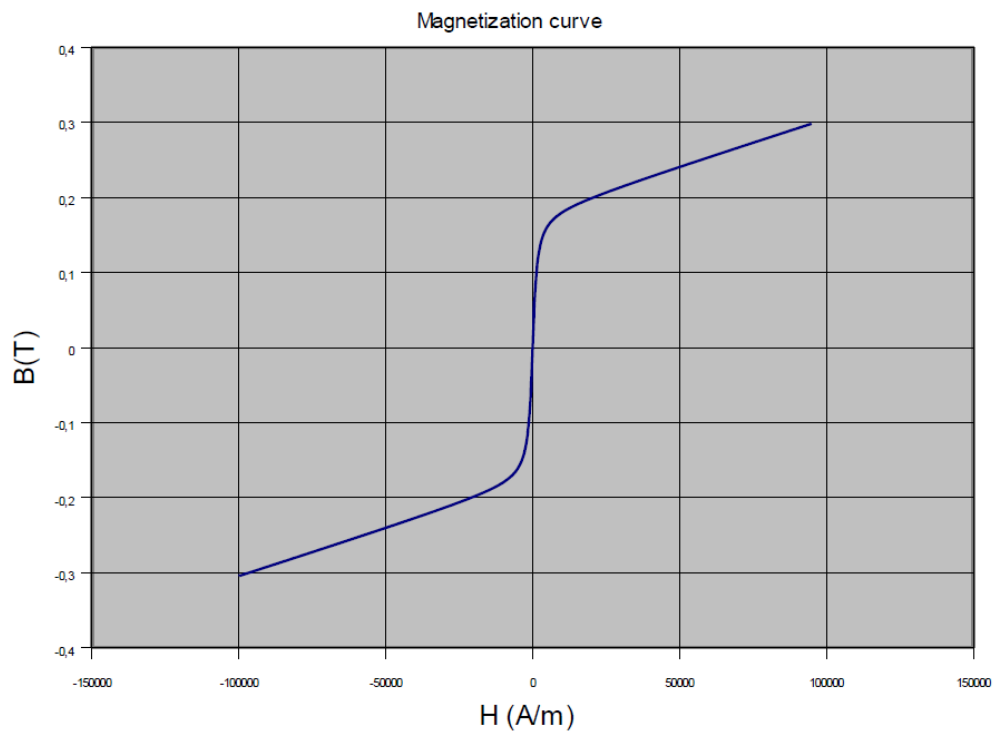**5 – Fluxmeter, 6 – Numeric oscilloscope.**

Fig. B.2: Electrical permeability as a function of the temperature for the 316L
Steel at a temperature of 21 °C

Appendix C

Computation of Planar circular inductors

In this appendix an analytical calculation of circular planar inductors with multiple coils, used for heating metallic plates is considered. The axis-symmetric geometrical configuration analyzed is constituted by a radially extended metallic disk heated by planar coils, placed in front of it on one or both sides, differently connected and independently supplied, with or without external ferromagnetic flux concentrators. The analytical solutions [47], [48] allows to evaluate the system performance (e.g. the induced current and power density distributions, the inductor's integral parameters, the system's impedance matrix, the influence of electrical and geometrical quantities) for a number of practical cases. Due to the low calculation requirements, the analytical solutions are particularly convenient for the system's preliminary optimization design.

C.1 Basic inductor-load system: single layer metal plate with magnetic yoke

The basic system under consideration is shown in Fig. C.1: it consists of one inductor constituted by several concentric planar circular coils of negligible axial thickness, each characterized by N concentric turns in which a sinusoidal current $I = Ie^{j\varphi}$ of angular frequency ω flows; the coils are placed in front and parallel to a load constituted by a metallic (or bimetallic) plate. The load has radial dimensions much larger than the inductor and is characterized by constant values of the electrical resistivity ρ and the relative magnetic permeability μ ; the system comprises an external ideal magnetic yoke of infinite permeability and no losses.

This configuration is typically used in the heating of carbon graphite disks for semiconductor-wafer processing, the brazing or hot-pressing of bottom Al disks on stainless steel cooking saucepans and the induction heating systems for domestic cooking.

With reference to a system of cylindrical coordinates (r,φ,z) the components of the electromagnetic field are functions of r and z only and independent on φ and the following equations hold for the magnetic potential vector $\overline{A}$:

$$\frac{\partial^2 \overline{A}}{\partial r^2} + \frac{1}{r}\frac{\partial \overline{A}}{\partial r} - \frac{\overline{A}}{r^2} + \frac{\partial^2 \overline{A}}{\partial z^2} \begin{cases} = 0 & \text{in air} \\ = j\,\dfrac{\omega\mu_0\mu}{\rho}\,\overline{A} & \text{in the metal} \end{cases} \tag{C.3}$$

Considering that in the geometry of Fig. C.1, only the azimuthal component of the magnetic potential vector is non zero, the solutions of eqns. (C.3) (for the different regions and for each exciting coil), can be written as follows:

$$\overline{A}_0 = \overline{A}_{0e} + \overline{A}_{0r} = \int_0^\infty \frac{\mu_0 N\overline{I}}{2(R_e - R_i)} \cdot C_{0e}(k)\left[e^{-k|z-h|} + F_0(k)\cdot e^{+kz} + G_0(k)\cdot e^{-kz}\right] J_1(kr)\,dk \tag{C.4}$$

$$\overline{A}_1 = \int_0^\infty \frac{\mu_0 N\overline{I}}{2(R_e - R_i)} \cdot C_{0e}(k)\cdot\left[F_1(k)\cdot e^{+\beta z} + G_1(k)\cdot e^{-\beta z}\right] J_1(kr)\,dk \tag{C.5}$$

$$\overline{A}_2 = \int_0^\infty \frac{\mu_0 N\overline{I}}{2(R_e - R_i)} \cdot C_{0e}(k)\cdot\left[F_2(k)\cdot e^{+kz} + G_2(k)\cdot e^{-kz}\right] J_1(kr)\,dk \tag{C.6}$$

with:

$$C_{0e}(k) = \int_{R_i}^{R_e} r\,J_1(kr)\,dr \qquad \text{and} \qquad \beta^2 = k^2 + j\,\frac{\omega\mu\mu_0}{\rho} \tag{C.7}$$
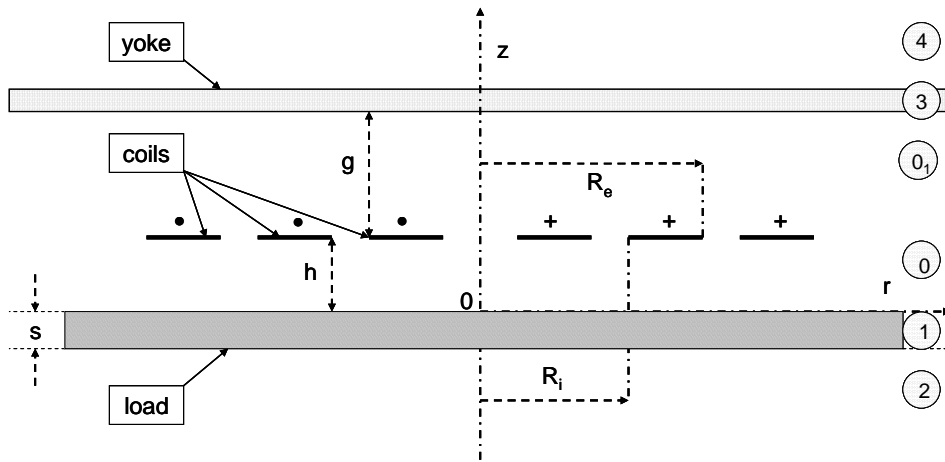

Fig. C.1: Schematic of the basic inductor-load system with several concentric coils, a metallic disc and an external ideal magnetic yoke

The symbols used in the above eqns., besides those defined in Fig. C.1, are: $\overline{A}_{0e}$ (and the corresponding first term of eqn. (C.4) in square brackets) - exciting potential vector produced by one source coil in the absence of the load; $\overline{A}_{0r}$ - so called reaction field potential of the load; $J_1(kr)$ - Bessel function of first kind and

first order; R_i, R_e - inner and outer radii of the coil; μ_0 - magnetic constant of vacuum; $F_0, G_0, F_1, G_1, F_2, G_2$ - unknown complex coefficients which can be determined by applying the relevant continuity conditions of the potential vector and its derivatives at the boundaries of the various regions.

Since the considered axis-symmetrical domain is infinitely extended in radial and axial directions and the material characteristics are uniform along the radial coordinate, the interface boundary conditions must be imposed on the values of the vector potential, or on his derivative on lines parallel to the radial direction.

For the case here considered, the boundary conditions specified in Tab. C.2 apply :

Interface 0-1 (at z = 0)		Interface 1-2 (at z = - s)	Interface 0-3 (at z = h+g)
$\overline{A}_0 = \overline{A}_1$ and	$\dfrac{\partial \overline{A}_0}{\partial z} = \dfrac{1}{\mu} \dfrac{\partial \overline{A}_1}{\partial z}$	$\overline{A}_1 = \overline{A}_2$	$\dfrac{\partial \overline{A}_0}{\partial z} = 0$

Tab. C.2: Boundary conditions

Moreover, a) in the region 4 the field is null due to the shielding effect of the ideal magnetic yoke; b) in the region 2 the term F_2 must be eliminated to satisfy the condition of null vector potential at the infinite.

From the above, a system of equations on the coefficients F and G results; in particular:

a) at the interface 1-0 the condition imposed to the potential vector at $z = 0$ gives:

$$F_0(k) + G_0(k) - F_1(k) - G_1(k) = -\, e^{-kh} \tag{C.8}$$

The boundary condition for the derivatives at the same interface, gives:

$$k\, F_0(k) - k\, G_0(k) + \frac{\beta}{\mu}\, F_1(k) - \frac{\beta}{\mu}\, G_1(k) = k \cdot e^{-kh} \tag{C.9}$$

b) At the interface 1-2 the argument of the integral is null for $z = -s$ if:

$$F_1(k)\, e^{-\beta s} + G_1(k)\, e^{\beta s} - F_2(k)\, e^{-ks} = 0 \tag{C.10}$$

while the condition on the derivatives becomes:

$$\frac{\beta}{\mu} \cdot F_1(k)\, e^{-\beta s} - \frac{\beta}{\mu} \cdot G_1(k)\, e^{\beta s} - k\, F_2(k)\, e^{-ks} = 0 \tag{C.11}$$

c) At the interface 3-0 ($z = h + g$), the magnetic field H is orthogonal to the surface of the ideal ferromagnetic layer and the tangential component of the magnetic field is null [49].

Considering eqn. (C.2) of the potential vector in the air region, the above boundary condition gives:

$$-k\, F_0(k)\, e^{k(h+g)} + k\, G_0(k)\, e^{-k(h+g)} = -k \cdot e^{-kg} \tag{C.12}$$

This procedure leads to a system of equations in number equal to the number of the unknown coefficients F and G which can be written in the matrix form (C.13).

The solution of the system (C.13) allows to completely define the potential vector in the various regions through the eqns. (C.4) to (C.7); the subsequent evaluation of the field components must be done by numerical integration.

$$
\begin{bmatrix}
1 & 1 & -1 & -1 & 0 \\
-k & k & \dfrac{\beta}{\mu} & -\dfrac{\beta}{\mu} & 0 \\
0 & 0 & e^{-\beta s} & e^{\beta s} & -e^{-ks} \\
0 & 0 & \dfrac{\beta}{\mu}e^{-\beta s} & -\dfrac{\beta}{\mu}e^{\beta s} & -\dfrac{k}{\mu}e^{-ks} \\
-k\,e^{k(h+g)} & k\,e^{-k(h+g)} & 0 & 0 & 0
\end{bmatrix}
\cdot
\begin{bmatrix}
F_0 \\ G_0 \\ F_1 \\ G_1 \\ F_2
\end{bmatrix}
=
\begin{bmatrix}
-e^{-kh} \\ k\cdot e^{-kh} \\ 0 \\ 0 \\ -k\cdot e^{-kg}
\end{bmatrix}
\tag{C.13}
$$

In particular, from the vector potential A_1 the current density in the plate, induced by a single excited coil, can be evaluated as:

$$
\overline{G}_1 = \overline{E}_1/\rho = -j\omega \overline{A}_1(r,z)/\rho
\tag{C.14}
$$

Taking into account the linearity of the system, the potential vector and the field quantities due to an inductor constituted by several coils can be obtained by superposition of the contribution of each coil.

Moreover, the values of self and mutual impedances of the coils can be found by the calculation of the e.m.f. induced in one coil, due to the current in the same or in another coil. From the vector potential it is also easy to calculate all the field values in the different regions and the mutual impedances $\overline{Z}_{m,n}$ seen at the terminals of the *n-th* coil due to the current in the *m-th* one:

$$
\overline{Z}_{m,n} = -\frac{\overline{E}_n^m}{\overline{I}_m} = -\frac{\displaystyle\int_{R_i^n}^{R_e^n} \overline{e}_{wn}^m \cdot \frac{N_n}{(R_e^n - R_i^n)}\,dr}{\overline{I}_m}
\tag{C.15}
$$

where $\overline{I}_m$ is the exciting current of *m-th* coil, N_n the number of turns of *n-th* coil, R_i^n and R_e^n the internal and external radius of the *n-th* coil and $\overline{e}_{wn}^m$ the *emf* induced in a filament turn at radius *r* of the *n-th* coil by the flux produced by the current $\overline{I}_m$, given by [50]:

$$
\overline{e}_{wn}^m = -j\,\omega\,2\pi\,r\,\overline{A}_0^m(r,h)
\tag{C.16}
$$

$\dot{Z}_{m,n}$ can be finally computed by eqns. (13), (14) and (2) with z=h:

$$
\overline{Z}_{m,n} = -\frac{\overline{E}_n^m}{\overline{I}_m} = j\,\frac{\pi\,\omega\mu_0 N_m N_n}{(R_e^m - R_i^m)(R_e^n - R_i^n)}\int_0^\infty C^m_{0e}(k)\cdot C^n_{0e}(k)\cdot\left[1 + F_0^m(k)e^{+kh} + G_0^m(k)e^{-kh}\right]dk
$$

$$
\tag{C.17}
$$

C.2 Other system configurations

The general method discussed before can be applied in a number of cases of practical interest. In this paper it will be further examined the case of inductors without magnetic yoke and with multiple coils symmetrically placed on the two sides of a single-layer disk, as shown e.g. in fig. 2 for an inductor with three coils on each side of the load and different excitations conditions which correspond to currents in the upper and lower coils respectively in phase (TFH – Transverse Flux Heating) or in phase opposition (RFH – Radial Flux Heating).

TFH		RFH	
Interface 1-0 (z=0)	$\overline{A}_0 = \overline{A}_1$; $\dfrac{\partial \overline{A}_0}{\partial z} = \dfrac{1}{\mu_1} \dfrac{\partial \overline{A}_1}{\partial z}$	Interface 1-0 (z=0)	$\overline{A}_0 = \overline{A}_1$ $\dfrac{\partial \overline{A}_0}{\partial z} = \dfrac{1}{\mu_1} \dfrac{\partial \overline{A}_1}{\partial z}$
Interface 0-symm (z=-s)	$\dfrac{\partial \overline{A}_1}{\partial z} = 0$	Interface 0-symm (z=-s)	$\overline{A}_1 = 0$
$\begin{bmatrix} 1 & -1 & -1 \\ k & \dfrac{\beta}{\mu} & -\dfrac{\beta}{\mu} \\ 0 & \beta e^{-\beta s} & -\beta e^{\beta s} \end{bmatrix} \cdot \begin{bmatrix} G_0 \\ F_1 \\ G_1 \end{bmatrix} = \begin{bmatrix} -e^{-kh} \\ -k \cdot e^{-kh} \\ 0 \end{bmatrix}$		$\begin{bmatrix} 1 & -1 & -1 \\ k & \dfrac{\beta}{\mu} & -\dfrac{\beta}{\mu} \\ 0 & e^{-\beta s} & e^{\beta s} \end{bmatrix} \cdot \begin{bmatrix} G_0 \\ F_1 \\ G_1 \end{bmatrix} = \begin{bmatrix} -e^{-kh} \\ -k \cdot e^{-kh} \\ 0 \end{bmatrix}$	

Fig. C.3: Systems with symmetrical multiple coil inductors, without magnetic yoke and single-layer load: TFH and RFH excitation with corresponding boundary conditions and matrices for evaluation of magnetic vector potentials

For the TFH and the RFH excitations, different symmetry conditions can be imposed on the central line of the plate parallel to the radius:

In the first case, i.e. TFH with currents in the upper and lower coils in phase, the conditions of normal magnetic field and null tangential component of the magnetic field can be exploited, giving a condition on the derivative of the potential vector.

In the second case - RFH - the condition of tangential magnetic field imposes a null normal flux on the work-piece symmetry line which can be set imposing a null potential vector on the whole line.

This last kind of symmetry can be used also to impose the interface condition in case of the presence of a ferromagnetic yoke with infinite permeability.

In the table of Fig. C.3 the resulting matrix systems for the determination of the unknown coefficients F_1, G_0, G_1 are also given.

As the equations of the vector potential are the same of the same given in the paragraph C.1, the impedance formulas are the same when the appropriate coefficients are used.

C.3 Numerical evaluation of the analytical solutions (basic system)

The evaluation of the integrals that appear in the solving equations can be done by numerical integration. The integration can be conveniently done applying the Gauss-Laguerre quadrature formulae, which give the following relationships for the calculation of the main parameters:

- Current density in the load:

$$G(r,z) = -j \frac{\omega}{\rho_n} \frac{\mu_0 N \overline{I}}{2(R_e - R_i)} \cdot \sum_{v=1}^{m} W_v \, e^{x_v} \, C_{0e}(k) \left[F_n(x_v) \, e^{\beta_{vn} z} + G_n(x_v) \, e^{-\beta_{vn} z} \right] J_1(x_v \, r)$$

where:

$$\beta_{vn} = \sqrt{x_v^2 + \frac{2j}{\delta_n^2}} \; ; \; m - \text{integration order}$$

x_v, W_v – abscissas and integration weights factors of Gauss-Laguerre integration.

Impedance of the inductor-load system:

$$\dot{Z}_{ij} = -\frac{\overline{E}_{ij}}{I_j} = j\pi\omega \frac{\mu_0 N^j N^i}{\left(R_e^j - R_i^j\right)\left(R_e^i - R_i^i\right)} \sum_{v=1}^{n} W_v \, e^{x_v} C^j_{0e}(x_v) \cdot C^i_{0e}(x_v) \cdot \left[1 + F_0^j(x_v) e^{+x_v h} + G_0^j(x_v) e^{-x_v h} \right]$$

It is therefore necessary, after the choice of the integration order m, to evaluate the corresponding values of F0, F1, F2, G0, G1, G2 for each value of x_v. Very high integration orders are necessary.

References

[1] B. Nacke, A. Muhlbauer, A. Nikanorov, G. Nauvertat, and H. Schulbe, "Transverse Flux Heating in Modern Energy Saving Lines for Metal Rolling and Treatment," in *Proceedings of International Scientific Colloquium Modelling for Saving Resources*, Riga, 2001.

[2] EU, "EU climate and energy saving package."

[3] H. Fujita, N. Uchida, and K. Ozaki, "Zone controlled induction heating (ZCIH) A new concept in induction heating," *Power Conversion Conference Nagoya (Japan) 2007*, pp. 1498-1504.

[4] A. M. Souley, "Contribution à l'etude et à la commande d'un systeme de chauffage par induction polyphasé," PhD, Université de Toulouse, 2011.

[5] G. Manot, "Modelisation couplee des dispositifs electromagnetiques associes a des circuits d'electronique de puissance. Integration de la commande des convertisseurs - aide a la conception d'undispositif de chauffage par induction a flux transvers," PhD, LAPLACE Laboratories Toulouse, 2003.

[6] A. Muhlbahuer, *History of induction heating and melting*. Vulkan.

[7] V. Rudnev, D. Loveless, R. Cook, and M. Black, *Handbook of induction heating*. .

[8] V. Demidovitch, A. Nikanorov, and A. Slukhotskii, "Energy parameters of induction transverse strip heaters," 1989.

[9] V. Peysakhovic, "Energetic relationships in the heating of flat metal products," *Proceedings of VNIITVCH*, vol. 7, pp. 41-57, 1966.

[10] A. Aliferov and S. Lupi, *Induction and conduction heating of metals (In russian)*, Novosibirsk State Technical University NSTU. 2011.

[11] V. Bukanin, F. Dughiero, S. Lupi, and A. Zenkov, "Edge effects in planar induction heating systems," *Proceedings di HIS-01, International Seminar on Heating by Internal Sources, Padua (Italy)*, pp. 533-538, Sep. 2001.

[12] M. Zlobina, S. Galunin, Y. Blinov, B. Nacke, A. Nikanorov, and H. Schulbe, "Numerical Modelling of Non-Linear Transverse Flux Heating Systems," in *Proceedings of International Scientific Colloquium MEP 2003 Modelling for Electromagnetic Processing, Hanover (Germany)*, 2003, pp. 51-56.

[13] A. Kuvaldin, *Low temperature induction heating of steel (In Russian)*, Energhia. Moskow, 1976.

[14] A. Nikanorov, H. Schulbe, B. Nacke, M. Zlobina, S. Galunin, and Y. Blinov, "Non linear effects in transverse flux heating systems," *Proceedings di HES-04, International Seminar on Heating by Internal Sources Padua (Italy)*.

[15] A. Ruhnke, A. Mulbahuer, A. Nikanorov, and V. Demidovitch, "Thermal deformation od the strip during transverse flux induction heating," *COMPEL: The International Journal for Computation and Mathematics in Electrical and Electronic Engineering*, vol. 19, p. 730, 2000.

[16] V. Fireteanu and T. Tudorache, "Electromagnetic forces in transverse flux induction heating," *IEEE Transactions on Magnetics*, vol. 36, p. 1792, 2000.

[17] Y. Neau, B. Paya, T. Tudorache, and V. Fireteanu, "Numerical Evaluation nd Experimental Validation of Eddy Currents and Electromagnetic Forces in Transverse Flux Induction Heating of Magnetic Steel Sheets," *Proceedings of EPM 2000 International Symposium on Electromagn Process Materials, Nagoya (Japan)*, pp. 211-217.

[18] T. Tudorache, "Magneto-thermal-motion coupling in transverse flux heating," *COMPEL: The International Journal for Computation and Mathematics in Electrical and Electronic Engineering*, vol. 27, no. 2, pp. 399-407, Jan. 2008.

[19] Y. Naeu et al., "High Power (3 MW) transverse flux inductor for industrial heating," *Proceedings of the International Conference EPM 2003 Electromagnetic Processing of Materials Lyon (France)*, pp. 570-575, Oct. 2003.

[20] H. Schulbe, A. Nikanorov, and B. Nacke, "Flexible Transverse Flux Heaters of Metal Strip," *Proceedings of the International symposium HES-04 Heating by Electromagnetic Sources, Padua (Italy)*, pp. 293-300, Jun. 2004.

[21] J. C. Thorpe, H. G. Heine, and V. Peysakhovic, "Transverse flux induction heating apparatus," U.S. Patent United States Patent 6576878.

[22] N. V. Ross, "Apparatus for the continuous induction heating of metallic strip," U.S. Patent United States Patent 475136014-Jun-1988.

[23] W. B. Jackson, "Transverse flux induction heating of flat metal products," *Proceedings of 7th UIE Congress, Warsav (Poland)*, 1972.

[24] W. Haubitzer, "Die optimierung von querfeld-induktoren zur kontinuierlichen blecherwarmung," *Electrowarme International*, 1984.

[25] A. Muhlbahuer et al., "Numerical Tools for Optimum Design of Transverse Flux Induction Heating of Non-Ferrous Metal Strip," in *Proceedings of EPM 2000 International Symposium on Electromagn Process Materials, Nagoya (Japan)*, 2000.

[26] Cedrat, "Inca3D user manual."

[27] Cedrat, "Flux user manual."

[28] "www.jmag-international.com."

[29] V. Fireteanu and T. Tudorache, "Couplings of electromagnetic field formulations in finite element analysis of transverse flux induction heating systems," in *Proceedings of ISEF 2005 - XII International Symposium on Electromagnetic Fields in Mechatronics, Electrical and Electronic Engineering Baiona (Spain)*, 2005, pp. 156-161.

[30] O. Biro and K. Preis, "Finite element analysis of 3-D eddy currents," *IEEE Transactions on Magnetics*, vol. 26, no. 2, pp. 418-423, 1990.

[31] Fishman, Lampi, Mortimer, and Peysakhovich, "Induction heating device and process for the controlled heating of a non-electrically conductive material," U.S. Patent US6121592.

[32] J. Simcock, "Multiple zone induction heating," U.S. Patent 5059762.

[33] V. Esteve, J. Pardo, J. Jordan, E. Dede, E. Sanchis-Kilders, and E. Maset, "High Power Resonant Inverter with Simultaneous Dual-frequency Output," in *Power Electronics Specialists Conference, 2005. PESC '05. IEEE 36th*, 2005, pp. 1278-1281.

[34] D. Miyagi, A. Saitou, N. Takahashi, N. Uchida, and K. Ozaki, "Improvement of zone control induction heating equipment for high-speed processing of semiconductor devices," *IEEE Transactions on Magnetics*, vol. 42, no. 2, pp. 292-294, 2006.

[35] Y. Okamoto et al., "Optimal design of induction heating equipment for high-speed processing of a semiconductor," *COMPEL: The International Journal for Computation and Mathematics in Electrical and Electronic Engineering*, vol. 23, no. 4, pp. 1045-1052, 2004.

[36] F. Forest, E. Laboure, F. Costa, and J. Gaspard, "Principle of a Multi-Load/Single

ConverterSystem for Low Power Induction Heating," *IEEE Transactions on Power Electronics*, vol. 15, no. 2, pp. 223-230, 2000.

[37] J. Spreen, "Electrical terminal representation of conductor loss in transformers," *IEEE Transactions on Power Electronics*, pp. 424 - 429, Oct-1990.

[38] Y. Cooren, M. Clerc, and P. Siarry, "Performance evaluation of TRIBES, an adaptive particle swarm optimization algorithm," *Swarm Intelligence*, vol. 3, no. 2, pp. 178, 149, Giugno. 2009.

[39] L. D. S. Coelho and P. Alotto, "Tribes Optimization Algorithm Applied to the Loney's Solenoid," *IEEE Transactions on Magnetics*, vol. 45, no. 3, pp. 1526-1529, 2009.

[40] M. Souley et al., "Methodology to characterize the impedance matrix of multi-coil induction heating device," *Proceedings of International Conference EPM 2009 Electromagnetic Processing of Materials, Dresden (Germany)*, Oct. 2009.

[41] Mathworks, *Matlab optimization Toolbox User Manual*. .

[42] Fluxtrol Inc., *www.fluxtrol.com*. .

[43] M. Battistetti, F. Dughiero, S. Lupi, M. Farina, P. Di Barba, and A. Savini, "Optimal Design of an Inductor for Transverse-Flux Heating using a Combined Evolutionary-Simplex Method," *COMPEL: The International Journal for Computation and Mathematics in Electrical and Electronic Engineering*, vol. 20, no. 2, pp. 507-522, 2001.

[44] S. Galunin, M. Zlobina, Y. Blinov, B. Nacke, A. Nikanorov, and H. Schulbe, "Numerical optimization in design of induction heating systems," *Proceedings di HES-04, International Seminar on Heating by Internal Sources, Padua (Italy)*.

[45] P. Alotto, A. Spagnolo, and B. Paya, "Particle swarm optimization of a multi coil transverse flux induction heating system," *Proceedings of Biennal international conference CEFC 2010 Computation of electromagnetic fields, Chicago (Illinois USA)*, pp. 1-1, May. 2010.

[46] A. Gentilucci, "Analysis of JMAG performances," Université de Toulouse, 2011.

[47] S. Lupi, "The Calculation of Planar Circular Coils for the Induction Heating of Bimetallic Plates," *Archiv fur Elektrotechnik*, vol. 60, pp. 313-318, 1978.

[48] S. Lupi, E. Sieni, and A. Spagnolo, "Analytical calculation of planar circular coils induction heating systems," in *Proceedings of HES-10 International Symposium on Heating by Electromagnetic Sources, Padua (Italy)*, 2010, pp. 121-128.

[49] A.D. Podoltsev, I.N. Kucheryavaya, and B.B Lebedev, "Analysis of effective resistance and eddy-current losses in multiturn winding of high-frequency magnetic components," *IEEE Transactions on Magnetics*, vol. 39, no. 1, pp. 539-548, 2003.

[50] M.S. Adler, "A field-theoretical approach to magnetic induction heating of thin circular plates," *IEEE Transactions on Magnetics*, vol. 10, no. 4, pp. 1118-1125, 1974.

Acknowledgements